UCL

The role of $\pi\sigma^*$ states in the ultrafast non-radiative dynamics of pyrrole, aniline and phenol

Oliver Michael Kirkby

A thesis submitted for the degree of

Doctor of Philosophy

University College London (UCL)

January 2015

I, Oliver Michael Kirkby, confirm that the work presented in this thesis is my own. Where information has been derived from other sources, I confirm that this has been indicated in the thesis.

Abstract

This thesis comprises three time-resolved photoelectron imaging (TRPEI) studies, examining the ultraviolet (UV) photorelaxation dynamics of molecules with low-lying $\pi\sigma^*$ states. Chapter 1 introduces important principles in molecular photochemistry, wavepacket dynamics and the relaxation mechanisms enabled by these $\pi\sigma^*$ states. Chapter 2 describes the experimental apparatus and data analysis techniques used to extract information from TRPEI spectra. Chapters 3–5 contain the experimental data.

Chapter 3 examines the UV photorelaxation dynamics of pyrrole, where the lowest excited singlet state is of $\pi\sigma^*$ character. We observe a single sub-50 fs, dissociative decay for all wavelengths studied, in keeping with the literature. The pyrrole dimer is used as a model for microsolvation, where a new decay pathway opens, relating to relaxation into stabilised charge transfer states.

Chapter 4 details the experimental study of aniline. Direct excitation to the $S_2(\pi\sigma^*)$ state with various excess vibrational energies, shows that the S_2/S_1 conical intersection is located close to the $S_2(\pi\sigma^*)$ origin and enables the dominant $S_2 \rightarrow S_1$ internal conversion mechanism. Population on the $S_1(\pi\pi^*)$ surface (following relaxation from the S_2 or direct excitation) undergoes considerably slower internal conversion to the ground state, the invariance of these decay times in deuterated aniline suggests that $S_1 \rightarrow S_2$ tunnelling is not favoured.

Chapter 5 studies the UV photodynamics of phenol, finding that internal conversion to the ground state is the dominant relaxation mechanism from the $S_1(\pi\pi^*)$ state, in agreement with the literature. Increasing the excitation energy to access to the $S_2(\pi\sigma^*)$ state opens a minority pathway to O-H dissociation, but IVR on the S_1 surface followed by internal conversion continues to dominate.

Finally, Chapter 6 summarises the surprising variety of mechanisms that $\pi\sigma^*$ states are found to facilitate, even in these closely related molecules, and provides an outlook for future work.

The work presented in this thesis is based upon the following publications:

Chapter 3:

- O.M. Kirkby and H.H. Fielding,
  'Time-resolved dynamics of pyrrole and solvent-induced electron transfer following excitation in the region 249.5–200 nm'
  In preparation

- O.M. Kirkby,
  'General discussion'
  Faraday Discussions (2012) **163**, 117–138

Chapter 4:

- O.M. Kirkby, G. Balerdi, M. Sala, S. Guerin, R. de Nalda, L. Banares, N. Kaltsoyannis and H.H. Fielding,
  'Competing non-radiative decay mechanisms in aniline and deuterated aniline, following excitation in the range 272–238 nm'
  In preparation

Chapter 5:

- O.M. Kirkby and H.H. Fielding, 'Time-resolved dynamics of phenol following excitation in the region 275–200 nm'
  In preparation

In addition, contributions were made to the following publications:

- M. Sala, O.M. Kirkby, S. Guerin and H.H. Fielding,
  'New insight into the potential energy landscape and relaxation pathways of photoexcited aniline from CASSCF and XMCQDPT2 electronic structure calculations'
  Physical Chemistry Chemical Physics (2014) **16**, 3122–3133

- R. Spesyvtsev, O.M. Kirkby and H.H. Fielding,
  'Ultrafast dynamics of aniline following 269-238 nm excitation and the role of the $S_2(\pi 3s/\pi\sigma^*)$ state'
  Faraday Discussions (2012) **157**, 165–179

- R. Spesyvtsev, O.M. Kirkby, M. Vacher and H.H. Fielding,
  'Shedding new light on the role of the Rydberg state in the photochemistry of aniline'
  Physical Chemistry Chemical Physics (2012) **14**, 9942–9947

- T.J. Penfold, R. Spesyvtsev, O.M. Kirkby, R.S. Minns, D.S.N. Parker, H.H. Fielding and G.A. Worth,
  'Quantum dynamics study of the competing ultrafast intersystem crossing and internal conversion in the "channel 3" region of benzene'
  The Journal of Chemical Physics (2012) **137**, 204310–204312

This thesis won the UCL Chemistry, 2013 Apley Prize for 'Best PhD Thesis Outline'.

Acknowledgements

I would like to give my sincere thanks to the following people, without whom I wouldn't have been able to complete this project. My supervisors Prof. Helen Fielding and Prof. Nik Kaltsoyannis for this opportunity to work with them on a diverse set of problems. I would like to thank Prof. Fielding for her energy, patience and guidance throughout this journey and to thank Prof. Kaltsoyannis for his continual support and enthusiasm throughout, even when the project moved further from his areas of interest.

Roman Spesyvtsev for his help and guidance throughout the first two years of this project, for teaching me to work safely and carefully in our lab environment and working through the rigors of analysis. Ciaran Mooney for constant discussions, for moral support and encouragement throughout long days in the lab and also for lending an essential extra pair of hands on countless occasions. Garikoitz Balerdi Villanueva for his help collecting the experimental data in Chapter 4. Mattieu Sala for his helpful discussions regarding the excited states of aniline. Russell Minns for teaching me the fundamentals of photodynamics and lasers, for helping out with his magic 'green fingers' whenever I got stuck in the lab and for being my troubleshooting hotline. I would also like to thank Russell for giving me the opportunity to help out on an interesting project at the ARTEMIS facility. The collaborators with whom I worked with at Artemis; Felix Frank, Emma Springate, Edmund Turcu, Vas Stavros and Gareth Roberts. Graham Worth and Simon Neville for many helpful discussion over the course of this project and for running many of the supporting calculations on pyrrole, which aided the understanding of the experimental work in Chapter 3.

I would also like to thank the EPSRC for their funding *via* the UCL doctoral training centre for Atomic and Molecular Control.

I would like to thank my parents for their help and support throughout my whole university career, and indeed life in general. Lastly and most importantly, I would like to thank my partner, Rebecca Schult for her unending support and love every day.

Contents

List of Figures

List of Tables

Chapter 1

Introduction

Sunlight is essential for life, but also contains ultraviolet (UV) radiation ($\lambda <$ 400 nm) capable of inducing electronic excitations in molecules. This is particularly important in biological chromophores, such as the DNA bases and amino acids, where UV-induced photochemical processes can trigger a chain of reactions that result in catastrophic damage and can subsequently lead to the destruction of cells by mutagenesis and carcinogenesis [1, 2]. Fortunately, many biological chromophores are considerably more photostable than other, similar molecules [3], due to efficient relaxation processes which convert dangerous electronic excitations into less dangerous vibrational or translational motions [4–8]. In order for relaxation processes to dominate, they must occur on a timescale that is faster than the competing photochemical reactions. The most rapid photochemical reactions occur on the timescale of molecular vibrational motion, which is typically on the order of hundreds of femtoseconds (1 fs = 10^{-15} s) and consequently experiments to monitor the competition between such processes require temporal resolution of this magnitude.

Substituted aromatics form a common motif amongst biological chromophores and the UV absorption spectra of such species are typically dominated by strong transitions to $^1\pi\pi^*$ states. Many of these molecules also have low-lying dissociative states of $^1\pi\sigma^*$ or $^1n\sigma^*$ character [9], which can be populated directly, albeit weakly, or indirectly by internal conversion from the optically bright $^1\pi\pi^*$ states. Since Sobolewski *et al.* [10] proposed that these dissociative states play an important role in the non-radiative decay of various biological chromophores, there has been interest in studying the photochemistry of substituted aromatics, in particular the role of $\pi\sigma^*$ states in this relaxation [11, 12]. This is the subject of the work presented in this thesis.

This thesis uses time resolved photoelectron imaging (TRPEI) (as described in Section 1.2), to examine the evolution of population in electronically excited states and to visualise the associated decay mechanisms. The TRPEI technique allows for both excellent control in the preparation of excited electronic states and a sensitive probe of the system dynamics following excitation. We have focussed on performing experiments in the gas phase, as this allow us to examine the evolution of the system without the complication of solvent effects.

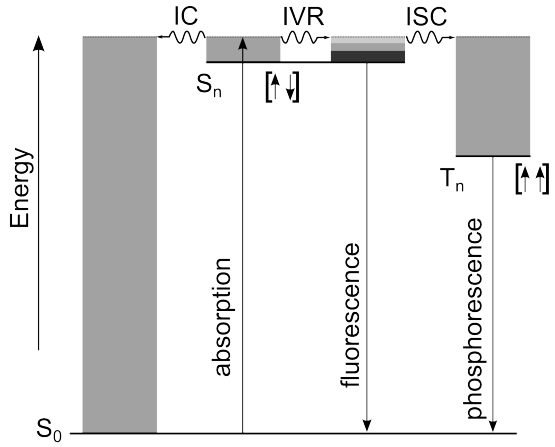

Figure 1.1: Jablonski diagram illustrating common intramolecular photophysical processes: absorption, intramolecular vibrational relaxation (IVR), fluorescence, internal conversion (IC), intersystem crossing (ISC), phosphorescence. Straight arrows represent radiative processes, while undulating arrows represent non-radiative transitions. The shaded blocks represent vibrational energy within a particular electronic state.

1.1 Excited state photophysical processes

Excited states are challenging to examine for many reasons, not least due to their inherent instability. When a molecule absorbs light, the energy of the photon is converted to internal energy, leading to a redistribution of charge and/or an increase in vibrational or rotational energy.

Various decay routes from electronically excited states are possible and many of the most common photophysical processes are illustrated in Figure 1.1. Closed-shell molecules have a singlet electronic ground state (S_0) and absorption of light enables promotion to an electronically excited singlet-state, S_n, because spin conserving absorption is typically favoured. Any excess vibrational energy in the excited state can be redistributed radiationlessly amongst stable vibrations *via* anharmonic couplings; this process is known as intramolecular vibrational redistribution (IVR). Following excitation, the molecule can return to the S_0 state by emitting the absorbed energy as fluorescence or by internal conversion (IC), a radiationless redistribution of the internal energy which maintains spin. Formally only states of the same sym-

metry should undergo IC, however in molecular systems vibronic coupling often relaxes rigorous symmetry constraints. Alternatively, the molecule in its S_n state can convert to a triplet state, T_m, by intersystem crossing (ISC). This type of transition is spin-forbidden, but can often occur due to spin-orbit coupling (usually to the first excited triplet T_1). Since the T_1 to S_0 transition is also spin-forbidden, phosphorescent photon emission is usually slow, leading to a relatively long-lived T_1 state. If the initial excitation is sufficiently energetic, other reactive relaxation mechanisms can occur, including dissociation, intermolecular charge transfer, reaction, isomerisation or ionisation. [13–16]. The different decay mechanisms compete with one another and typically each occurs on a different timescale, with more likely processes occurring on faster timescales.

The rates of each specific process are highly system dependent, and are governed by the coupling between states. For this reason quantum mechanically forbidden processes such as phosphorescence or ISC, tend to occur relatively slowly (milliseconds to minutes), whereas allowed processes occur much more quickly (femto- to nano-second scale). In many cases, the fastest processes are IVR and internal conversion. Indeed, Kasha's rule states that radiative emission, whether fluorescence or phosphorescence, usually occurs from the lowest excited state of a given multiplicity, suggesting that rapid IC is a very common process [17].

1.1.1 Born-Oppenheimer approximation

Studying molecules in the gas phase allows us to neglect intermolecular interactions and treat them as isolated systems. Consequently, solutions to the (non-relativistic, time-independent) Schrödinger equation describe the molecular properties:

$$\hat{H}\,\Psi_{\mathrm{mol}}(\boldsymbol{r},\boldsymbol{R}) = E\,\Psi_{\mathrm{mol}}(\boldsymbol{r},\boldsymbol{R}), \tag{1.1}$$

where $\hat{H}$ is the molecular Hamiltonian, E is the system energy and Ψ_{mol} is the wavefunction of the system in a particular state, which is a function of the electronic and nuclear spatial coordinates, $\boldsymbol{r}$ and $\boldsymbol{R}$, respectively.

The molecular Hamiltonian consists terms describing the kinetic energy of the nuclei and electrons, as well as potential terms:

$$\hat{H}(\boldsymbol{r}, \boldsymbol{R}) = \hat{T}_{\mathrm{e}}(\boldsymbol{r}) + \hat{T}_{\mathrm{N}}(\boldsymbol{R}) + \hat{V}_{\mathrm{ee}}(\boldsymbol{r}) + \hat{V}_{\mathrm{NN}}(\boldsymbol{R}) + \hat{V}_{\mathrm{eN}}(\boldsymbol{r}, \boldsymbol{R}) \tag{1.2}$$

where $\hat{T}_{\mathrm{e}}$ and $\hat{T}_{\mathrm{N}}$ are the electronic and nuclear kinetic energy operators respectively, while $\hat{V}_{\mathrm{ee}}$ is the potential formed by Coulombic electron-electron repulsion, $\hat{V}_{\mathrm{NN}}$ is nuclear-nuclear repulsion potential and $\hat{V}_{\mathrm{eN}}$ is electron-nuclear attraction potential.

In practice, solving the complete Schrödinger equation is intractable for many electron systems. However, the problem can be simplified by application of the Born-Oppenheimer approximation (BOA) [18], which postulates that since nuclei are several orders of magnitudes heavier than electrons, the nuclei can be assumed to be stationary on the timescale of electron motion. This equates to assuming that $\hat{T}_{\mathrm{N}} = 0$, such that electrons rapidly adjust to changes in nuclear position, while the nuclei experience the electrons only as an average field. This allows the molecular wavefunction to be separated into independent electronic and nuclear components, as shown in Equation 1.3:

$$\Psi_{\mathrm{mol}}(\boldsymbol{r}, \boldsymbol{R}) = \chi(\boldsymbol{r}, \boldsymbol{R})\phi(\boldsymbol{r}, \boldsymbol{R}), \tag{1.3}$$

where χ is the nuclear wavefunction and ϕ is the electronic wavefunction.

Under the BOA, the partial Schrödinger equation can be solved for the electronic wavefunctions, for a particular nuclear arrangement, $\boldsymbol{R}$:

$$[\hat{T}_{\mathrm{e}}(\boldsymbol{r}) + \hat{V}_{\mathrm{ee}}(\boldsymbol{r}) + \hat{V}_{\mathrm{eN}}(\boldsymbol{r}, \boldsymbol{R})]\phi_n(\boldsymbol{r}, \boldsymbol{R}) = E_n(\boldsymbol{R})\phi_n(\boldsymbol{r}, \boldsymbol{R}), \tag{1.4}$$

where the n possible eigenvalues each relate to a different electronic state.

Deformation of the nuclear positions changes the nuclear potential and consequently the character and ordering of the electronic states. Therefore, systematically deforming the nuclei along each of the possible $3N - 6$ dimensions (where N is the number of constituent atoms) of a standard, non-linear polyatomic molecule and solving for

the electronic wavefunctions generates a detailed picture of the energies of these states as a function of molecular geometry. These are known as potential energy surfaces (PES), under the BOA where nuclear motion is completely decoupled from the underlying potential surface, these are called adiabatic potential energy surfaces. The computation and study of these potential energy surfaces form the basis of electronic structure theory. A wide variety of sophisticated methods have been developed to perform these types of calculations efficiently, the details of which can be found elsewhere [19, 20]. For large polyatomic molecules, the potential energy surface is highly multidimensional, as such they are typically only visualised in a few of the most significant deformation coordinates. The selection of these relevant deformation coordinates is dependent upon the molecule and photophysics of interest, but vibrational modes (or combinations of modes) which lead to electronic states converging in energy or lead to the formation of photoproduct states. For example, in our studies of $\pi\sigma^*$ states, one of the important coordinates is known to be the X–H stretch motion, which leads to H atom dissociation and parent radical formation..

Following solutions to the Equation 1.4, the nuclear wavefunction, $\chi(\boldsymbol{R})$, can be obtained:

$$[\hat{T}_{\mathrm{N}}(\boldsymbol{R}) + E_n(\boldsymbol{R}) + \hat{V}_{\mathrm{NN}}(\boldsymbol{R})]\chi_m(\boldsymbol{R}) = E_m(\boldsymbol{R})\chi_m(\boldsymbol{R}), \tag{1.5}$$

where E_n is the adiabatic energy of the n^{th} electronic state obtained from solving Equation 1.4. Solutions to Equation 1.5 yield a set of m eigenvalues relating to the rotational and vibrational levels within each electronic state.

1.1.2 Non-adiabatic effects

The BOA can provide a powerful qualitative description of a molecular system, however assuming the separability of the wavefunction into electronic and nuclear components completely neglects vibronic coupling, *i.e.* where motion of the nuclei and electrons are inherently coupled. As the magnitude of these non-adiabatic effects becomes non-negligible, the BOA breaks down allowing for many of the important

photochemical processes described in Section 1.1 [13, 14, 21, 22]. However, due to the difficulty of solving the Schrödinger equation without inducing the BOA, these types of non-adiabatic effect are often considered as perturbations upon the BOA regime.

The flaws in adiabatic potential surfaces are particularly notable in regions where the nuclear configuration brings multiple electronic states into close energetic proximity. As the energies of the states converge, they can increasingly couple to one another to form an important class of non-adiabatic effect, known as a conical intersection (CI) [23, 24]. In simple molecules, electronic states with the same symmetry will not cross or become degenerate, instead the potential surfaces deform to generate an avoided crossing. In larger systems, vibrations can break the symmetry of the molecule and therefore the symmetry of the electronic states, effectively relaxing these rules. This allows multiple electronic states to become degenerate in energy at certain nuclear configurations and form CIs, where the identity of the states become unclear and inducing strong non-adiabatic couplings, forming a mechanism by which rapid radiationless population transfer between electronic states can occur.

The occurrence of conical intersections is particularly important in large polyatomic molecules, as they frequently occur due to the large number of spatial degrees of freedom and the typically small energy difference between excited states [25, 26]. Furthermore, CIs can act as a branching point, where excited state population may emerge on either of the electronic states forming the intersection. Furthermore, in such systems conical intersections rarely occur as simple pointwise features, instead forming multidimensional seams. The topography surrounding a CI seam dictates the fate of excited state population entering its vicinity, for example, specific vibrational modes may promote or deny access through a CI. Furthermore, the stronger the coupling between electronic states, the broader and larger the effective CI volume, which 'delocalises' the ability of the CI to facilitate population transfer [27]. The study of CIs and their associated dynamics is challenging for both theoretical and experimental studies, particularly due to the loss of distinct state identities in the region of the CI.

1.1.3 Franck-Condon principle

Molecular photochemistry concerns itself with processes initiated when a molecule absorbs light, where a photon of sufficient energy excites the system to a higher energy electronic state. These electronic transitions can be treated as instantaneous *i.e.* occurring on a timescale much faster than the motion of the nuclei, due to the relatively high mass of the nuclei compared to the electrons. This approximation is known as the Franck-Condon principle [15, 28] and allows transitions to be represented as a vertical excitation from a point of origin on the lower energy potential surface to the same nuclear configuration on an upper potential surface. Many types of electronic transitions can be treated using the Franck-Condon principle, wherein the coupling between two vibronic states can be described by the transition moment:

$$S(f,i) = \langle \varepsilon' \upsilon' | \hat{\mu} | \varepsilon \upsilon \rangle, \tag{1.6}$$

where $|\varepsilon\upsilon\rangle$ and $|\varepsilon'\upsilon'\rangle$ are the vibronic wavefunctions of the initial and final states, respectively, and $\hat{\mu}$ is the dipole moment operator, which can defined in terms of nuclear $\hat{\mu}_N$ and electronic $\hat{\mu}_e$ components:

$$\begin{aligned} \hat{\mu} &= \hat{\mu}_{\mathrm{e}} + \hat{\mu}_{\mathrm{N}} \\ &= -e \sum_j r_j + e \sum_k Z_k R_k, \end{aligned} \tag{1.7}$$

where r_j and R_k are the displacements from the molecular centers of charge for the electronic and nuclear wavefunctions, respectively.

Within the BOA, the state wavefunction is separable into electronic and vibrational (nuclear) components ($\Psi_{\varepsilon\upsilon}(\boldsymbol{r}, \boldsymbol{R}) = \Psi_{\varepsilon}(\boldsymbol{r}, \boldsymbol{R})\, \Psi_{\upsilon}(\boldsymbol{R})$). Substituting this and Equa-

tion 1.7 into Equation 1.6:

$$\begin{aligned}\langle \varepsilon' \upsilon' | \hat{\mu} | \varepsilon \upsilon \rangle &= \int \Psi_{\varepsilon'}(\boldsymbol{r}, \boldsymbol{R})\, \Psi_{\upsilon'}(\boldsymbol{R})\, (\hat{\mu}_{\mathrm{e}} + \hat{\mu}_{\mathrm{N}})\; \Psi_{\varepsilon}(\boldsymbol{r}, \boldsymbol{R})\, \Psi_{\upsilon}(\boldsymbol{R})\, d\tau_{\mathrm{e}} d\tau_{\mathrm{N}} \\ &= \int \Psi_{\upsilon'}(\boldsymbol{R}) \left\{ \int \Psi_{\varepsilon'}(\boldsymbol{r}, \boldsymbol{R})\, \hat{\mu}_{\mathrm{e}}\; \Psi_{\varepsilon}(\boldsymbol{r}, \boldsymbol{R})\, d\tau_{\mathrm{e}} \right\} \Psi_{\upsilon}(\boldsymbol{R})\, d\tau_{\mathrm{N}} \\ &\quad + \int \Psi_{\upsilon'}(\boldsymbol{R})\, \hat{\mu}_{\mathrm{N}} \left\{ \int \Psi_{\varepsilon'}(\boldsymbol{r}, \boldsymbol{R})\, \Psi_{\varepsilon}(\boldsymbol{r}, \boldsymbol{R})\, d\tau_{\mathrm{e}} \right\} \Psi_{\upsilon}(\boldsymbol{R})\, d\tau_{\mathrm{N}}, \end{aligned} \tag{1.8}$$

The electronic term in the final line of Equation 1.8 is zero, because electronic states are orthogonal by definition, for any particular nuclear configuration. Under the Franck-Condon approximation, the electronic transition component of Equation 1.8 is assumed to be effectively independent of the nuclear position, which is an acceptable approximation close to the equilibrium geometry. Consequently, the electronic integral term may be approximated as a constant, $\boldsymbol{\mu}_{\varepsilon'\varepsilon}$, and the overall electric dipole transition moment is given by:

$$\begin{aligned}\langle \varepsilon' \upsilon' | \hat{\mu} | \varepsilon \upsilon \rangle &= \boldsymbol{\mu}_{\varepsilon'\varepsilon} \int \Psi_{\upsilon'}(\boldsymbol{R})\, \hat{\mu}_{\mathrm{N}}\; \Psi_{\upsilon}(\boldsymbol{R})\, d\tau_{\mathrm{N}} \\ &= \boldsymbol{\mu}_{\varepsilon'\varepsilon}\, \langle \upsilon' | \upsilon \rangle \end{aligned} \tag{1.9}$$

Equation 1.9 shows that the transition moment between two states is dictated by the dipole moment of the transition between the electronic states and a vibrational overlap term. As a consequence, electric dipole transition moment is largest when vibrational states have the greatest overlap. The square of the vibrational overlap term determines the probability (P_{FC}) of populating a particular vibrational level and is commonly known as the Franck-Condon factor [15, 16, 28–30]:

$$P_{FC} \propto |\langle \upsilon' | \upsilon \rangle|^2, \tag{1.10}$$

Figure 1.2, inset illustrates the Franck-Condon factors of various vibrational states, which can be populated following excitation from the ground state. The region to which vertical excitation occurs from the ground state equilibrium geometry is known as the vertical Franck-Condon region (vFC).

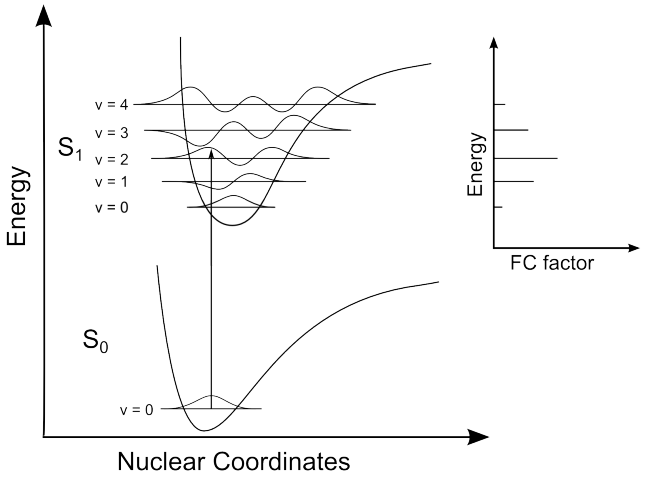

Figure 1.2: Illustration of the Franck-Condon factor, the probability of an excitation populating a specific state is given by the integral of the initial and final state vibrational wavefunctions. In this example the most probable, single final state in this case is $\upsilon = 2$ of the S_1 state, although some population will enter states $\upsilon = 0 - 4$.

1.1.4 Wavepacket dynamics

Electronic excitations can often populate a progression of several vibrational states, depending upon the bandwidth of the excitation pulse. Consequently, the excitation forms a coherent superposition of all the accessible vibronic wavefunctions $|N\rangle$, generating a spatially localised wavepacket. The specific proportions each vibronic state comprising the wavepacket are dictated by the wavelength of the excitation pulse, its amplitude and phase, as well as the Franck-Condon factors with the final state vibrational levels. After formation, the wavepacket can evolve in time according to [31]:

$$|\,\Psi_i(\Delta t)\rangle = \sum_N A_N\, e^{-iE_N t/\hbar}|N\rangle, \tag{1.11}$$

where the complex coefficients, A_N, contain both the amplitudes and initial phase of the molecular eigenstates and E_N are the energies of these eigenstates.

The evolution of each state within the wavepacket, relative to the initial excitation, is described in Equation 1.11 by the phase factor $e^{-iE_N t/\hbar}$. If the wavepacket is probed (*e.g.* ionisation) by a laser pulse, $\hat{E}_{\text{probe}}(\omega)$, some time after the initial excitation, Δt, the evolved wavepacket will be projected onto some final state Ψ_f. The time

dependence of this observed final state signal $S_f(t)$ can be expressed as:

$$\begin{aligned} S_f(t) &= |\langle \Psi_f | \hat{E}_{\text{probe}}(\omega).\hat{\mu} | \Psi_i(\Delta t) \rangle| \\ &= \left| \sum_N B_N \, e^{-iE_N t/\hbar} \right|^2, \end{aligned} \tag{1.12}$$

where $\hat{\mu}$ is the transition dipole moment of the probe excitation and the complex coefficients, B_N, contain both the state amplitude, A_N, for each state comprising the wavepacket and the transition dipole coupling between these states and the final state:

$$B_N = A_N \langle \Psi_f | \hat{E}_{\text{probe}}(\omega).\hat{\mu} | N \rangle \tag{1.13}$$

Equation 1.12 can be expanded as:

$$S_f(t) = 2 \sum_N \sum_{M \leq N} |B_N| \, |B_M| \cos[(E_N - E_M)t/\hbar + \Phi_{NM}], \tag{1.14}$$

where the phase factor, Φ_{NM}, includes the initial phase difference between the eigenstates, $|N\rangle$ and $|M\rangle$, and the phase of the transition dipole moment between these states and the final state $|\Psi_f\rangle$.

Equation 1.14 shows that the final state generated is a coherent sum of the projection of all the states comprising the wavepacket onto the final state. The observed signal $S_f(t)$ will contain time-dependent modulations at frequencies $(E_N - E_M)/\hbar$, which correspond to the energy level spacings of the eigenstates within the excited state wavepacket. Every eigenstate will have a different overlap with the final state and only those with a strong Franck-Condon overlap to the final state will significantly contribute to the observed signal. Consequently, selection of a relevant final state or states is critical to observing the desired temporal evolution of the excited state wavepacket. Some experimental techniques, such as total fluorescence or ion yield measurements only observe the integrated signal generated by all accessible final states, $I_{\text{tot}} = \sum_f S_f(\Delta t)$. These techniques are unable to distinguish the contributions of specific final states, whereas differential techniques, such as translational energy spectroscopy or photoelectron spectroscopy are more information rich and

Figure 1.3: (a) NaI potential energy curves, showing the turning points on the upper 'bound' surface formed by the avoided crossing and the dissociative surface. There is a 10% probability of population transferring to the dissociative state each time the wavepacket reaches the avoided crossing. (b) The laser-induced fluorescence signal produced by (I) off-resonance probing of the transition state (bound wavepacket) and (II) the resonant fluorescence of product Na atoms. Reproduced from Ref. [32].

can allow observation of the contribution of particular final states.

Professor Ahmed Zewail won the 1999 Nobel prize [33] for his contributions to the design and implementation of femtosecond experimentation to examine the motion of excited-state wavepackets. One of Zewail's most celebrated experiments [32] uses a femtosecond excitation of the NaI molecule to generate a coherent superposition of excited vibrational states. The excited wavepacket oscillates in a bound region on the excited state surface, formed by an avoided crossing with a dissociative state, see Figure 1.3(a). On each oscillation, as the Na-I bond extends to $\sim$0.25 nm 10% of the population crosses non-adiabatically to a lower, dissociative potential (leading to the formation of neutral Na and I atoms). Any population remaining on the excited state surface continues to oscillate, decaying with each cycle. The molecule was probed using laser-induced fluorescence, with various wavelengths used to examine different regions of the excited state surface. A 589 nm probe is resonant with the sodium D-line emission and therefore allows measurement of the formation of dissociated Na atoms (Figure 1.3, b, II). If the probe wavelength is detuned from this energy, the population of the bound wavepacket can be monitored as it oscillates on the bound surface, due to laser-induced fluorescence (Figure 1.3, b, I). This experiment beautifully illustrates the power of ultrafast spectroscopic techniques to illuminate the temporal evolution of excited state wavepackets. Laser-induced fluorescence can provide an sensitive probe of ultrafast dynamics, however it is intrinsically limited to systems with a fluorescent product state and is therefore other techniques are

usually required to examine the ultrafast dynamics of larger molecular systems.

1.2 Photoelectron spectroscopy

Photoelectron spectroscopy is a powerful technique for examining the energetics of electronic states [34–36]. In photoelectron spectroscopy, a molecule is ionised by the absorption of a photon with energy in excess of the molecular ionisation potential. The kinetic energy of the resultant photoelectron provides information regarding the state populated prior to ionisation;

$$eKE = \mathrm{h}\nu - I, \tag{1.15}$$

where eKE is the kinetic energy of the ejected photoelectron, I is the ionisation energy of the molecule and $\mathrm{h}\upsilon$ is the energy of the incident photon.

If the energy of the incident photon in Equation 1.15 is known, then measurement of the photoelectron's kinetic energy provides a probe of the energy difference between the occupied state of the molecule and the 'free' electron in a continuum state. If the highest occupied molecular orbital (HOMO) is the ground state this is the ionisation energy, in other states are populated this can provide information on the energy of the occupied state [37]. Most spectroscopic techniques are limited by a multitude of selection rules, which govern the allowed transitions. In contrast, virtually all states can be ionised, and consequently photoelectron spectroscopy suffers from very few 'dark' transitions.

1.2.1 Time-resolved photoelectron spectroscopy

Photoelectron spectroscopy allows for measurement of the electronic states populated in a particular molecule, this can occur either at equilibrium or following preparation by some other method. Time-resolved photoelectron spectroscopy (TR-PES) employs a 'pump-probe' scheme, which involves two photon pulses staggered

in time. The first pulse controls the initially excited state and the second pulse allows examination of the evolved state, using the same principle as photoelectron spectroscopy. If the delay between the two photons is varied, then a series of snapshots can be built up to observe the evolution of the molecule following absorption of the pump laser pulse. The process is summarised in Equation 1.16. TRPES has the potential to allow us to observe the complete dynamics following excitation, including any intermediate states populated during the electronic relaxation process [31, 38–42].

$$AB \xrightarrow{h\nu_{\text{pump}}} AB^{**} \xrightarrow{\Delta t} AB^{*} \xrightarrow{h\nu_{\text{probe}}} AB^{+} + e^{-} \tag{1.16}$$

In order to ascertain information on the energetics and identity of the states involved, it is essential to consider the conservation of energy:

$$E_0(\upsilon) + E_{\text{pump}} + E_{\text{probe}} = D_n + E_{\text{ion}}(\upsilon) + eKE \tag{1.17}$$

where $E_0(\upsilon)$ is the initially populated state, E_{pump} and E_{probe} are the energies of the pump and probe photons, respectively, D_n are the electronic states of the cation, $E_{\text{ion}}(\upsilon)$ is the vibrational energy retained in the ion and eKE is the kinetic energy of the ejected photoelectron.

Furthermore, if a molecule is deliberately cooled, virtually all of the population will begin in the ground state. Thus $E_0(\upsilon) \approx 0$:

$$\begin{aligned} eKE &= E_0(\upsilon) + E_{\text{pump}} + E_{\text{probe}} - D_n - E_{\text{ion}}(\upsilon) \\ &\approx E_{\text{pump}} + E_{\text{probe}} - D_n - E_{\text{ion}}(\upsilon) \end{aligned} \tag{1.18}$$

$$\tag{1.19}$$

When ionising a non-bonding excited state, there is a propensity for the greatest Franck-Condon overlap between ionised and cation states to occur where $\Delta\upsilon = 0$ *i.e.* vibrational energy is approximately conserved in the cation when projected into the ionisation continuum (as opposed to being transferred to the ejected electron). This $\Delta\upsilon = 0$ propensity rule typically holds true for large, rigid molecules and can be

Figure 1.4: TRPES techniques can differentiate between different electronic states, as long as the excited and ionised state energies are sufficiently well characterised. The downward pointing arrows represent the energy carried away by the ejected photoelectrons, and illustrates how different states and ionisation pathways can be differentiated. Reproduced from Ref. [43]

invoked to simplify the process of state identification in a photoelectron spectrum:

$$\begin{aligned} E_{\text{ion}}(\upsilon) &= E_{\text{S}_n}(\upsilon) \\ &\approx E_{\text{pump}} - E_{\text{S}_n}(\upsilon = 0) \end{aligned} \tag{1.20}$$

where $E_{\text{S}_n}(\upsilon)$ is the vibrational energy imparted to the excited state following absorption of the pump photon. This can be calculated, as shown in Equation 1.20, if $E_{\text{S}_n}(\upsilon = 0)$ (the energy of the $\upsilon = 0$ level) is known. This principle is illustrated in Figure 1.4.

Substituting Equation 1.20 into Equation 1.18:

$$eKE \approx E_{\text{probe}} - [D_n - E_{\text{S}_n}(\upsilon = 0)] \tag{1.21}$$

Equation 1.21 shows that, under certain circumstances, it is possible to identify and differentiate electronic states by measurement of the eKE, as long as the energies of the excited and ionised states are sufficiently well characterised *i.e.* if D_n and $E_{\text{S}_n}(\upsilon = 0)$ are known. Notably, Equation 1.21 is not dependent upon the pump wavelength selected, although the selection of the pump energy will alter the specifics of the initial wavepacket, by selecting the electronic or vibrational states can be populated at the point of excitation.

The temporal resolution of the TRPES technique is dictated by the (temporal) width of the excitation and ionisation pulses. It is now routinely possible to reduce laser

Figure 1.5: (a) Energy level scheme of 2,4,6,8-decatetraene (DT). (b) The TRPES for DT, showing the internal conversion between the initially excited S_2 state (ε_1) ionised to the D_0. This state rapidly decays to the S_1 state, ionised to the D_1 state (ε_2). Reproduced from Ref. [44].

pulse duration to the femtosecond scale, allowing for observation of bond breaking and rearrangement phenomena. A seminal example of the fidelity of the TRPES technique, is the imaging of the internal conversion occurring between the second and first singlet excited states (S_2 and S_1, respectively) of 2,4,6,8-decatetraene (DT). This work by Stolow *et al.* is shown in Figure 1.5. In this experiment, the DT molecule is initially excited to the S_2 state, which has an overlap in the observation window with the cationic state ground state (D_0), while the S_1 state can be ionised to the first excited cationic state (D_1). Collecting photoelectron images a several pump-probe delays allows for visualisation of the decay of the initially excited S_2 state and the simultaneous rise of the S_1 state. Allowing for the observation of the S_2 state rapidly decaying into the S_1 state, on the timescale of several hundred femtoseconds.

As mentioned in Section 1.1, an excited electronic state can decay by several competing mechanisms, including internal conversion to a different electronic state or IVR, which involves distributing excess vibrational energy amongst the vibrational modes of the molecule. The efficiency of IVR processes typically increases as the molecule gets larger, due to the increasing vibrational density of states. Large molecules are notorious for distributing their excess energy into their vibrational modes on a very short time-scale, allowing the molecule to rapidly cross from one electronic state to another. This change in state population can be observed using TRPES and the interpretation of these spectra forms a significant portion of this project.

1.2.2 Photoelectron angular distributions

Time-resolved photoelectron imaging (TRPEI) is a variation of TRPES, where the photoelectron angular distribution (PAD) is measured simultaneously to the photoelectron energy distribution. The PAD can give additional information on the character of the electronic states populated, as photoionisation is governed by symmetry based selection rules. In the case of a single photon ionisation process, it is required that the direct product of the irreducible representations spanned by the initial (excited) state wavefunction, Γ_{i}, the final (ionised) state wavefunction, Γ_{f}, the wavefunction of the ejected electron, Γ_{e}, and the molecular frame transition dipole moment, Γ_{dipole}, contain the totally symmetric molecular point group, Γ^{S} [45, 46]:

$$\Gamma_{\mathrm{i}} \otimes \Gamma_{\mathrm{f}} \otimes \Gamma_{\mathrm{dipole}} \otimes \Gamma_{\mathrm{e}} \supset \Gamma^{\mathrm{S}} \tag{1.22}$$

Consequently, if the character of the excited state is retained upon ionisation (Koopman's theory), the symmetry of the excited state wavefunction must be reflected in the symmetry of the outgoing photoelectron [47]. Photoelectron angular distributions have been studied extensively in the literature and several comprehensive reviews are available [31, 42, 48]. As long as cylindrical symmetry exists about the excitation and ionisation laser axes, the observed laboratory frame PAD is only dependent upon θ, the ejection angle with respect to the symmetry axis. The PAD generated by isotropically oriented molecules, which are ionised by linearly polarised light (oscillating parallel to the detection plane) can be expressed by the following form [49]:

$$I(\theta) \propto \sum_{L=0}^{L_{\mathrm{max}}} \beta_L P_L(\cos\theta) \tag{1.23}$$

where β is the anisotropy parameter (constrained to lie between -1 and 2, such that Equation 1.23 always remains positive) and $P_{\mathrm{L}}(\cos\theta)$ is the Legendre polynomial of order L.

For one-photon ionisation, only even terms up to $L = 2$ need be considered, while two-photon processes require consideration of the even terms up to $L = 4$. In the

current work, we typically consider up to the 4^{th} order term, in order to ensure that multiphoton effects are not observed:

$$I(\theta) \propto 1 + \beta_2 P_2(\cos\theta) + \beta_4 P_4(\cos\theta) \tag{1.24}$$

In our experiments, the pump and probe laser pulses are always linearly polarised and oriented parallel to the detection plane, ensuring that the cylindrical symmetry constraint is fulfilled and Equation 1.24 can be used to analyse the PADs we obtain.

1.3 Introduction to $\pi\sigma^*$ states

In aromatic molecules, the lowest excited electronic states are often ring-centered $\pi\pi^*$ states, whose importance have long been recognised because their high absorption cross-section tends to dominate absorption spectra. In 2002, Sobolewski *et al.* [10] suggested that $^1\pi\sigma^*$ states play an important role in the non-radiative decay of substituted aromatic molecules, particularly those containing NH and OH groups. These $^1\pi\sigma^*$ states have mixed Rydberg (diffuse, atomic-like) and valence antibonding character, and are formed due to an avoided crossing at modest X-H (X = N,O) separations. The lower adiabatic potential energy surface of the avoided crossing is best described as a singlet $\pi 3s/\pi\sigma^*$ state, but is usually referred to as a $\pi\sigma^*$ state for simplicity [9, 10].

The shape and consequent dynamics of wavepackets on the $\pi\sigma^*$ potential energy surface is highly dependent on the relative stabilities of the Rydberg and valence configurations. If the $\pi 3s$ and $\pi\sigma^*$ components are nearly degenerate in the vFC region, as is the case in phenol [50], the potential surface is almost totally dissociative, as is illustrated in Figure 1.6(a). If, however, the Rydberg state is lower in energy than the dissociative valence state, as is the case in aniline [51–53], the $\pi\sigma^*$ potential energy surface has a pronounced well in the vertical Franck-Condon region and only becomes dissociative at longer N–H bond distances. This is illustrated in Figure 1.6(b).

Figure 1.6: A schematic illustration of the adiabatic potentials arising from the interaction between the $^1\pi 3s$ (Rydberg, blue curve) and $^1\pi\sigma^*$ (valence, red curve) configurations in two contrasting cases. (a) shows the case where the two states are nearly degenerate in the vFC region, and the resultant surface is almost purely repulsive. (b) shows the case where the Rydberg configuration is energetically stabilised (relative to the valence state) at short X-H distances, forming a stable, bound region. Reproduced from Ref. [51]

Critically, the $\pi\sigma^*$ state formed can intersect lower-lying states, including any $^1\pi\pi^*$ states or the electronic ground state forming conical intersections and thereby forming a mechanism by which rapid non-radiative relaxation can occur [11, 50, 54–56]. These mechanisms are critical to understanding the photodynamics of many of the molecules studied in this thesis.

1.4 Conclusion

In this chapter, the underlying principles of molecular photochemistry have been introduced. The origins of non-adiabatic dynamics were described, followed by an introduction to the TRPEI technique. This powerful experimental method allows for the unravelling the non-adiabatic dynamics which occur following UV excitation of small organic molecules. The TRPEI technique is the main procedure used in this thesis, in order to study the ultrafast dynamics of several molecules containing low-lying, singlet $\pi\sigma^*$ states. Chapter 2 examines the experimental equipment and data analysis techniques necessary to perform TRPEI. The results and analysis of the experimental data produced from the TRPEI studies of pyrrole, aniline and phenol are presented in Chapters 3–5, respectively.

Chapter 2

Experimental setup and data analysis

This chapter provides an overview of the experimental equipment and general data analysis methods used throughout this thesis, any modifications of the analysis methodology which might arise on an experiment-by-experiment basis are expanded upon in the relevant chapters. The experimental apparatus used for the TRPEI experiments in this project employs a continuous wave (CW) or pulsed molecular beam, crossed perpendicularly by a pair of co-linear pump and probe laser beam-lines. The molecular beam is contained in a ultra-high vacuum (UHV) chamber (see Figure 2.1) capable of reaching pressures of 1×10^{-8} mbar, in order to maintain a collision-free environment. The laser beams cross the molecular beam in the 'interaction region' and any ejected electrons are deflected (perpendicular to both the laser beam and the molecular beam) towards our imaging array by electric fields.

2.1 Experimental arrangement

2.1.1 Gas delivery systems

In order to examine the dynamics of isolated gas-phase molecules, it is first necessary to vapourise them. For molecules which are gaseous at room temperature and pressure, this is a trivial condition, however the molecules studied in this work are either liquid or solid at room temperature. For liquids, the sample is seeded into a carrier gas stream by bubbling an inert gas through the sample. Where the sample has a particularly low vapour pressure or is solid, it may be necessary to increase the temperature of the sample in order to obtain an appreciable number density of sample molecules in the gas phase.

The sample is cooled by expanding the sample from the region of (relative) high pressure behind the nozzle to the low pressure region inside the vacuum chamber. If the pressure differential across this expansion is sufficiently large, the sample can achieve supersonic speeds as internal energy is transferred into translational energy. Figure 2.2 shows a schematic of the different pressure regions formed upon supersonic expansion (adapted from Ref. [57]). The zone of silence (where Mach

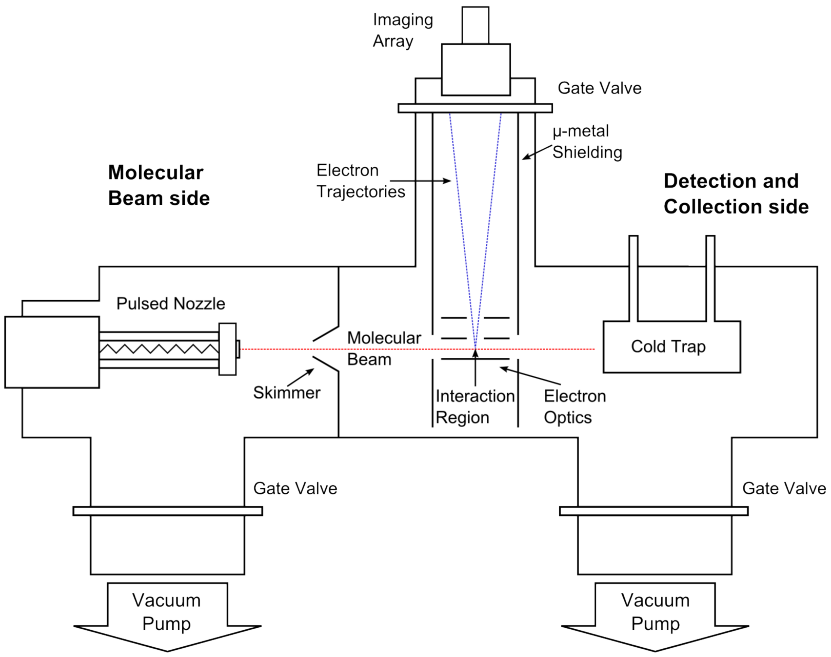

Figure 2.1: Schematic of the experimental chamber. The two sides of the chamber are only connected by the skimmer orifice, which reduces gas density in the interaction region. The generation of the molecular beam can be varied between an Even-Lavie pulsed valve (shown) and a continuous nozzle, mounted on an xyz manipulator. The cold trap is liquid nitrogen cooled, in order to further reduce background gas concentrations.

Figure 2.2: Schematic of adiabatic gas expansion which forms a supersonic jet. The zone of silence is the collision free region, where Mach number, M >> 1. Other regions, where M < 1 are not collision free and contain undesirable pressure shock waves. Reproduced from Ref. [57].

number, M >> 1) is of particular interest as it is collision-free, effectively cooling the internal temperature of the gas to only a few Kelvin [58, 59]. This is an ideal environment in which to study spectroscopic transitions, because it dramatically simplifies which states are initially populated [60–62]. A rigorous treatment the pressure effects in supersonic molecular beams and the procedures and technologies for their production can be found in Ref. [57].

Both continuous and pulsed nozzles are employed for the experiments presented in this thesis. In both cases, we use helium as the carrier gas, delivered by $1/16^{th}$ inch tubing with a backing pressure between 0.5–2 bar. The continuous nozzle (used for Chapter 3 regarding pyrrole and Chapter 4 regarding aniline) produces a molecular beam by expanding helium gas through a 50 μm nozzle, mounted on an xyz manipulator for alignment purposes. The pulsed nozzle (used in Chapter 5 regarding phenol) is an Even-Lavie, high temperature, high repetition rate nozzle [59, 63]. This is a commercial, solenoid controlled valve capable of producing 10 μs duration pulses at a rate of up to 1 kHz. The Even-Lavie nozzle also contains a small chamber, in which solid or liquid sample can be contained and an associated heating element (10 < T < 250 °C), to encourage vapourisation of the sample. This sample chamber is situated as close to the expansion nozzle as possible, in order to reduce condensation of sample inside the valve. In this work we operate the pulsed nozzle at 500 Hz and maintain a backing pressure of He at 1 bar, under these conditions the nozzle self-heats to ∼75 °C. Consequently, we use the heating coils to maintain a constant temperature of 80 °C, in order to minimise depletion of the phenol sample.

Whichever nozzle is used, the beam is collimated with a 1 mm diameter skimmer

approximately 40 mm from the nozzle aperture, before entering the interaction region, which selects a portion of the beam which has virtually no velocity in the transverse direction [64]. In our experimental setup, the skimmer also separates the initial expansion region from the interaction region, allowing us to differentially pump the vacuum chamber. The molecular beam side of the chamber is maintained below 5×10^{-6} mbar during experimental operation, while the detector chamber pressure is maintained below 1×10^{-7} mbar to ensure that the interaction region remains collision free. A liquid nitrogen cooled trap is also positioned in the path of the molecular beam (after the interaction region), which further reduces background gas concentrations.

2.1.2 Femtosecond laser system

The development of ultrafast laser systems is an active field of research and there are many excellent review articles available [65–67]. Our ultrafast laser systems use titanium doped sapphire (Ti:sapphire) as the gain medium, which consist of Ti^{3+} ions suspended at low concentration in a sapphire (Al_2O_3) host lattice. This is desirable because Ti^{3+} ions exhibit a broad absorption band centred around 500 nm, resulting from vibronically allowed d-d transitions. The emission spectrum of Ti^{3+} in sapphire spans a wide range of wavelengths, owing to a very large number of closely spaced vibronic states in the medium [68, 69]. Pulse durations of as short as 6 fs have been observed using Ti:sapphire systems (with dispersion compensation) [70, 71].

A schematic view of the setup we use to produce our femtosecond, tunable laser pulses for TRPEI experiments is shown in Figure 2.3. The method uses a 5 W, 532 nm continuous-wave laser (Coherent Verdi) to pump a cavity containing a Ti:sapphire crystal (Coherent Mira). Ultrafast pulses are generated by a process known as Kerr lens mode-locking, and our system produces 35 fs pulses centered around 785 nm (40 nm FWHM), at a 76 MHz repetition rate. The average power output of this oscillator is 1 W.

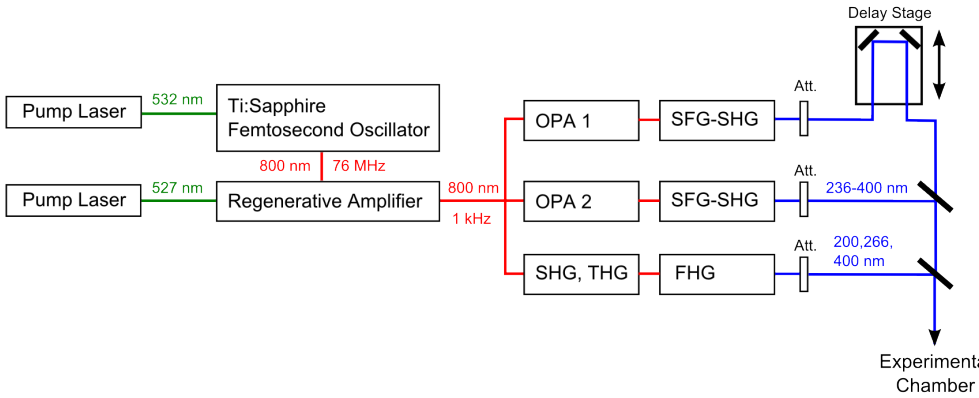

Figure 2.3: Schematic of the laser systems used to produce pump and probe pulses in our TRPEI setup. The Ti:sapphire oscillator generates ultrafast pulses of 800 nm light. This is used to seed the regenerative amplifier, which generates significantly more power per pulse. The output is then split and used to drive either harmonic generation optics or the two optical parametric amplifiers (OPAs), which can produce femtosecond pulsed of light in the region 200-600 nm. Delay between the different beamlines is introduced using a piezoelectric translation stage.

These femtosecond pulses are then used to seed a regenerative amplifier (Coherent Legend). The seed pulses are stretched temporally in order to avoid the destruction of optical components in the cavity, which can occur due to non-linear focussing. In the amplifier, another Ti:sapphire crystal is used as the gain medium and is pumped by a 20 W nanosecond Nd:YLF laser centered at 527 nm (Coherent Evolution). The seed pulses are passed through the gain medium repeatedly, increasing in intensity each round trip and are released from the cavity by an externally triggered Pockels cell. After amplification, the pulse is compressed temporally back to 50–70 fs duration. We measure and check this duration on a regular basis, using an Coherent FR-103 autocorrelator. Under optimal conditions, the cavity produces a beam centred at 800 nm with an output power of ∼2 mJ per pulse, at a repetition rate up to 1 kHz. An autocorrelation width of ∼80 fs is typical.

The amplified pulses are then split into multiple beam lines, to pump the two optical parametric amplifiers (OPAs, Coherent Opera) or harmonic generation optics, which produce our pump and probe pulses. Harmonics of the fundamental output of the Ti:sapphire amplifier can be obtained by second harmonic generation (SHG) and sum-frequency generation (SFG) processes in β-barium borate (BBO) crystals. If

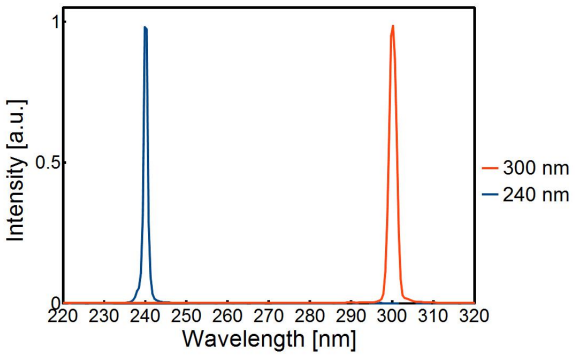

Figure 2.4: Spectral profiles of some representative laser pulses produced by our experimental apparatus.

the fundamental wavelength is 800 nm, harmonic generation can produce 400 nm, 267 nm and 200 nm pulses [72]. Compared to simple harmonic generation, OPAs offer far greater tunability of the wavelength produced [73–75]. In the OPA, the input light is focused onto a sapphire window, in order to generate a white light continuum [75, 76], which is then mixed with the fundamental in a BBO crystal. This produces tunable light over the range 1150–2630 nm, which can again be mixed with fundamental wavelength light using SHG, SFG and difference frequency generation (DFG) to obtain wavelengths over the UV, visible and IR ranges. The OPAs used in this thesis are able to generate output wavelengths over the ranges 472–613 nm and 236–400 nm. We use combinations of the OPAs and harmonic generation techniques to produce the pump and probe pulses necessary for our TRPEI studies. The beam exiting the OPAs is checked using a spectrometer (Ocean Optics, HR2000-UV), in order to confirm the central wavelength and spectral width of the pulses produced. Some examples of the spectral profiles of pump or probe pulses produced by this method are shown in Figure 2.4.

A time delay between the pump and probe pulses is introduced by a commercial computer controlled translation stage (Physik Instrument, M510.12), see Figure 2.3. In our experimental setup, the pump and probe pulses are generated by the same cavity and therefore any jitter due to physical or electronic noise does not significantly affect the relative spacing of the pulses. However, the precision of the translation stage must still be on the micrometer scale to be able to resolve femtosecond time delays, this is achieved using a combination of DC motors and piezoelectric compo-

nents for fine control. The pump and probe pulses are recombined, prior to entry to the vacuum chamber, using a dichroic mirror and focused into the interaction region using a fused silica lens with a focal length of 250 mm. The energies of the pump and probe pulses are attenuated (using neutral density filters) to less than 0.5 μJ prior to entry into the vacuum chamber, in order to minimize multiphoton absorption of the species in our molecular beam. At the focal point, our beam has a diameter of ∼0.5 mm, consequently the peak power density of a 100 fs pulse is at most $I \sim 1^{12}$ W/cm^2, thus limiting the power of our excitation and ionisation pulses ensures that the experiment is conducted in the perturbative regime ($I \leq 1^{14}$ W/cm^2) [77].

The time resolution of TRPEI experiments is limited by the temporal pulse width of the laser, the relationship between the temporal and spectral bandwidths being limited by the following inequality (for Gaussian pulses):

$$\Delta\upsilon \, \Delta t \geqslant 0.441 \tag{2.1}$$

where $\Delta\upsilon$ is the full-width half-maximum (FWHM) uncertainty in frequency and Δt is the temporal FWHM of the pulse.

Equation 2.1 can be rearranged to:

$$\Delta\lambda \text{ [nm]} \geqslant 1.471 \times 10^{-3} \, \frac{\lambda^2 \text{ [nm}^2\text{]}}{\Delta t \text{ [fs]}} \tag{2.2}$$

For example, a pulse centered at 300 nm with a spectral FWHM of 2 nm (e.g. Figure 2.4) is transform limited to a temporal FWHM of 66 fs, or a pulse centered on 240 nm, with a temporal FWHM of 100 fs, is spectrally limited to 0.85 nm FWHM.

Consequently, even in the ideal limit, ultrafast excitation pulses are spectrally broad and often capable of populating multiple excited states. Experimental planning involves consideration of the temporal and spectral resolution required and, where femtosecond dynamics are to be examined, a limit will always exist on the achievable

energy resolution and it is not usually possible to resolve rotational or vibrational levels. This complimentary information can be attained, for example by employing experiments with excitation pulses which are temporally broad, but have a small frequency bandwidth.

It is possible to approach Fourier limited pulses when initially generating femtosecond pulses, however pulse durations observed inside our experimental chamber are typically around 100 fs, due to dispersion occuring in optical elements responsible for amplification and wavelength tuning, as well as entry into the vacuum chamber. A description of the measurement of the pulse cross-correlation is described in Section 2.3.1.

2.2 Velocity map imaging (VMI)

There are two primary techniques used for the measurement of photoelectron spectra, based upon time of flight (ToF) and velocity map imaging (VMI) methods. ToF spectrometers measure the time taken to traverse the distance between the interaction region and detector and can simply comprise a linear field-free region and a detector. Such an arrangement would have poor collection efficiency, so magnetic field guides are used, for example magnetic bottle arrangements can achieve 50% collection efficiency [78, 79]. Well designed ToF spectrometers can achieve excellent energetic resolution, over a broad range of spectral energies, which is especially powerful in the VUV or x-ray excitation regions.

VMI uses inhomogenous, static electric fields to project the complete photoelectron velocity distribution onto a planar electron detector and allows for the simultaneous measurement of both the energy and angular photoelectron distributions. By application of appropriately configured fields (see Figure 2.5), it is possible to remove the lateral spatial uncertainly in the starting points of ions (*i.e.* parallel to the detection plane), in effect producing an image that appears to emanate from a single point [80].

Figure 2.5: Ions focused through use of the VMI method. (a) The 2D projection of the repeller (−1000 V), extractor (−750 V) and ground (0 V) plates. Some electric field lines and ion propagation paths are also shown, (b) initial trajectories of the ions are isotropic, with subsequent deflection by the electric field, (c) the three origin points are spaced across a 3 mm region, (d) all ions with the same velocity are focused to the same point on the detector, regardless of the position from which they originate. Reproduced from Ref. [80].

Our VMI apparatus consists of a set of three parallel plates (called the extractor, repeller, and ground), a time of flight tube and an imaging array, arranged as shown in Figure 2.6. The photoelectron energy range observable with a VMI setup depends on the magnitude of repeller and extractor voltages used, while the focusing conditions dictated by the ratio of $V_{\text{extr}}/V_{\text{rep}}$. The optimal ratio varies, depending upon the exact detector geometry and the length of the time-of-flight region [81]. Simulations performed by previous members of the group found that, for our equipment the optimal extractor/repeller ratio is ∼0.7 [82].

The VMI technique requires that the detector is position sensitive, our detection array consists of two microchannel plates (MCP), a phosphor screen and a charged-coupled device (CCD). The MCPs plates amplify each incident electron by producing an electron cascade, localised to the point of impact. The cascade leads to fluorescence upon colliding with the phosphor screen, which is then imaged by the CCD positioned above. Our imaging array is a commercial unit (Photek VID240).

MCPs generate electron cascades for all incident photons, ions or electrons and therefore our detection array cannot inherently distinguish these particles. In order to reduce noise from scattered light or background sources, the VMI equipment in our apparatus is positioned perpendicular to both the laser beam and the molecular beam. Additionally, the voltages driving the MCP are temporally gated, such that incidental ion fragments reaching the detector do not contribute significantly to our

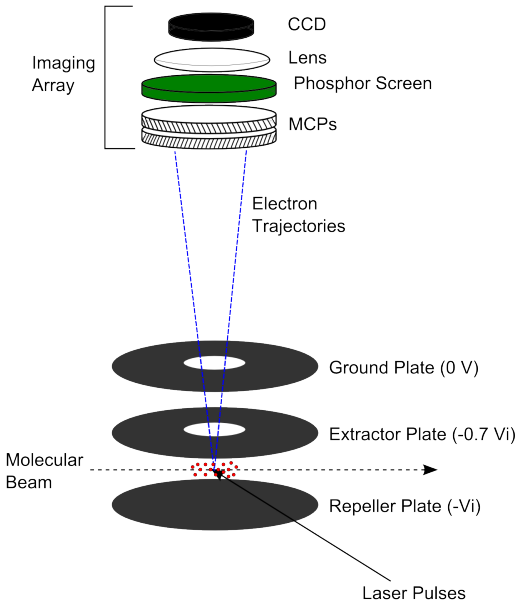

Figure 2.6: Diagram of the VMI photoelectron imaging equipment used in our TRPEI experiments. The interaction region lies between the extractor and repeller plates. The region between the electron optics and the MCPs is shielded by μ-metal shielding, in order to prevent stray fields from affecting the electron trajectories.

measured signal.

The analysis necessary to convert the raw CCD images into useful data involves several steps, described in the sections which follow. For each pump-probe temporal delay, we must subtract away the one-colour pump-only and probe-only contributions. Our collection software is configured to capture 20 seconds of integrated pump-probe image, then 20 seconds of pump-only image, then 20 seconds of probe-only image. We repeat this process for 20-60 minutes in order to obtain a good signal-to-noise ratio and then perform the subtraction of the pump-only and probe-only images to eliminate one-colour contributions to the observed signal. We then invert our VMI images, to generate the photoelectron velocity distributions. These are converted to energy space, using the appropriate calibration factor. We repeat this process for a relevant selection of pump-probe delays (typically $\sim$20 different delays) and then perform the fitting procedure described in Section 2.3.

$$\begin{pmatrix}\text{Raw}\\\text{Image}\end{pmatrix} \xrightarrow{\text{Inversion}} \begin{pmatrix}\text{Velocity}\\\text{Distribution}\end{pmatrix} \xrightarrow{\text{Calibration}} \begin{pmatrix}\text{Photoelectron}\\\text{Spectrum}\end{pmatrix} \tag{2.3}$$

[83]

2.2.1 VMI inversion

VMI involves the projection of a three-dimensional distribution onto a two dimensional imaging array. Following (effectively instantaneous) ionisation, photoelectrons are ejected from the parent molecule and form a series of nested Newton spheres, the radii of which are dependent on their kinetic energy. These spheres propagate the time-of-flight tube and are focussed onto the two dimensional detector plate. Extraction of the original three dimensional kinetic energy distribution from this two dimensional image is commonly carried out using the pBasex inversion method [84], which uses Abel transforms [85] to produce a spectrum relating radius (and therefore photoelectron velocity) to intensity. The pBasex algorithm is popular because it provides rapid, clear inversions, in part due to its tendency to move noise artefacts towards the centre of the image where data is less likely to be useful.

Additionally, using pBasex to reconstruct the velocity distribution also allows resolution of angular distributions, such that photoelectron angular anisotropies can be extracted [48, 86]. Our group has previously developed a program (ImageInversion [87]), which is designed to take a raw CCD image matrix and invert it to produce the photoelectron velocity distribution. It is worth noting that other algorithms for VMI inversion have been developed, generally with the intention of increasing the speed of inversion, at the expense of some accuracy [88]. The pBasex algorithm was used for all the analysed data presented in this thesis.

Photoelectron angular distributions are also obtained *via* our analysis with the pBasex inversion algorithm, producing the anisotropy parameters described in Section 1.2.2. However, anisotropy in the photoelectron images is not generally observed in the data contained in this thesis, unless otherwise mentioned.

2.2.2 Calibration of VMI

In VMI, the ratio of $V_{\text{extr}}/V_{\text{rep}}$ dictates the focusing conditions, meaning that any VMI detector must be calibrated after any change in the detector geometry, such as realigning the molecular beam. Using a known photoelectron distribution allows us to ascertain the absolute energy scale and thereby calibrate the energy range and resolution of the detector. The photoelectron velocity v and energy E distributions are related, as described in Equation 2.4:

$$\begin{aligned} E &= \frac{m_e}{2} v^2 \\ &= cr^2 \end{aligned} \tag{2.4}$$

where m_e is the mass of an electron, r is the radial index of the inverted image point and c is the calibration factor, an experimentally determined value which depends upon the detector geometry and VMI voltages.

It is usually preferable to select a gas to calibrate the detector, as it is reduces the changeover time between samples, and the gas is usually selected to produce photoelectrons in the same energetic range as those expected from the sample of interest [37].

The experiments described in this thesis were calibrated using xenon, which is selected because $2 + 1$ photon resonant multiphoton ionisation (REMPI) is possible at 249.6 nm excitation, due to the presence of an intermediate $6p$ Rydberg state which lies at 9.93 eV. Additionally, the two relevant ionisation energies of xenon are well characterised: $\text{Xe}(^1\text{S}_0) \rightarrow \text{Xe}^+(^2\text{P}_{3/2})$ with an IP of 12.13 eV and $\text{Xe}(^1\text{S}_0) \rightarrow \text{Xe}^+(^2\text{P}_{1/2})$ with an IP of 13.437 eV [89]. Using this data and Equation 2.4, it is simple to obtain the velocity distribution of the photoelectrons and determine the calibration factor.

A raw photoelectron image of the Xe peaks is shown in Figure 2.7(a) and the inverted spectrum is shown in Figure 2.7(b). The photoelectron peak width in VMI depends

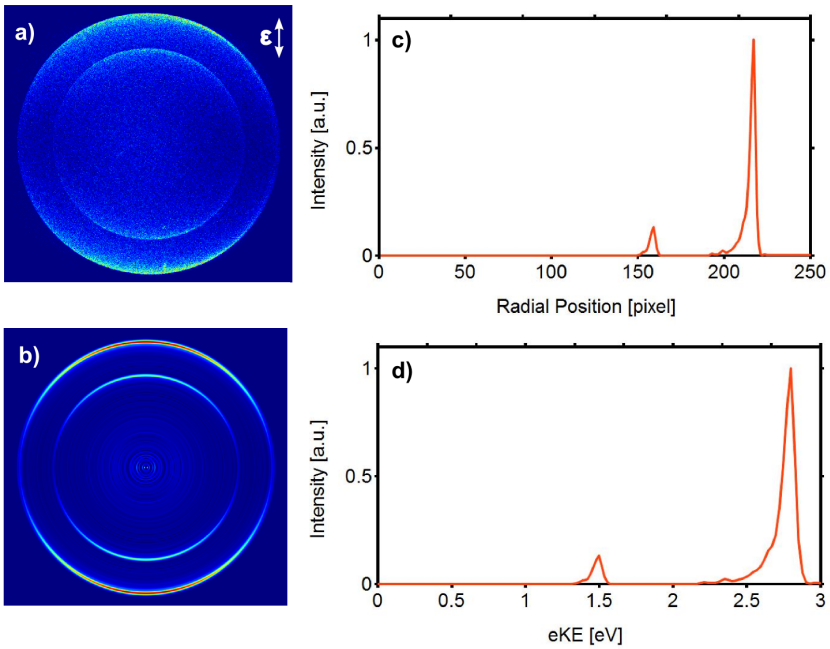

Figure 2.7: (a) Raw photoelectron image, showing the 2 + 1 ionisation of xenon at 249.6 nm excitation. (b) Inverted image, using pBasex. The $^2P_{1/2}$ and $^2P_{3/2}$ peaks are clearly visible. (c) Velocity spectrum obtained following inversion. Using the known positions of the peaks the calibration factor, $c = 5 \times 10^{-5}$. (d) eKE spectrum using the calibration factor from image (c). The relative spacing of the peaks changes due to the non-linear relationship between velocity and energy, with peaks broadening towards higher eKE for the same reason.

on many factors, such as the minimum resolution of the detector (CCD or MCP pixel density), the bandwidth of the laser used, the inversion algorithm and the focusing of the electron optics. The selected ionisation peaks in xenon are short lived, so the full-width half-maximum (FWHM) of the calibration peaks (see Figure 2.7(c)) gives an indication of the maximum energy resolution achievable for a given detector arrangement. Since the ratio of $V_{\text{rep}}/V_{\text{extr}}$ can affect resolution, but is easily altered, measurement of the FWHM of these two peaks can be used to check and optimise the detector resolution, using Equation 2.5. Because the peaks broaden towards higher eKE values, energy resolution is usually quoted as $\Delta E/E$ [90], in Figure 2.7(d) the optimal energy resolution is $\Delta E/E = 3.5$ % (a representative value for our equipment).

$$\Delta E = 2cr\Delta r \tag{2.5}$$

where r is the radial position of the peak (in pixels), Δr is the FWHM of the calibration peak and c is the calibration factor.

2.2.3 Ion imaging

It is important to ascertain the composition of the molecular beam, to check for impurities and the formation of molecular clusters. Theoretically this can be achieved using time of flight (ToF) measurements, between the excitation laser pulse and the arrival of the ions at the microchannel plate. The current induced by the electron cascade resulting from ions impacting upon the MCP should be measurable. However, several attempts to achieve this showed that our electronics were not sensitive enough to detect the relevant signal.

An alternate method of determining the extent of clustering in the molecular beam is to examine VMI ion images. The supersonic expansion method ensures that the constituents molecules have a tight velocity distribution in the propagation direction, such that clusters and fragments will have the same velocity as monomer species. When projecting electrons along the VMI apparatus, all particles have the same mass

and with sufficiently strong electric fields, the image is centered on the interaction region. However, unlike electrons, the relatively heavy mass of positive ions causes them to retain an appreciable proportion of the momentum from the molecular beam. This manifests as an offset of the positive ions from the interaction region; the heavier the ion, the larger the offset. We can therefore use this method to monitor cluster formation in our molecular beam. If all species are singly ionised, as is likely at our laser fluences, a cluster will appear on the detector with an offset, y_i, proportional to its mass m_i, as shown in Equation 2.6:

$$y_i \propto v_y \sqrt{m_i} \tag{2.6}$$

where v_y is the component of the velocity in the propagation direction.

One of the reasons helium is used as the seed gas in our molecular beam is due to its low propensity to form clusters. It can therefore be assumed that clusters are only composed of the sample material. Using Equation 2.6, the ratio of the y-axis offset between different cluster sizes can be derived, and is shown below for dimer (Equation 2.7) and trimer cases (Equation 2.8):

$$\frac{y_{\text{dimer}}}{y_{\text{monomer}}} = \sqrt{\frac{m_{\text{dimer}}}{m_{\text{monomer}}}} = \sqrt{2} \tag{2.7}$$

$$\frac{y_{\text{trimer}}}{y_{\text{monomer}}} = \sqrt{\frac{m_{\text{trimer}}}{m_{\text{monomer}}}} = \sqrt{3} \tag{2.8}$$

This measurement method assumes that any ionised molecular clusters are retained during the flight along the VMI region. If the clusters dissociate following excitation by the pump pulse, they will not observed. The ToF for ions in our VMI is of the order of 5 μs, suggesting that clusters have sufficient time to undergo these dissociation processes if they are energetically favourable. Consequently, any proportion clusters measured by this method forms a lower limit on the proportion of clusters actually present in our TRPEI experiments and other experimental methods are required to resolve this more accurately [91].

Figure 2.8(a) shows a VMI ion image of xenon, ionised from the molecular beam with a backing pressure of 1 bar. Xenon would not be expected to form clusters and, as such, only a single offset peak is observed, in addition to the statistical background signal caused by ionised background gases and scattered light.

Figure 2.8(b) and (c) show the ion images for pyrrole at two different helium expansion pressures. Higher expansion pressures generate a molecular beam with a higher velocity, increasing the offset of the monomer ions from the centre. Additionally, higher expansion pressures cause the molecular beam to be cooled further and consequently, the probability of cluster formation is increased. Figure 2.8(b) shows that a pyrrole beam, with a He expansion of 0.4 bar, forms only monomers species. However, Figure 2.8(c) shows that increasing the expansion pressure to 1.0 bar produces a small additional peak, because the increased cooling is sufficient to stabilise dimers. The effect of this dimerisation upon the photorelaxation of pyrrole is explored in Chapter 3.

We found that at 0.4 bar He expansion pressure only singly ionised pyrrole was produced, with no cluster formation or fragmentation detectable. In keeping with the findings of Buck *et al.* [91], we found that increasing the expansion pressure of the He seed gas induces cluster formation. Using the ion images, we estimate that at 1.0 bar He pressure approximately 3% of the signal is attributable to dimers and at 1.8 bar this rises to 7%. Some relevant ion images are shown in Figure 2.8. We do not observe a measurable trimer signal or any signal attributable to fragmentation. It should be noted that these proportions are considerably lower than those observed in the literature, however we do not cool the reservoir where the pyrrole is seeded into the He gas stream. Additionally, as noted above our technique is only able to provide a lower limit on their number density in the interaction region, due to the possibility of the photoexcited clusters dissociating during propagation in the ToF region.

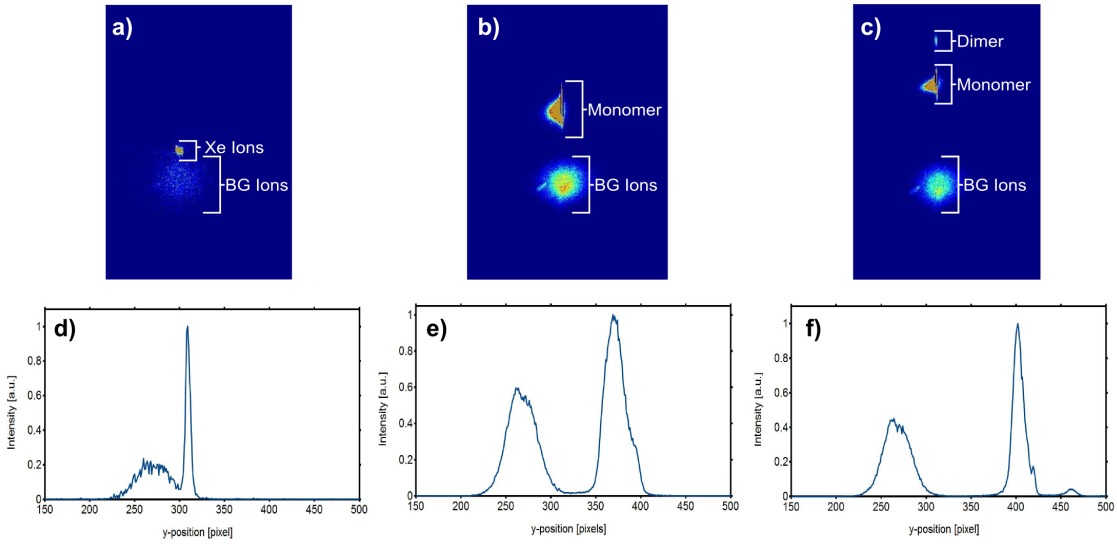

Figure 2.8: (a) Ion image for xenon (249.5 nm ionisation). The statistical ions can be observed in the center of the image and a single ion peak is visible, displaced from this center. This is indicates that xenon does not form clusters, as expected. (b) Ion image for pyrrole (0.4 bar expansion pressure, 249.5 nm ionisation), again only the statistical ions and the monomer peak are visible. (c) Ion image for pyrrole (1.0 bar expansion pressure, 249.5 nm ionisation), in addition to the statistical ions and the monomer peak, a dimer peak is visible. (d) Integrated Xe ion count with respect to the molecular beam propagation direction (y-axis). Very few stationary (background) ions are observed in this case. (e) Integrated pyrrole ion count (0.4 bar expansion pressure) with respect to the molecular beam propagation direction (y-axis). The pyrrole monomer ion is offset from the stationary ions more than Xe, due to its higher momentum. (f) Integrated pyrrole ion count (1.0 bar expansion pressure) with respect to the molecular beam propagation direction (y-axis). Both the monomer and a small proportion of dimer ions are observed.

2.3 Determination of decay lifetimes

One of the primary aims of our experimental work is to elucidate the timescales upon which electronic decays occur, following UV excitation. TRPEI allows us to achieve this by building up a series of photoelectron images with varying delays between the pump and probe pulses, in order to study the evolution of spectral features. However, the extraction of a single characteristic lifetime, associated with the decay of a specific state, requires us to fit to a model function. Our characteristic equation, for a state A, is the result of convoluting an exponential decay with a Gaussian function, which has been derived rigorously elsewhere [87]:

$$I_A = y + e^{-\lambda_A \Delta t}\, \sigma_{\text{gnd.A}}\, \sigma_{\text{ion.A}}\, \frac{I_{\text{pump}} I_{\text{probe}}}{2}\, e^{\frac{(\sigma\,\lambda_A)^2}{2}} \left(1 + \text{erf}\left(\frac{\Delta t - \sigma^2\,\lambda_A}{\sqrt{2}\,\sigma}\right)\right) \quad (2.9)$$

where y is the background, σ is the instrument response function, I_{pump} and I_{probe} are the intensities of the pump and probe pulses respectively, Δt is the time delay between the pump and probe pulses (where pump followed by probe is the positive direction), $\sigma_{\text{gnd.A}}$ is the absorption cross-section from the ground state to state A, $\sigma_{\text{ion.A}}$ is the ionisation cross-section from state A and λ_A is the total decay rate of state A.

Collecting all of the constants into a single coefficient, c_A, this simplifies to:

$$I_A = y + c_A\, e^{-\lambda_A \Delta t}\, e^{\frac{(\sigma\,\lambda_A)^2}{2}} \left(1 + \text{erf}\left(\frac{\Delta t - \sigma^2\,\lambda_A}{\sqrt{2}\,\sigma}\right)\right) \quad (2.10)$$

This technique does not attempt to examine the topology of the electronic states or explicitly take into account quantum effects occurring as population decays, it merely attempts to characterise the rates of population transfer between observable states, such that different decay processes can be measured and compared. The procedure for fitting these decay functions to out data are described in Section 2.3.2.

2.3.1 Instrument response function and time zero position

Extraction of decay lifetimes using Equation 2.10 requires determining two other important experimental parameters, the 'time zero' position (where the centers of the pump and probe pulses are coincident) and the instrument response function. The width of the instrument response function produces a lower bound on the temporal resolution of our experiment and is primarily dependent on the cross-correlation of the pump and probe pulses ($\sigma = \sqrt{\sigma^2_{\text{pump}} + \sigma^2_{\text{probe}}}$).

We can determine both the cross-correlation and the time zero position using non-resonant ionisation. In properly selected molecules, no population is transferred into the intermediate state and the photoelectron response function is Gaussian, with a width corresponding to the cross-correlation and the central value relating to the time-zero position. Our interaction region resides inside a vacuum chamber, entry into which requires passing through a fused silica window of appreciable thickness. Transition through this medium causes the laser pulses to significantly broaden and we find that accurate measurement of the cross-correlation requires that it be determined in the interaction region.

In many experiments, we have used the $2 + 1'$ ionisation of either xenon or butadiene (C_4H_6) to obtain the cross correlation and time-zero position, both of which can be ionised using 249.5 nm and 300 nm. Both molecules can be ionised by $2 + 1$ one-colour multiphoton processes (249.5 nm), but the photoelectron flux is enhanced around time zero by the 300 nm flux. The width and location of the enhancement can be fitted to a Gaussian to determine the time-zero location and the cross-correlation by scanning the temporal delay between the two pulses in the usual fashion. Figure 2.9(a) shows a representative example of the cross-correlation, as measured using the $2 + 1'$ non-resonant ionisation of butadiene (249.5 nm and 300 nm, respectively). The fitted Gaussian function has a FWHM of 220 ± 10 fs.

Typically, in our experimental procedure we fit the cross correlation and time zero position (see procedure described below). In order to ensure that this fitting does not introduce significant error into our results, we periodically perform compar-

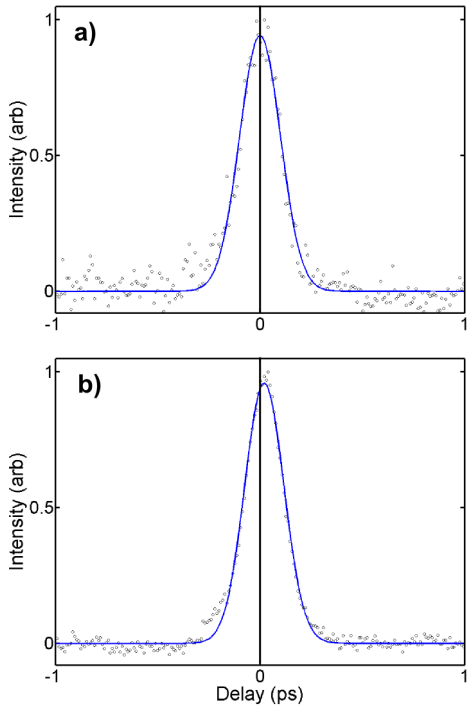

Figure 2.9: a) Data (circles) and fit (line) for the cross-correlation and time zero determination, using non-resonant $2 + 1'$ ionisation (249.5 nm and 300 nm, respectively) of butadiene. The fitted cross-correlation (FWHM) is 220 ± 10 fs and the time zero position on our delay stage is 43.8198 mm.
b) Data (circles) and fit (line) for the cross-correlation and time zero determination, using $1 + 1'$ resonant pump-probe ionisation (249.5 nm and 300 nm, respectively) of the pyrrole monomer (0.4 bar seed pressure). An additional lifetime is included to account for the ultrafast decay of the populated state (< 50 fs), leading to the delay in the signal maxima. The fitted cross-correlation (FWHM) is 235 ± 10 fs and the time zero position on our delay stage is 43.8199 mm.

isons between experimentally measured cross-correlations and time zero positions and those obtained by our fitting procedure. We generally find that the time zero position is shifted by less than 5 fs, while the cross-correlation has (at most) at 10% disparity between the methods. Figure 2.9(b) displays an example of this, fitting the pyrrole monomer ultrafast decay (including a < 50 fs lifetime), the cross-correlation (235 ± 10 fs) and time zero position simultaneously. The results obtained are in excellent agreement with those obtained using butadiene above. In our experience, this method is best applied when energetically separated peaks are observed. Fitting two decay lifetimes, the time-zero position and the cross-correlation is a considerable number of free parameters and can cause issues with reliable convergence during fitting.

2.3.2 Fitting methods

Obtaining reliable and unbiased lifetimes from TRPEI data requires the definition of a generalised extraction procedure. Even when using a specified model, such as Equation 2.10, it can be challenging to disentangle the dynamics of individual states in a complex spectrum. In simple cases, for example where only a single decay is observed, lifetime extraction can be relatively simple. Fitting continues to be unproblematic when dealing with two decays which are well separated in energy or time. However, as spectra become more congested, finding a truly representative description becomes increasingly challenging, primarily due to the highly multivariate nature of the fit [92].

The fitting procedure developed and used in our group involves a number of sequential steps, as summarised in the flowchart in Figure 2.10. The details of each step are described in the following paragraphs. An example dataset (the pyrrole dimer following 245 nm excitation - discussed in detail Chapter 3) is treated as an illustration, allowing each step of the analysis to be explained with some context. This set of data was selected as it contains only two resolvable decay lifetimes and consequently the interpretation is relatively simple.

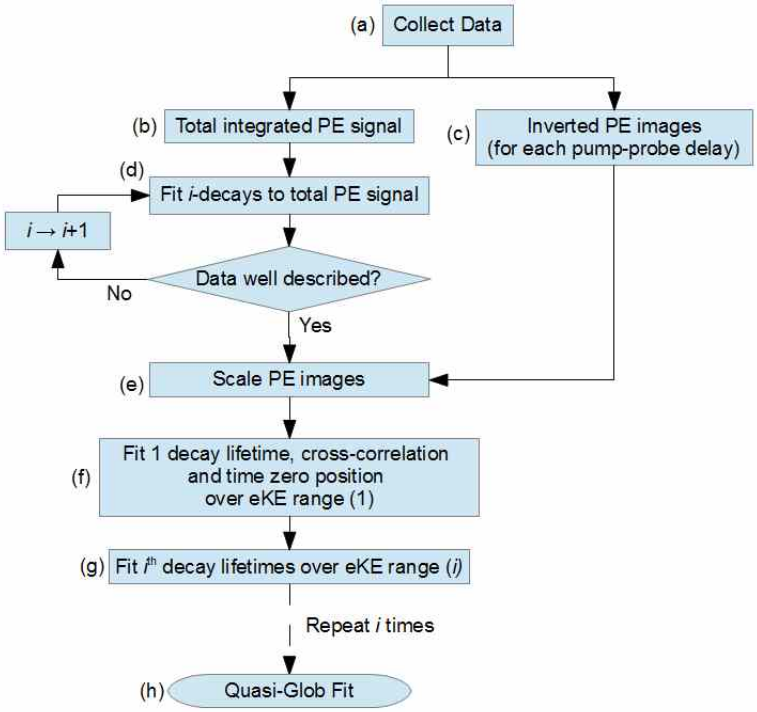

Figure 2.10: Flowchart showing the steps in our analysis procedure, in order to determine the decay lifetimes from a series TRPEI spectra.

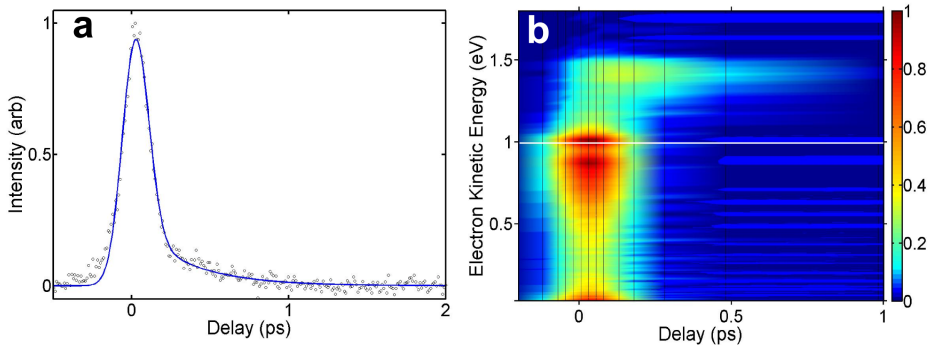

Figure 2.11: Example data analysis using data for the pyrrole dimer following 245 nm excitation (300 nm probe). A fit to the decay of the total photoelectron signal (a) is used to scale the photoelectron images. The scaled photoelectron images can be plotted as a surface to illustrate the evolution of the individual features, as shown in (b). The maximum accessible $(1 + 1')$ eKE is marked by a solid white line.

Following inversion and calibration, our primary data comprises a series of energy resolved spectra at various pump-probe delay times ((c) in Figure 2.10). We also collect a plot of the total integrated intensity of the photoelectron signal with respect to pump-probe delay as a separate set of data (Figure 2.10(b)). The information contained in the total integrated photoelectron signal could be obtained by integrating each photoelectron image, however we treat these data separately in order to ensure that any variation in the laser fluence over the data collection window does not aversely affect the lifetimes extracted. Collecting photoelectron images with acceptable signal-to-noise ratios takes ∼12 hours, whereas collecting a well-resolved plot of the total integrated photoelectron signal takes ∼30 minutes.

For our example data, the evolution of the total integrated photoelectron signal is plotted with respect to the relative delay between pump and probe pulses in Figure 2.11(a). We fit this experimental data to a sum of i decays (convoluted with an instrument function representing the cross-correlation of our laser pulses) to the function shown in Equation 2.11:

$$I(t) = \sum_i c_i \, \mathrm{e}^{-t/\tau_i} \otimes \mathrm{g}(t), \tag{2.11}$$

where τ_i is the i^{th} exponential decay time and $\mathrm{g}(t)$ is the instrument function (cross-

correlation). The explicit formulation was given in Equation 2.10. This fitting process labelled (d) in Figure 2.10. The selection of a suitable value of i is critical, which should be the lowest number required to adequately describe the data. Usually i is less than or equal to the number of electronic states accessible at the excitation energy selected. We typically begin by attempting to fit using a minimal number of decays, which is increased if the data cannot be well described, as it is often the case that some electronic states to not significantly contribute to the overall signal. The example data, shown in Figure 2.11(a) is fitted to the sum of two exponential decay lifetimes, one with a lifetime $\tau_1 < 50$ fs and the other with a lifetime $\tau_2 = 267$ fs. It can be seen that the data could not be adequately fitted with fewer than two lifetime and fitting with the inclusion of additional lifetime components does not improve the fit.

Our inversion process normalises the each photoelectron spectrum, consequently we use the fit to the total integrated signal (described above) to scale the area under each photoelectron spectrum and thus recover their relative intensities (process (e) in Figure 2.10). The resultant photoelectron images can be plotted as a surface, in order to examine the temporal evolution of energy resolved features. This is shown for the example data in Figure 2.11(b).

It is possible to calculate the maximum possible electron kinetic energy accessible $1+1'$ ionisation, given the excitation and probe wavelengths, which serves as a useful check on the energy calibration:

$$eKE_{\max} = [h\nu_{\text{pump}} + h\nu_{\text{probe}}] - E(\mathrm{D}_n), \tag{2.12}$$

where D_n is the ground state of the cation. In the example of pyrrole excited by 245 nm light, the maximum accessible eKE for the pyrrole monomer is determined to be 0.98 eV and is marked on Figure 2.11(b) as a solid white line. Interestingly, in our example data it can be seen that a feature is observed above the 'maximum' $1+1'$ eKE, this specific to dynamics in the pyrrole dimer and the reasons are discussed in Chapter 3.

The next step in the fitting procedure involves attempting to obtain characteristic

lifetimes relating to each feature observed in the time and energy resolved images. This can be carried out in a number of ways. Global fitting is a well used method, which refers to a procedure of fitting linear combination of exponential decay lifetimes across each energy pixel of the photoelectron spectrum. The decay lifetimes are forced to be common across the entire spectrum, but the coefficients in the linear combination can be distinct for each electron kinetic energy (eKE) pixel in the spectra:

$$I(eKE, t) = \sum_i c_i(eKE)\, \mathrm{e}^{-t/\tau_i} \otimes \mathrm{g}(t), \tag{2.13}$$

where $c_i(eKE)$ is the intensity of the i^{th} decay at a given eKE, τ_i is the corresponding exponential decay lifetime and $g(t)$ is the instrument response function (cross-correlation).

After substituting Equation 2.10, this becomes:

$$I(eKE, \Delta t) = y + \sum_i c_i(eKE)\, \mathrm{e}^{-\lambda_i \Delta t}\, \mathrm{e}^{\frac{(\sigma\,\lambda_i)^2}{2}} . \left(1 + \mathrm{erf}\left(\frac{\Delta t - \sigma^2\,\lambda_i}{\sqrt{2}\,\sigma}\right)\right) \tag{2.14}$$

involves integrating each photoelectron image over specific energetic regions, using an approach based upon global fitting procedures.

Ideally, Equation 2.14 can be applied across every pixel in the spectrum (usually 256 in our experimental apparatus) and fitted using an appropriate optimisation algorithm. This approach is virtually unbiased in its treatment of the data, however in complex spectra this method can be prone to misrepresentation. A highly multivariate optimisation problem is generated, with the number of degrees of freedom to be fitted equal to $N + N.x$, where N is the number of decay lifetimes to be fitted and x is the number of energy pixels in each photoelectron spectrum. Using our apparatus, this potentially leaves a thousand or more free parameters to be fitted. Consequently this approach can perform very well when treating simple spectra containing few decays, but when the data is complex and congested the result is prone to finding local minima and can be heavily dependent upon the initial values selected for each parameter.

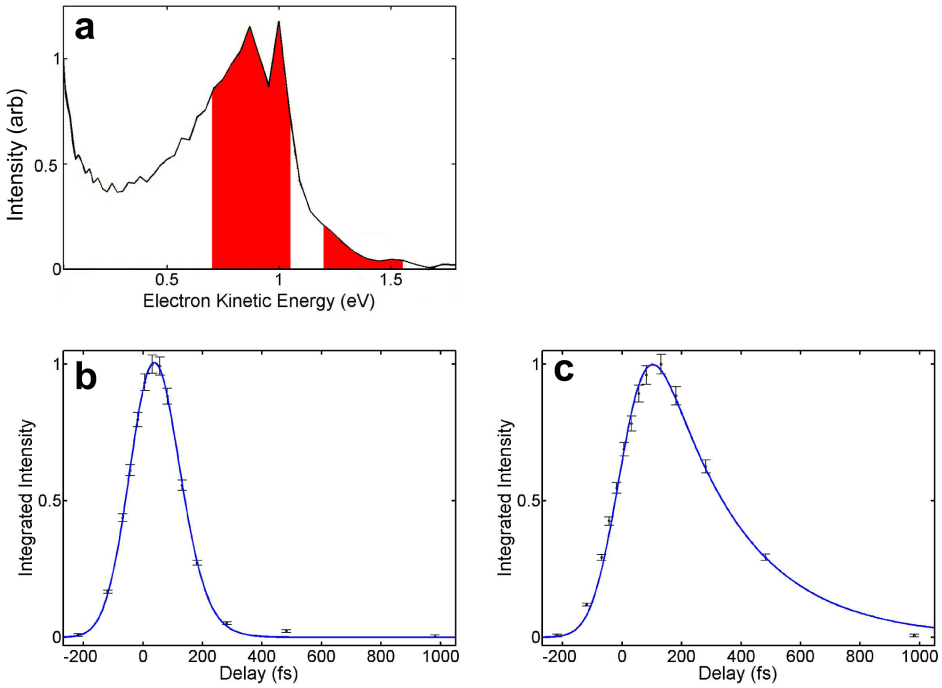

Figure 2.12: (a) Photoelectron spectrum (0 fs pump-probe delay) illustrating the regions over which the photoelectron signal is integrated (shaded red) for the images collected at each pump-probe delay. (b) Plot of the points generated by integrating over the range 0.7–1.05 eV, as well at the fit to Equation 2.14 ($i = 1$). The error bars show the 2σ variation in the photoelectron intensity over the integrated range. (c) Plot of the points generated by integrating over the range 1.2–1.55 eV, as well at the fit to Equation 2.14 ($i = 2$, where one lifetime, the instrument function and the time zero position are fixed).

One method of avoiding this optimisation problem is to allow the decay lifetimes to be different for each energy pixel. This approach is fast and simple and will virtually always produce a good reproduction of the original data. However, the variation in lifetimes from one energy pixel to another makes interpretation very challenging. Consequently, this approach can be useful to generate a qualitative understanding of the dynamics present or in situations where the spectral features evolve in energy space as well as time, which can occur in solution phase biological fluorescence studies.

As an alternative, we have developed a 'quasi-global' fitting procedure, which reduces the degrees of freedom available to the optimisation algorithm at any one time. The

aim being to improving the reliability and accuracy of the converged solution, while still producing distinct lifetimes for each spectral feature. This method revolves around sequentially integrating the photoelectron spectrum over discrete electron kinetic energy ranges, each containing an identifiable number of rise or decay lifetimes. The selection of each energy integration range requires the understanding of the chemical system, for example the expected eKEs associated with each electronic state (based upon the energy of the origin of each electronic state accessible and the $\Delta\upsilon = 0$ rule).

Using the pyrrole example, we have already ascertained that two decay lifetimes are present following 245 nm excitation (from the total photoelectron signal fit above). The peaks in Figure 2.11(b) appear reasonably well separated with respect to eKE and the integration ranges 0.7–1.05 eV and 1.2–1.55 eV are selected (as illustrated in Figure 2.12(a)). Integrating each photoelectron image over the range 0.7–1.05 eV generates the points marked in Figure 2.12(b) (the error bars show the 2σ variation in the photoelectron intensity over the integrated range). Fitting the cross-correlation, time zero position and a single decay lifetime in Equation 2.10 to this integrated data generates the blue curve shown in Figure 2.12(b). In this case, the decay lifetime is faster than we can resolve from our instrument function ($\tau_1 < 50$ fs). Integrating over the eKE range 1.2–1.55 eV generates the points marked in Figure 2.12(c) and we fit Equation 2.10 with $i = 2$, but only the additional lifetime τ_2 is a optimised parameter, while the values for τ_1, the instrument function and the time zero position are fixed to the values obtained from fitting Figure 2.12(b). This second fit generates a decay lifetime of $\tau_2 = 267 \pm 44$ fs.

When using the quasi-global approach, it is important to begin by integrating over the most separable spectral feature, which should only contain a single decay and is usually the peak at highest eKE. This is because we also fit our cross correlation and time zero position over this first, separated peak (process (f) in Figure 2.10). We then integrate over the energy regions with the next least number of lifetimes present and include the lifetimes ascertained from the previous fits (which is fixed and not fitted in this step). This is process (g) in Figure 2.10. It is important to include all of the previously ascertained decay lifetimes, in order to accurately de-

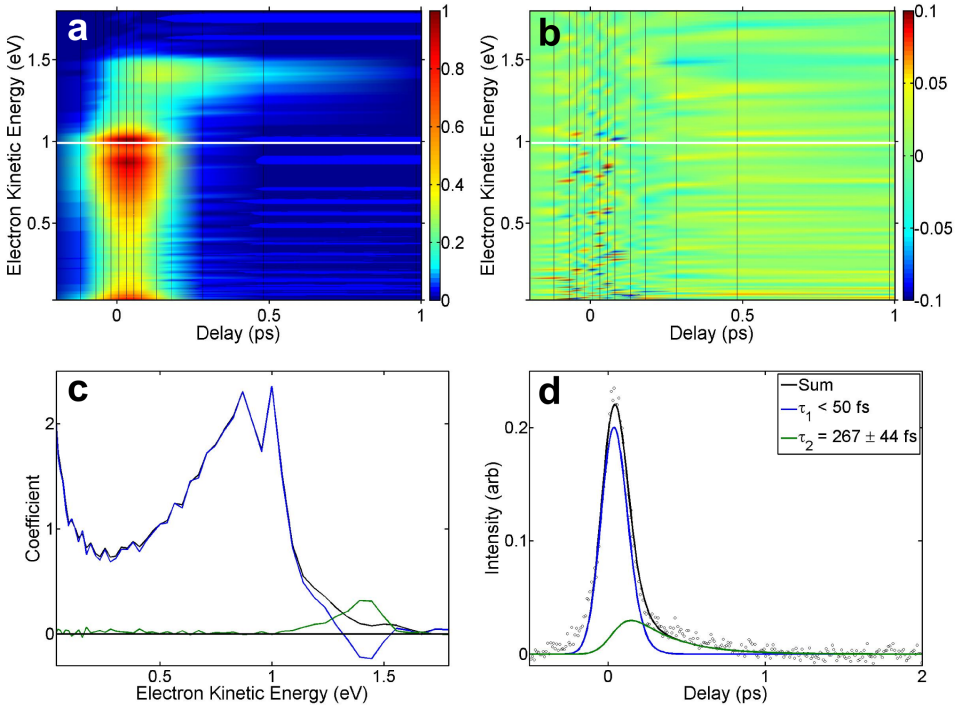

Figure 2.13: (a) The photoelectron surface fitted to the data shown in Figure 2.11(b), subtracting these two datasets generates the residual produced shown in (b). It can be seen that the disparity between the fit and the data is $< 10\%$ of the normalised intensity and is randomly distributed across the plot, suggesting that the error is statistical in nature. (c) Decay associated spectra, relating to the fit shown in (a). (d) Refitting the total integrated decay data to the lifetimes obtained from our quasi-global fitting procedure. This plot is normalised to $\sum_i c_i = 1$, excluding states which feed other observable states. Consequently the limit at long pump-probe delay time indicates the proportion of the initially excited wavepacket which remains within our observation window.

scribe any contribution the other features may provide, due to overlapping features. We continue to select eKE integration ranges until we have determined all of the identifiable state lifetimes.

Our quasi-global fitting procedure then performs a standard global fit using Equation 2.14 and all of the energy and time resolved data (process (h) in Figure 2.10). However, in our quasi-global fit, the lifetimes obtained from our energy integrated fitting and the time zero and instrument response function, are fixed and not allowed to vary. This reduces the number of free parameters available to the optimisation

algorithm at any one time.

The time-resolved photoelectron spectra can then be reconstructed using the timescales, τ_i and fitted coefficients, c_i(eKE), as shown for our pyrrole example in Figure 2.13(a). The quality of this fit is discernible from Figure 2.13(b), which shows the residual generated by subtracting the surface depicted in Figure 2.13(a) from the data shown in Figure 2.11(b). The residual plot shows that the maximum disparity between the fit and the data surfaces is $\sim$10%. The residual data should, ideally, be distributed randomly across the plot if it arises purely from statistical fluctuations.

The coefficients obtained from fitting Equation 2.14 shows the contribution of each decay lifetime at each energy pixel and can be used to generate a so-called 'decay associated spectrum' (DAS), by plotting the coefficients with respect to eKE. The DAS plot is a simple method of visualising the contribution of any given decay lifetime at each energy pixel and can provide valuable information when interpreting energy flows between electronic states [93–96]. With this scheme, positive coefficients indicate an exponential decay (at the given eKE pixel), while negative coefficients indicate a rise in photoelectron signal. Therefore, physically meaningful negative coefficients must relate to corresponding positive coefficients and this situation would imply that population is decaying out of the state associated the negative coefficient into the state(s) associated with the positive coefficient(s), on the timescale of the decay of the former (negative coefficient) state. As long as all of the fitted timescales are distinguishable from one another, DAS can provide powerful insight and a useful visual method of unravelling the cascade of population transfer that characterises photorelaxation mechanisms. Another useful feature of DAS coefficients, is that if all coefficients are summed at each energy pixel, the 'true' zero time delay spectrum is generated, *i.e.* without cross-correlational broadening. In a congested spectrum, this approach can help determine which states are initially populated.

Again, using the example pyrrole data, the DAS is presented in Figure 2.13(c) (three-point averaged for clarity). The initially excited state is that associated with the sub-50 fs lifetime (blue line). This feature has a negative coefficient in the region 1.2–1.5 eV and a corresponding positive coefficient is observed, associated

with the τ_2 lifetime. The state associated with this τ_2 is not initially excited (see the delay in Figure 2.13(a)). Together these observation suggests that population transfer is occurring from the state associated with the τ_1 decay lifetime into the state associated with the τ_2 lifetime. The increase in eKE upon population transfer is an interesting and anomalous finding, the reasons for which are explored in Chapter 3 (population transfer between states usually leads to a reduction in eKE, as greater vibrational energy is excited in the lower energy electronic state in order to conserve energy, which is then conserved upon ionisation).

Finally, we use the lifetimes extracted and fit back to the total photoelectron signals, in order to demonstrate that the correct temporal decay distribution is recovered from our quasi-global fitting procedure. These graphs are normalised such that $\sum_i c_i = 1$, such that the graph will tend to the proportion of the initial photoelectron signal remaining after the first few picoseconds. An example of this, using the pyrrole data, is presented in Figure 2.13(d), where it can be seen that all of the total photoelectron signal decays out of the observation window within 1 ps.

I have coded the fitting procedure described above into a MATLAB based program, called FSfit, which includes a graphical user interface (GUI). The data analysis procedure (including background subtraction and inversion) typically requires handling several hundred separate images for each wavelength studied. The program was designed and built to increase the ease with which our analysis procedure could be carried out, and also to ensure that such a complex procedure can be followed in a standardised and reproducible fashion. FSfit systematises the processes described in Figure 2.10, as well as automating the background subtraction of the pump only and probe only non-resonant ionisation pathways. The scaling of the inverted photoelectron spectra is automated, following the fitting of the total integrated signal. The program is capable of fitting the scaled photoelectron spectra using the energy integrated method described above, or by the pure global fitting method, where all lifetimes and weightings are fitted simultaneously. The ability to fit using either of these techniques means that we can easily compare the effects of either procedure. We usually compare the results for dataset, because each approach has its own strengths and weaknesses. For example global fitting is prone to finding local

minima, depending upon the initialisation values selected 2 or more decay lifetimes often converge to the same value and the uncertainties in the derived values reported are considerably larger (due to the lareg number of free parameters presented to the optimisation simultaneously), while quasi-global fitting cannot be used if the spectral features are not sufficiently distinguishable to select meaningful eKE integration ranges. In favourable circumstances the two approaches produce very similar results. One advantage of using the FSfit program, is that it is simple and rapid to iterate the fitting procedure with various fit parameters (such as number of decay lifetime included or the energy ranges over which we integrate when fitting decay lifetimes) and we can therefore ensure that lifetimes obtained are representative of the data and not heavily dependent upon the initial values chosen.

The fitting optimisation procedure implemented in FSfit is based upon least-squares fitting, using the Levenberg-Marquardt optimisation algorithm. Uncertainties in the fitted decay lifetimes are derived from the Jacobian of this least-squares fit and are quoted to the 2σ level. A more detailed description of this program and a user manual are included in Appendix A. The fitting procedure in FSfit is slightly modified compared to our previously published results and a comparison in Appendix B demonstrates that the alterations have a minimal effect on the results obtained.

2.4 Conclusion

This chapter has covered the experimental equipment used to carry out the TRPEI experiments in this thesis. Some relevant underlying theory is discussed and the data analysis techniques and fitting procedures required to extract meaningful decay lifetimes are detailed. The following chapters contain the results and analysis of our experimental TRPEI studies. The studies regarding pyrrole, aniline and phenol are presented in Chapters 3–5, respectively.

Chapter 3

Time-resolved dynamics of pyrrole and solvent-induced electron transfer in the region 249.5–200.0 nm

3.1 Introduction

Pyrrole forms a common motif in many biologically important molecules, such as the amino acid proline and indole (which forms part of tryptophan). Furthermore, tetrapyrrole systems, such as porphyrins and phthalocyanines, form the chromophores in many critical biomolecules, such as haemoglobin and those involved in photosynthesis. Pyrrole is known to contain a low-lying $\pi\sigma^*$ state [10, 97], which makes it an excellent case with which to examine the role of these states in the UV relaxation dynamics of aromatic systems.

The gas-phase, UV absorption spectrum of pyrrole has long been known [98–103], and is shown in Figure 3.1. A strong peak is observed, centered on 220 nm, with an extended edge trailing towards longer wavelengths and eventually terminating at 250 nm. Although these bands are easily discernible in the absorption spectrum, the nature and ordering of even the lowest lying states has historically been the subject of some debate, which is discussed in detail below.

3.1.1 Spectroscopy of pyrrole

The prevalence of pyrrole has long made it a favourite subject for excited state theoreticians [104–119]. Its small size and high symmetry means studies are comparatively computationally cheap, however the lowest excited states are non-trivial and have proven difficult to characterise accurately. The challenging nature of these calculations have made pyrrole excited states something of a benchmark case for excited state theoretical methods, with many earlier studies failing to produce consistent energetic ordering or identify the nature of the long wavelength edge of the absorption spectrum (at wavelengths $\sim$250 nm).

In the most recent works [101, 116–118, 120], agreement has been reached that the lowest excited state is of $^1A_2$ symmetry and has significant $\pi\sigma^*$ character (hereafter referred to as the $S_1(\pi\sigma^*)$ state), with a 0–0 excitation of 4.96 eV (249.9 nm). The $\pi\sigma^*$ Rydberg character associated with this state indicates that the excitation

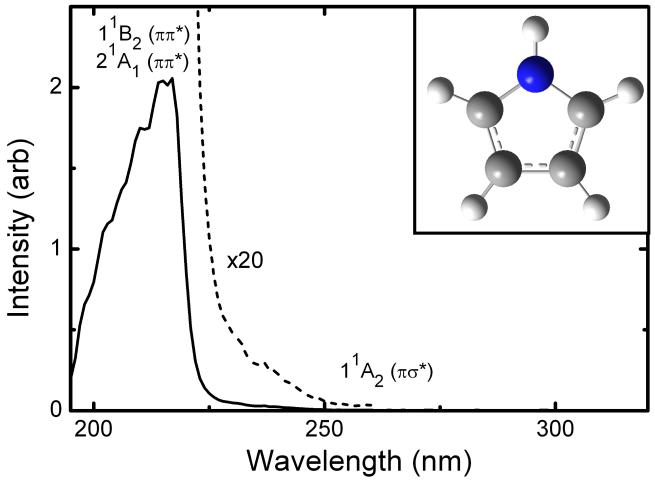

Figure 3.1: Gas phase UV absorption spectrum of pyrrole, recorded using a Perkin-Elmer Lambda 950 UV-VIS spectrometer. Inset: pyrrole molecule (C atoms - black, H atom - white, N atom - blue).

occurs from the π-based HOMO into a primarily dissociative, orbital centered on the N atom. Excitation from the ground state to the $S_1(\pi\sigma^*)$ state is formally forbidden, but is nonetheless weakly observed (see Figure 3.1) due to vibronic coupling to this nearby $\pi\pi^*$ state [114, 121]. The second, singlet excited state of pyrrole is of $^1B_2$ symmetry and has predominantly $\pi\pi^*$ character (hereafter referred to as $S_2(\pi\pi^*)$), its 0–0 transition lies at 5.70 eV (217.5 nm). A further $\pi\pi^*$ state of ($^1A_1$) symmetry also lies in close proximity, with a 0–0 transition at 5.57 eV (222.6 nm). However, the transition from the ground state to this excited state has an oscillator strength roughly an order of magnitude weaker than the $S_2(\pi\pi^*)$ state. Furthermore, one theoretical study has identified an additional $\pi\sigma^*$ state of $^1B_1$ symmetry has been predicted to lie below the $S_2(\pi\pi^*)$ state [122], however this finding has not been reflected in other theoretical works [117], or by any experimental evidence of which we are aware thus the above mentioned this state ordering is considered in the current work.

The one-photon photoelectron spectrum of ground state pyrrole is shown in Figure 3.2 [123]. The first ionisation potential leads to the formation of a $^2A_2$ state and lies at 8.2 eV (hereafter referred to as D_0). The first excited state of the singly ionised cation is of $^2B_1$ symmetry and lies at 9.2 eV (hereafter referred to as D_1) [97, 123–

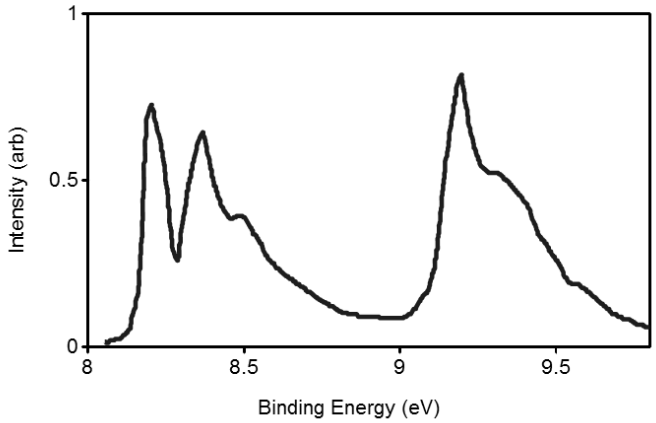

Figure 3.2: The gas-phase VUV photoelectron spectrum of pyrrole ionised from the ground state [123]. The characteristic vibrational progressions associated with the $D_0(^2A_2)$ and $D_1(^2B_1)$ states of the cation are clearly visible.

125]. At higher energies the spectrum becomes considerably more congested and it is difficult to disentangle the states involved, however we avoid accessing this region of the spectrum in the current study. Both of the first two cationic states have pronounced vibrational progressions which have been theoretically characterised, but are not directly relevant to the current work [126].

3.1.2 Potential energy surfaces

In order to understand the photodynamics of the excited states of pyrrole, it is important to understand the characteristics of the potential energy surface (PES). As described in Section 1.3, the pioneering work of Sobolewski and Domcke [10] identified the X-H (X = O,N) stretch coordinate as crucial in the non-adiabatic relaxation dynamics of molecules with low-lying $\pi\sigma^*$ states. This arises because the $\pi\sigma^*$ state is dissociative in this coordinate and couples with the ground state, thereby forming a mechanism by which population can rapidly relax from excited states prior to fluorescence. In biological systems the prompt dissipation of this energy is critical to avoiding potentially dangerous photoreactions.

The nature of the $S_1(\pi\sigma^*)$ state in pyrrole is primarily of dissociative σ^* character

at all N-H separations. However, both experiment and theory have indicated that a very small, quasi-bound region occurs in the vertical Franck-Condon (vFC) region. This region is bounded by a barrier to dissociation of ∼0.4 eV height, forming a well potentially capable of temporarily trapping population [127, 128]. Dissociation which occurs following population of the $S_1(\pi\sigma^*)$ state and subsequent motion along the N-H stretch coordinate, leads to formation of the pyrrolyl radical (C_4H_4N) and an H atom.

Several experimental studies [121, 129–132] have indicated that mechanisms involving N-H stretching vibrations account for a significant fraction of the deactivation processes. Blank *et al.* [129] used photofragment translational spectroscopy to study photoproduct formation, following excitation at 248 nm and 193 nm. It was found that following excitation to the $S_1(\pi\sigma^*)$ state at 248 nm, more than 90% of the photodissociation products are formed by N-H bond cleavage, either by direct dissociation or following relaxation to the ground state, with the remaining decay assigned as C-H dissociation. This study is unable to monitor relaxation pathways which do not result in fragmentation, consequently this finding does not imply that unreactive relaxation to the ground state is negligible. Following excitation 193 nm, N-H bond cleavage accounted for over 50% of the detected photoproducts, with decay again proceeding *via* both direct dissociation (30%) or relaxation to the ground state and subsequent dissociation (21%). Other decay channels included HCN production and C-N bond cleavage (NH product formed).

Temps and coworkers expanded upon this work by examining the velocity distribution of H atoms emitted following excitation at 243 nm ($S_1(\pi\sigma^*)$ state) and 217 nm ($S_2(\pi\pi^*)$ state) [130, 131]. In both cases, the authors reported a bimodal distribution with the more intense peak corresponding to 'fast' dissociation, resulting from breaking of the N-H occurring on a timescale significantly faster than the molecular rotation period. A weaker slow channel is also observable. This suggests that H atom dissociation can proceed either by direct dissociation on the excited state surfaces (producing fast H atoms) or by 'statistical' dissociation following internal conversion to the ground state (producing slow H atoms). Substituting the H atom bonded to the nitrogen, with a methyl group, results in the disappearance of the fast

H atoms, confirming that this spectral feature is indeed caused by direct dissociation of the NH group. These studies also examined d_1-pyrrole and found that upon deuteration the fast emission channel (of D) was increased in intensity compared to the equivalent channel in the undeuterated case, suggesting that a more efficient N-H(D) dissociation pathway is accessible in the deuterated case. This finding shows that the N-H dissociation branching ratio is dependent upon the specific N-H vibrational modes excited upon absorption. Even though theoretical modelling has shown that the $S_1(\pi\sigma^*)$ state is almost exclusively dissociative in the N-H direction, other important dynamical processes must be occurring in the undeuterated case.

Ashfold *et al.* examined pyrrole excited in the range 193.3–254 nm, using H Rydberg atom photofragment translational spectroscopy [97, 132]. Their findings are consistent with the results described above; excitation to the $S_1(\pi\sigma^*)$ state occurs at $\lambda > 225$ nm, with excitation to the $S_2(\pi\pi^*)$ state occurring at shorter wavelengths. In both cases 'fast' H atoms are observed and well-defined peaks are discernible within this distribution, suggesting that the pyrrolyl radical is only produced in certain vibrational states. They therefore conclude that, particular vibrational modes promote the N-H bond fission. At shorter wavelengths, slow H atoms become increasingly prevalent, until they dominate at $\lambda < 218$ nm, suggesting that relaxation to the ground state becomes increasingly favoured towards shorter wavelengths. It is not clear whether this relaxation proceeds *via* the $S_1(\pi\sigma^*)$ state and subsequent motion through the $\pi\sigma^*/S_0$ CI or occurs directly in some other coordinate. It is also notable that a minority of 'fast' H atoms continue to be observed in this higher energy region, suggesting that rapid radiationless relaxation to the $S_1(\pi\sigma^*)$ state continues to occur upon excitation to the $S_2(\pi\pi^*)$ state.

3.1.3 Time-resolved spectroscopy of pyrrole

Radloff *et al.* were the first to use ultrafast time-resolved spectroscopy to examine the timescale of H atom production in pyrrole [121]. They excited pyrrole to the $S_1(\pi\sigma^*)$ state with 250 nm light, using 243.1 nm REMPI to probe the nascent H atoms ejected. Two time-dependent H atom signals were observed, with lifetimes

of 110 ± 80 fs and 1.1 ± 0.5 ps, assigned to direct dissociation on the $\pi\sigma^*$ surface and slow H atom production *via* the ground state, respectively. These results are in keeping with the nanosecond experiments described above.

More recently, Stavros *et al.* also used ultrafast time-resolved photoion spectroscopy to study the dynamics of H atom production in pyrrole excited in the region 250–200 nm (243.1 nm H atom REMPI probe) [127]. The technique used in this study allowed for measurement of the kinetic energy of the H atoms ejected. Excitation very close to the $S_1(\pi\sigma^*)$ state origin, using 250 nm light, resulted in a single observable lifetime for N-H bond fission (high kinetic energy H atoms). This was measured at 126 ± 28 fs, which agrees with the ultrafast dissociation observed by Radloff and coworkers, although no $\sim$1.1 ps lifetime was observed. In fact, negligible low kinetic energy H atoms are observed, suggesting that, in this case, very little population relaxes back to the ground state and subsequently dissociates by hot 'statistical' processes. In order to further explore the bound region in the $S_1(\pi\sigma^*)$ state vFC, the same experiment was conducted with d_1-pyrrole. It was found that the D atoms associated with N-D fission appeared on a 1.4 ± 0.3 ps timescale and this increase in lifetime could support a tunnelling mechanism, because the directly dissociative dynamics on a purely repulsive surface would not be expected to vary significantly upon deuteration. 238 nm excitation was used to excite the $S_1(\pi\sigma^*)$ state with greater vibrational energy, whereupon the H atom dissociation lifetime is found to reduce to 46 ± 22 fs. This is attributed to excitation above the barrier to dissociation in the N-H stretching coordinate, therefore dissociation could be expected to proceed directly, on a faster timescale. At 200 nm, excitation to both the $S_1(\pi\sigma^*)$ and the $S_2(\pi\pi^*)$ states is possible. In this case, N-H fission was observed to occur on a 52 ± 12 fs timescale and is postulated to occur by a $S_2(\pi\pi^*) \rightarrow S_1(\pi\sigma^*) \rightarrow$ N-H fission mechanism. Given that this lifetime is very similar to that observed at 238 nm, this would require the initial relaxation from the $\pi\pi^*$ and $\pi\sigma^*$ states to be very fast, suggesting a strong coupling of states. This conclusion is supported by the intensity borrowing effect which causes the dipole forbidden $\pi\sigma^*$ state to have non-negligible oscillator strength in the first place. Furthermore, at 200 nm excitation, low kinetic energy H atoms associated with 'statistical' dissociation on the ground state surface

Figure 3.3: (a) Transient yield of pyrrole$^+$ (circles - data, red line - fit) and ethylene (blue) following excitation at 264 nm (800 nm probe). The green and black line represent the contribution of the decay lifetime associated with the $\pi\sigma^*$ and $\pi\pi^*$ states respectively. (b) Transient yield of pyrrole$^+$ and ethylene following excitation at 252 nm (800 nm probe). (c) Transient yield of pyrrole$^+$ and ethylene following excitation at 225 nm (800 nm probe). (d) Transient yield of pyrrole$^+$ and ethylene following excitation at 217 nm (800 nm probe). Reproduced from Ref. [134].

are observed, and occur with a rise time of $\tau > 1.2$ ns. This is a normal timescale for H atom emission [133] on the ground state surface and suggests that, following excitation to the $\pi\pi^*$ state, a branching of population occurs very rapidly, with some dissociating on the $\pi\sigma^*$ surface and some relaxing back to the ground state before dissociating.

Longarte and coworkers used ultrafast time-resolved photoion imaging to study the evolution of pyrrole following excitation in the region 265–217 nm, using 800 nm light as the ionisation probe [134]. In this study, the authors examine the generation of the pyrrole cation, rather than ejected H atoms. At all excitation wavelengths they observe two 'distinct' lifetimes of 19 ± 3 fs and 15 ± 3 fs, which are assigned to relaxation from the $S_2(\pi\pi^*) \rightarrow S_1(\pi\sigma^*)$ state and from the $\pi\sigma^*$ state to products (be that N-H bond dissociation or relaxation to the ground state). Figure 3.3 shows the associated fits produced, following excitation at 264–217 nm (800 nm probe), where the pyrrole$^+$ data points are shown as circles and the fit as a red line, the ethylene signal used to determine the cross-correlation of the excitation pulse is shown in blue, the green and black line represent the contribution of the decay lifetime associated with the $\pi\sigma^*$ and $\pi\pi^*$ states, respectively. It is unclear how the $\pi\pi^*$ state can provide a significant a contribution to the dynamics at wavelengths at which it would not be energetically accessible, for example 252 nm. Although, the results allow insight into the extremely rapid timescale upon which population leaves the vFC region, they conflict with the findings of Stavros *et al.*, who observe evidence (at 250 nm

excitation) for trapped population in the vFC region with a decay lifetime of over 100 fs. Furthermore, a recent publication by the same group [135] has revisited the findings described above. The conclusions of this analysis suggested that the apparent dynamics observed previously were instead caused by multiphoton effects resulting from their choice of ionisation wavelength, and that no conclusive evidence of ionisation from the $S_1(\pi\sigma^*)$ state was observed. We would tentatively suggest that this lack of observation of population in the S_1 state is due to a lack of sensitivity, as the works of Radloff *et al.* and Stavros *et al.* observe H atoms ejected as a result of populating this $\pi\sigma^*$ state.

Domcke *et al.* have employed theoretical modelling to understand the dynamics of the first four excited states of pyrrole (two $\pi\sigma^*$ states and two $\pi\pi^*$ states) using wavepacket propagation over CASSCF potential surfaces [122]. The potential energy surfaces are generated using a reduced dimensionality model, chosen to include the symmetry allowed conical intersections between the $\pi\sigma^*$ states and the ground state; the most significant of which is the N-H stretch dimension. It was found that the timescale and branching ratio of excited state population to reach dissociation or relax back to the ground state heavily depends upon the specific vibrational modes prepared by the excitation. If the excitation populates N-H stretching vibrations, NH bond fission was strongly favoured and occurred in under 50 fs. However, the study is limited by the number of dimensions considered and does not allow the system to undergo IVR to distribute energy to other vibrational modes, a process which might promote relaxation to the ground state.

Following on from this study, theoreticians have attempted to improve the model to examine the non-adiabatic dynamics of these excited states. Recently, Lischka *et al.* used on-the-fly trajectory simulations at the MRCI level to model the dynamics occurring in the first 200 fs, following excitation to the S_4 excited state of pyrrole [136]. They found that relaxation of the S_4 state primarily resulted in trajectories leading to pyrrolyl + H dissociation and that the N-H stretch is the principal relaxation mechanism, accounting for 80 % of the calculated trajectories, with a further 13 % deactivated by ring-bending modes (the remaining trajectories did not relax in the modelled time period). They found that relaxation to the $S_1(\pi\sigma^*)$ state occurred

on a 44 fs timescale, with subsequent relaxation occurring on an 80 fs timescale. Further studies by the Lischka group have also reached similar conclusions [137–139].

Recently, another study has looked at the dynamics occurring following excitation to the first two excited states of pyrrole, using multiconfigurational Ehrenfest simulations [140]. This method, in principle, allows access to all degrees-of-freedom on the potential surfaces, however much of the work is performed semiclassically and does not include a full quantum description, such as dynamic correlation effects. The authors find very complex decay mechanisms involving transfers between many states, but ultimately excitation to either of the first or second excited singlet states causes the majority of population to undergo NH bond fission in less than 20 fs. It is also found that, upon excitation to the second excited state population does not remain stable in this state for a measurable period, due to extremely rapid relaxation onto the $S_1(\pi\sigma^*)$ state.

These studies illustrate that the photodynamics of pyrrole following UV excitation continue to raise challenging questions and these questions have continued to generate significant interest over recent years. The fact that the lowest excited state is of $^1\pi\sigma^*$ character allows for the examination of dynamics on a energetically separated $\pi\sigma^*$ state, without the complication of coupling to lower lying states, and provides an interesting comparison to the molecules studied in later chapters of this thesis. It is then possible to study the changes in dynamics which occur following excitation to the higher lying $\pi\pi^*$ state. Furthermore, a small, but notable disparity exists between the dynamical lifetimes observed in the literature, following excitation to the $S_1(\pi\sigma^*)$. Studies measuring H-atom loss observe lifetimes of over 100 fs when exciting close to the origin of this state, excitation to higher vibrational excess energies results in a shorter lifetime. This decrease in lifetime with increased excitation energy has been attributed to tunnelling out of a very small, bound vFC region. In contrast, the existing time-resolved photoion study observed sub-20 fs lifetimes for all excitation wavelengths in the same spectral region. We aim to shed further light on this disparity.

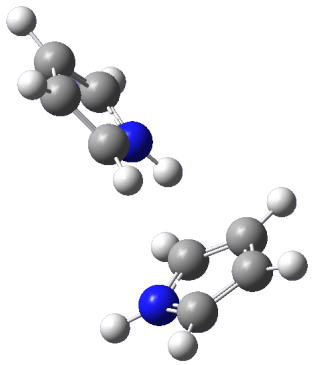

Figure 3.4: The optimised structure of the pyrrole dimer, as described in Ref. [145].

3.1.4 Cluster formation in pyrrole and their effect on excited states

The gas phase provides an excellent situation in which to study the fundamental electronic structure and states of molecules. However, even in the gas phase, molecules cannot usually be found in complete isolation, indeed our experiment goes to great lengths to create and isolate this type of environment. The solution phase offers information about interactions with other molecules and their effect on excited state dynamics, however this spectral information is often congested and difficult to disentangle. It is therefore informative to bridge this gap between gas and solution phases, by progressively building in the perturbations caused by molecular interactions and many studies have examined this concept in recent times [8, 141–144]. When building up pictures of molecular interactions, a logical first step is to examine the dimer, which forms a focus of the current study.

A theoretical study of the structure of the pyrrole-pyrrole dimer in its ground electronic state has been carried out, using MP2 and CCSD(T) methods [145]. The most stable structure for the pyrrole dimer is found to take the form of an approximately T-shaped complex (see Figure 3.4). It was found that the barrier to interconversion between the two possible conformers (both conformers have the same geometrical structure, but the 'inward-facing' molecule changes) is ∼0.035 eV, suggesting that

Figure 3.5: Schematic comparing the potential energy surfaces for the pyrrole monomer and dimer, in the N-H stretching coordinate and a representative ring bending coordinate. These schematics are supported by CASSCF/CASPT2 calculations. Reproduced from Ref. [91].

rapid interconversion is possible between these states.

Research by Buck *et al.* examined cluster formation occurring in a molecular beam, under various conditions [91]. The authors used an experimental setup similar to that described in our experimental section, in order to generate their molecular beam. Namely, pressurised He seed gas is passed through neat pyrrole solution and subsequently expanded through a small orifice (60μm in their work, 50μm in the current work) into a vacuum chamber, in order create a supersonic molecular jet. The authors found that molecular clusters were increasingly formed as the pressure of the seed gas was raised (hereafter referred to as the expansion pressure) and reducing the temperature of the pyrrole reservoir also encouraged cluster formation. With an expansion pressure of 1 bar, they found that the mean cluster size was 1 (*i.e.* monomers dominate), however after modestly increasing the expansion pressure to 1.5 bar, the average cluster size was found to be 3 (trimer). Given the carrier gas used, it is unlikely that clusters with helium were formed. Furthermore, these authors also present CASSCF/CASPT2 calculations which demonstrate that, upon dimerisation, the $S_1(\pi\sigma^*)$ state is preferentially stabilised in the vFC region, as compared to the ground state and other $\pi\pi^*$ states, but that upon extension of N-H bond, the $\pi\sigma^*$ state becomes strongly destabilised (see Figure 3.5). This destabilisation is sufficiently large to avoid the occurrence of an S_1/S_0 CI in this dimension. Consequently, dissociation along the N-H stretching coordinate of the $S_1(\pi\sigma^*)$ state is no longer believed to be an energetically favourable relaxation pathway, but the potential well formed instead may be capable of trapping population. Furthermore, it is also found that dimer formation did not substantially perturb the

lowest $\pi\sigma^*$ and $\pi\pi^*$ states in the relevant ring bending modes, it is therefore likely that relaxation to the ground state can still occur on rapid timescales.

Subsequent work by the Buck group has used DFT and MP2 quantum calculations to study small clusters and their various cationic states [146] to show that the ionisation potential of the dimer is approximately 0.4 eV lower in the dimer, than for the pyrrole monomer.

In many of the biological applications which underlie the motivation to the current work, photoreactions occur in a solvated environment. Due to the congested nature of much of excited state chemistry, bridging the gap between gas phase studies and those conducted in the liquid phase is of considerable importance. However, even after acquiring a strong understanding of gas phase dynamics in a particular system, the extension to condensed phase is non-trivial. Based upon the literature, dimerisation and clustering in pyrrole affects the relative spacing of the low lying $\pi\sigma^*$ and $\pi\pi^*$ states leading to novel and fascinating dynamics, which serves to motivate the cluster portion of the current study.

3.1.5 Experimental method

Our investigation of the excited state decay dynamics of pyrrole employed time-resolved photoelectron imaging (TRPEI), as described in Chapter 2. For the experiments in this chapter a continuous molecular beam was crossed with the co-linear pump and probe pulses produced by our 1 kHz femtosecond laser system.

We excited pyrrole at the origin of the $S_1(\pi\sigma^*)$ state using 249.5 nm (4.97 eV) femtosecond laser pulses, then with various amounts of excess vibrational energy in the S_1 state using 245.0 nm (5.06 eV) and 240.0 nm (5.17 eV) excitations. We also excited low in the S_2 state using 200.0 nm (6.20 eV) light, as shown in Figure 3.6(b). The excited state population is projected onto the photoionisation continuum using a delayed 300 nm (4.13 eV) femtosecond laser pulse, this wavelength was selected to access as much of the ionisation continuum as possible, whilst avoiding significant S_1–S_0 absorption (see Figure 3.6(a)), thereby reducing one-colour background signal.

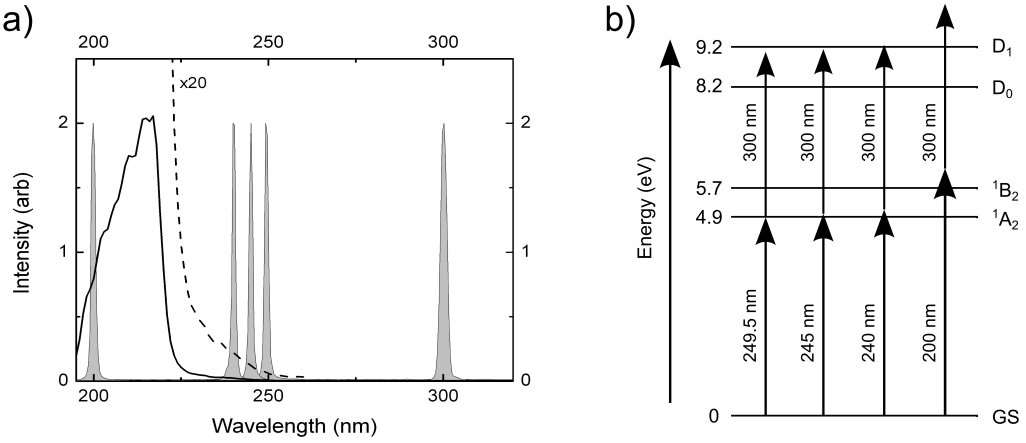

Figure 3.6: (a) Gas-phase UV absorption spectrum of pyrrole, with pump and probe pulse profiles superimposed. (b) Excitation scheme: pyrrole is excited using 249.5 nm (4.97 eV), 245.0 nm (5.06 eV), 240.0 nm (5.17 eV) and 200.0 nm (6.20 eV) pump pulses. The excited state population is projected onto the photoionisation continuum using a delayed 300 nm (4.13 eV) probe pulse. Assuming the $\Delta v = 0$ propensity rule for photoionisation, the electron kinetic energy following ionisation out of the Franck-Condon region is expected to increase in the order $S_1 < S_2$.

Photoelectron images are then recorded for a series of pump-probe delays between -250–1000 fs.

Photoelectron angular distributions are also obtained *via* our analysis with the pBasex inversion algorithm, producing the anisotropy parameters described in Section 1.2.2. These parameters were found to be isotropic ($|\beta_2| < 0.5$) throughout the energy ranges studied in this chapter, and are therefore not discussed further.

We monitored the formation of clusters in our molecular beam by examining displacement of the ion images produced when using a positive VMI polarity, as discussed in Section 2.2.3. We found that at 0.4 bar He expansion pressure only singly ionised pyrrole was produced, with no cluster formation or fragmentation detectable. In keeping with the findings of Buck *et al.* [91], we found that increasing the expansion pressure of the He seed gas induces cluster formation. Using the ion images, we estimate that at 1.0 bar He pressure approximately 3% of the signal is attributable to dimers and at 1.8 bar this rises to 7%.

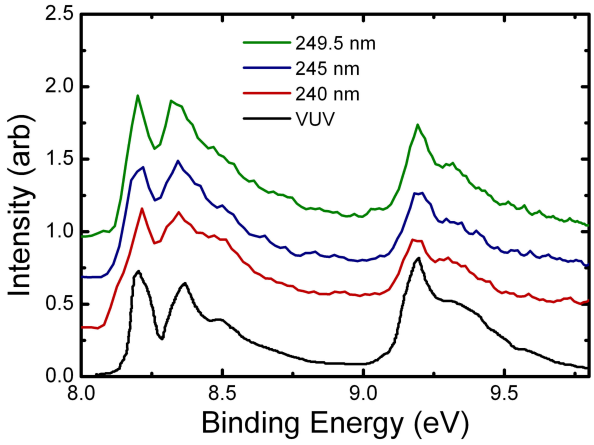

Figure 3.7: The one-colour $(1 + 1)$ photoelectron spectrum at various excitation wavelengths (vertically offset by 0.3). The published spectrum obtained by one-photon (VUV) ionisation of the ground state is also shown for reference [123].

3.2 TRPEI results for pyrrole excited in the region 249.5–200.0 nm

In this section, we examine the situation where only pyrrole monomers are present in the molecular beam (*i.e.* He expansion pressure of 0.4 bar). In order to confirm that only the monomer species was present, we examined the one-colour $(1 + 1)$ ionisation spectrum and compared it to the VUV one-photon photoelectron spectrum available from the literature. The comparison is shown in Figure 3.7, where we find excellent agreement,with no additional peaks (as compared to the one-photon photoelectron spectrum). The close match in observed structure indicates that excitation and ionisation are near simultaneous in the $(1 + 1)$ case, occurring on a timescale much faster than nuclear motion and therefore the Franck-Condon factor experienced is essentially conserved from the ground state. This is perhaps not surprising behaviour, given the short temporal width of our excitation pulse, but is in contrast to the additional vibrational structure seen in the $(1 + 1)$ photoelectron spectrum collected by a nanosecond experiment in the literature [132].

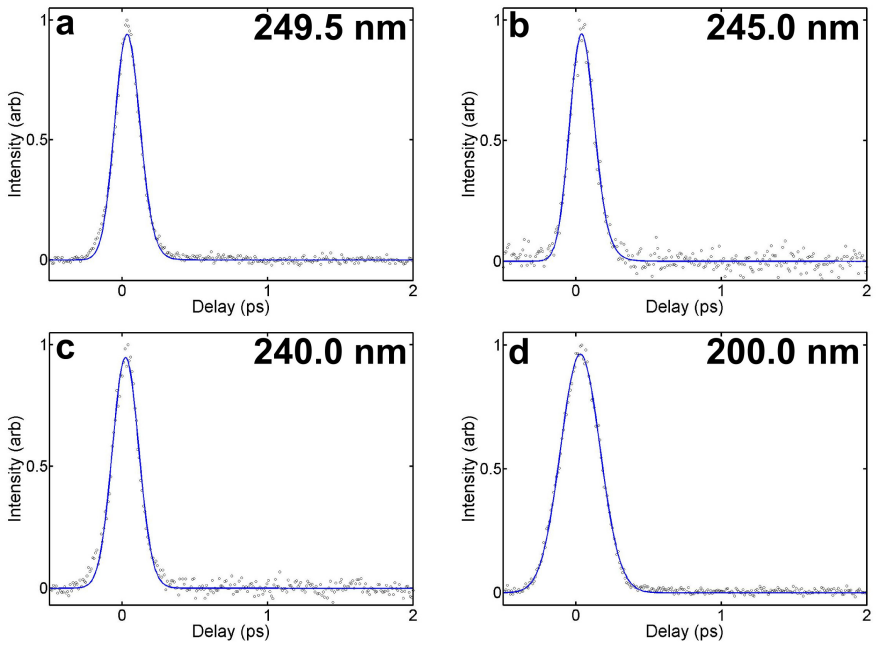

Figure 3.8: Total integrated photoelectron signal decay for pyrrole at 0.4 bar He expansion pressure, excited at 249.5 nm (a), 245.0 nm (b), 240.0 nm (c) and 200.0 nm (d).

3.2.1 Total integrated photoelectron signal

The evolution of the total integrated photoelectron signal, following excitation of pyrrole at 249.5, 245.0, 240.0 and 200.0 nm, is plotted with respect to the relative delay between pump and probe pulses in Figure 3.8(a-d). We fit this experimental data to a sum of exponential decays, convoluted with an instrument function representing the cross-correlation of our laser pulses, as described by Equation 2.11.

In the excitation range 249.5–240.0 nm, only the $S_1(\pi\sigma^*)$ state is energetically accessible. The cross-correlation obtained by fitting is 175–205 fs and the decay lifetimes obtained by fitting are < 50 fs in all cases, as shown in Table 3.1. However, failure to include the decay lifetime, *i.e.* fitting to Gaussian only, gives a poor description of the data. Given that this is less than 25% of our temporal pulse width, we conclude that the decay of this state occurs on a timescale faster than our minimum temporal resolution.

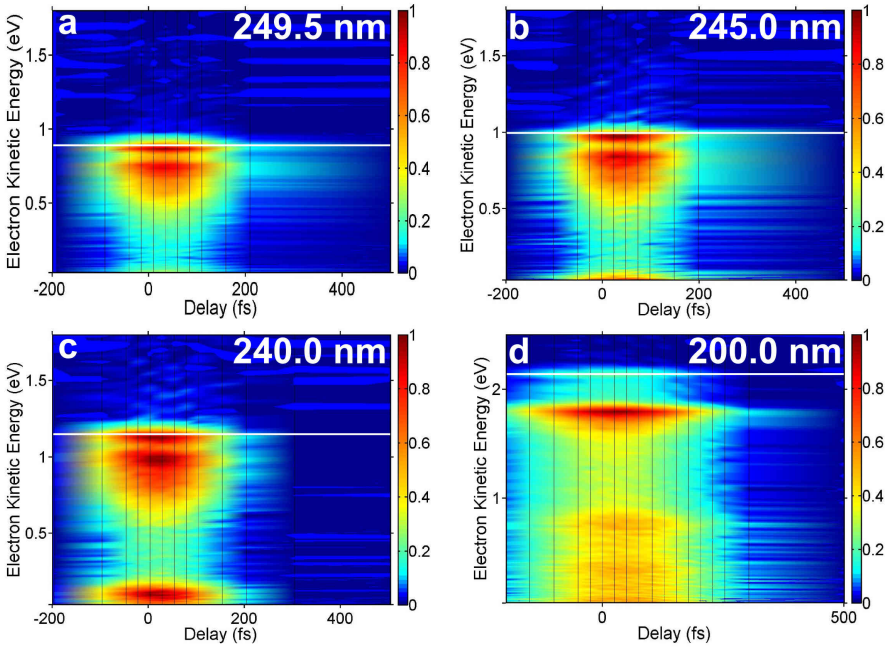

Figure 3.9: Surfaces produced by scaling the photoelectron images of pyrrole (at 0.4 bar He expansion pressure) to the total photoelectron decays shown in Figure 3.8. Images are shown for 249.5 nm (a), at 245.0 nm (b), at 240.0 nm (c) and at 200.0 nm (d) excitation wavelengths. Maximum accessible $(1 + 1')$ eKE are marked for each wavelength by solid white lines. Vertical black lines mark the delay times at which images were collected.

In pyrrole excited at 200.0 nm, the $S_2(\pi\pi^*)$ state can be accessed and based upon the absorption spectrum, this state is expected to account for much of the initial absorption. However, at this wavelength we continue to only observe a single sub-50 fs decay lifetime, although the temporal width of our cross correlation is noticeably longer (310 ± 10 fs) in this case.

The fitted functions in Figure 3.8 are used to scale the integrated intensity of the photoelectron spectra recorded at specific pump-probe delays (as described in Section 2.3), with the resultant surfaces are shown in Figure 3.9. Given that only a single decay lifetime is observed, decay associated spectra simply show the spectral profile of the photoelectron signal, which are analogous in all cases to those shown in Figure 3.7. It is possible to calculate the maximum possible electron kinetic energy accessible for a given excitation and probe wavelength, which serves as a useful

Table 3.1: Summary of pyrrole exponential decay lifetimes (monomer) obtained in the current work , and comparison to literature values.

Wavelength [nm]	Current Work	Longarte *et al.* [134]	Stavros *et al.* [127]	Radloff *et al.* [121]	Barbatti *et al.* [136]	Lischka *et al.* [139]
Method	TRPEI	Parent Ion	H atom formation	H atom formation	Theory	Theory
250	< 50 fs	15 ± 3 fs	126 ± 28 fs	110 ± 80 fs	-	-
245	< 50 fs	-	-	-	-	-
240	< 50 fs	-	46 ± 22 fs	-	-	-
217–200	< 50 fs	19 ± 3 fs	52 ± 12 fs	-	139 fs	100 fs

check that on the energy calibration and can be found using Equation 2.12. The D_0 of pyrrole (first ionisation potential) has been determined to be 8.21 eV [101, 124, 132, 147]. Therefore, the maximum accessible electron kinetic energies for our selected pump wavelengths are 0.89 eV for 249.5 nm, 0.98 eV for 245.0 nm, 1.08 eV for 240.0 nm and 2.12 eV for 200.0 nm (all using 300 nm probe). These energies are marked by solid white lines on Figure 3.9. The first excited state of the singly ionised pyrrole cation (D_1) lies at 9.2 eV and only becomes accessible above 240.0 nm excitation. The maximum accessible eKE would be 0.08 eV for 240.0 nm and 1.12 eV for 200.0 nm excitation (300 nm probe).

The ionisation potential for the pyrrolyl radical has been theoretically determined to be 9 eV [132], however given that this is a product peak, if any signal is attributed to ionisation of this species we would expect it to be delayed in time relative to the initially excited states. No photoelectron signal attributable to this species is observed in our results.

3.2.2 Discussion

Table 3.1 summarises the pyrrole monomer decay lifetimes we observed in this study and compares them to the results described in the literature. The decay lifetimes we observe are all limited by the temporal cross-correlation of our excitation and ionisation laser pulses ($\sim$50 fs). Indeed, we find the same decay lifetime upon excitation to the $S_2(\pi\pi^*)$ state. Although observation of lifetimes which are cross-

correlation limited is not ideal, determining an upper bound on decay from the vFC region is important, in light of findings in the literature. Furthermore, we find that the decay of the $S_1(\pi\sigma^*)$ state does not increase beyond 50 fs, regardless of whether excitation occurs very close to the state origin or if a greater amount of vibrational energy is imparted upon excitation. Notably, we find excellent agreement between our results and those measured in the time-resolved photoion study by Longarte *et al.* [134] *i.e.* both works find sub-50 fs lifetimes when exciting near the $S_1(\pi\sigma^*)$ origin and also, upon excitation to the $S_2(\pi\pi^*)$ state.

The close match between the studies of the parent molecule is particularly interesting when compared to H atom emission studies of Radloff *et al.* [121] and Stavros *et al.* [127]. Both of the H atom emission works observed rise times of ∼120 fs when exciting close to the $S_1(\pi\sigma^*)$ origin (250 nm), but found that this timescale reduced to ∼50 fs when excitation occurred higher on the $S_1(\pi\sigma^*)$ surface or to the $S_2(\pi\pi^*)$ state (at 200.0 nm). The latter observation is in keeping with our findings, however when studying excitation close to the $S_1(\pi\sigma^*)$ origin the different techniques generate lifetimes which lie outside of their respective experimental errors. The study by Stavros *et al.* also examined the decay of pyrrole, selectively deuterated at the N-H bond, where they found a significant increase in the D atom rise time (to ∼1.4 ps). The explanation given for this change is that excited state population on the $S_1(\pi\sigma^*)$ surface can become trapped in the vFC region by the quasi-bound region, created by the slight barrier to dissociation.

When exciting close to the $S_1(\pi\sigma^*)$ origin, our work does not observe such increase in decay lifetime, which would suggest that the population in not becoming trapped in the vFC region. Given that the H atom emission experiments agree with one another and, separately, the photoelectron/photoion experiments have good agreement, but a noticeable discrepancy exists between the results produced by the different methods, this suggests more complex dynamics at play. One explanation to reconcile this discrepancy is the existence of a previously unobserved energetic barrier between the two observable regions (*i.e.* vFC region and photoproducts), however no significant barrier has been noted in any of the numerous theoretical studies of pyrrole. As discussed above, the lack of wavelength dependence when examining the vFC region

suggests that any barrier to N-H dissociation is likely to be insignificantly small (at least in the vFC region). Another explanation could be that population traversing the dissociative channel can become temporarily trapped in a feature on the potential energy surface, delaying H atom emission. The only significant feature on the critical N-H dissociative coordinate is the $S_1(\pi\sigma^*)/S_0$ CI. It has not been previously suggested that this feature would be likely to trap population, but we hope that the current study will prompt theoretical studies of this region, in order to provide greater insight into this phenomenon.

The work of Temps and coworkers [130, 131] observed a bimodal distribution of H atoms, following excitation to the S_1 and S_2 states, showing that multiple decay pathways exist. Furthermore, these authors demonstrated that replacing the H atom (attached to the N) with a methyl group removed the dominant 'fast' H atom decay channel. This implies that N-H dissociation is the most significant decay channel, as would be expected from the potential energy surfaces. They also found that singly deuterating pyrrole produces an enhanced yield of fast H(D) atoms, compared to the undeuterated case. If dissociation along the N-H coordinate were the only significant decay mechanism in pyrrole excited to the S_1 state, it would not be possible to provide an enhancement in H(D) yield upon deuteration, therefore this finding suggests that other deactivation processes must exist in the undeuterated system. However, our results only observe a single decay lifetime, so if multiple decay channels exist, they must all occur on a sub-50 fs timescale.

Ashfold *et al.* [97] concluded that slow H atom production becomes the dominant relaxation mechanism at wavelengths $\lambda < 218$ nm and that N-H bond fission is a minor decay route in this excitation region. Our results do not conflict with this conclusion, however we do not find additional evidence to support it. The ultrafast decay lifetime observed at 200.0 nm excitation is also in the sub-50 fs region, as observed at the other wavelengths in this study, and we do not observe a second decay lifetime. It is perfectly plausible that both internal conversion and dissociation mechanisms occur on a sub-50 fs timescale, in which case the current study is unable to differentiate between them.

Finally, the theoretical investigation of Lischka *et al.* [148] suggests that a ring-opening mechanism becomes accessible upon excitation to the $S_2(\pi\pi^*)$ state. Our results do not exclude this possibility, as long as it also occurs on a sub-50 fs timescale. However, we do not find any additional evidence to support such a deactivation mechanism, furthermore a similar mechanism has been proposed to occur on a > 1 ps lifetime in furan [149].

3.3 TRPEI results for the pyrrole dimer excited in the region 249.5–200.0 nm: the effect of microsolvation

As described in Section 3.1.5, increasing the expansion pressure of the He seed gas induces the formation of pyrrole dimers within our molecular beam. Proportionally, the number of dimers formed is relatively small, however as will be shown, their presence reveals significant additional features in the photoelectron spectrum. We will use this section to examine the effects of the presence of these dimer species upon the relaxation dynamics of pyrrole. The photodynamics of electronically excited pyrrole are critically dependent on the $S_1(\pi\sigma^*)$ state, which comprises significant Rydberg (diffuse) character in the Franck-Condon region. Given that the most stable dimer structure is T-shaped (shown in Figure 3.4), it is expected that the binding of the second subunit until will strongly interact with the diffuse orbitals associated with the N atom in the first subunit [150, 151]. Consequently, the stability of the $S_1(\pi\sigma^*)$ state is strongly affected by clustering effects, relative to the $S_2(\pi\pi^*)$ state.

Further to the evidence of dimerisation, presented in Section 3.1.5, we have also collected the $(1 + 1)$ photoelectron spectrum for 240.0 nm excitation at various He expansion pressures, shown in Figure 3.10. At this wavelength, the maximum eKE that is accessible in the monomer is 2.11 eV (marked by a vertical dashed line), however at higher expansion pressures we clearly see an additional feature at eKE

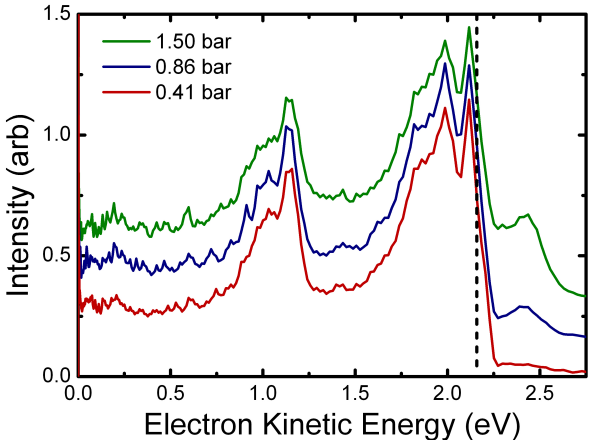

Figure 3.10: One-colour $(1+1)$ photoelectron spectrum at 240.0 nm excitation, at various He expansion pressures (vertically offset by 0.2). The dashed line marks the maximum $(1+1)$ eKE accessible (2.13 eV), the pressure dependent peak visible above this line relates to the dimer.

$\sim$2.45 eV. The intensity of this peak dependent upon the He expansion pressure. Additionally, it should be noted that the intensity of this peak is linearly dependent upon either the pump or the probe intensities, which effectively excludes multi-photon processes as the origin of the feature, as a higher order dependency would be expected to be observed. Furthermore, as the data presented below will show, this feature is time-dependent, excluding the possibility of $(1+1)$ resonant dynamics caused by non-simultaneous absorption of two pump photons. We can exclude the possibility of simultaneous pump and probe photon excitation, because this will access an auto-ionising state, which would also not result in a time-dependent signature. Furthermore, as described in the introduction, the dimer ionisation potential is predicted to be about 0.2 eV lower in energy than the monomer case, allowing for the ejection of higher kinetic energy photoelectrons [146]. We therefore believe that this peak arises from clustering effects, namely those attributable to the pyrrole dimer. This section will therefore examine the dynamics of pyrrole with increasing proportions of dimers present in the molecular beam, which is achieved by using medium (0.85–1.0 bar) and higher (1.8 bar) He expansion pressures and collecting data excited at the same excitation and probe wavelengths used in Section 3.2.

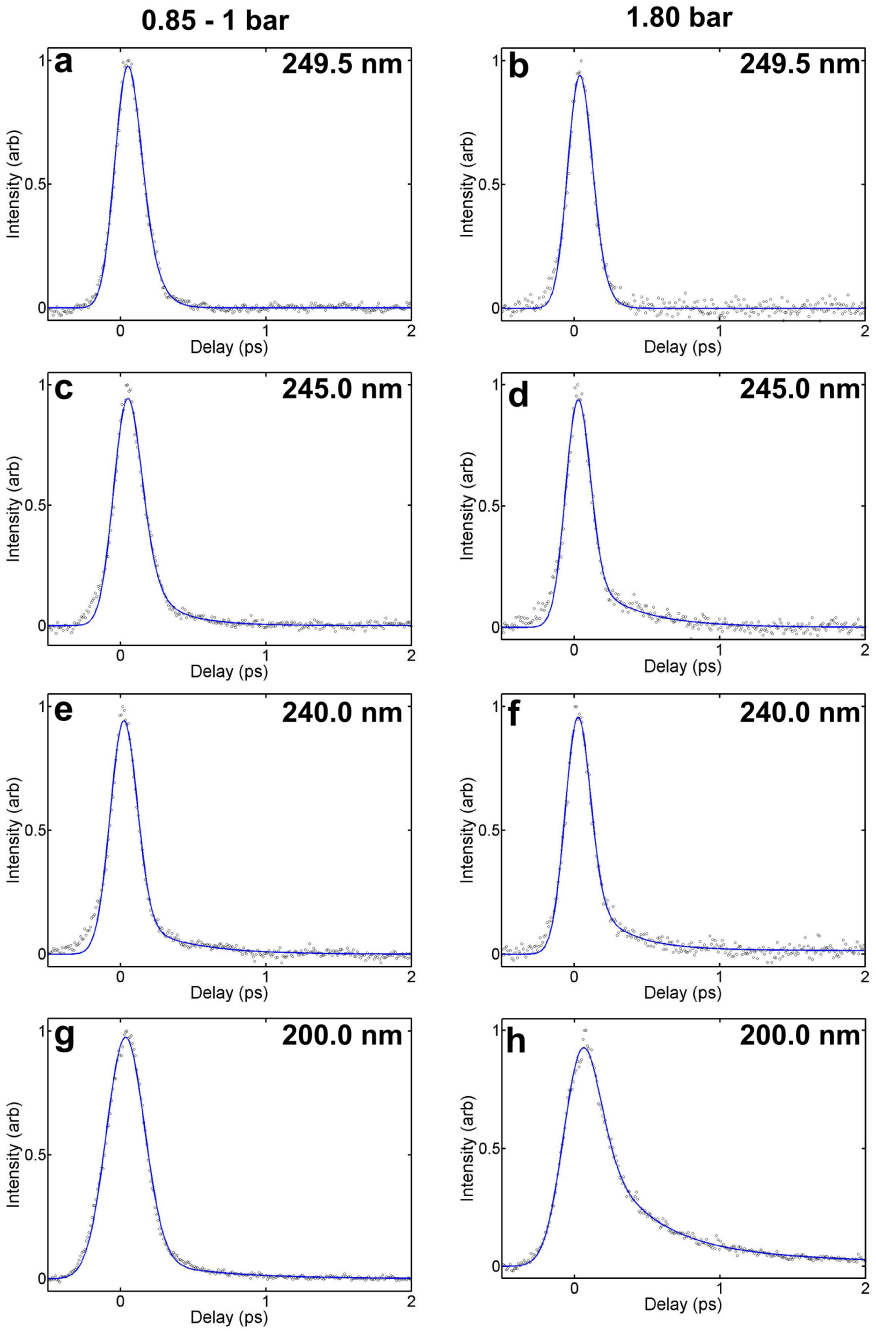

Figure 3.11: Total integrated photoelectron signal decay for pyrrole with various He expansion pressures. Plots of pyrrole with expansion pressure in the 0.85–1.0 bar range, excited at 249.5 nm (a), 245.0 nm (c), 240.0 nm (e) and 200.0 nm (g) are shown. Plots of pyrrole with higher He expansion pressure (1.8 bar) are also shown for 249.5 nm (b), 245.0 nm (d), 240.0 nm (f) and 200.0 nm (h) excitation.

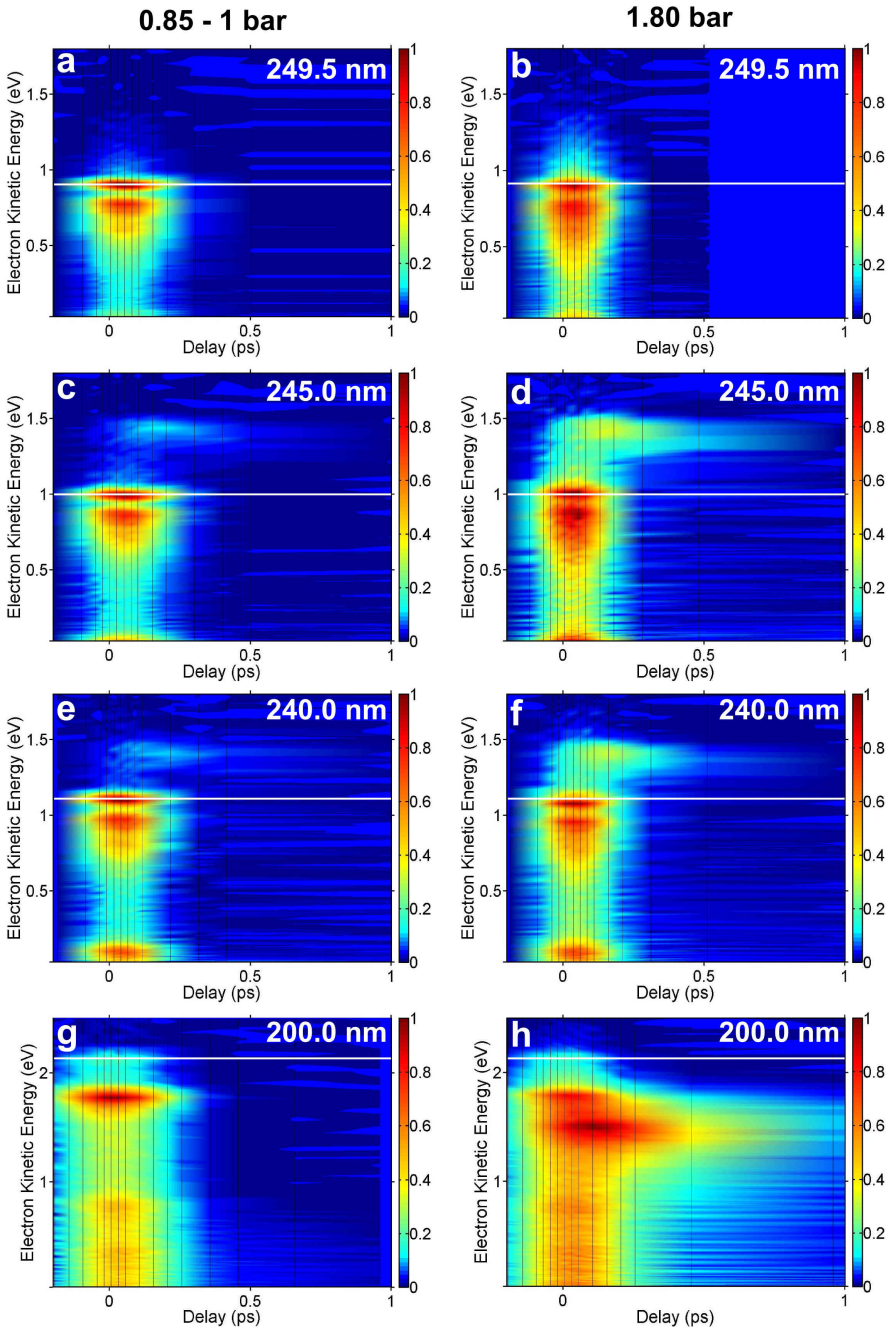

Figure 3.12: Surfaces produced by scaling the photoelectron images of pyrrole to the total photoelectron decays shown in Figure 3.11, with medium (0.85–1.0 bar) and high (1.8 bar) He expansion pressure. Images are shown for 249.5 nm (a) and (b), at 245.0 nm (c) and (d), at 240.0 nm (e) and (f) and at 200.0 nm (g) and (h) excitation wavelengths. Maximum accessible (1+1′) eKE are marked for each wavelength by solid white lines. Vertical black lines mark the delay times at which images were collected. It is notable that as the expansion pressure, and therefore clustering, increases an additional feature becomes visible in the photoelectron spectrum above the maximum accessible $(1 + 1')$ eKE (except 200.0 nm excitation).

3.3.1 Total integrated photoelectron signal

As described in Section 3.2.1, the first stage of our lifetime extraction involves fitting the total integrated photoelectron signal to a sum of exponential decays, convoluted with an instrument function. In the studies of the pyrrole monomer detailed above only a single decay lifetime was observed for all excitation wavelengths studied, in contrast multiple decay lifetimes are observed for the dimer system. The fitted curves shown in Figure 3.11 are used to scale our photoelectron spectra, with the resultant surfaces shown in Figure 3.12. The maximum accessible electron kinetic energy (for the monomer) for each excitation and probe wavelength is calculated using Equation 2.12 and is plotted as a solid white line, again it is notable that the cluster dependent peak appears above this limit.

3.3.2 Decay lifetimes

The multiple ultrafast decay lifetimes are extracted by sequentially integrating over limited energy regions of the photoelectron spectra, as described in Section 2.3.2. This is in contrast to the fitting procedure in Section 3.2.1, where only a single ultrafast decay lifetime is observed. We usually fit the highest energy feature of the photoelectron spectrum first, then move systematically towards the lowest energy feature, in order to avoid overlapping peaks from distorting the measured lifetimes. However, the new feature arising from clustering effects is not the first feature fitted for two reasons. Firstly, it is significantly weaker than the other spectral feature, and secondly, this new feature appears to have a delayed rise time with respect to the zero delay position, as can be observed in Figure 3.12. We therefore fit the most intense feature first and then fit the cluster dependent peak at higher eKE afterwards.

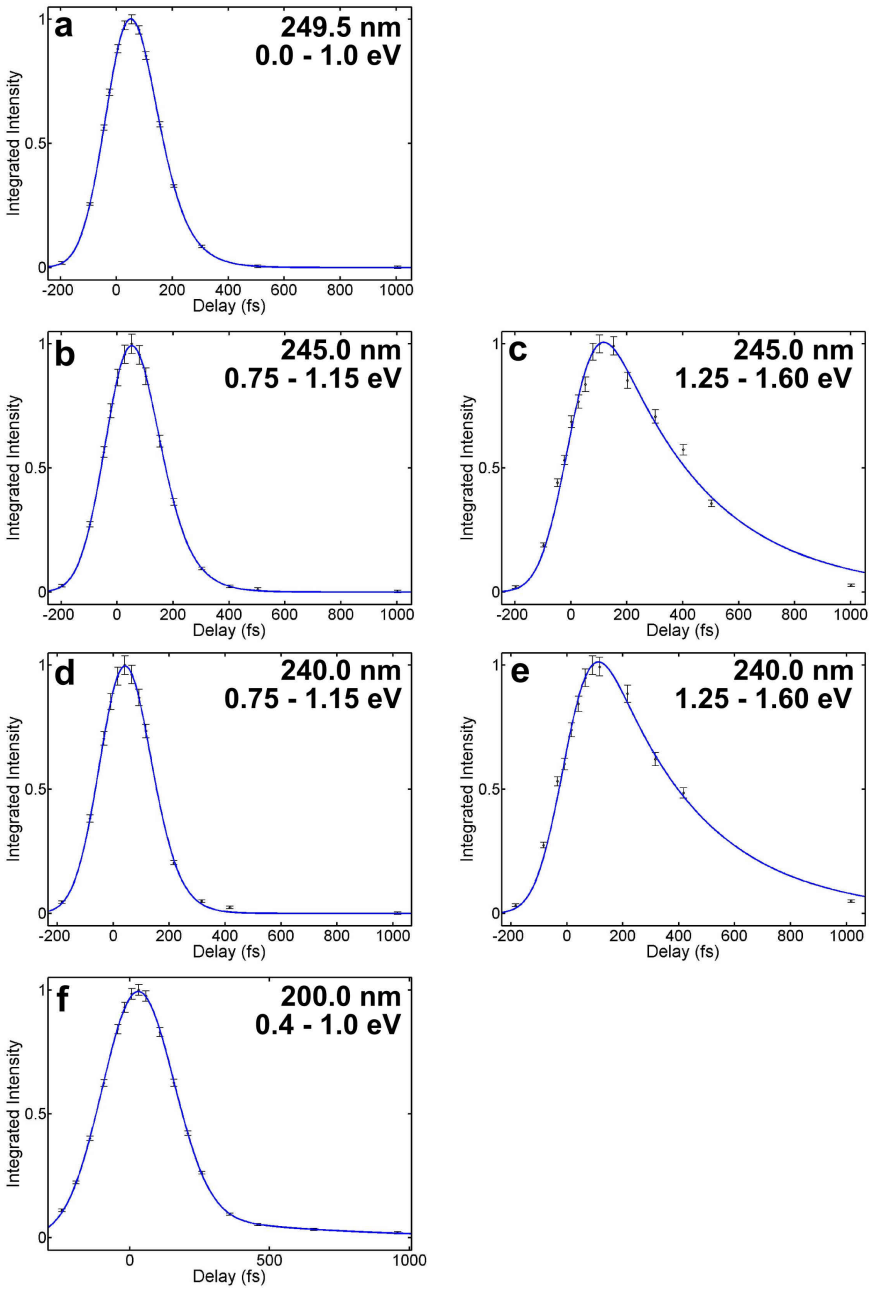

Figure 3.13: Fits to the photoelectron spectra (0.85–1.0 bar He expansion) integrated over discrete regions, used to obtain the lifetimes shown in Table 3.2. Fits are shown for integrations over the entire photoelectron spectrum for 249.5 nm (a), and over the energy region 0.75–1.15 eV region for 245.0 nm (b) and 240.0 nm (d), over the 1.25–1.6 eV region for 245.0 nm (c), 240.0 nm (e) and finally over the 0.4–1.0 eV region for 200.0 nm excitation (f). Error bars show the (2σ) standard deviation in photoelectron intensity over the integrated region.

Medium expansion pressure (0.85–1.0 bar)

The dynamics observed following 249.5 nm excitation are similar to those of the monomer system, where only a single exponential decay lifetime is observed and no additional feature is visible at higher eKE. A decay lifetime of $\tau_1 = 70 \pm 10$ fs was extracted from integrating over the entire photoelectron spectrum (Figure 3.13(a)). The cross-correlation was found to be 187 ± 10 fs.

Following 245.0 and 240.0 nm excitation, an additional peak is weakly observable at eKE ∼1.4 eV. As described above, we obtain the zero delay position and cross-correlation from fitting over the most intense feature of the spectra *i.e.* the energy region 0.75–1.15 eV. The cross-correlation was found to be 197 ± 10 fs for both excitation wavelengths. The decay lifetime of the intense peak was found to be $\tau_1 = 69 \pm 10$ fs and $\tau_1 = 52 \pm 10$ fs, following 245.0 and 240.0 nm excitation respectively (Figure 3.13(b) and (d)). The lifetime of the additional feature was found by integrating over the range 1.25–1.6 eV, the additional decay lifetime was found to be $\tau_2 = 346 \pm 71$ fs following 245.0 nm excitation and $\tau_2 = 335 \pm 64$ fs following 240.0 nm excitation (Figure 3.13(c) and (e)).

When exciting with 200.0 nm light, the additional peak in the eKE region 1.4 eV is no longer of observable intensity. It is entirely possible that the cluster dependent feature continues to be produced at this excitation wavelength, but cannot be discerned due to its weak intensity. In this case, we obtain the zero delay position and cross-correlation from fitting over the energy range 0.4–1.0 eV. The cross-correlation was found to be 294±10 fs and two distinct decay lifetimes were found to be $\tau_1 < 50$ fs and $\tau_2 = 486 \pm 160$ (Figure 3.13(f)).

Higher expansion pressure (1.8 bar)

Again, following 249.5 nm excitation, we observe a situation analogous with the monomer. A single exponential decay lifetime of $\tau_1 < 50$ fs was extracted from integrating over the entire photoelectron spectrum and no additional feature is visible at higher eKE. The cross-correlation was found to be 180 ± 10 fs.

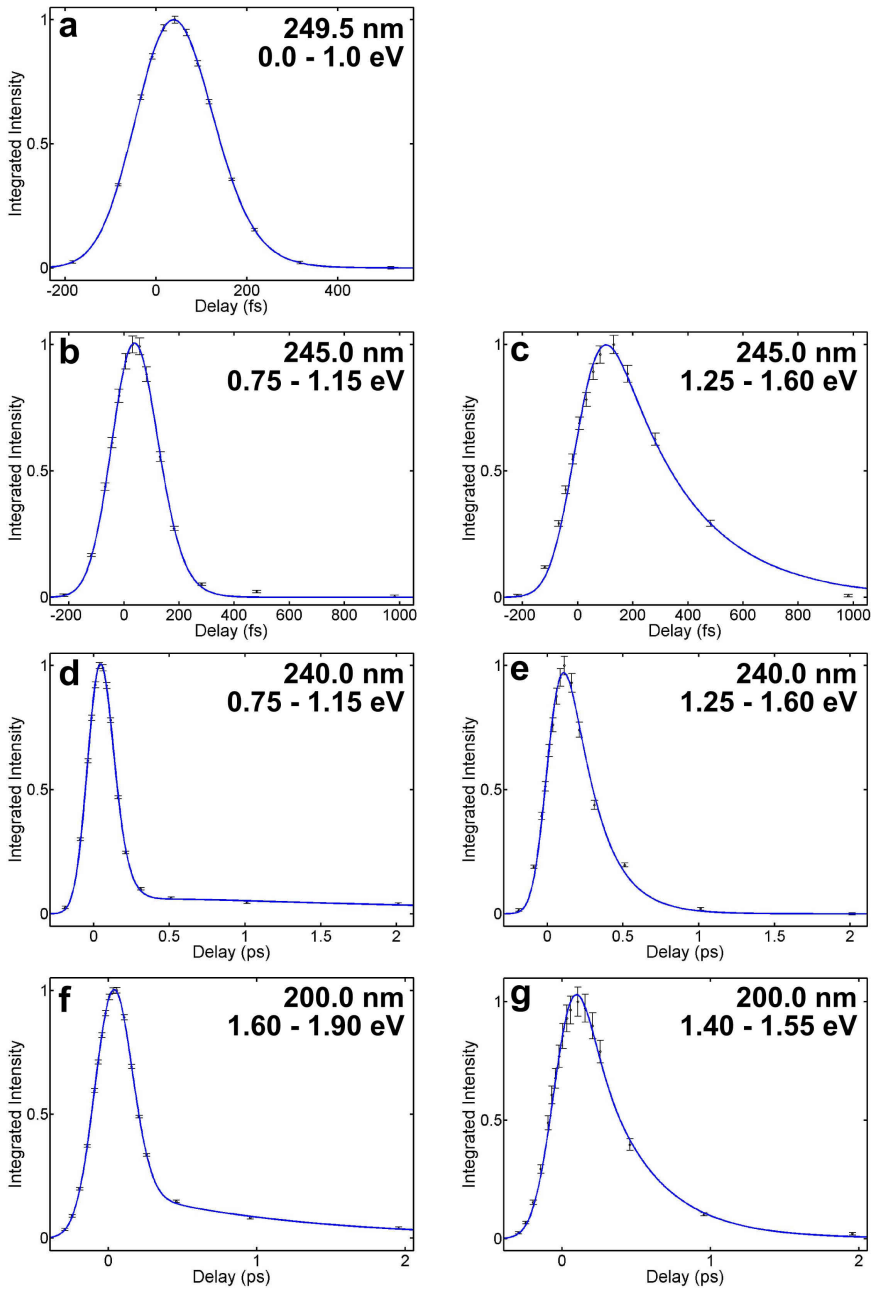

Figure 3.14: Fits to the photoelectron spectra (1.8 bar He expansion) integrated over discrete regions, used to obtain the lifetimes shown in Table 3.2. Fits are shown for integrations over the entire photoelectron spectrum for 249.5 nm (a), and over the energy region 0.75–1.15 eV region for 245.0 nm (b), 240.0 nm (d), over the range 1.6–1.9 eV for 200.0 nm (f), over the 1.25–1.6 eV region for 245.0 nm (c) and 240.0 nm (e) and over the range 1.4–1.55 eV for 200.0 nm (g). Error bars show the (2σ) standard deviation in photoelectron intensity over the integrated region.

Following 245.0 and 240.0 nm excitation, the additional peak at eKE around 1.4 eV continues to be weakly observable. As described above, we obtain the zero delay position and cross-correlation from fitting over the most intense part of the quickly decaying state (the energy region 0.75–1.15 eV). The cross-correlation was found to be 179 ± 10 fs for both 245.0 and 240.0 nm excitation. The decay lifetime of the intense peak was found to be $\tau_1 < 50$ fs and $\tau_1 = 57 \pm 10$ fs following 245.0 nm and 240.0 nm excitation, respectively (Figure 3.14(b) and (d)). The lifetime of the cluster dependent feature was found by integrating over the range 1.25–1.6 eV. The decay is found to occur on a $\tau_2 = 267 \pm 44$ fs timescale when 245.0 nm excitation was used and a $\tau_2 = 185 \pm 28$ fs lifetime when 240.0 nm is used (Figure 3.14(c) and (f)). Following 240.0 nm excitation, a third weak lifetime was also found, which covers a broad eKE range. When we integrate over the range 0.03–0.5 eV, this lifetime is found to be $\tau_3 = 2.6 \pm 1.5$ ps where the large error is likely to be the result of the weak intensity of this peak.

200.0 nm excitation leads to the continued observed of a cluster dependent peak in the 1.4 eV eKE region. This is curious because the the remainder of the photoelectron spectrum is shifted to higher eKE, due to the increased energy of the pump wavelength. In this case, we obtain the zero delay position and cross-correlation from fitting over the energy range 1.6–1.9 eV. The cross-correlation was found to be 289 ± 10 fs and the decay lifetime was found to be $\tau_1 < 50$ fs (Figure 3.14(f)). The decay associated with the cluster dependent peak is found by integrating over the range 1.4–1.55 eV, a lifetime of $\tau_2 = 364 \pm 118$ fs is fitted (Figure 3.14(g)). Again, a longer time peak is observed with very weak intensity over the range 0.03–0.5 eV, with a lifetime of $\tau_3 = 1.1 \pm 0.2$ ps.

A summary of the lifetimes obtained by this fitting procedure is shown in Table 3.2.

3.3.3 Global fitting

Our quasi-global fitting procedure (described in Section 2.3.2) uses the lifetimes obtained above, but examines their relative contribution across the eKE range. This

Table 3.2: Summary of pyrrole exponential decay lifetimes

Excitation [nm]	Low Pressure (0.4 bar) [fs]	Medium Pressure (0.85–1.0 bar) [fs]	Higher Pressure (1.8 bar) [fs]
249.5	$\tau_1 < 50$	$\tau_1 = 70 \pm 10$	$\tau_1 < 50$
245.0	$\tau_1 < 50$	$\tau_1 = 69 \pm 10$	$\tau_1 < 50$
		$\tau_2 = 346 \pm 71$	$\tau_2 = 267 \pm 44$
240.0	$\tau_1 < 50$	$\tau_1 = 52 \pm 10$	$\tau_1 < 50$
		$\tau_2 = 335 \pm 64$	$\tau_2 = 185 \pm 28$
			$\tau_3 = 2600 \pm 1500$
200.0	$\tau_1 < 50$	$\tau_1 < 50$	$\tau_1 < 50$
			$\tau_2 = 364 \pm 118$
		$\tau_2 = 486 \pm 160$	$\tau_3 = 1100 \pm 200$

procedure is seen to reproduces all of the dynamical features observed in the experimental spectra, as shown in Figure 3.15 and Figure 3.17.

Medium expansion pressure (0.85–1.0 bar)

Figure 3.15(a) depicts the fitted surfaces reproduced by our quasi-global fitting method, with medium He expansion pressure, following the 249.5 nm excitation of pyrrole. The spectral shape of the feature associated with τ_1 is indistinguishable from the monomer case (Figure 3.9(a)). Figure 3.15(b) displays the residual produced by subtracting the fitted surface in (a) from the original data surface presented in Figure 3.12(a). The residual surface is included to illustrate the level of agreement between the fitted surfaces and the original data. As can be seen, the residual amplitude is typically not more than 5% (of the normalised maximum signal) and fairly evenly distributed across the image, suggesting it originates from statistical fluctuations rather than any systematic error in the data or fit. The decay associated spectra (DAS) are shown in Figure 3.16 (three-point averaged for clarity), along with a series of plots where the lifetimes extracted are fitted back to the total integrated photoelectron yield. At 249.5 nm excitation only a single lifetime is observed, so Figure 3.16(a) and (b) are self-explanatory.

Figure 3.15(c) shows the fitted surfaces for pyrrole excited at 245.0 nm, using τ_1 and τ_2 detailed in Table 3.2. The shape of the main feature (at eKE $<$ 1 eV) is

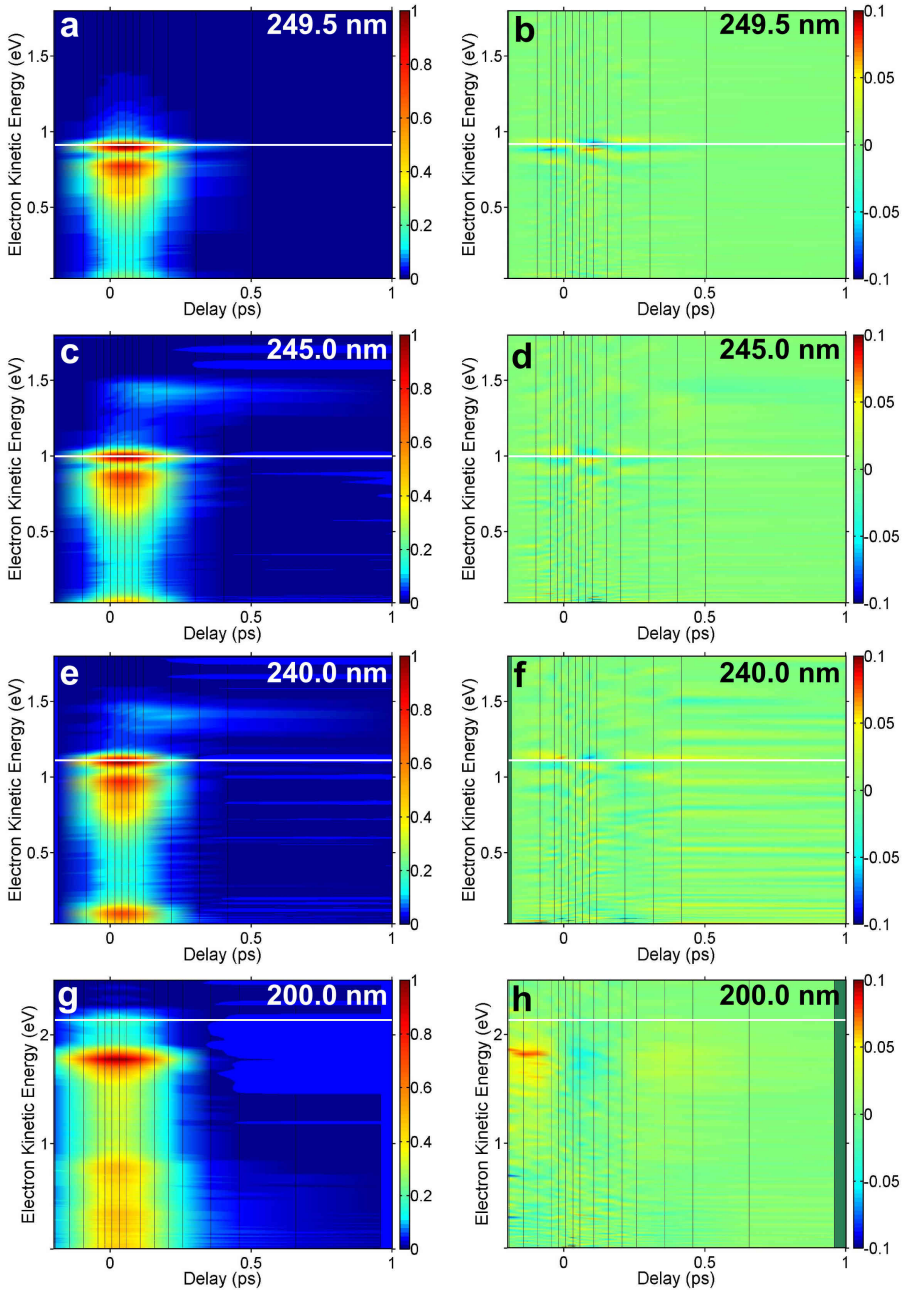

Figure 3.15: Fitted surfaces (0.85–1.0 bar He expansion), using lifetimes detailed in Table 3.2. Surfaces are show for 249.5 nm (a), 245.0 nm (c), 240.0 nm (e) and 200.0 nm (g) pump wavelengths. Residuals of the fit subtracted from the experimental data are shown for 249.5 nm (b), 245.0 nm (d), 240.0 nm (f) and 200.0 nm (h) pump wavelengths. Maximum accessible $(1 + 1')$ eKE are marked for each wavelength by solid white lines.

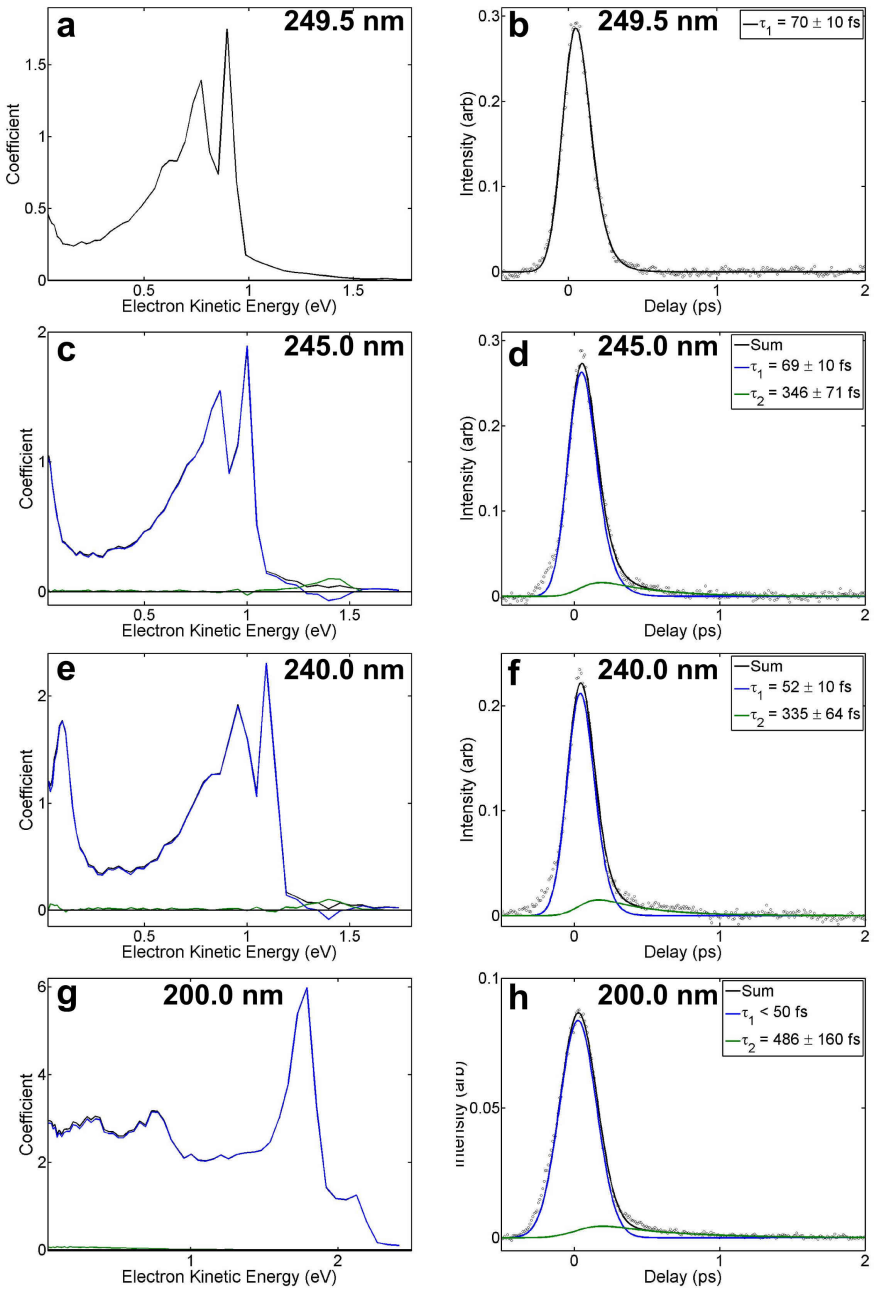

Figure 3.16: Decay associated spectra (0.85–1.0 bar He expansion) relating to the surfaces in Figure 3.15, for 249.5 nm (a), 245.0 nm (c), 240.0 nm (e) and 200.0 nm (g) pump wavelengths. Refitting these same lifetimes to the total integrated decay data (presented in Figure 3.11) are shown for 249.5 nm (b), 245.0 nm (d), 240.0 nm (f) and 200.0 nm (h) pump wavelengths, where these plots are normalised to $\sum_i c_i = 1$, excluding states which feed other observable states. Consequently the limit at long delay time indicates the proportion of the initially excited wavepacket remaining.

similar to that of the monomer species, *i.e.* the vibrational states observed are those of the cation. The DAS presented in Figure 3.16(c) shows that, upon excitation at 245.0 nm, the two distinct decay lifetimes cover separate spectral regions and the longer lived state (τ_2) does not have any contribution to the spectrum outside of the eKE range 1.4–1.6 eV. Furthermore, the majority of the state associated with the feature below 1 eV eKE is analogous to the dynamics observed in the monomer, to some extent this is expected as our molecular beam comprises a mixture of monomers and dimers. Based upon the ionisation potential know that the eKE range associated with τ_2 component is not energetically accessible in the monomer, but could be attributed to an electronic state in the dimer which has a lower ionisation potential in the vFC region. An additional complication arises from the observation of a delay in the rise time of the τ_2 component (see Figure 3.15(d)). This manifests in the DAS as a negative coefficient relating to τ_1 in the region where τ_2 has a positive coefficient (1.4–1.6 eV). This suggests that population is decaying from the state associated with τ_1 into the state associated with τ_2 and could not occur if both states were directly populated. These observations suggest that some proportion of the signal attributed to τ_1 must originate in the dimer system. However, the vibrational progression observed is analogous to that observed for the monomer suggesting that the state in the dimer is very monomer-like.

The fitted surface and residual for the 240.0 nm excitation of pyrrole is presented in Figure 3.15(e) and (f), respectively. The spectral features observed and implications regarding evolution of the excited wavepacket are analogous to those described following 245.0 nm excitation: the signal associated with the τ_1 is much stronger and dominates the spectrum, the peak associated with τ_2 is energetically inaccessible in the monomer and appears to be populated by a decay associated with τ_1. Notably, the spectral features associated with τ_1 covers the equivalent eKE range as would be expected when increasing the excitation photon from 245.0 nm to 240.0 nm, however the spectral feature associated with τ_2 does not shift in energy.

Again, the fitted surface and residual following 200.0 nm excitation are presented in Figure 3.15(g) and (h), respectively. The signal-to-noise ratio is slightly worse compared with the other wavelengths studied in this chapter, due to the lower in-

tensity excitation used in order to reduce background ionisation. The predominant, sub-50 fs τ_1 component has the same characteristics as observed in the monomer case. The longer lifetime τ_2 component has a weak intensity and does not strongly contribute to the photoelectron signal at any individual eKE region, as shown in the DAS (Figure 3.16(g)). Instead, the τ_2 component covers a very broad eKE range and this feature is integrated across the entire eKE range, its contribution to the photoelectron signal which cannot be neglected (Figure 3.16(h)). Notably, the character of the state associated with τ_2 at this wavelength appears different from that observed at 240.0 and 245.0 nm.

Higher expansion pressure (1.8 bar)

When the He seed gas is raised to higher pressure (1.8 bar), we continue to observe the additional dynamics noted in the previous section, although the intensity of the additional features increases in intensity. However, at this elevated expansion pressure only a single decay lifetime continues to be observed following 249.5 nm excitation (Figure 3.18(a)).

The fitted surface and residual following 245.0 nm excitation are shown in Figure 3.17(c) and (d), respectively. Again, the DAS presented in Figure 3.18(c) shows that the two distinct decay lifetimes cover separate eKE ranges, however the spectral feature associated with τ_2 has a considerably stronger intensity than was previously observed. Using similar logic to that described in the previous section, it is also likely that population decays from a state associated with the τ_1 component into the state associated with the τ_2 component.

Following 245.0 nm excitation, the fitted surface in Figure 3.17(e) displays the same features observed following 245.0 nm excitation at this expansion pressure, as confirmed by the DAS (Figure 3.18(e)). As was observed at medium expansion pressure, the eKE range spanned by the τ_2 component does not increase when the excitation wavelength is decreased from 245.0 to 240.0 nm. However, an additional τ_3 component is observed which is considerably longer lived than either τ_1 or τ_2. This τ_3 component is weak in intensity and cannot be easily discerned directly from the sur-

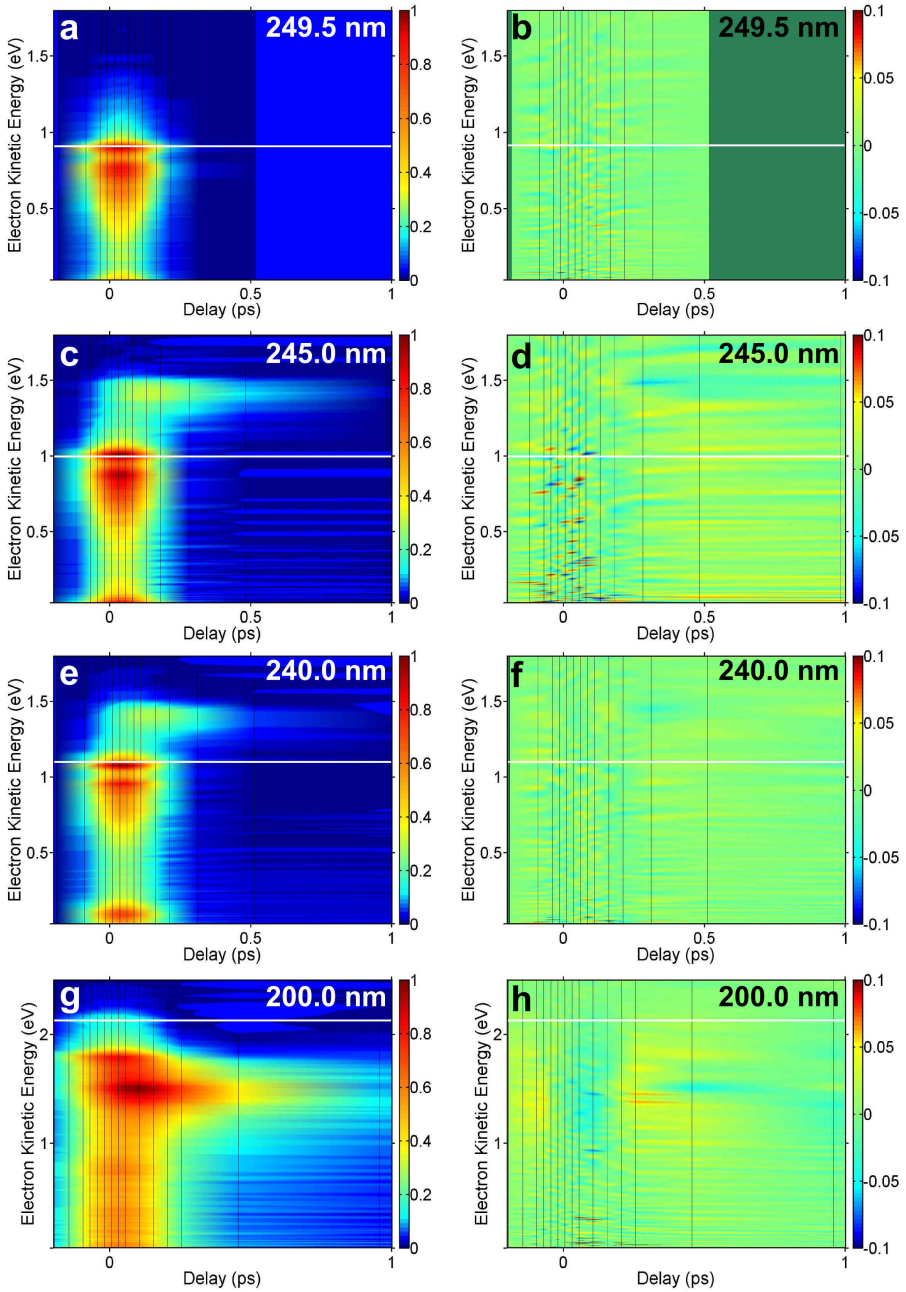

Figure 3.17: Fitted surfaces (1.8 bar He expansion), using lifetimes detailed in Table 3.2. Surfaces are show for 249.5 nm (a), 245.0 nm (c), 240.0 nm (e) and 200.0 nm (g) pump wavelengths. Residuals of the fit subtracted from the experimental data are shown for 249.5 nm (b), 245.0 nm (d), 240.0 nm (f) and 200.0 nm (h) pump wavelengths. Maximum accessible $(1 + 1')$ eKE are marked for each wavelength by solid white lines.

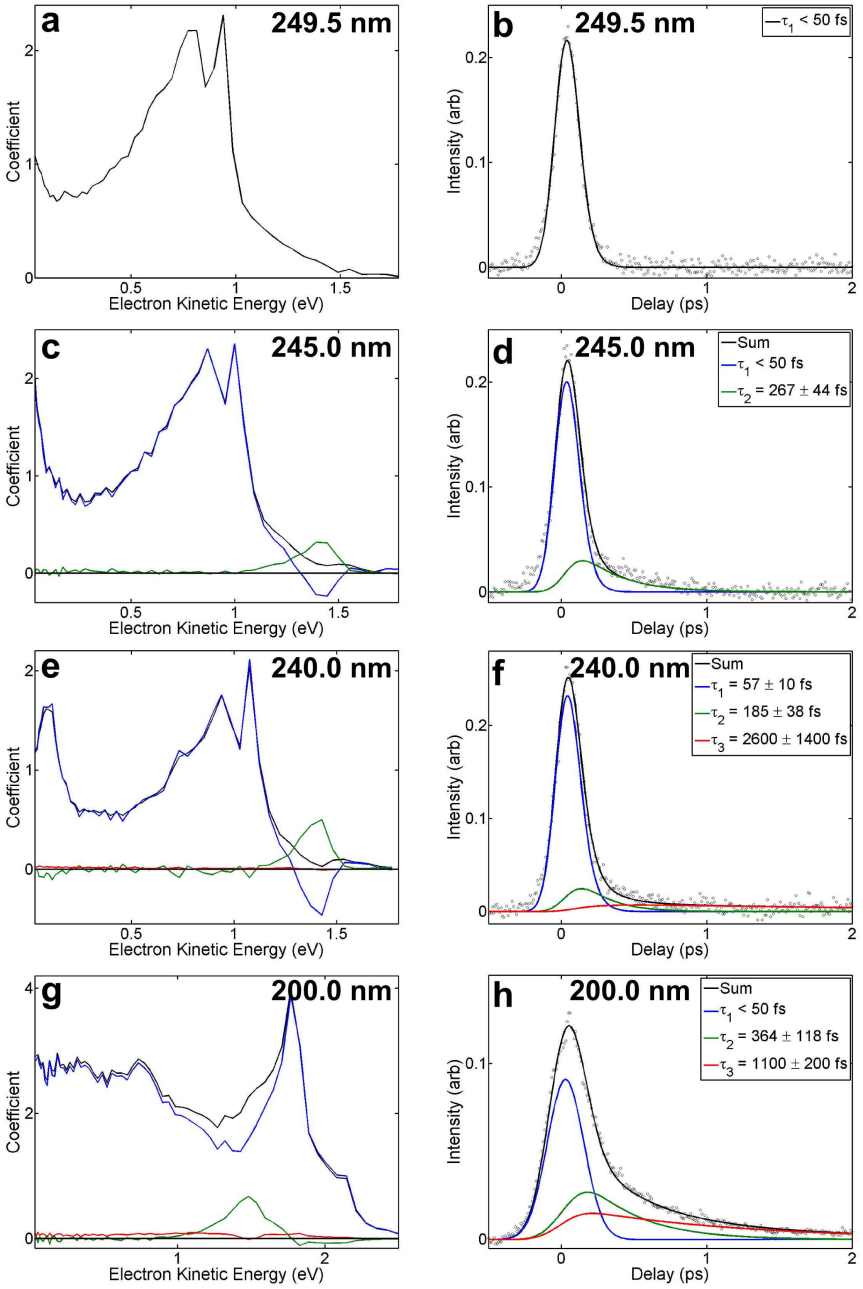

Figure 3.18: Decay associated spectra (1.8 bar He expansion) relating to the surfaces in Figure 3.17, for 249.5 nm (a), 245.0 nm (c), 240.0 nm (e) and 200.0 nm (g) pump wavelengths. Refitting these same lifetimes to the total integrated decay data (presented in Figure 3.11) are shown for 249.5 nm (b), 245.0 nm (d), 240.0 nm (f) and 200.0 nm (h) pump wavelengths, where these plots are normalised to $\sum_i c_i = 1$, excluding states which feed other observable states. Consequently the limit at long delay time indicates the proportion of the initially excited wavepacket remaining.

face shown in Figure 3.12(f). The DAS shows that this feature covers a broad eKE range, similar to the broad τ_2 component observed following 200.0 nm excitation in the last section. Unfortunately, the τ_1 and τ_3 states are completely energetically overlapped and therefore, it cannot be inferred from this data whether the τ_3 state is initially populated or becomes populated following the decay of the τ_1 component.

Figure 3.17(g) presents the fitted surfaces following 200.0 nm excitation, using τ_{1-3} (Table 3.2). The τ_1 component decays on a sub-50 fs timescale, as observed in the medium expansion pressure case. However, an additional feature with decay lifetime τ_2 is observed at $\sim$1.4 eV. The lifetime and eKE range of this feature closely match the cluster dependent peak observed following 245.0 and 240.0 nm excitation at this higher expansion pressure. This is notable because it suggests that eKE of this feature is invariant, despite significantly increasing the excitation energy, the reasons for this are included in the discussion. The τ_3 component has a lifetime of > 1 ps and covers a very broad eKE range, similar to the additional τ_3 component observed following 245.0 nm excitation at this expansion pressure. Unfortunately all of the τ_{1-3} components are energetically overlapped and it is not possible to infer whether information regarding population transfer using the DAS. However, based upon the results at other excitation energies, it seems likely that the τ_3 component does not relate to a state which is directly excited.

Finally, it should be noted that the data in Figure 3.18(b), (d) and (f) display a weak, tail at negative time delays (probe-pump region), which is not fully described by our fits. This effect has been identified in some previous experimental results within our group [152], although the effect is more noticeable in this case due to the rapid timescale of the dynamics observed at positive pump-probe delays. 300 nm was selected as the probe wavelength, such that it is insufficiently energetic to electronically excite pyrrole with a single photon. We therefore believe that these negative delay dynamics must be due to excitation by 2×300 nm photons, with subsequent ionisation by the pump photon. Future experiments will ensure that the probe laser is attenuation, such that this effect is eliminated.

3.3.4 Discussion

Buck *et al.* [91] have previously shown that increasing the expansion pressure of the He seed gas used to generate and cool a molecular beam can generate an appreciable proportion of pyrrole clusters within that molecular beam. Our experimental work is consistent with these findings. Furthermore, we have shown that increasing the proportion of dimers in the molecular beam opens up new relaxation dynamics, as additional pathways become accessible to electronically excited pyrrole. The decay timescales we have determined are summarised in Table 3.2.

Firstly, we found that the presence of pyrrole dimers did not affect the relaxation dynamics observed following excitation close to the $S_1(\pi\sigma^*)$ origin (250 nm). In the monomer case, we found that a single sub-50 fs decay lifetime describes our data well. When the expansion pressure is increased in order to generate pyrrole dimers, a sub-50 fs lifetime continues to describe the most intense peak well. This leads us to believe that the τ_1 lifetime component corresponds to excitation and subsequent evolution on a monomer-like surface.

When exciting pyrrole dimer to higher energies, we observe the emergence of a new decay mechanism, with a lifetime of 185–346 fs (τ_2). Notably, the intensity of this component increases as the expansion pressure of the He carrier gas is increased. This feature also increases in intensity as excitation energy increases, *i.e.* it is not visible following excitation close to the S_1 origin, but becomes increasingly apparent upon increasing the excitation wavelength towards 240.0 nm. Furthermore, the eKE associated with the τ_2 feature is not energetically accessible by pump-probe ionisation ($1 + 1'$) in the monomer species. We have also ruled out the possibility of multiphoton excitation or ionisation, as we found that decreasing the intensity of either the pump or probe pulses lead to a linear decrease in the intensity of the τ_2 feature (rather than the higher order relationship expected for multiphoton processes). Altogether, this behaviour suggests that the τ_2 feature relates to a relaxation occurring on the dimer surface. Unfortunately, the low intensity of this τ_2 component means that the error in the fitted lifetime of this feature is higher than for more clearly defined states.

At all wavelengths where the τ_2 component is observed, its rise is delayed with respect to the initial excitation pulse. This indicates that the τ_2 component is not directly populated by the pump pulse, but instead becomes populated following decay of the initially prepared state. Furthermore, the delay in the τ_2 rise time is essentially independent of excitation wavelength or expansion pressures, within the range examined in this study. Additionally, the DAS produced show that the decay time of the τ_1 component matches the τ_2 component rise time, which suggests that population decays from the τ_1 component into the τ_2 component. The eKE range at which the τ_1 component is associated closely matches those observed between experiments conducted with only the monomer species present and those including the dimer species, indicate that the state associated with τ_1 is very 'monomer-like' (no shift in the τ_1 spectral peaks is observed upon formation of the dimer species) and continues to relate to the $S_1(\pi\sigma^*)$ state.

Interestingly, the eKE of the τ_2 feature does not increase as the energy of the excitation (pump) photon increases, this can be seen by comparing Figure 3.16(c) and (e) or Figure 3.18(c) and (e). In both of these comparisons, the eKE of the spectral features associated with the τ_1 component clearly increases as the pump energy increases (as is expected by the $\Delta v = 0$ propensity rule). However, the feature associated with the τ_2 component does not shift and remains centered on 1.4 eV. Indeed, careful examination of the data following 200.0 nm excitation (Figure 3.18(g)) also shows that the τ_2 feature continues to be centered at roughly 1.4 eV. This could suggest that, in the dimer, very efficient dissipation of any excess vibrational energy occurs when populating the state associated with τ_2 occurs, allowing relaxation to a stable energetic minimum.

To further explore the invariance of the τ_2 component eKE with respect to excitation energy, we decreased the probe wavelength from 300 nm to 275 nm and collected another set of results for the 245.0 nm excitation wavelength (1.80 bar expansion pressure). The results are presented graphically in Figure 3.19. In this case, increasing the probe energy does induce the anticipated increase in eKE for all spectral features, including the τ_2 component. It is also found that altering the probe energy does not significantly change the decay lifetimes observed ($\tau_1 = 60 \pm 10$ fs,

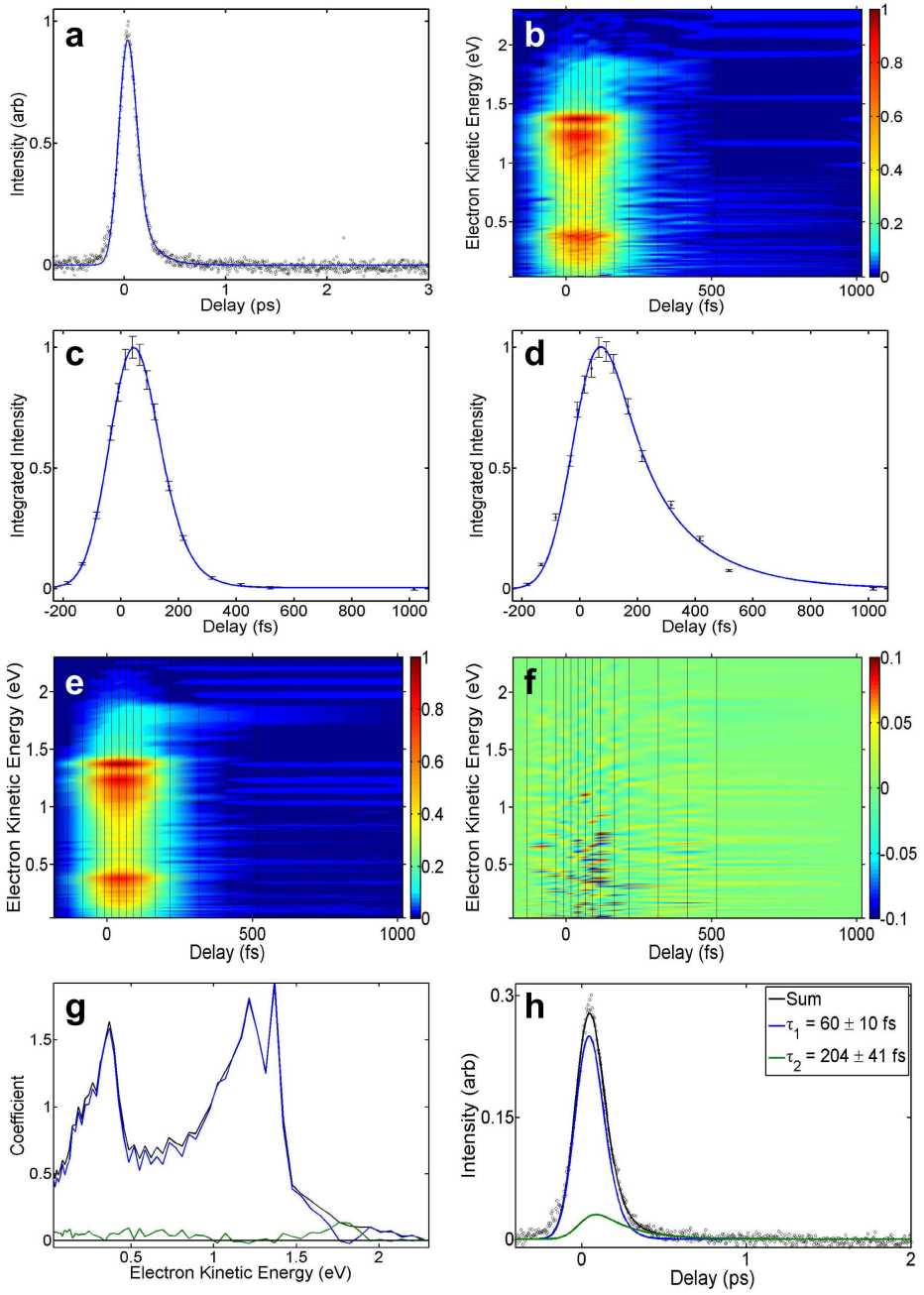

Figure 3.19: (a) Total integrated photoelectron signal decay for pyrrole (1.8 bar He expansion) for 245.0 nm pump and 275 nm probe. (b) Experimental data surface. (c) Energy integrated (over the range 1.15–1.4 eV) fit used to obtain decay lifetimes. Error bars are obtained from the (2σ) standard deviation in photoelectron intensity over the integrated region. (d) Energy integrated fit, over the range 1.6–1.85 eV. (e) Fitted surface. (f) Residual of the fit in (e) subtracted from the experimental data in (b). (g) Decay associated spectra. (h) Refitting using the lifetimes obtained from (c) and (d), normalised such that $\sum_i c_i = 1$.

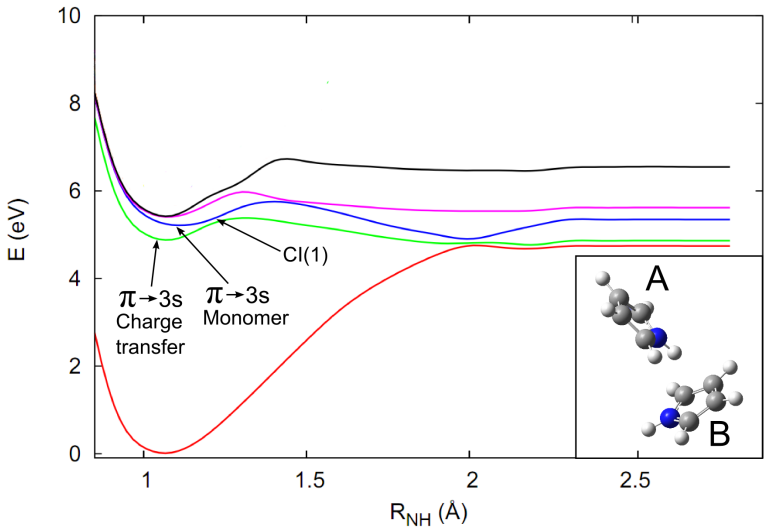

Figure 3.20: Potential energy surface for the excited states of the pyrrole dimer along the N-H stretch mode of the exposed molecule (B), computed at the DFT/MRCI level of theory. The character of these states are predominantly (listed with respect to ascending energy in the vFC region):
S_1: $\pi(B) \rightarrow 3s(A)$ charge transfer state,
S_2: $\pi(A) \rightarrow 3s(A)$ monomer-like state,
S_3: $\pi(B) \rightarrow 3p_z(A)$ charge transfer state,
S_4: $\pi(B) \rightarrow 3p_y(A)$ charge transfer state.
Inset: the optimised geometry of the pyrrole dimer, including labels for the H atom constrained (A) and the unconstrained (B) molecules.

$\tau_2 = 204 \pm 41$ fs). This confirms our assertion that, in pyrrole, a 300 nm probe is sufficiently energetic to observe motion in the vFC region and the lifetimes we have measured are not highly sensitive to the ionisation wavelength used.

In order to elucidate the nature of the state associated with the τ_2 decay in more detail, Graham Worth and Simon Neville (Birmingham University) have assisted us by conducting some preliminary quantum mechanical modelling on the excited state ordering in the pyrrole dimer system at the DFT/MRCI level of theory, using an aug-cc-pVDZ basis set [153]. The potential energy curves in the N-H extension coordinate (of molecule (B), inset Figure 3.20) were calculated and the potential curves for the first four excited states (ground state geometry) are shown in Figure 3.20. A new, lowest energy, singlet excited state is found in the dimer system, which appears below the $\pi(A) \rightarrow 3s/\sigma^*(A)$ state which was the lowest state in the monomer. This

new state is identified as a charge transfer states consisting of excitation from the HOMO of the molecule B to the $3s$ orbital of molecule A *i.e.* $\pi(B) \rightarrow 3s/\sigma^*(A)$. This newly identified charge transfer state has an extremely low oscillator strength and is therefore unlikely to be directly populated upon excitation. However, this new charge transfer state does cross the monomer-like $\pi 3s/\pi\sigma^*$state (now the second singlet excited state) at slightly extended N-H distances (labelled CI(1) in Figure 3.20). Excitation of the dimer very close to the origin of the monomer-like $\pi 3s/\pi\sigma^*$ state (*e.g.* 249.5 nm excitation), would leave the wavepacket with very little vibrational energy which, depending upon the geometry and nature of CI(1), could prohibit internal conversion *via* CI(1). In this case, population could proceed to dissociation on the monomer-like surface. More energetic excitations provide excess vibrational energy, which could enable the wavepacket to pass through CI(1) and relax onto the lower lying charge transfer state. The more stable charge transfer state could be expected to decay on a longer timescale, such as that observed for our τ_2 component. This arrangement could therefore qualitatively explain the lack of a τ_2 decay component when exciting at 249.5 nm, but increasing contribution of this feature with increased excitation energy. The current calculations require refinement to provide greater detail regarding the location and nature of the minimum energy CI(1) or to resolve the local topology. Indeed it would be interesting to determine the stabilisation of the lowest energy charge transfer state, following geometric relaxation and how this correlates to the energy and geometry of the cationic dimer system. Further work on these potential energy surfaces is ongoing and will be published in due course.

Finally, we observe an additional τ_3 component when 1.8 bar He expansion pressure is used. This component is spectrally very broad and has a much longer decay lifetime than the other decay components observed in this study. The lifetime is extremely difficult to resolve accurately, due to the very low intensity of the state, but our fitting indicate the τ_3 component decays with a lifetime of $1 > \tau > 3$ ps. This is consistent with previous observations of IVR occurring on the ground state surface [127]. The eKE associated with this process would be consistent with ionisation of the dimer ground state by 2×300 nm probe photons (max. eKE = 1.0 eV).

Multiphoton processes would be expected to be very weak, which would also go some way to explaining the low intensity of this component. The fact that this component is only observed at high expansion pressure suggests that this ionisation mechanism is only favoured when certain vibrational modes are populated and that the population of these modes is related to the decay processes occurring in the dimer, or larger clusters.

3.4 Conclusion

Our time-resolved photoelectron imaging study of pyrrole has examined the decay mechanisms following excitation in the range 249.5–200.0 nm. We have provided information on the decay lifetimes of the excited states of this biologically important chromophore, including the low lying $S_1(\pi\sigma^*)$ state and our findings complement the time resolved studies found in the literature.

The non-radiative dynamics we observe in the pyrrole monomer are summarised in Figure 3.21. We find that excitation to either of the lowest two excited states results in ultrafast relaxation on a timescale faster than 50 fs. No longer lifetime component is observed, regardless of the excitation wavelength used or the excess vibrational energy imparted to the S_1 state. The $S_1(\pi\sigma^*)$ state has formally mixed $\pi 3s/\pi\sigma^*$character and the lack of wavelength dependence of the ultrafast decay timescale observed (including close to the state origin), implies that the barrier to dissociation in the vFC region is insignificantly small.

Our findings are broadly in keeping with the existing literature, however some H atom emission studies have observed H atom rise times which are noticeably longer (110-120 fs) than the decay lifetimes we observe in the vFC region. This suggests that a feature of the dissociative channel on the S_1 surface delays the emission of H atoms after they leave the vFC region, we suggest that the S_1/S_0 CI may fulfil this role. Furthermore, some studies have observed that the H atom emission time on the S_1 surface is wavelength dependent. We do not observe such a dependence in the vFC region, but it could equally relate to the local topology close to the

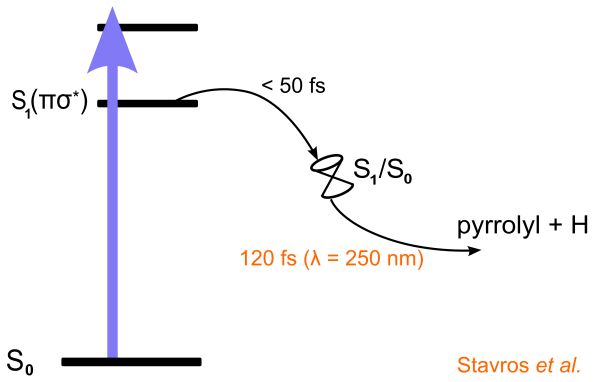

Figure 3.21: Schematic diagram of the proposed non-radiative decay pathways in the pyrrole monomer, along with the associated timescales.

S_1/S_0 CI, with less vibrationally excited molecules becoming trapped and traversing this region more slowly. Another study [130, 131] observed a bimodal H atom distribution following excitation at 243 and 217 nm, which suggests that multiple decay routes occur following excitation to the S_1 state. This could be consistent with our findings, however any competing decay pathways must also leave the vFC region on a sub-50 fs timescale with bifurcation presumably occurring in the region of the S_1/S_0 CI.

Future experiments could help to differentiate between these multiple decay pathways. One study observed that the H atom emission lifetime of pyrrole excited close to the S_1 state origin increased from 120 fs to 1.4 ps following deuteration [127]. We therefore suggest that studying the ultrafast TRPEI of deuterated pyrrole may allow us to differentiate the lifetimes of the distinct decay pathways present. It may also be possible to resolve the decay mechanisms with greater detail by a reduction in the temporal width of the laser cross-correlation, although this presents an experimental challenge. Additionally, the use of a higher energy probe photon in the VUV region would allow ionisation of population on both the pyrrolyl radical or the pyrrole ground state surfaces, such that wavepacket evolution can be monitored into these regions.

Upon generating pyrrole dimers within our molecular beam, we observe the opening of a fascinating new decay pathway, as summarised in Figure 3.22. We continue

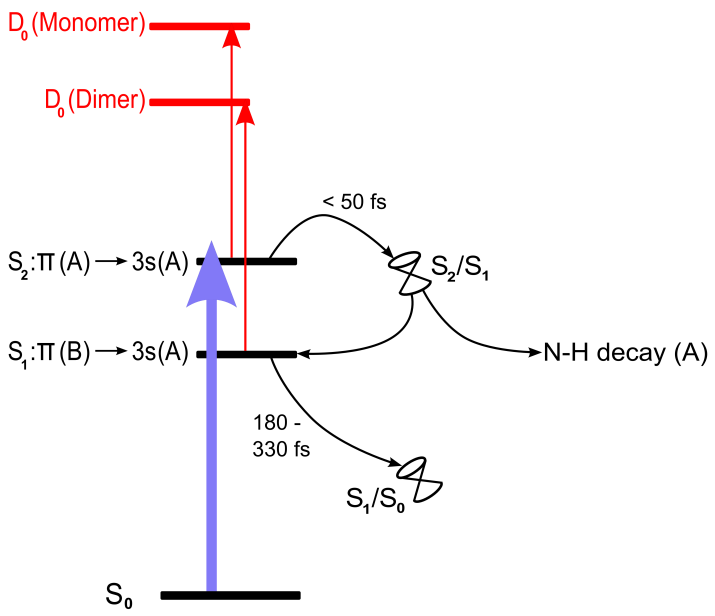

Figure 3.22: Schematic diagram of the proposed non-radiative decay pathways in the pyrrole dimer, along with the associated timescales.

to observe the same spectral features as seen in the monomer (the $S_1(\pi\sigma^*)$ state), with the same sub-50 fs decay time. However, in the dimer system, we find that this initially populated, 'monomer-like' state can rapidly decay into a newly identified $\pi(B) \rightarrow 3s/\sigma^*(A)$, charge-transfer state. This charge-transfer state is more stable than the monomer-like state from which it is formed and consequently we observe a longer decay lifetime of ∼200–350 fs. The fact that we see similar initial states following excitation of the monomer and dimer is perhaps unsurprising, as our molecular beam primarily comprises pyrrole monomers, even when dimers are formed. However, when dimers are present, we do not observe any additional directly populated states. This suggests that the additional charge-transfer states present in the dimer do not couple to the pyrrole ground state efficiently, precluding absorption. Transfer from the initial monomer-like state, to the charge transfer state, is believed to occur *via* a state crossing we have identified in the N-H stretch direction, although further characterisation of this feature is required in future work.

Using the dimer system as a model for solvation effects, we have observed microsolvation induced electron-transfer following UV excitation. The opening of this new decay pathway can channel population away from N-H dissociation, which dominates

in the monomer system. Consequently, the solvation of pyrrole could be expected to inhibit the formation of pyrrolyl radicals, compared to the unsolvated case. Our study provides the first step towards a deeper understanding of the effect of solvation on molecular photorelaxation. We have shown that new, energetically inaccessible decay pathways are possible upon dimerisation and the subsequent change in dynamics is likely to be significant when considering the dissipation of absorbed UV light in more complex, realistic biological systems. Further quantum mechanical modelling of the potential energy surfaces of the pyrrole dimer would provide much greater insight into the accessible decay pathways and the interstate couplings, as would modelling of the excited state surfaces in solvated pyrrole. We also believe that future work examining the ultrafast relaxation dynamics of solvated pyrrole is required and would serve as an interesting extension of the findings of this study. Our group intends to construct a liquid jet TRPEI experiment in the near future which may assist in the acquisition of such results.

Chapter 4

Time-resolved dynamics of aniline and deuterated aniline following excitation in the region 272–238 nm

4.1 Introduction

Aromatic amines are a common structural motif in biological molecules, for example many neurotransmitters, such as epinephrine, dopamine and serotonin are aromatic amines. Aniline (see Figure 4.1, Inset) is the smallest aromatic amine, making it an excellent prototypical system to study [8, 154].

Like the other molecules studied in this thesis, aniline has a low-lying $^1\pi\sigma^*$ state, which provides a mechanism for rapid coupling of excited state population back to the ground state or can induce bond fission, as described in Section 1.3. This $^1\pi\sigma^*$ state has mixed Rydberg and valence antibonding character, the N-centered $^1\pi 3s$ and $^1\pi\sigma^*$ configurations form an avoided crossing at modest N–H internuclear separations (see Figure 4.1). This state crosses the first excited $\pi\pi^*$ state, which lies lower in energy, and the ground state surface along the N–H coordinate, providing an efficient pathway for ultrafast relaxation [10].

4.1.1 Potential energy surfaces

Honda *et al.* reported a detailed theoretical study of the electronic structure of aniline using symmetry adapted cluster/configuration interaction (SAC-CI) [53]. They determined that the lowest singlet excited state was a $^1\pi\pi^*$ state (hereafter referred to as $S_1(\pi\pi^*)$), whose character is mainly charge-resonance on the π ring, with a small proportion of $NH_2 \rightarrow C_6H_5$ charge transfer. The vertical excitation energy to this state was calculated to be 4.20 eV (295 nm). The second singlet excited state was determined as having mixed Rydberg-valence character and a calculated vertical excitation energy of 4.53 eV (273.7 nm) (hereafter referred to as $S_2(\pi\sigma^*)$). However, the oscillator strength of this state was calculated to be 25% that of the $S_1(\pi\pi^*)$ state. The third singlet excited state was identified as another $^1\pi\pi^*$ state, resulting from local excitation on the benzene ring (hereafter referred to as $S_3(\pi\pi^*)$). The vertical excitation energy of this state was determined to be 5.34 eV (232.2 nm). These calculations are consistent with the gas-phase absorption

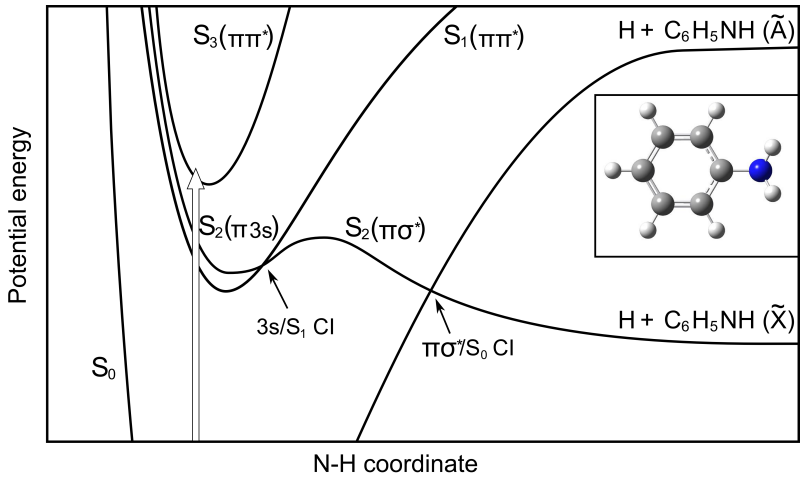

Figure 4.1: Schematic potential energy curves for the four lowest singlet states of aniline along the N-H stretch coordinate. The S_0, $S_1(\pi\pi^*)$ and $S_3(\pi\pi^*)$ states are bound whereas the $S_2(\pi\sigma^*)$ state has mixed Rydberg and valence character and is dissociative along the N-H stretch coordinate. Inset:- The aniline molecule, in the ground-state equilibrium geometry (C atoms - black, H atom - white, N atom - blue). The NH_2 group lies slightly out of the plane formed by the ring.

spectrum of aniline (Figure 4.2(b)) which displays two prominent absorption maxima around 4.4 eV (∼280 nm) and 5.4 eV (∼230 nm) and a significant, but structureless, background between the two.

More recently, Worth *et al.* [155], re-examined the excited states of aniline using other high-level computational techniques. A model Hamiltonian parametrised using equation-of-motion coupled cluster theory (EOM-CCSD) was employed to reproduce the experimental absorption spectrum, including vibrational states, to extraordinary accuracy. The result is compared to the experimental spectrum in Figure 4.2. This analysis also identified two previously neglected $3p$ Rydberg states slightly below the onset of the $S_3(\pi\pi^*)$ state. It seems likely that these two $3p$ states would play a critically important role following excitation to the $S_3(\pi\pi^*)$ state, as strong coupling is found between these states. Dynamics simulations run as part of their work found that, upon excitation to the $S_3(\pi\pi^*)$ state, very little population returned to the ground state within 300 fs. However, they concede that this is likely to be caused by the reduced dimensionality of the selected model Hamiltonian. Note that, although these $3p$ states are predicted to lie below the second $\pi\pi^*$ state, for consistency with

Figure 4.2: (a) Theoretical absorption spectrum of the lowest six electronic states of aniline, as calculated using wavepacket propagations over model potential surfaces fitted to EOM-CCSD results. The upper band corresponds to vertical excitation to the $S_3(\pi\pi^*)$ state and the lower band corresponds to excitation to the $S_1(\pi\pi^*)$ state. (b) Experimental spectrum, adapted from Ref. [51]. Reproduced from Ref. [155].

the literature we continue to refer to the second $\pi\pi^*$ state as $S_3(\pi\pi^*)$.

A recent paper by Stavros *et al.* included theoretical work by Paterson and coworkers [156], which used CASSCF to examine the excited states of aniline and to identify the nature and associated geometries of the conical intersections that couple electronic states. Important results are summarised in Figure 4.3, which shows arrows in the vertical Franck-Condon region (vFC) representing excitations to various states. The potential energy curves to the right of the vFC region represent the N-H fission coordinate, while the potential energy curves to the left represent out-of-plane, prefulvene-like deformations, similar to those observed in the 'channel-3' deactivation of benzene [157–159]. The $S_2(\pi\sigma^*)$ state is dissociative in the N-H fission dimension; however, it is notable that Figure 4.3 includes a break in the $S_1(\pi\pi^*)$ state, shown by the solid blue lines, pictorially representing that no degeneracy between these two states was found at elongated NH bond lengths. Such a feature should exist even in the case where the states do not couple to form a CI. A low-energy coupling is found between these two states in a ring-bending coordinate, which lies lower in energy than the barrier in the N–H stretch coordinate, which creates a mechanism to allow rapid population loss from the $S_2(\pi\sigma^*)$ state into the $S_1(\pi\pi^*)$. Notably, the surface of the $S_3(\pi\pi^*)$ state in the out-of-plane dimension of Figure 4.3 does not possess a barrier to relaxation, suggesting that excitation to this state is unlikely to be stable. Upon continued deformation in this prefulvene-like coordinate, a conical intersection forms with the S_1 state, creating a mechanism for rapid relaxation. A further conical intersection couples the $S_1(\pi\sigma^*)$ state directly to

Figure 4.3: Potential energy curves of the S_0, $S_1(\pi\pi^*)$, $S_2(\pi\sigma^*)$, and $S_3(\pi\pi^*)$ electronic states in aniline, along some significant displacement coordinates (out-of-plane motions, left, and N-H stretch, right). Dashed light-blue lines represent pathways to electronic state couplings in other coordinates. Significant calculated CASSCF geometries are labelled. Reproduced from Ref. [156].

the ground state also exists in close proximity, although access requires a slightly different ring deformation mode. Collectively these observations open a pathway for population excited to the S_3 state to reach the ground state non-radiatively in a very short timescale.

More recently, a detailed study by Sala *et al.* [160] has been published. The authors study the potential energy surfaces of the $S_1(\pi\pi^*)$, $S_2(\pi\sigma^*)$ and $S_3(\pi\pi^*)$ excited states using CASSCF calculations, with XMCQDPT2 perturbations to include dynamic correlation effects. This study finds a new conical intersection between the $S_1(\pi\pi^*)$ state and the ground state in coordinate of the prefulvene-like distortion, where the amino carrying carbon is moved out of the molecular plane (see Figure 4.4(a)). This CI provides a plausible mechanism for rapid non-radiative internal conversion to the ground state. Furthermore, the location of the conical intersection between the $S_2(\pi\sigma^*)$ and the $S_1(\pi\pi^*)$ states is located in the N-H stretch dimension. This CI is found to lie very close to the $\pi 3s$ minimum of the $S_2(\pi\sigma^*)$ state, as shown in Figure 4.4(b) and Inset. This S_2/S_1 CI provides a mechanism for photoexcited population on the S_2 state surface to relax into the S_1 state very efficiently, as effectively no barrier to internal conversion exists. The geometry of this CI is shown in Figure 4.4(c). Finally, the study also locates a new, minimum energy pathway for relaxation from the S_3 state to the S_0 ground state *via* a three state conical intersection in a ring bending mode.

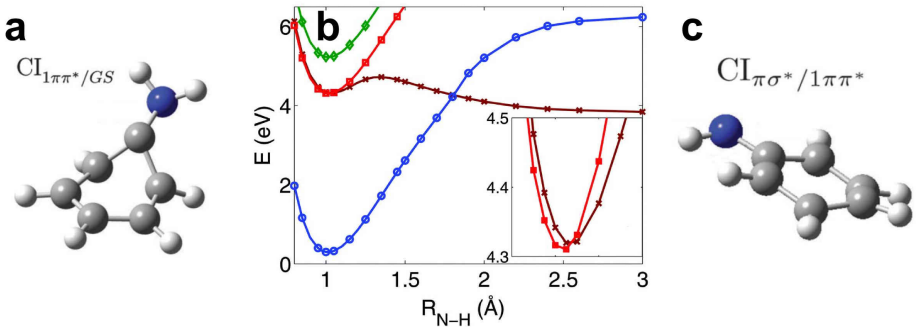

Figure 4.4: a) Prefulvene-like distortion, leading to the CI between the $S_1(\pi\sigma^*)$ state and the ground state. b) Potential energy scan along the NH coordinate, using geometries optimised in the $S_2(\pi\sigma^*)$ state, computed at the XMCQDPT2 level of theory. The ground-state (blue circles), $S_1(\pi\pi^*)$ state (red squares), $S_2(\pi\sigma^*)$ state (brown crosses), $S_3(\pi\pi^*)$ state (green diamonds). The geometries are optimized on the $S_2(\pi\sigma^*)$ state at the SS-CASSCF level of theory using Cs′ symmetry. Inset: Enlarged section of the $1\pi\pi^*$ and $1\pi\sigma^*$ states potential scans around the $1\pi\sigma^*$ minimum. c) The distortion associated with the $S_2(\pi\pi^*)/S_1(\pi\sigma^*)$ conical intersection. All images are reproduced from Ref. [160].

4.1.2 Spectroscopy of aniline

There have been numerous spectroscopic investigations of the $S_1(\pi\pi^*)$ state, including accurate measurement of the origin transition energy of 4.22 eV [161–164]. Rice *et al.* [165] determined the intersystem crossing lifetime of the ground vibrational state of $S_1(\pi\pi^*)$ to be 8.5 ns and Weber *et al.* [166] confirmed formation of the triplet states using picosecond time-resolved photoelectron spectroscopy. Reilly *et al.* [161] have carried out a detailed ZEKE spectroscopy study of the ground state of the cation *via* the $S_1(\pi\pi^*)$ state of aniline.

The $S_2(\pi\sigma^*)$ state was first observed experimentally by Ebata *et al.* [162], who employed UV-IR double-resonance spectroscopy to study the vibrational levels of $S_1(\pi\pi^*)$. However, they discovered a number of broad transitions at energies greater than 0.43 eV above the $S_1(\pi\pi^*)$, the origin of which could not be assigned to fundamental vibrations of the $S_1(\pi\pi^*)$ state. The authors then used $2 + 2$ resonance-enhanced multiphoton ionisation (REMPI) spectroscopy to identify the $S_2(\pi\sigma^*)$ band origin at 4.60 eV (269.5 nm) above the ground state. Furthermore, the ob-

Figure 4.5: H atom photofragment translational spectra, showing the dissociation signal as a function of the internal energy remaining in the anilino fragment. The peaks labelled $v = 0$ correspond to the ground state of the anilino fragment. Reproduced from Ref. [51].

servation of a short vibronic progression led to the conclusion that the potential energy surface was not purely repulsive, but had a shallow minimum close to the Franck-Condon region.

Ashfold *et al.* have undertaken a comprehensive study of the photodissociation of aniline using H atom (Rydberg) photofragment translational spectroscopy [51]. Below the $S_2(\pi\sigma^*)$ origin (269 nm), they found that H atom loss occurred mainly by multiphoton processes, resonantly enhanced at the one-photon level. Decreasing the excitation wavelength to 269–260 nm (see Figure 4.5(a-d)) was found to excite the first few vibrational levels of the $S_2(\pi\sigma^*)$ state, which subsequently induced N–H bond fission, creating H atoms with anisotropic velocity distributions and anilino radicals in low vibrational states of the ground electronic state. The H atoms produced are attributed to tunnelling through the barrier on the $S_2(\pi\sigma^*)$ state (along the N–H bond stretch coordinate), onto the repulsive region of the surface. The anisotropy is caused by H-atom ejection on a timescale faster than either molecular rotation. The rotation constants for aniline are 0.06–0.2 cm^{-1} in the ground and first excited singlet states [167, 168], assuming rotational temperatures of approximately 20 K these correspond to rotational periods of tens of picoseconds. Decreasing the excitation wavelength below 260 nm (see Figure 4.5(e-j)), led to the loss of the vibrational structure, but produced anilino radicals with greater vibrational energy. This was attributed to direct excitation to $S_1(\pi\pi^*)$ followed by internal conversion through an S_1/S_2 conical intersection to the dissociative $\pi\sigma^*$ potential energy surface. At around 230 nm, changes in the profile of the kinetic energy distribution were interpreted in terms of direct excitation to $S_3(\pi\pi^*)$ followed by internal con-

Figure 4.6: Femtosecond pump–probe photoionisation study of aniline. Aniline ion signal as a function of pump–probe delay time, for various excitation wavelengths in the region 274–240 nm. The probe wavelength was 400 nm. Circles represent the data, while the coloured lines correspond to the exponential decay fits, the red line is the total fit. Lifetimes are common between all fits and are indicated in (f). Reproduced from Ref. [52].

version through an S_3/S_2 conical intersection or through successive S_3/S_1 and S_1/S_2 conical intersections to the dissociative $\pi\sigma^*$ potential energy surface.

4.1.3 Time-resolved spectroscopy of aniline

Longarte and coworkers carried out the first femtosecond time-resolved study of electronic relaxation in aniline using pump-probe photoionisation spectroscopy [52]. They examine the formation of the parent cation following excitation in the range 274–240 nm. In all cases a > 45 ps decay lifetime is observed, relating to decay of population in the $S_1(\pi\pi^*)$ state back to the ground state. Above the onset of the $S_2(\pi\sigma^*)$ state (269–240 nm) a 165 fs decay lifetime is observed, which was attributed to dynamics on the $S_2(\pi\sigma^*)$ surface through the S_2/S_1 conical intersection. The presence of the picosecond lifetime following excitation to the $S_2(\pi\sigma^*)$ state leads the authors to conclude that population decays to both the dissociative $\pi\sigma^*$ potential energy surface and the $S_1(\pi\pi^*)$ state in this excitation range. Additionally, the relatively small amplitude of the 165 fs component leads the authors to conclude that the dissociative $S_2(\pi\sigma^*)$ potential energy surface plays a minor role in the photochemistry of aniline, as can be seen in Figure 4.6. Decreasing the excitation wavelength to 234 nm resulted in the appearance of an additional 21 fs timescale, attributed to direct population of the $S_3(\pi\pi^*)$ which undergoes extremely rapid internal conversion to $S_1(\pi\pi^*)$ and subsequently relaxes to the ground state on a

Figure 4.7: Aniline total kinetic energy release spectra of H atoms produced following 240 and 200 nm excitation. A 'statistical' multiphoton background component is subtracted from the signal, (red area in (a) and (c)), the H atom rise times are then fitted in (b) and (d). Reproduced from Ref. [156].

timescale of tens of picoseconds. This study therefore establishes the population and ultrafast decay of the S_2 state and the onset of the S_3 state.

Our group has studied the decay dynamics of aniline following excitation between 269–236 nm [87, 152, 169]. We used time-resolved photoelectron imaging (TRPEI) to study the electronic dynamics occurring after excitation to the S_2 state, with various amounts of excess vibrational energy. We observed a sharp, symmetric peak in the region of the photoelectron spectrum associated with the $S_2(\pi\sigma^*)$ state. The photoelectron signal arising from this state was highly anisotropic, as would be expected from ionising a state with predominantly $3s$ character. Notably, we found that this $S_2(\pi\sigma^*)$ state can be directly excited by absorption processes, as opposed to indirectly populated *via* initial population high in the $S_1(\pi\pi^*)$ state. We also found that the population in the $S_2(\pi\sigma^*)$ appears to decay rapidly into the $S_1(\pi\pi^*)$ state, with a lifetime of 200–230 fs and no systematic dependence on vibrational energy initially excited. Subsequent to this ultrafast decay, the $S_1(\pi\pi^*)$ state was seen to decay on a picosecond timescale, rising from 81 ps following 236 nm excitation to > 1 ns following excitation close to the $S_2(\pi\sigma^*)$ origin at 269 nm. Additionally, we examined the effect of excitation above the onset of the $S_3(\pi\pi^*)$ state with various amounts of excess vibrational energy by using 240–236 nm light. We found that the $S_3(\pi\pi^*)$ state was populated directly, but decayed very rapidly, leaving our observation window in 50 fs. In this region, the $S_2(\pi\sigma^*)$ and $S_1(\pi\pi^*)$ states display very similar behaviour to that seen below the $S_3(\pi\pi^*)$ onset, with direct excitation to the S_2 and subsequent decay into the S_1 state with the same sim200–330 fs timescale observed at longer wavelengths.

Figure 4.8: Decay associated spectra for aniline excited at 273 nm (a), 269.5 nm (b), 267.7 nm (c) and 265.9 nm (d). Decay lifetimes are globally fitted. Reproduced from Ref. [96].

Stavros *et al.* have employed femtosecond pump-probe velocity map imaging to monitor the formation of H atoms following the excitation of aniline between 250 nm and 200 nm [156]. Interestingly, when studying excitations longer than 250 nm, no ultrafast rise time is observed that could be associated with decay of the $S_2(\pi\sigma^*)$ state. This is ascribed to population becoming trapped in the bound region of the $S_2(\pi\sigma^*)$ state, which then decays into lower lying states before dissociation can occur. When exciting with higher energies they observe the formation of H atoms on timescales of 155 ± 30 fs at 240 nm excitation and 170 ± 20 fs for 200 nm excitation. The H atoms observed have two distinct distributions, one with low kinetic energy associated with 'statistical' multiphoton processes and one with higher kinetic energy associated with H atoms emitted upon dissociation on the $S_2(\pi\sigma^*)$ surface. The results can be seen in Figure 4.7, with the 'statistical' signal shaded in red and the anilino signal shaded in blue. The proportion of statistical H atoms produced increases as the wavelength decreases, suggesting that relaxation to the ground state becomes more favourable upon accessing the $S_3(\pi\pi^*)$ state.

A recent publication by Townsend *et al.* [96] has also looked at the ultrafast relaxation of aniline excited in the range 273–266 nm, and also uses the TRPEI method. The excitation wavelengths 269.5–266 nm were selected to excite various vibrational levels in the bound region of the $S_2(\pi\sigma^*)$ state (barrier height ∼260 nm [51]). The 273 nm excitation is used as a reference to examine dynamics slightly below the onset of the $S_2(\pi\sigma^*)$ state. The results are summarised in Figure 4.8, which shows the decay associated spectra for each excitation wavelength studied. Absorption is assigned predominantly to direct excitation of the $S_1(\pi\pi^*)$ state, with some direct population of the $S_2(\pi\sigma^*)$ state. The $S_2(\pi\sigma^*)$ state was found to decay on a

110–180 fs timescale, which broadly agrees with our previous work and that of the Stavros group. The $S_1(\pi\pi^*)$ state is found to be populated directly and the subsequent 400–640 fs timescale observed is interpreted as intramolecular vibrational relaxation (IVR) within the $S_1(\pi\pi^*)$ state. This IVR timescale is largely independent of excitation wavelength, suggesting that it is not caused by the $S_2(\pi\sigma^*)$ state. Interestingly, these authors find the $S_1(\pi\pi^*)$ state to only become populated by direct excitation and they cannot discern any non-adiabatic coupling or exchange of population between the $S_2(\pi\sigma^*)$ and $S_1(\pi\pi^*)$ states. Although the lifetimes observed and the shapes of the spectral components associated with each decay component in the Townsend study are in excellent agreement with our earlier observations [87, 152, 169] and those reported in this chapter, the interpretation is slightly different. Critically, Townsend *et al.* suggest that following excitation close to the $S_2(\pi\sigma^*)$ origin (the $\pi 3s$ region), population decays by tunnelling through the barrier onto the dissociative $\pi\sigma^*$ region of this state on a 110-180 fs timescale and no population decays into the $S_1(\pi\pi^*)$ state. In contrast, our data (in this study and the previous publications) suggests that the primary decay route following excitation to the $S_2(\pi\sigma^*)$ state involves rapid population transfer to the $S_1(\pi\pi^*)$ state *via* a conical intersection close to the vFC region. This conclusion is supported by the recent theoretical study of Sala *et al.*, where an S_2/S_1 CI is found close to the vFC region, within the bound region of the $S_2(\pi\sigma^*)$ state (see Figure 4.4). This would provides population excited to the S_2 state with an accessible mechanism by which to relax, prior to tunnelling onto the dissociative region of the surface.

Despite recent interest in the excited states of aniline and their associated dynamics, a number of inconsistencies exist in the literature which we seek to resolve. Since our previous studies, we have refurbished our detector array, which should improve our the signal-to-noise ratio in collected data. Additionally, by improving the density of temporal points collected, we aim to improve our temporal resolution. In the current work we excite above the onset of the $S_3(\pi\pi^*)$ state (at 238 nm), and by using this improved temporal resolution we aim to observe the contribution of the newly predicted $3p$ states found by Worth *et al.* [155]. Ashfold *et al.* and, more recently, Stavros *et al.* suggest that the $S_2(\pi\sigma^*)$ state may not be populated directly, but our

previous studies on aniline found this not to be the case. Consequently, we wish to re-examine this region, in the hopes of resolving these observations. Comparisons are often made between the dynamics of phenol and aniline, because they are both prototypical molecules containing low-lying $\pi\sigma^*$ states. In phenol, excitation to the $S_1(\pi\pi^*)$ state, below the onset of the $S_2(\pi\sigma^*)$ state, results in some population tunnelling onto the $S_2(\pi\sigma^*)$ surface on a ns timescale. We therefore wish to examine excitation to the $S_1(\pi\pi^*)$ and $S_2(\pi\sigma^*)$ states for evidence of tunnelling dynamics, by comparing fully deuterated aniline with the undeuterated case. Finally, in our previous studies we identified one of the weak, low-energy decay channels as a bifurcation of the population in the $S_2(\pi\sigma^*)$ state onto the primarily dissociative part of the $\pi\sigma^*$state. Recent work by Townsend *et al.* observed similar dynamical timescales, but suggested these could instead be interpreted as IVR occurring on the $S_1(\pi\pi^*)$ surface, as has been observed in phenol, catechol and other related systems [170]. In light of this suggestion, we also wish to explore the dynamics of aniline slightly below the $S_2(\pi\sigma^*)$ onset.

4.2 Experimental method

We employ time-resolved photoelectron imaging (TRPEI) to examine the decay dynamics of the excited state of aniline. The experimental apparatus is described in detail in Chapter 2, a continuous molecular beam crossed with the laser pulses generated by our femtosecond laser system (1 kHz repetition rate). The molecular beam is generated by passing helium carrier gas through liquid aniline (Sigma-Alrich, $> 99\%$) or fully deuterated aniline (Sigma Aldrich, 98% D) at 800 mbar and expanding through a 50 μm nozzle. Switching the VMI polarity and examining the ion image we observed no detectable cluster formation or fragmentation.

Aniline was excited slightly below the origin of the S_2 state using 272 nm (4.56 eV) and subsequently with various amounts of excess vibrational energy in the S_2 state using 250 nm (4.96 eV) and 245 nm (5.06 eV) femtosecond laser pulses. We also used 238 nm (5.21 eV) light to excite to the S_3 state. The pump wavelengths are il-

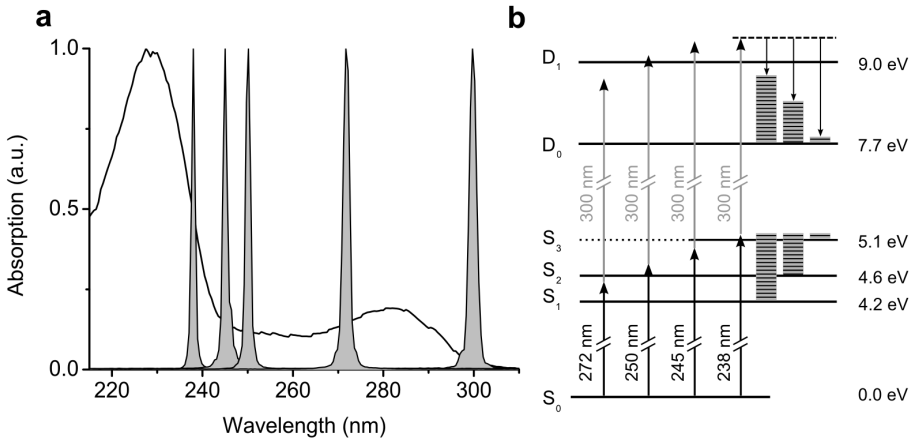

Figure 4.9: (a) Gas-phase UV absorption spectrum of aniline, recorded using a Perkin-Elmer Lambda 950 UV-VIS spectrometer. Pump and probe pulse profiles are superimposed. (b) Excitation scheme: aniline is excited using 272 nm (4.56 eV), 250 nm (4.96 eV), 245 nm (5.06 eV) and 238 nm (5.21 eV) pump pulses. The excited state population is projected onto the photoionisation continuum using a delayed 300 nm (4.13 eV) probe pulse. Assuming the $\Delta v = 0$ propensity rule for photoionisation, the electron kinetic energy following ionisation out of the Franck-Condon region is expected to increase in the order $S_1 < S_2 < S_3$. The vibrational energies (blocks of horizontal lines) and corresponding eKEs (downward vertical arrows) are illustrated for 238 nm excitation.

lustrated in Figure 4.9(b). In the case of d–aniline excitation wavelengths of 272, 250 and 238 nm were employed. The excited state population is projected onto the photoionisation continuum using a delayed 300 nm (4.13 eV) pulse, which was selected to avoid significant background signal from S_1–S_0 absorption (see Figure 4.9(a)). Photoelectron images are then recorded for a series of pump-probe delays between -250–1500 fs. In this work photoelectron images are collected at approximately 18 pump-probe time delays, for each excitation wavelength. We have improved the number of images collected in the region ± 100 fs delay, compared with our previous works, in order to improve confidence in the position of the zero delay and cross-correlation produced by our analysis.

Deuteration can often provide a useful probe of ultrafast dynamical processes, particularly when tunnelling has been implicated. This is because replacing hydrogen atoms with deuterium does not change the electronic structure of the ground or excited states of a molecule, due to the same density and distribution of electronic charge. However, the increased mass does alter vibrational states, decreasing the spacing between states significantly. Also, because quantum tunnelling is mass-dependent, deuterating molecules inhibits the tunnelling of H atoms without significantly affecting other decay processes.

Photoelectron angular distributions are also obtained *via* our analysis with the pBasex inversion algorithm, producing the anisotropy parameters described in Section 1.2.2. The anisotropy parameter β_4 is found to be zero for all data presented in this chapter, while the regions where a measurable β_2 parameter is observed are discussed below.

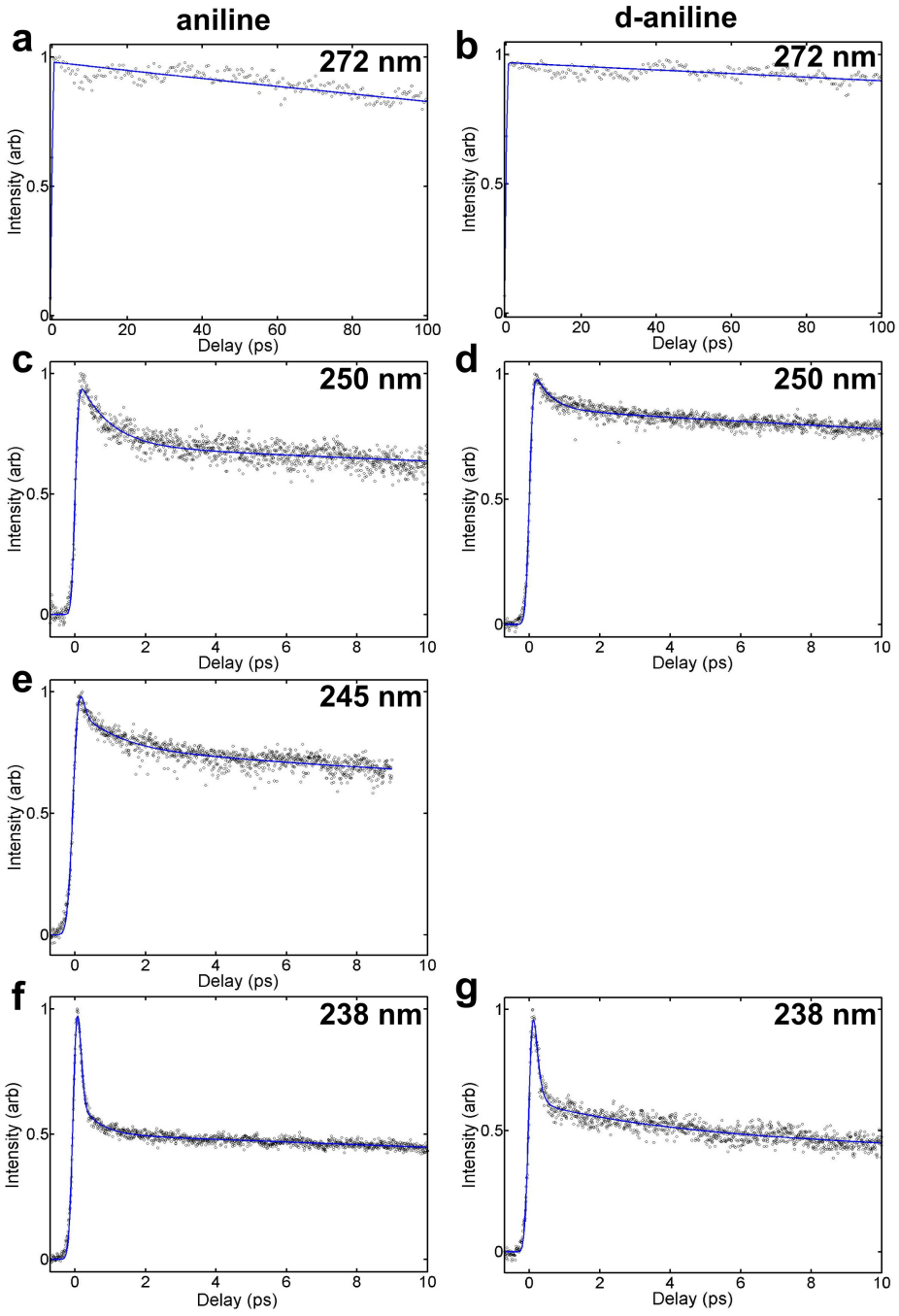

Figure 4.10: Total integrated photoelectron signal decay for 272 nm excitation in aniline (a) and d_7-aniline (b), 250 nm excitation in aniline (c) and d_7-aniline (d), 245 nm excitation in aniline (e) and 238 nm excitation in aniline (f) and d_7-aniline (g).

4.3 TRPEI results for aniline and d_7-aniline excited in the region 272–238 nm

4.3.1 Total integrated photoelectron signal

The evolution of the total integrated photoelectron signal, following excitation of aniline at 272, 250, 245 and 238 nm, is plotted with respect to the relative delay between pump and probe pulses in Figure 4.10. We fit this data to a sum of exponential decays, convoluted with an instrument function, as described by Equation 2.11.

The 272 nm excitation of aniline excites only the $S_1(\pi\pi^*)$ state and no ultrafast decay of the total photoelectron signal can be discerned. Consequently, fitting to a single decay lifetime reproduces the data well, the lifetime fitted is $\tau_1 = 600 \pm 35$ ps and $\tau_1 = 1300 \pm 40$ ps for aniline and deuterated aniline respectively.

At the other excitation wavelengths studied we are able to access additional electronic states and observe ultrafast dynamics. In these cases, the picosecond lifetime decays can be reliably determined from the total integrated photoelectron signal fits, while the ultrafast timescales are extracted in the following section. In aniline excited at 250 nm, two decay lifetimes were necessary to reproduce the data, the longer of which was $\tau_1 = 100 \pm 8$ ps and $\tau_1 = 100 \pm 6$ ps for aniline and deuterated aniline, respectively. Following the 245 nm excitation of aniline, two decay lifetimes were fitted, the longer of which was $\tau_1 = 77 \pm 14$ ps.

Based upon the absorption spectrum shown in Figure 4.2(b), excitation at 238 nm can be expected to predominantly populate the $S_3(\pi\pi^*)$ state. At this wavelength, three decay lifetimes were necessary to reproduce the data, the longest of which was $\tau_1 = 90 \pm 5$ ps and $\tau_1 = 82 \pm 5$ ps for aniline and deuterated aniline, respectively.

These fits are used to scale the integrated intensity of the photoelectron spectra recorded at each pump-probe delay, as described in Section 2.3. The resultant surfaces are shown in Figure 4.11, for both aniline (a,c,e,f) and d_7-aniline (b,d,g). The

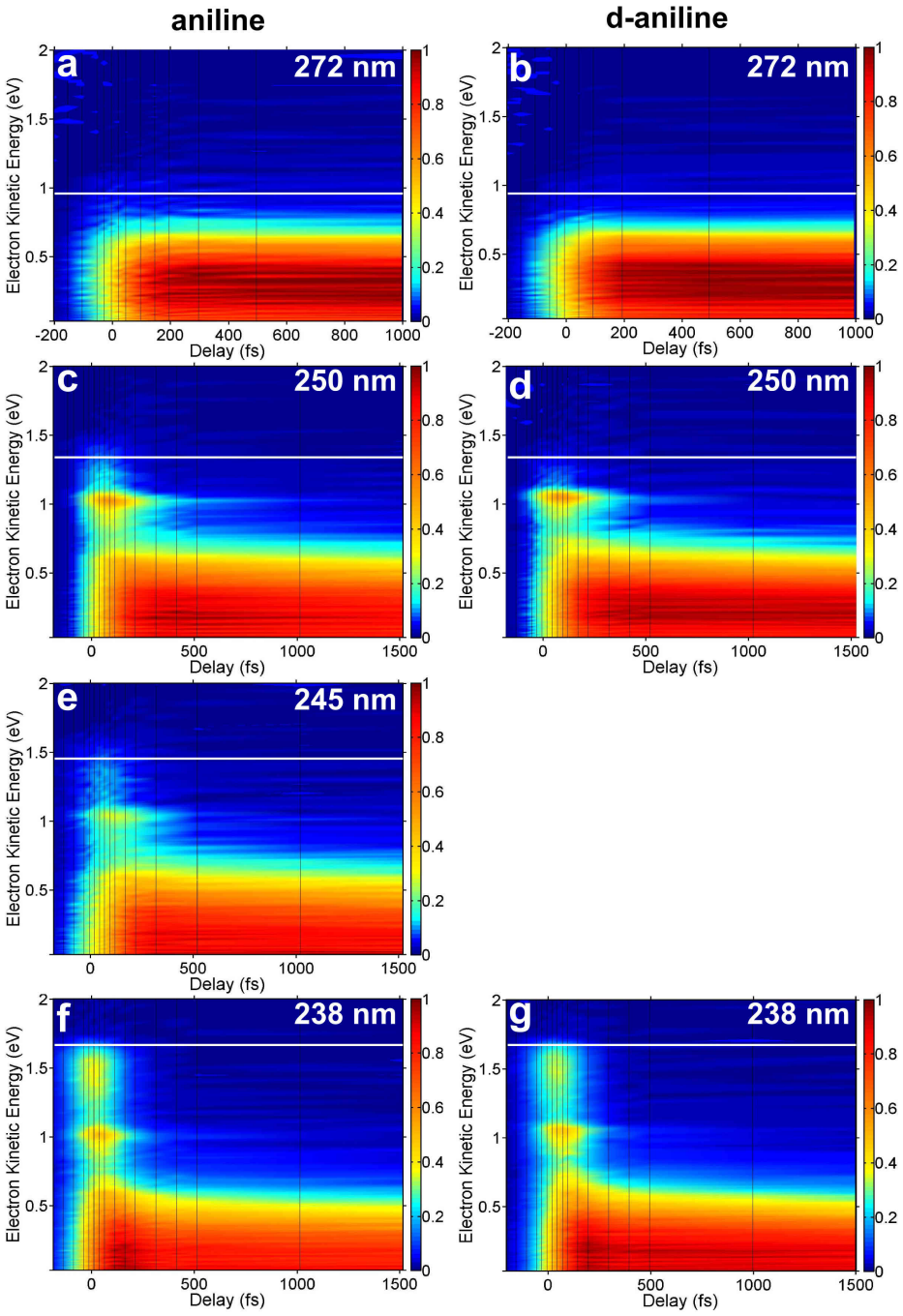

Figure 4.11: Surfaces produced by scaling the photoelectron images to the total photoelectron decays shown in Figure 4.10. Images are shown for aniline excited at 272 nm (a), d_7-aniline excited at 272 nm (b), aniline excited at 250 nm (c), d_7-aniline excited at 250 nm (d), aniline excited at 245 nm (e), aniline excited at 238 nm (f), d_7-aniline excited at 238 nm (g). Maximum accessible $(1 + 1')$ eKE are marked for each wavelength by solid white lines. Vertical black lines mark the delay times at which images were collected.

maximum accessible electron kinetic energy for each excitation and probe wavelength is calculated using Equation 2.12. The maximum accessible electron kinetic energies (for ionisation to D_0) for our selected pump wavelengths are 0.97 eV for 272 nm, 1.37 eV for 250 nm, 1.47 eV for 245 nm and 1.62 eV for 238 nm (all 300 nm probe). These energies are marked by solid white lines on Figure 4.11.

4.3.2 Photoelectron spectra

In order to assign the features in the photoelectron spectra, we utilise the $\Delta\upsilon = 0$ propensity rule and equation Equation 1.21, which requires knowledge of the energies of the 0–0 electronic transitions to the excited states and cation states. The origins of the D_0 and D_1 states in aniline have been determined to be 7.72 eV [161, 171] and 9.03 eV [166] respectively. The 0–0 excitation energies for the $S_1(\pi\pi^*)$, $S_2(\pi\sigma^*)$ states of aniline are 4.22 eV [161], 4.60 eV [162], respectively. To the best of our knowledge, an accurate experimental value for the $S_3(\pi\pi^*)$ 0–0 transition of aniline has not been reported, however using the gas-phase absorption spectrum presented in Figure 4.9, we estimate it to be around 5.1 eV. This information leads us to assign the observed peaks in eKE at around 1.5, 1.0 and 0.63 eV to ionisation to the D_0 state from the $S_3(\pi\pi^*)$, $S_2(\pi\sigma^*)$ and the $S_1(\pi\pi^*)$ states, respectively. $D_1 \leftarrow S_3$ ionisation is also possible (eKE < 0.2 eV), but is expected to be approximately a factor of 10 weaker than ionisation to the cation ground state [161].

A typical raw photoelectron image recorded at 250 nm excitation and 4 fs pump-probe delay is presented in Figure 4.12(a), inset. The corresponding photoelectron spectrum and photoelectron angular distribution are presented in Figure 4.12(a). As described above, the sharp peak visible at 1.0 eV is expected to correspond to the $S_2(\pi\sigma^*)$ state. This peak is present at all excitation wavelengths studied in this chapter, except 272 nm which lies below the onset for the $S_2(\pi\sigma^*)$ state. From the position of maximum peak intensity in the photoelectron spectrum, we calculate the 0–0 transition to be 4.67 eV, in good agreement with the more precise value of 37104 cm^{-1} (4.6003 eV) obtained using 2+2 REMPI [162]. Inspection of Figure 4.11 suggests that this peak is populated directly and decays on a timescale of around

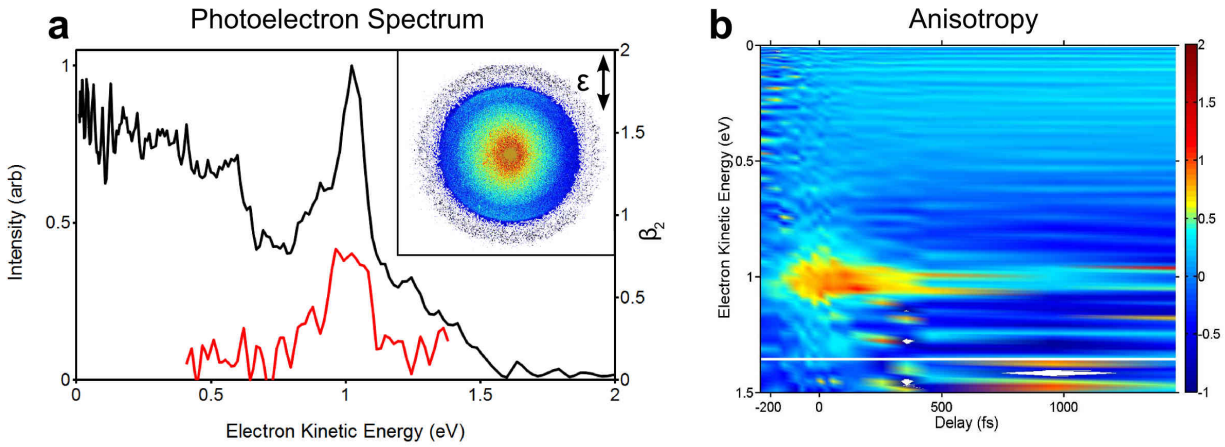

Figure 4.12: (a) Inverted photoelectron spectrum (solid line) for the image collected with 250 nm pump, 300 nm probe and 4 fs delay between pulses (raw image inset), along with eKE dependence of the anisotropy parameter, β_2 (red line). (b) Aniline anisotropy surface (250 nm pump), illustrating the temporal decay of the anisotropic feature. The maximum accessible eKE is marked by a solid white line.

200 fs. Figure 4.12(a) illustrates a photoelectron anisotropy corresponding to the peak centered at 1.0 eV (maximum value $\beta_2 = 0.8$), which is consistent with the assignment as a $\pi 3s$ Rydberg state. The anisotropy surface is plotted with respect to time in Figure 4.12(b) and shows that the high anisotropy is retained throughout the decay of the $\pi 3s$ state. Furthermore, the disappearance of this high anisotropy closely matches the associated $S_2(\pi\sigma^*)$ decay observed in Figure 4.11(c-e). The photoelectron anisotropy at all other eKE regions is found to be low (< 0.4), for all wavelengths studied in this chapter.

The broad spectral feature in Figure 4.11 lying at eKEs lower than 0.6 eV consists of two distinct components (except at 272 nm (4.56 eV) excitation, where the $S_2(\pi\sigma^*)$ state cannot be accessed). One component has a broad, approximately Gaussian profile centered on ∼0.25 eV and decays with a lifetime of tens to hundreds of picoseconds, depending upon the excitation energy (longer wavelengths produce longer decay times). From Figure 4.11 is is not possible to tell if this state is directly populated or not due to the overlap with other peaks. This band seems most likely to correspond to population in the $S_1(\pi\pi^*)$ state. Additionally, a higher kinetic energy component is observed at approximately 0.6 eV, the assignment of

this state is more complex and is considered in the discussion (Section 4.4.4).

Following 238 nm excitation, we begin to see evidence of population in another electronic state relating to the broad asymmetric peak with it maximum intensity at ∼1.5 eV. The eKE of this feature in Figure 4.11(f) and (g) closely match that expected for the $S_3(\pi\pi^*)$ state and show no discernible rise time, suggesting that the state is populated directly upon excitation.

4.3.3 Decay lifetimes

While the longer lifetime components of the decay can be extracted reliably from the total energy integrated data, extraction of decay lifetimes faster than a few picoseconds is less straightforward, particularly when multiple lifetimes exist. We extract these faster lifetimes by integrating over limited energy regions of the photoelectron spectra for each time delay, and fitting an appropriate number of decay lifetimes to Equation 2.11, as described in Section 2.3.2.

Following 272 nm excitation in both aniline and d_7-aniline, we observe a lack of ultrafast lifetimes and therefore no additional fitting was required (Figure 4.10(a,b)). At this wavelength, we see no evidence of the component centered on 0.6 eV (as observed at higher excitation energies), or indeed any other ultrafast lifetime.

For aniline excited at 250 nm, a lifetime of 100 ps was extracted from the total integrated photoelectron decay fit. The next decay lifetime were extracted by fitting data integrated over the range 0.95–1.5 eV (Figure 4.13(a)), producing a cross-correlation FWHM was 185 ± 13 fs and a decay lifetime of $\tau_2 = 111 \pm 17$ fs. Integrating across the region 0.5–0.8 eV determines an additional lifetime of $\tau_3 = 571 \pm 175$ fs (Figure 4.13(c)). The high error associated with the fit is due to the relatively weak intensity associated with this feature and significant spectral overlap with other features of the spectrum. The equivalent treatment of d_7-aniline, produces a cross-correlation FWHM of 180 ± 16 fs, and lifetimes of $\tau_2 = 131 \pm 23$ fs when fitted to the data integrated over the range 0.95–1.1 eV (Figure 4.13(b)). When the d_7-aniline spectra collected are integrated over the range 0.5–0.8 eV, the τ_3 lifetime was found

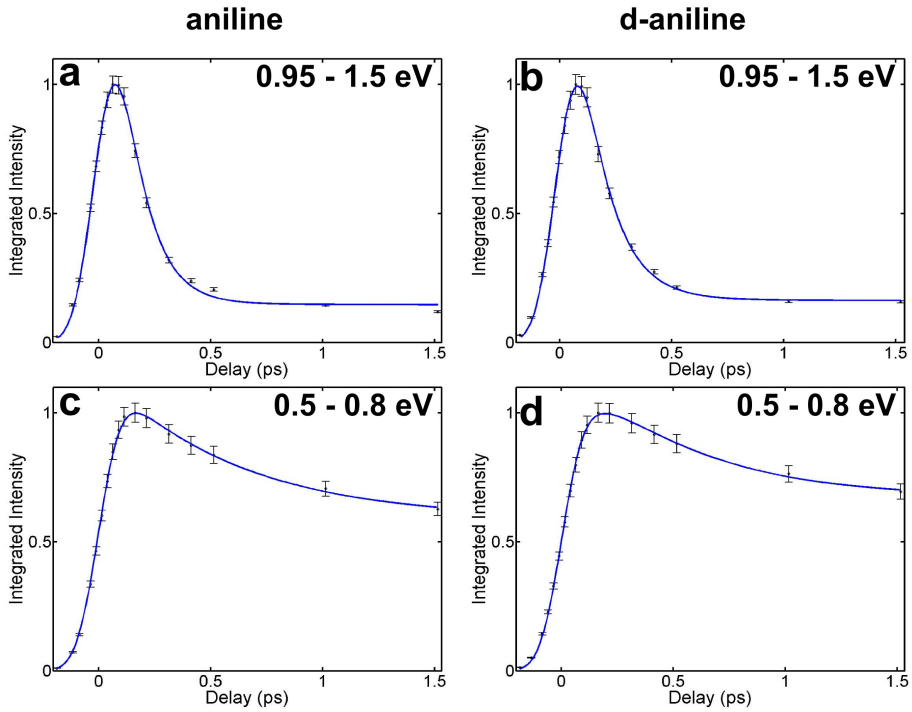

Figure 4.13: 250 nm:- Fits to the photoelectron spectra integrated over discrete regions, used to obtain the lifetimes shown in Table 4.1. Fitted curves are shown for integrations over the energy region 0.95–1.5 eV region in aniline (a) and d_7-aniline (b) and over the 0.5–0.8 eV region for aniline (c) and d_7-aniline (d). Error bars are obtained from the (2σ) standard deviation in photoelectron intensity over the integrated region.

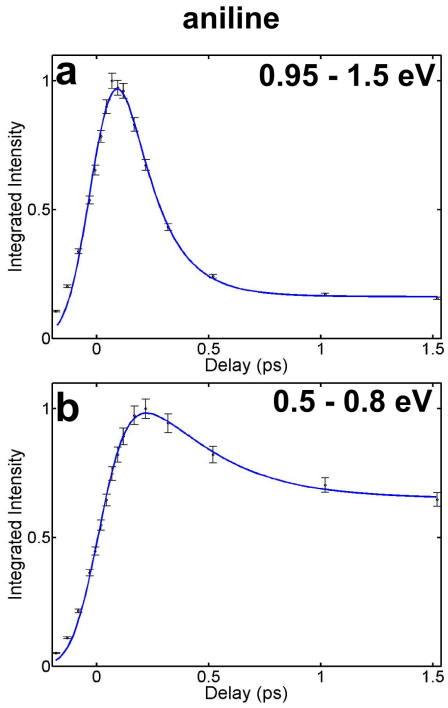

Figure 4.14: 245 nm:- Fits to the photoelectron spectra integrated over discrete regions, used to obtain the lifetimes shown in Table 4.1. Fitted curves are shown for integrations over the energy region 0.95–1.5 eV region in aniline (a) and over the 0.5–0.8 eV region for aniline (b). Error bars are obtained from the (2σ) standard deviation in photoelectron intensity over the integrated region.

to be 478 ± 146 fs (Figure 4.13(d)).

The analysis of the 245 nm excitation followed the same procedure as described above, using the $\tau_1 = 60$ ps lifetime extracted from the total integrated decay. A cross-correlation FWHM of 219 ± 32 fs and an ultrafast lifetime of $\tau_2 = 145 \pm 31$ fs were extracted by fitting over the range 0.93–1.4 eV (Figure 4.14(a)). A further ultrafast lifetime of $\tau_3 = 523 \pm 200$ fs was found by fitting over the range 0.5–0.8 eV (Figure 4.14(b)). No d_7-aniline data were collected for this wavelength.

The 238 nm excitation of aniline is sufficient to access the S_3 state and, consequently an additional step was necessary in the fitting procedure. The decay of the long-lived $S_1(\pi\pi^*)$ state was fitted over the region 1.3–1.6 eV (Figure 4.15(a)), obtaining a cross-correlation of 226 ± 10 fs and a lifetime of $\tau_4 = 50 \pm 10$ fs. Fitting over the energy range 0.95–1.1 eV determined and additional lifetime of $\tau_2 = 134 \pm 36$ fs

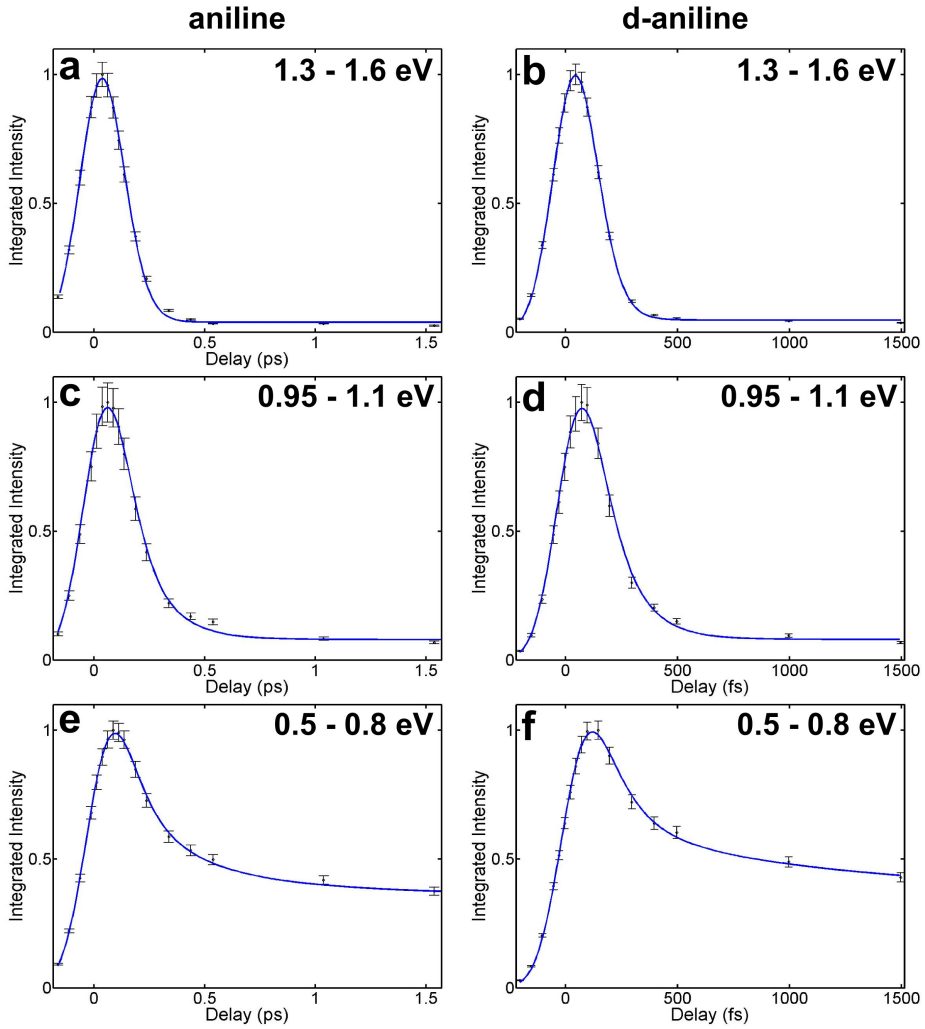

Figure 4.15: 238 nm:- Fits to the photoelectron spectra integrated over discrete regions, used to obtain the lifetimes shown in Table 4.1. Fitted curves are shown for integrations over the energy region 1.3–1.6 eV in aniline (a) and d_7-aniline (b), the 0.95–1.1 eV region in aniline (c) and d_7-aniline (d) and over the 0.5–0.8 eV region for aniline (e) and d_7-aniline (f). Error bars are obtained from the (2σ) standard deviation in photoelectron intensity over the integrated region

Table 4.1: Summary of aniline and d_7-aniline exponential decay lifetimes

Pump wavelength [nm]	τ_1 [ps]	τ_2 [fs]	τ_3 [fs]	τ_4 [fs]	Cross-correlation (FWHM) [fs]
Aniline					
272	600 ± 35	-	-	-	220 ± 115
250	100 ± 8	111 ± 17	571 ± 175	-	185 ± 13
245	77 ± 14	145 ± 31	523 ± 200	-	219 ± 32
238	90 ± 5	134 ± 36	450	50 ± 10	226 ± 10
d_7-Aniline					
272	1300 ± 40	-	-	-	224 ± 112
250	100 ± 6	131 ± 23	478 ± 146	-	180 ± 16
238	82 ± 5	125 ± 30	976 ± 514	50 ± 10	219 ± 10

(Figure 4.15(c)). Finally, we integrated and fitted over the range 0.5–0.8 eV. This fit had difficulty converging, due to the relatively weak nature of the feature associated with the τ_2 lifetime component, however neglecting this decay component produced a poor fit to the data. Due to the lifetimes extracted for other excitation wavelengths, this lifetime was fixed to $\tau_3 = 450$ fs (Figure 4.15(f)). The analogous fitting procedure was carried out for d_7-aniline, producing a cross-correlation of 219 ± 10 fs and a lifetime of $\tau_4 = 50 \pm 10$ fs when fitted over the range 1.3–1.6 eV (Figure 4.15(b)). Fitting over the ranges 0.95–1.1 eV and 0.5–0.8 eV, determined further lifetimes of $\tau_2 = 125 \pm 30$ fs and τ_3 to be 976 ± 514 fs, respectively (Figure 4.15(d) and (f)).

The fitted lifetimes for aniline and d_7-aniline are summarised in Table 4.1.

4.3.4 Global fitting

Our quasi-global fitting procedure (described in Section 2.3.2) uses the lifetimes obtained above, but examines their relative contribution across the eKE range. The time-resolved photoelectron spectra can be reconstructed using the timescales, τ_i, determined in Section 4.3.3 and fitted coefficients, c_i(eKE). This procedure is seen to reproduce all of the dynamical features observed in the experimental spectra, as shown in Figure 4.16(a,b), Figure 4.17(a,b), Figure 4.18(a), Figure 4.19(a,b).

The surfaces generated for 272 nm excitation of aniline and d_7-aniline are shown in

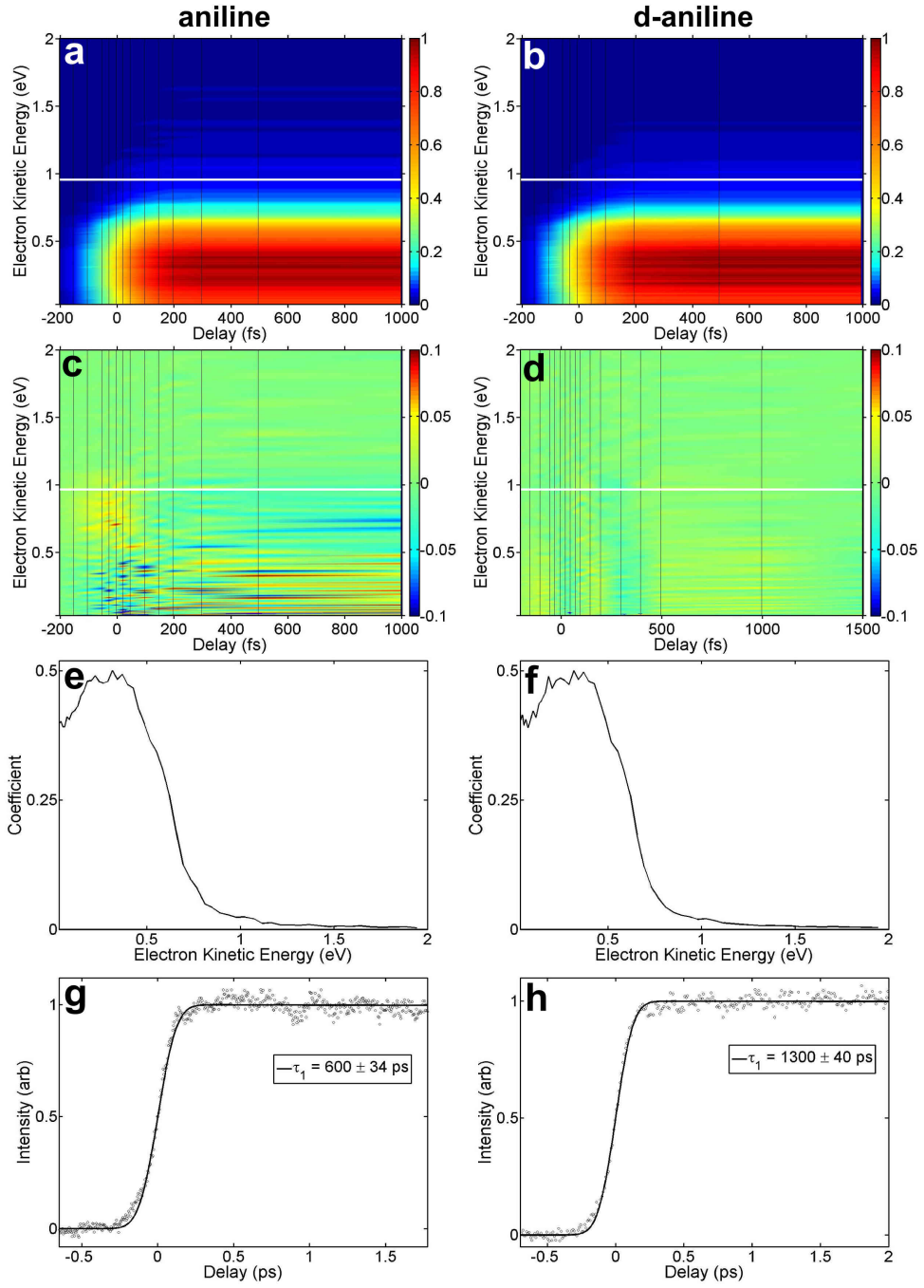

Figure 4.16: Summary of 272 nm excitation data. Fitted surfaces using τ_1 detailed in Table 4.1, for aniline (a) and d_7-aniline (b). The solid white line represents the maximum possible eKE accessible by $1 + 1'$ ionisation (0.97 eV). Residuals of the fit subtracted from the photoelectron spectra (see Figure 4.11) are presented for aniline (c) and d_7-aniline (d). The decay associated spectra related the fitted surfaces are shown for aniline (e) and d_7-aniline (f). The same lifetimes fitted to the total photoelectron signal for aniline (g) and d_7-aniline (h), to show that the correct integrated distribution is recovered.

Figure 4.16(a) and (b), respectively. The associated three-point averaged DAS are plotted in Figure 4.16(e) and (f). At 272 nm excitation, only a single lifetime is observed in both aniline and d_7-aniline, which must therefore be populated directly. We do not observe any evidence for a changing peak shape, such as could be associated with IVR processes. Figure 4.16(g,h) shows that since the only decay lifetime detected is greater than 500 ps, a negligible proportion of the total photoelectron signal decays in the first 2 ps.

Figure 4.17(a-d) shows the fitted surfaces and residuals for aniline and d_7-aniline following 250 nm excitation. The presence of a broad peak at eKE < 0.25 eV is similar to that observed following 272 nm excitation, with the notable exception that this peak is no longer symmetric. The sharp peak assigned to the $S_2(\pi\sigma^*)$ Rydberg state is also visible with an eKE of 1 eV. The DAS presented in Figure 4.17(e,f), based upon the sum of the DAS coefficients (black lines), the states associated with the τ_2 and τ_3 components are populated directly by the excitation pulse, while the state associated with the τ_1 component does not appear to be populated directly. Furthermore, the DAS shows that the coefficient for the τ_2 decay lifetime is significantly negative at eKEs less than 0.5 eV and with a shape similar to the positive coefficients associated with the τ_1 lifetime in that eKE region. This suggests that a portion of the population in the state associated with the τ_2 component decays directly into the state associated with τ_1. The τ_3 component does not have a significantly negative coefficient in any energetic region. However, given the complete overlap with the τ_2 component, it is impossible use the DAS to infer whether population transfer between the states associated with the τ_2 and τ_3 components occurs. Finally, we cannot exclude the possibility that some proportion of the population associated with the τ_1 lifetime is directly excited at this wavelength, however we do not see any evidence for this. Figure 4.17(g,h) shows that approximately 60% of the total photoelectron signal decays out of our observation window within 3 ps of the initial excitation. This must be due to the state associated with the τ_3 component and any fraction of τ_2 decay which does not lead to transfer population into the $S_1(\pi\pi^*)$ state associated with τ_1. Similar behaviour is seen for both deuterated and undeuterated cases.

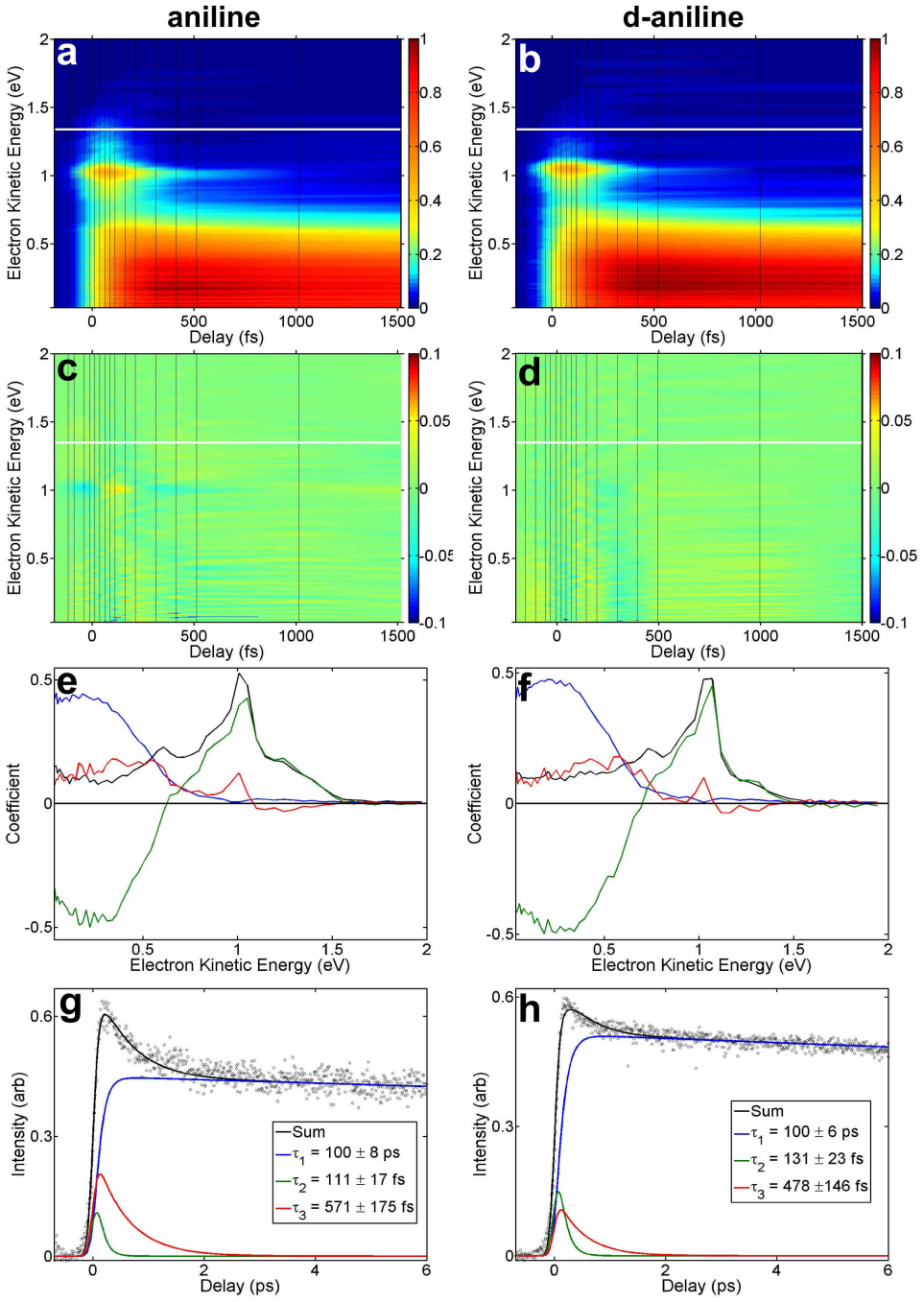

Figure 4.17: Summary of 250 nm excitation data. Fitted surfaces using τ_{1-3} detailed in Table 4.1, for aniline (a) and d_7-aniline (b). The solid white line represents the maximum possible eKE accessible by $1 + 1'$ ionisation (1.37 eV). Residuals of the fit subtracted from the photoelectron spectra (see Figure 4.11) are presented for aniline (c) and d_7-aniline (d). The decay associated spectra related the fitted surfaces are shown for aniline (e) and d_7-aniline (f). The same lifetimes fitted to the total photoelectron signal for aniline (g) and d_7-aniline (h), to show that the correct integrated distribution was recovered.

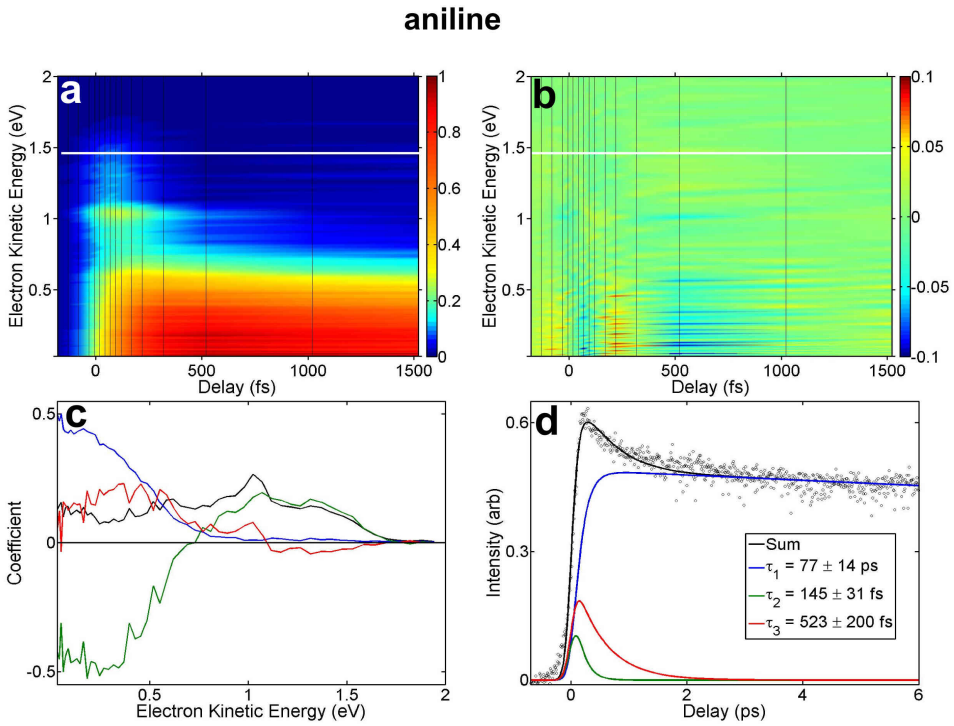

Figure 4.18: Summary of 245 nm excitation data. Fitted surfaces using τ_{1-3} detailed in Table 4.1, for aniline (a). The solid white line represents the maximum possible eKE accessible by $1 + 1'$ ionisation (1.47 eV). Residuals of the fit subtracted from the photoelectron spectra (see Figure 4.11) are presented for aniline (b). The decay associated spectra related the fitted surfaces is shown for aniline (c). The same lifetimes fitted to the total photoelectron signal for aniline (d), to show that the correct integrated distribution was recovered.

The fitted surface for 245 nm excitation is presented in Figure 4.18(a). The DAS produced following 245 nm excitation (Figure 4.18(c)) has analogous features and implications regarding evolution of the excited wavepacket to those observed following 250 nm excitation. The τ_2 and τ_3 lifetime components both appear to be populated by the excitation pulse. A negative coefficient of the τ_2 component is observed mirroring the shape of the τ_1 component, again suggesting a transfer of population. Figure 4.18(d) shows that again approximately 60% of the total photoelectron signal decays out of our observation window within 3 ps.

The fitted surfaces following 238 nm excitation of aniline and d_7-aniline are shown in Figure 4.19(a) and (b), respectively. In both cases, the broad peak below 0.6 eV is visible and is asymmetric with respect to eKE. The sharp, symmetric peak at 1.0 eV is also observed, however an additional asymmetric peak is observed in the eKE region 1.2–1.6 eV. This final peak is associated with the τ_4 decay component in the DAS (Figure 4.19(e)) and based upon the sum of the DAS coefficients the state associated with this component appears to be populated directly by the excitation pulse. Similarly, the states associated with the τ_2 and τ_3 components are populated directly at this wavelength, as observed above. The eKE ranges covered by the components τ_{1-3} are also similar to those observed at the other excitation wavelengths, although the intensity of the τ_3 and τ_1 components appear to be lower than at other, longer wavelengths. Figure 4.19(g) and (h) show that approximately 85% of the total photoelectron signal decays out of our observation window within 2 ps, for both aniline and d_7-aniline.

The DAS of aniline and d_7-aniline excited at 238 nm display fundamentally different behaviour for the τ_2 and τ_4 components. In d_7-aniline, as with the other excitation wavelengths studied in this work, population is indicated to transfer between the states associated with the τ_2 and τ_1 components. The τ_4 component does not have a significantly negative coefficient at any eKE suggesting population in the associated state leaves our observation window without populating any other excited electronic state. In contrast, in aniline a significant negative coefficient is associated with the τ_4 component at low eKE (in the region of the component τ_1) and the τ_2 component has a positive coefficient at low eKE. The anti-correlation between

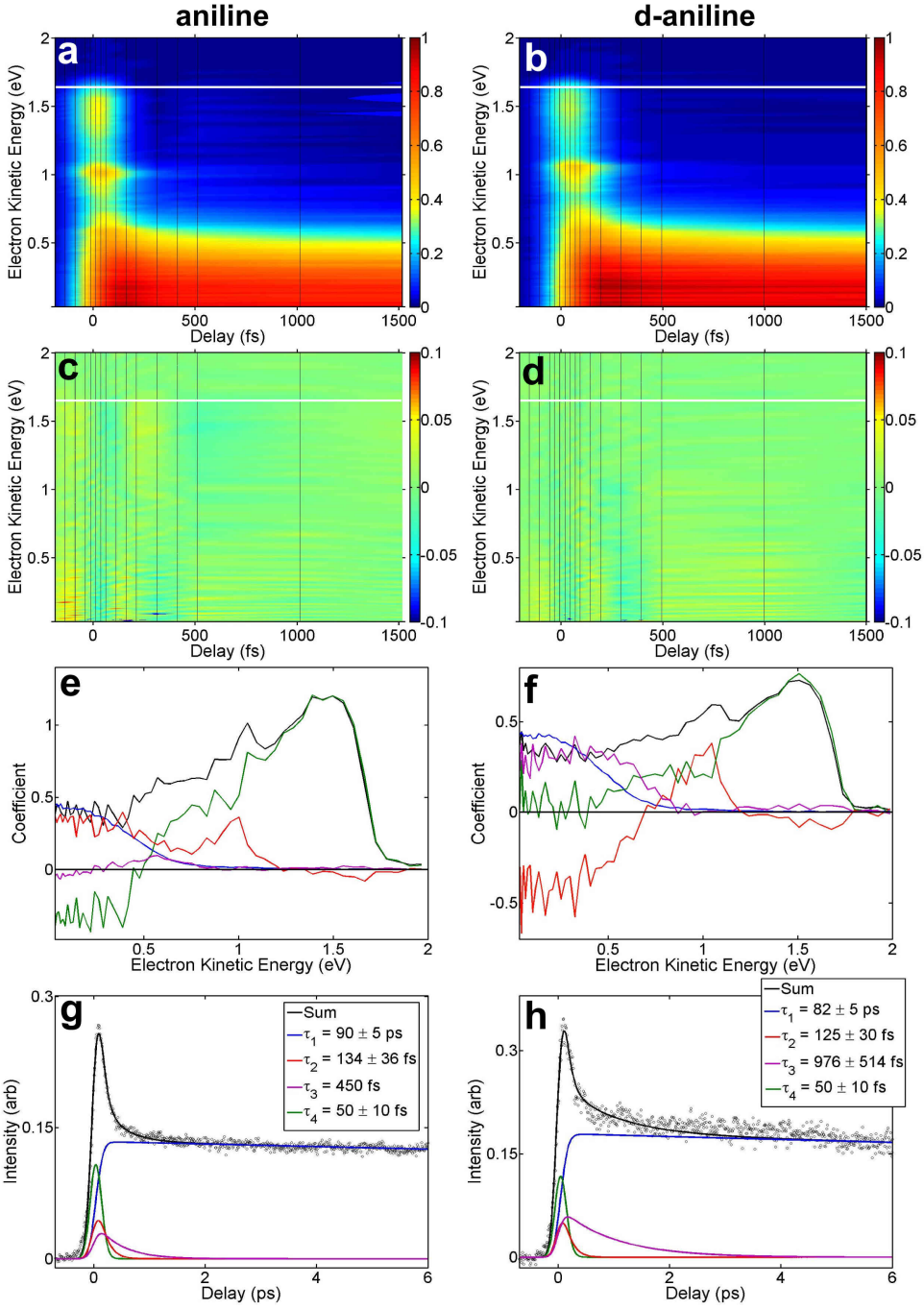

Figure 4.19: Summary of 238 nm excitation data. Fitted surfaces using τ_{1-4} detailed in Table 4.1, for aniline (a) and d_7-aniline (b). The solid white line represents the maximum possible eKE accessible by $1 + 1'$ ionisation (1.62 eV). Residuals of the fit subtracted from the photoelectron spectra (see Figure 4.11) are presented for aniline (c) and d_7-aniline (d). The decay associated spectra related the fitted surfaces are shown for aniline (e) and d_7-aniline(f). The same lifetimes fitted to the total photoelectron signal for aniline (g) and d_7-aniline (h), to show that the correct integrated distribution was recovered.

the coefficients relating to the τ_4 and τ_2 components in the case of aniline raises questions regarding the quality of their fit, however the full details of this disparity are not fully understood. In both deuterated and undeuterated cases, the results indicate that the τ_1 component rise, suggesting that the associated $S_1(\pi\pi^*)$ state is not populated directly at these short wavelengths. However, the disparity between these results indicates a certain amount of uncertainty regarding the exact timescale of the rise and therefore which state responsible for initiating the population transfer. At longer wavelengths we have already observed population transfer between the states associated with the τ_2 and τ_1 components and have established from the decay of the total photoelectron signal that the majority of the τ_4 component leaves our observation window. However, the fit presented in Figure 4.19(e) does leave the possibility that some proportion of the population associated with τ_4 does decay into the state associated with the τ_1 component.

4.4 Discussion

4.4.1 $S_3(\pi\pi^*)$ decay

Following excitation above the $S_3(\pi\pi^*)$ origin (238 nm excitation), we find that excitation to the $S_3(\pi\pi^*)$ state is the dominant process in both aniline and d_7-aniline, as may be expected from the absorption spectrum. We observe an asymmetric peak in the photoelectron spectrum, in the region 1.2–1.6 eV, the eKE of which can only correspond to the $S_3(\pi\pi^*)$ state. The fitting described in Section 4.3 showed that the decay lifetime associated with this state is extremely rapid, $\tau_4 = 50 \pm 10$ fs, in both aniline and d_7-aniline. This decay lifetime is in keeping with Longarte *et al.* [52], who observed a sub-50 fs lifetime upon exciting aniline at 234 nm. Our probe is capable of ionising population in the $S_1(\pi\pi^*)$, yet we observe a significant decrease in the total photoelectron intensity occurring on a $\sim$50 fs timescale. This, in addition to the analysis of the DAS in Figure 4.19(c,d), suggests that the decay of the $S_3(\pi\pi^*)$ state causes population to leave our ionisation window. Furthermore, no increase in the $S_1(\pi\pi^*)$ or $S_2(\pi\sigma^*)$ state populations is observed, the decay must presumably be

to the S_0 ground state. These results are in keeping with our previously published work regarding excitation to the $S_3(\pi\pi^*)$ state of aniline.

Previous theoretical modelling has suggested that the $S_3 \leftarrow S_0$ transition is a localised ring excitation [53], as such it is anticipated that an S_3/S_0 conical intersection might lie along a mode similar to the prefulvene mode which facilitates rapid internal conversion in the 'channel three' region of benzene [157, 159, 172, 173]. Rapid relaxation of the S_3 population is consistent with the recent work of Paterson *et al.* [156] who find that the $S_3(\pi\pi^*)$ is not bound in at least one dimension (prefulvene motion) and this dimension leads directly to a conical intersections with the $S_1(\pi\pi^*)$ state, as shown in Figure 4.3. A further CI exists in the vicinity, which couples to the ground state. Consequently, a pathway is identified, which could plausibly allow population to traverse both of these adiabatic transitions and reach the ground state on the observed timescales. Similarly, Sala *et al.* find that the $S_3(\pi\pi^*)$ state is not bound in the prefulvene-like, ring-bending dimension and that a three-state CI involving the S_3, S_2 and S_1 states occurs, entry to which CI is barrierless [160]. This provides a mechanism for the rapid deactivation of the $S_3(\pi\pi^*)$ population with the majority of the population leaving our observation window. It also allows for transfer of population to the S_1 state, as suggested by Figure 4.19(e).

Notably, the above proposed mechanism might not be expected to produce H atoms. However Ashfold *et al.* [51] observe H atom loss at wavelengths shorter than 240 nm. The observed kinetic energy of these H atoms is bimodal, with the lower energy peak relating to statistical dissociation on the ground state surface. This finding is consistent with our proposed mechanism. However, the fast H atoms indicate another relaxation process which must presumably occur either *via* a S_3/S_2 CI or *via* successive S_3/S_1 and S_1/S_2 CIs. Additional experiments by Stavros *et al.* also observed fast H atoms following excitation of aniline at 200 nm, which as determined to be generated by a $S_3(\pi\pi^*) \rightarrow S_1(\pi\pi^*) \rightarrow S_2(\pi\sigma^*) \rightarrow$ N-H fission process. We do not observe evidence to support either of these proposed mechanisms, instead we observe instantaneous population of both the $S_3(\pi\pi^*)$ and $S_2(\pi\sigma^*)$ states, simultaneously. No delayed rise in population is associated with the $S_2(\pi\sigma^*)$ state. It may be possible that some population decays *via* a S_3/S_1 CI, because the overlap of states in

the eKE < 0.6 eV region would make it very difficult for us to discern a weak rise from the significant rise caused by the population transfer from the $S_2(\pi\sigma^*)$ state (discussed below). As described above, we believe that the dominant decay pathway for the $S_3(\pi\pi^*)$ state is a 50 fs decay to the electronic ground state. However, once population has returned to the ground state, two possible routes could lead to fragmentation. The first involves passing adiabatically through S_0/S_2 CI at extended N-H bond lengths to generate H atoms with high translational energy, the second involves unimolecular dissociation of the highly vibrationally excited S_0 to generate H atoms with low translational energy. These mechanisms would be consistent with the bimodal distribution observed in H atom photofragment translational spectroscopy [51].

The newly suggested existence [155] of two low-lying $3p$ states in aniline is extremely interesting, especially if these states couple population out of the strongly absorbing $S_3(\pi\pi^*)$ state. We had hoped that using an improved experimental set up and increasing our temporal resolution around the zero delay position would allow direct observation these states and allow us to isolate their associated lifetimes. However, due to the congested nature of the aniline spectrum, with multiple ultrafast decays overlapping in the region where these states are expected to arise (eKE ∼1.1–1.5 eV when using 300 nm probe), we do not have the resolution to provide this analysis.

4.4.2 $S_2(\pi\sigma^*)$ decay

At all wavelengths shorter than 272 nm, we observe a feature centered on a photoelectron energy of 1.0 eV, which decays with the lifetime τ_2. This feature has been assigned to the $S_2(\pi\sigma^*)$ state, based upon the expected eKE. As has been previously noted, ionisation from this state has generates an anisotropic photoelectron distribution, which derives from its predominantly $3s$ character in the vFC region [162, 174]. As we have observed in our previous publications [87, 152, 169], the $S_2(\pi\sigma^*)$ state is populated directly at all wavelengths where it can be energetically accessed. This state decays with a lifetime of 111–145 fs, which appears to be invariant to the amount of excess vibrational energy imparted upon excitation. This is also in

keeping with our previous findings, where we found that this lifetime invariance holds true, regardless of whether excitation occurs below or above the barrier to dissociation in the N-H stretch dimension (see Figure 4.3). Importantly, we find that this lifetime is not affected by deuteration. Townsend *et al.* had suggested that this decay lifetime could be due to tunnelling from the $S_1(\pi\pi^*)$ state onto the dissociative region of the S_2 surface, however this is not in keeping with the results of our deuterated study.

It should also be noted that Ashfold *et al.* and Stavros *et al.* suggest that the signal attributed to the S_2 Rydberg state could be generated by initial excitation of $S_1(\pi\pi^*)$ character, with subsequent internal conversion to the $S_2(\pi\sigma^*)$ state. The data we present in this chapter, along with our previous publications on aniline, cannot support such a mechanism, because we observe the S_2 state to be populated directly. This is particularly interesting when compared to the analogous case in phenol, where above the origin of this state population is assumed to proceed by excitation to the lower-lying $S_1(\pi\pi^*)$ state, with subsequent population transfer due to vibronic coupling [175, 176].

The lifetimes presented in our previous work on aniline [87, 152, 169] have been re-examined, due to developments in our fitting procedures, as been described in Chapter 2. The comparison between the lifetimes found in the current work and those in our previous publications (following re-analysis) are presented in Table 4.2. Our interpretation remains unchanged, however the lifetimes associated with the $S_2(\pi\sigma^*)$ state decay reduced to 90–180 fs, which is in excellent agreement with our findings in the current work. The details of the re-analysis are contained in Appendix B. Furthermore, the $S_2(\pi\sigma^*)$ decay lifetimes we identify in this work (110–145 fs) are in excellent agreement with those published by Longarte *et al.* [52], who identify a decay lifetime of 165 fs associated with the $S_2(\pi\sigma^*)$ state, when exciting in the range 294–234 nm. Additionally, we find excellent agreement with Townsend *et al.* [96], who observe $S_2(\pi\sigma^*)$ decay lifetimes of 110–180 fs in the region 269.5–265.9 nm. Collectively these results emphasize that, despite the known presence of a bound region in the vFC region of the $S_2(\pi\sigma^*)$ state surface, the decay of population in the vFC region appears insensitive to the amount of excess vibrational energy excited.

Table 4.2: Summary of fitted exponential decay lifetimes for aniline, compared with our previous analysis

Lifetimes (This work)					
Pump wavelength [nm]	$S_3(\pi\pi^*)$ lifetime [fs]	$S_2(\pi\sigma^*)$ lifetime [fs]	S_2 IVR lifetime [ps]	$S_1(\pi\pi^*)$ lifetime [ps]	Cross–correlation (FWHM) [fs]
272	-	-	-	600 ± 35	220 ± 115
250	-	111 ± 20	571 ± 175	100 ± 8	185 ± 13
245	-	145 ± 31	523 ± 200	77 ± 14	219 ± 32
238	50 ± 10	134 ± 36	450	90 ± 5	226 ± 10
Lifetimes (Refs. [169] and [152]) - see Appendix B					
269	-	181 ± 41	-	> 1 ns	150 ± 10
250	-	141 ± 16	1.0 ± 0.2	600 ± 35	180 ± 15
240	52 ± 10	91 ± 27	1.4 ± 0.3	185 ± 15	192 ± 10
238	50 ± 10	112 ± 33	1.3 ± 0.7	100 ± 10	203 ± 10
236	123 ± 10	185 ± 47	1.2 ± 0.3	81 ± 10	202 ± 12

The DAS presented in Figure 4.17(e,f), Figure 4.18(c) and Figure 4.19(e,f) show negative amplitudes associated with the $S_2(\pi\sigma^*)$ lifetime in the region corresponding to the $S_1(\pi\pi^*)$ state, with the coefficients associated with components mirroring one another in the region where they overlap. This suggests population in the $S_2(\pi\sigma^*)$ state primarily decays into the $S_1(\pi\pi^*)$ state. Theoretical modelling by Paterson *et al.* has suggested that the $S_2(\pi\sigma^*)$ and $S_1(\pi\pi^*)$ state cross at modest distances along the N-H stretch coordinate, inside the region bounded by barrier to dissociation as shown in Figure 4.3. However, it should be noted that the Paterson group could not locate a CI associated with this crossing. Recently published work by Sala *et al.* [160] has used high level XMCQDPT2 modelling to locate this CI and it is found very close to the S_2 origin (as shown in Figure 4.4). This is in keeping keeping with our findings and consequently we believe the dominant relaxation process upon excitation to the $S_2(\pi\sigma^*)$ state involves rapid relaxation through this S_2/S_1 conical intersection. The S_2 to S_1 mechanism is not obvious by direct inspection of Figure 4.11, but demonstrates the ability of the global fitting technique and DAS to elucidate decay pathways. These dynamical pathways are in keeping with our earlier work on aniline [152, 169].

Interestingly, although the lifetimes and spectral profiles associated with each state observed in the current study are similar to those observed by Townsend *et al.*,

however these authors do not observe population transfer between the $S_2(\pi\sigma^*)$ and $S_1(\pi\pi^*)$ states, for reasons we cannot adequately explain. Due to this disparity, Townsend *et al.* attribute the decay following excitation close to the $S_2(\pi\sigma^*)$ origin to tunnelling through the barrier onto the dissociative $\pi\sigma^*$ region of this state and specifically state that no population decays into the $S_1(\pi\pi^*)$ state. In contrast, our data (in this study and the previous publications) finds that the population excited to the S_2 primarily decays by rapid population transfer to the $S_1(\pi\pi^*)$ state *via* a conical intersection close to the vFC region. This conclusion is supported by the recent theoretical study of Sala *et al.*, as described above. The location of the S_2/S_1 CI so close to the S_2 origin provides an easily accessible method of relaxation and it seems challenging to explain how population could survive on the S_2 potential long enough to tunnel onto the dissociative region of the surface.

The recent work by Stavros *et al.* [156], sheds much light on the ultrafast dynamics of H atom formation in aniline. H atom formation is not observed at wavelengths equal to, or longer than, 250 nm. However, ultrafast H atom emission is observed with rise times of 155 and 170 fs, at 240 and 200 nm excitation respectively. Interestingly, the decay lifetimes observed by these authors closely match those we observe relating to the decay out of the $S_2(\pi\sigma^*)$ state (110–145 fs). However, both the current work and our previous study of aniline showed that the decay dynamics of the $S_2(\pi\sigma^*)$ state do not change significantly as the vibrational energy imparted upon excitation is increased. H atom detection is extremely sensitive and could possibly detect small signals that we fail to resolve. We note that our proposed S_2/S_1 relaxation mechanism could lead to H atom 'leakage' onto the dissociative $\pi\sigma^*$ surface, with some population traversing this CI diabatically and remaining on the S_2 surface. Population on the dissociative part of the $S_2(\pi\sigma^*)$ surface would be expected to leave the vFC region very rapidly and our experiment is typically blind to this type of dynamics, as the probe wavelengths used are incapable of ionising population far from the vFC region. We would be interested in further dynamical wavepacket modelling of this region of the potential energy surface.

4.4.3 $S_1(\pi\pi^*)$ decay

The lowest excited singlet state of aniline, $S_1(\pi\pi^*)$ is found to have a significantly longer decay lifetime than the other states observed in this work, with τ_1 = 82–1300 ps. The decay lifetime of this component varies significantly with excitation energy, decreasing as shorter excitation wavelengths are used. There are two possible decay routes for population in this state to leave our observation window. Firstly, IC could occur to the electronic ground state. Secondly, population could tunnel under the barrier formed by the conical intersection between the S_2 and S_1 states in the N-H stretch dimension. Both of these mechanisms have been observed following the analogous excitation to the $S_1(\pi\pi^*)$ state in phenol [175, 177]. A reduction in decay lifetime with increasing excitation energy is consistent with both S_1/S_0 internal conversion and tunnelling processes, as excitation higher up the vibrational manifold increases the density of states in both the excited state and the ground state, increasing the likelihood of internal conversion, and because excitation at higher energies reduces the height of the barrier under which tunnelling occurs (see analogous image in Figure 5.2).

Deuteration of aniline should provide a method of differentiating these decay pathways, as deuteration should significantly inhibit tunnelling processes, while leaving diabatic (or indeed adiabatic) motion on the potential surfaces relatively unchanged. The results presented in Table 4.1, show that the majority of lifetimes observed in the deuterated and undeuterated cases are equal, within experimental error. The significant exception is the $S_1(\pi\pi^*)$ lifetime observed at 272 nm excitation, which displays an increase from 600 ps to 1300 ps upon deuteration. For excitation $\lambda \leq 250$ nm, this suggests that tunnelling is unlikely to explain the decay behaviour of this state. As stated in the previous section, theoretical works by Sala *et al.* [160] and Paterson *et al.* [156] have found an S_1/S_0 CI in the ring-bending coordinate and we suggest that at excitation wavelengths shorter than 250 nm this decay channel is open allowing for rapid non-radiative relaxation. However, upon excitation at 272 nm we find that deuteration does increase the decay lifetime associated with the $S_1(\pi\pi^*)$ state by a factor of 2. We believe that this shows that passage through the S_1/S_0 CI

becomes increasingly dependent upon the precise vibrational states excited as the excitation energy decreases.

We note good agreement with the decay lifetimes associated with this state in our group's previous work, as shown in Table 4.2 [152, 169]. Longarte *et al.* [52] identified a lifetime greater than 45 ps associated with the decay of the $S_1(\pi\pi^*)$ state for all excitation wavelengths in the range 294–234 nm. This is in agreement with our findings. Furthermore, Townsend *et al.* [96] observe the decay of the $S_1(\pi\pi^*)$ state with a lifetime greater than 1 ns for all excitation energies in the range 273–266 nm, which is slightly longer than most of lifetimes we observe related to this state.

It should be noted that at 272 nm excitation, the photoelectron spectra for both aniline and d_7-aniline (see Figure 4.16(a,b)) show only a single excited state to be populated, with no discernible population transfer and only a single decay lifetime. This is true for both the deuterated and undeuterated cases and conflicts with the observation by Townsend *et al.* that IVR processes occur on a 400–640 fs timescale following 273 nm excitation.

4.4.4 Additional decay lifetime

In our analysis, the $S_1(\pi\pi^*)$, $S_3(\pi\pi^*)$ and $S_2(\pi\sigma^*)$ states were relatively simple to identify using their spectral position and photoelectron anisotropies. However, we see an additional feature in the photoelectron spectrum. For example, at 250 nm excitation, only two known electronic states are accessible, yet we identify three distinct decay lifetimes. Similarly, at 238 nm only three experimentally observed electronic states are accessible, yet we identify four decay lifetimes. The additional lifetime component can be observed in the DAS in Figure 4.17(e,f) and corresponds to component described by τ_3, with an asymmetric spectral profile centered around 0.6 eV. The measured lifetime of this state is found to be 478–976 fs, and does not vary significantly upon deuteration. The wide range of values found for this lifetimes and large error associated with it (see Table 4.1) are due to the weak intensity of this state.

Townsend *et al.* observe an analogous decay when exciting at 273–266 nm, with a measured lifetime of 400–640 fs and a spectral profile very similar to that shown for τ_3 in Figure 4.18(c) and Figure 4.18(c). These authors observe this component for all excitation in the range 273–266 nm and attribute this decay to IVR processes experienced by some portion of the initially excited wavepacket on the $S_1(\pi\pi^*)$ surface. Interestingly, these authors also find another less vibrationally excited, component of the $S_1(\pi\pi^*)$ state to also be directly excited. Such a finding suggests that excitation to the S_1 state induces instantaneous bifurcation of the wavepacket in the vFC region and subsequent recombination following IVR. This interpretation is interesting and could be convincing, however results in the current work fail to observe any signature of the τ_3 spectral component following 272 nm excitation (*i.e.* below the onset of the S_2 state). As we only observe this τ_3 component upon accessing the S_2 state, we instead attribute it to IVR processes occurring on the $S_2(\pi\sigma^*)$ state surface.

4.5 Conclusion

Our TRPEI study of aniline, following absorption of ultraviolet light in the range 272–236 nm, has provided detailed information about the electronic states involved in the electronic relaxation of this molecule, supporting some conclusions reached in previous studies and contradicting some others. Our previously published work on the ultrafast decay dynamics of aniline utilised a series of pump wavelengths 269, 250, 240, 238 and 236 nm. Some of these excitation wavelengths are common with the current study, it is therefore interesting to note the excellent agreement between the results presented in this study and those found in our groups previous publications.

Our experiments and analysis have allowed us to visualise the ultrafast electronic relaxation process in aniline. Our findings suggests that, when the $S_3(\pi\pi^*)$ state can be accessed (238 nm excitation), it accounts for the vast majority of absorption cross-section. Population decays back to the electronic ground state on a 50 fs

timescale, *via* the recently identified, three-state CI which occurs in the prefulvene-like motion [160].

When the $S_2(\pi\sigma^*)$ state is energetically accessible, direct excitation can occur, as has been described in our previous papers on aniline. Thereafter, the population instantly bifurcates into two distinct non-radiative decay pathways. The lifetimes of both $S_2(\pi\sigma^*)$ relaxation pathways are found to be independent of excitation energy. The weaker channel involves IVR processes on the $S_2(\pi\sigma^*)$ surface occurring on a $\sim$500 fs timescale. The other, dominant channel involves relaxation back to the $S_1(\pi\pi^*)$ state by rapid internal conversion (110–145 fs) through an S_2/S_1 conical intersection, recently identified close to the $S_2(\pi\sigma^*)$ origin (Sala *et al.* [160]). We believe a minority of population on the $S_2(\pi\sigma^*)$ state does not pass though this CI and instead proceeds to a dissociation, producing the ultrafast H atoms observed by other groups. Once the majority of this population reaches the $S_1(\pi\pi^*)$ state, subsequent slower decay is observed, with a 82–600 ps lifetime. A wavelengths, $\lambda \leq 250$ nm, this decay is invariant following deuteration. Our probe is sufficiently energetic to ionise from the S_1 origin and we observe loss of photoelectron signal on these picosecond timescales, which suggests that the primary decay is due to internal conversion to the S_0 state.

Following excitation at 272 nm, only the $S_1(\pi\pi^*)$ state can be accessed. We find only a single, lifetime is observable, decaying on a picosecond-nanosecond timescale. We find no evidence of IVR relaxation within the S_1 state, in contradiction to the conclusions of Townsend *et al.*, who attribute the minority $S_2(\pi\sigma^*)$ decay to this process. We find that the decay lifetime of this state is modestly increased following deuteration, which could indicate that the passage through the S_1/S_0 CI is dependent upon the precise vibrational modes populated upon excitation, as the pump energy decreases. An alternate explanation for the mass dependent lifetime involves population tunnelling onto the $S_2(\pi\sigma^*)$ state, under the barrier formed by the S_1/S_2 CI, as has been observed in phenol [175]. Unfortunately we cannot observe either the S_0 or $S_2(\pi\sigma^*)$ product states following this decay, which would allow us to conclusively differentiate these decay mechanisms. Further experimental studies could resolve this uncertainty through the use of higher energy (VUV) probe pulses,

as the ability to ionise population from the ground state or the anilino product state, would allow differentiation of these possibilities. The complexity and numerousness of decay mechanisms possible serves to demonstrate that the UV photostability of aniline arises from a delicate balance of decay dynamics across the accessible potential energy surfaces.

We have attempted to conduct UV pump-VUV probe femtosecond TRPES experiments examining the photodecay of aniline in collaboration with other universities using the ARTEMIS facility at Rutherford Appleton Laboratory (RAL). High energy VUV photons (around 20 eV) were obtained via high harmonic generation in argon from 800 nm femtosecond pulses. These photons are sufficiently energetic to ionise aniline from the ground electronic state. In pump-probe experiments, the initial pump step typically excites only a small fraction of the total molecules present, but VUV probes are capable of ionising every molecule present, consequently signal-to-noise ratios are often low and excited state dynamics are difficult to detect. Considerable progress has been made using the RAL setup, where a UV-VUV pump-probe experiment was able to detect the UV-VUV resonant ionisation of helium. However, we were unable to detect a UV-VUV pump-probe signal for aniline, due to the low signal to noise ratio.

Chapter 5

Time-resolved dynamics of phenol following excitation in the region 275–200 nm

5.1 Introduction

The phenolic group is a common structural motif in biological molecules, for example it forms a suitable model for the dynamics of tyrosine [5, 178], a molecule which plays a key role in the catalysis of a wide range of enzymes, including photo-system II the water oxidizing enzyme [179].

Like the other studies reported in this thesis, phenol has a low-lying $^1\pi\sigma^*$ state, which provides a potential mechanism for rapid coupling of excited state population back to the ground state, as described in Section 1.3. This $^1\pi\sigma^*$ state has mixed Rydberg and valence antibonding character; the O-centered $^1\pi 3s$ and $^1\pi\sigma^*$ configurations form an avoided crossing at modest O-H internuclear separations. This state crosses the first excited $\pi\pi^*$ state, which lies lower in energy, and the ground state surface along the O-H coordinate, providing an efficient pathway for relaxation.

5.1.1 Potential energy surfaces

Roos *et al.* [180] carried out an early theoretical study to characterise the excited states of phenol. They determined that the lowest singlet excited state was a $^1\pi\pi^*$ state (hereafter referred to as $S_1(\pi\pi^*)$) and the 0–0 excitation energy was found to be 4.53 eV (273 nm). The second singlet excited state was determined as having mixed $3s$ Rydberg-valence character and a calculated vertical excitation energy of 5.76 eV (215 nm) (hereafter referred to as $S_2(\pi\sigma^*)$). However, the oscillator strength of this state was calculated to be 35 times weaker than that of the $S_1(\pi\pi^*)$ state [180]. The third singlet excited state was identified as another $^1\pi\pi^*$ state, resulting from local excitation on the benzene ring (hereafter referred to as $S_3(\pi\pi^*)$). The vertical excitation energy of this state was determined to be 5.80 eV (214 nm). These calculations are consistent with the gas-phase absorption spectrum of phenol (see Figure 5.1), which shows two strongly absorbing bands centered around 4.68 eV (265 nm) and 6.05 eV (205 nm), with a weak, structureless background between the two. Phenol has been determined experimentally to be planar in both the ground

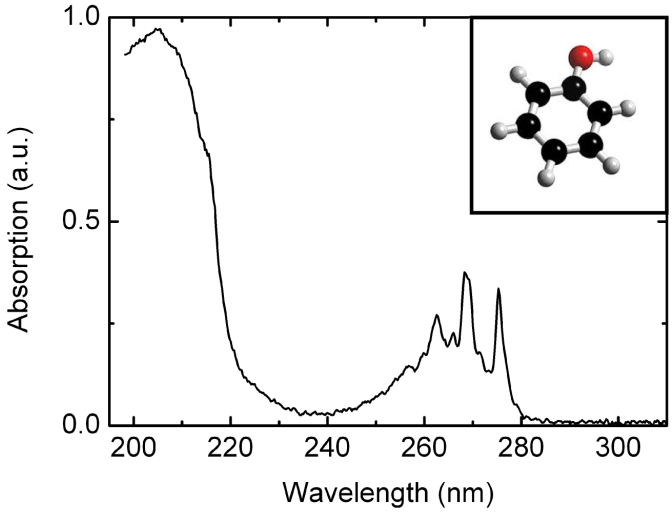

Figure 5.1: The gas-phase absorption spectrum of phenol, recorded using a Perkin-Elmer Lambda 950 UV-VIS spectrometer. Inset: The phenol molecule, in the planar ground-state equilibrium geometry (C atoms - black, H atom - white, O atom - red).

and first excited states (S_1), with barriers to OH rotation of 0.15 and 0.58 eV, respectively [181].

More recently, Domcke *et al.* have used the complete-active-space-self-consistent-field (CASSCF) and multi-reference configuration interaction (MRCI) methods to examine the potential energy surfaces of the first two excited states of phenol, particularly in the dimensions relating to OH stretching and rotation [54, 182]. The $S_1(\pi\pi^*)$ state displays a Morse potential in the O-H stretch dimension with a small barrier to OH rotation. The $S_2(\pi\sigma^*)$ state is formed by the mixing of Rydberg and valence antibonding configurations, as mentioned above. However, in phenol the $\pi 3s$ Rydberg state is relatively unstable compared to the $\pi\sigma^*$ region of the surface, as such the surface formed is almost entirely dissociative along the OH stretch coordinate and no bound region is known. Upon O-H elongation, the S_2 surface crosses the lower-lying $S_1(\pi\pi^*)$ and ground states, as shown schematically in Figure 5.2. The authors show that these crossings form conical intersections when the OH torsional modes are taken into account and subsequent modelling showed that wavepacket dynamics on these surfaces can transfer population back to the ground state in tens of femtoseconds if some vibrational energy is imparted to the O-H stretching vibra-

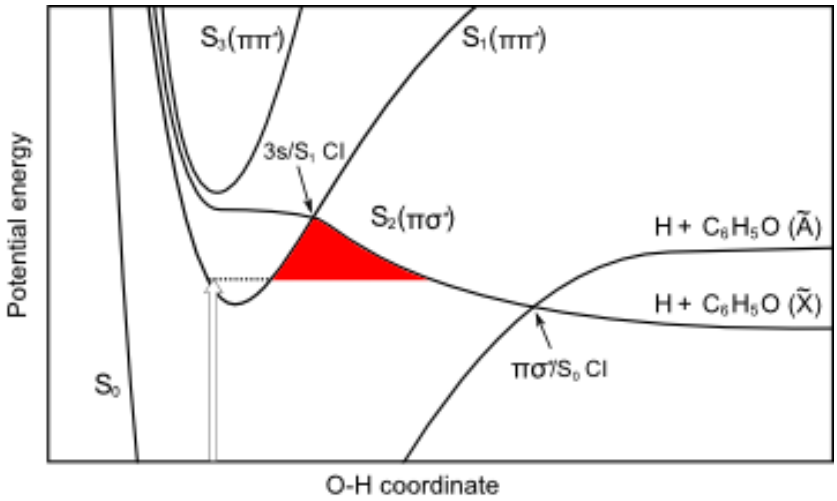

Figure 5.2: Schematic of the potential energy surface of phenol in the O-H stretch dimension (planar geometry). The barrier under which H atoms tunnel is formed by the $S_1(\pi\pi^*)$ state, the $S_2(\pi\sigma^*)$ state and the conical intersection formed by their crossing and is highlighted in red.

tion upon excitation. Out-of-plane, prefulvenic motion is known to couple the S_1 and S_0 surfaces in benzene and recent work has shown that this pathway also exists in phenol, but is inhibited by a barrier which is ∼0.3 eV higher than the $S_2(\pi\sigma^*)/S_1$ CI [183]. Therefore, below the $S_2(\pi\sigma^*)/S_1$ CI, population could be anticipated to remain on the S_1 surface. Less than 0.3 eV above this CI, internal conversion to the S_2 state followed by rapid O-H dissociation can compete, and 0.3 eV higher than this, S_1/S_0 internal conversion also competes.

An and Baeck used theory to extend this work to examine the isotope effect on the dissociation dynamics, following direct excitation to the $S_1(\pi\pi^*)$ and $S_2(\pi\sigma^*)$ states [184]. They found that upon (theoretical) excitation to the $S_2(\pi\sigma^*)$ state, dissociation occurred on a 100 fs timescale and was unaffected by deuteration. However, when population was excited low on the $S_1(\pi\pi^*)$ surface, the relaxation lifetime increased by a factor of 15 (100 fs to 1.5 ps). They interpreted this as population tunnelling out of the $S_1(\pi\pi^*)$ state onto the $S_2(\pi\sigma^*)$ surface.

5.1.2 Spectroscopy of phenol

The $S_1(\pi\pi^*)$ state of phenol is well characterised, with the origin located at 275.11 nm (4.507 eV) [185–187]. The fluorescence lifetime of the $S_1(\upsilon = 0)$ state of phenol has been measured to be ∼2 ns [177]. It was found that internal conversion (IC) to the ground state was the dominant decay mechanism, rather than intersystem crossing (ISC) into triplet states [188, 189]. The quantum-yields of several photodecay processes of phenol in cyclohexane have been measured: fluorescence, ISC to the T_1 state and dissociation were determined to be 0.083, 0.27 and 0.07, respectively, with the remaining 58% of the population decaying by IC to the ground state [190]. Further studies by Lipert *et al.* [191, 192] examined the deuterated analogue and the fluorescence lifetime increased by an order of magnitude, suggesting that the difference in vibrational level spacing in the deuterated molecule reduces the overlap with the ground state vibrational levels and thus impedes the IC pathway considerably. Furthermore, substitution of bulky butyl groups at the *ortho* and *para* positions significantly reduces the fluorescence lifetime ($\tau_{fluo} = 120$ ps), as steric hindrance of the OH rotation enhances vibrational overlap with the ground state levels [190].

Kimura *et al.* [193] examined the UV absorption spectrum of phenol and found that the absorption maxima of the second $\pi\pi^*$ band lies at 5.82 eV. To the best of our knowledge an accurate experimental value for the $S_2(\upsilon = 0)$ excitation energy has not been reported, however Roos *et al.* calculated the 0–0 energy as 5.80 eV. Furthermore, the first ionisation potential (IP) of phenol has been found to be 8.51 eV [194], while the second IP of phenol has been determined to be 9.36 eV [147]. The $S_2(\pi\sigma^*)$ state of phenol is usually considered optically dark because the region of the absorption spectrum between the $S_1(\pi\pi^*)$ and $S_3(\pi\pi^*)$ states has almost zero absorption (as can be seen in Figure 5.1). Consequently, to the best of our knowledge, no experimental value for the absorption cross section to this state is known, but as mentioned earlier theoretical modelling has predicted that the vertical excitation energy lies at 5.76 eV. However, it has been noted that the $S_2(\pi\sigma^*)$ state may gain some oscillator strength due to vibronic coupling to the $S_1(\pi\pi^*)$ [170].

Pino *et al.* [195] were the first to demonstrate that when phenol in small clusters with

Figure 5.3: H atom photofragment translational spectra following excitation between 275.113–218 nm. (a): a bimodal distribution of H atoms is observed, with a distinct vibrational progression relating to vibrations on the phenoxyl radical. (b): these vibrations diminish when exciting above the S_2/S_1 CI, but the bimodal distribution remains. (c): vibrations can be observed relating to the S_3 state. Reproduced from Ref. [175].

ammonia is excited to the S_1 state, H atom transfer occurs. The mechanism for such transfer is now suspected to entail excitation to the S_1 state with transfer onto the dissociative $S_2(\pi\sigma^*)$ state, along the O–H stretch coordinate [196]. Tseng *et al.* [197] used multimass ion imaging to demonstrate that equivalent H atom loss occurs in isolated phenol following 248 nm and 193 nm excitation.

Ashfold *et al.* [198] employed H (Rydberg) atom photofragment translational spectroscopy (HRA-PTS) to identify two distinct decay mechanisms occurring above and below 248 nm excitation. Exciting between 275.11 nm (the $S_1(\pi\pi^*)$ origin) and 248 nm (the approximate location of the S_2/S_1 CI) produces a bimodal distribution, with a broad peak formed by the release of H atoms as the S_1 state decays into highly vibrationally excited regions of the electronic ground state surface, as shown in Figure 5.3(a). In addition, there are clearly defined vibrational progressions attributed to the vibrational states of the phenoxyl radical (ground state) [199]. Both this feature and the unstructured feature produce angularly isotropic H distributions. Additional experiments on d_5-phenol in the range 275–193.3 nm had similar findings [200]. The mechanism for H atom production, following excitation in the range 275–248 nm was originally assigned as $S_1 \rightarrow S_0^* \rightarrow S_2$ [198]. However, subsequent investigation of the vibrational progressions discovered that the experimental evidence did not support this conclusion. Instead, population reaches dissociation on the S_2 state by tunnelling under the barrier formed by the S_2/S_1 CI (see the shaded red region in Figure 5.2) [175]. At excitation wavelengths approaching 248 nm, the

Figure 5.4: H atom time-resolved signal for the high TKER component, for excitations in the range 275–253 nm. Fitted curves are shown using a Gaussian (cross-correlation) convoluted with two decay components, of 160 fs and 1.2 ns lifetime. Reproduced from Ref. [176].

vibrational progression associated with the $S_1 \rightarrow S_2$ tunnelling process diminishes (see Figure 5.3(b)), although the bimodal distribution is retained. The continued observation of a bimodal H atom distribution suggests that dissociation *via* both the ground state and the $S_2(\pi\sigma^*)$ state continues to occur, while the disappearance of of the vibrations associated with the tunnelling process infers the location of the S_2/S_1 conical intersection. Furthermore, the angular distribution of H atoms produced at $\lambda \leq 248$ nm is anisotropic, suggesting that the ejection process occurs on a timescale significantly faster than the rotational period, in contrast to the isotropic H atom distribution observed when the slower tunnelling process occurs. The vibrational progressions visible in Figure 5.3(c) relate to vibrations on the second $^1\pi\pi^*$ state surface.

5.1.3 Time-resolved spectroscopy of phenol

Stavros *et al.* have examined the dynamics of phenol excited to the $S_1(\pi\pi^*)$ state (below the S_2/S_1 CI) with various amounts of excess energy in the region 275–253 nm [176]. This work used time-resolved imaging to detect H atoms eliminated from the parent molecule on ultrafast timescales. They found two distinct H atom rise times are observed, a fast lifetime (< 160 fs) is attributed to 'Boltzmann-like' statistical H loss on the S_0 surface, while another process forms H atoms with a rise time greater than the maximum measurable 1.2 ns. These lifetimes were invariant with regard to the excitation wavelength used, as presented in Figure 5.4. The invariance in the H atom emission timescales shows that dissociation cannot proceed

Figure 5.5: (a) Surface formed by TRPEI images of phenol excited at 267 nm (300 nm probe). (b) The globally fitted decay associated spectra. Reproduced from Ref. [170].

via a $S_1 \rightarrow S_0{}^* \rightarrow S_2$ mechanism, because higher excitation energies should increase the rate of the first step of this process, in contrast to the observations. In order to clarify, the authors also examined the phenol$^+$ ion signal using the same excitation wavelengths as for the H atom study, they found that the lifetime did decrease as the excitation energy increased, in line with Fermi's Golden Rule. Consequently, it is suggested that the majority of the parent ion formation occurs by dissociation on the ground state surface, while the H atom signal observed arises from some smaller portion of the excited population relaxing rapidly to the $S_1(\upsilon = 0)$ level and subsequently tunnelling directly onto the dissociative S_2 surface *i.e.* without populating the ground state as an intermediate.

In a separate work, the Stavros group have used the same technique to examine the dynamics following direct excitation to the $S_3(\pi\pi^*)$ state (200 nm excitation) [201]. A rapid H atom rise time of 103 fs is observed, presumably arising from rapid relaxation through a S_3/S_2 CI followed by O-H dissociation. This finding is in keeping with the observations of Ashfold *et al.* (Figure 5.3(c)), who observed vibrational progressions in the H atoms ejected following excitation to this state, which implies that the dissociation occurs faster than IVR processes. Further work within the Stavros group examined d_5-phenol excited to the S_3 state (200 nm) [202], finding rise times of 146 fs and 88 fs for the statistical distribution and those originating from dissociation on the $S_2(\pi\sigma^*)$ state, respectively. These timescales are similar to those observed in undeuterated phenol, suggesting large amplitude ring-bending motions do not significantly contribute to these H atom loss mechanisms.

Recently, Townsend *et al.* have used time-resolved photoelectron imaging (TRPEI)

to examine the decay dynamics of phenol and substituted phenols, following excitation to the $S_1(\pi\pi^*)$ state using 267 nm radiation [170]. They find two distinct decay lifetimes (see Figure 5.5), one occurring on a 720 fs timescale and one occurring on a 980 ps timescale. At the chosen excitation wavelength, only the $S_1(\pi\pi^*)$ state is directly accessible, thus both processes must be occurring on this surface. It is concluded that the sub-picosecond decay is due to IVR relaxation within the S_1 state, while the longer lifetime is attributed to tunnelling onto the $S_2(\pi\sigma^*)$ surface. This is broadly in keeping with the work of Stavros *et al.*.

The interest in the dynamics of phenol following UV excitation over the last decade has been considerable. A general consensus on the mechanisms appears to have been reached, following fascinating contributions using a range of complementary techniques. A particular emphasis has been placed on the importance of the H atom tunnelling mechanism where, following excitation to the $S_1(\pi\pi^*)$ state, population transfers into the $S_2(\pi\sigma^*)$ state. In the present work, we observe dynamics of the electronic wavepacket near the onset of this tunnelling process by exciting slightly below and above the S_2/S_1 CI, comparing with the dynamics closer to the $S_1(\pi\pi^*)$ origin. We also examine the dynamics following excitation at higher energies, in the region of the $S_3(\pi\pi^*)$ state, to provide complimentary information to the existing H-atom emission studies.

5.2 Experimental method

In our investigation of the excited state decay dynamics of phenol, we employ the time-resolved photoelectron imaging (TRPEI) technique using the experimental apparatus as described in Chapter 2. The pulsed nozzle is used to generate the molecular beam for the experiments in this chapter (500 Hz repetition rate). Vapourisation of phenol required heating the nozzle to 80 °C, which is possible using heating coils built into the nozzle. Switching the VMI polarity and examining the ion image showed only singly ionised phenol was produced and no detectable cluster formation or fragmentation is observable.

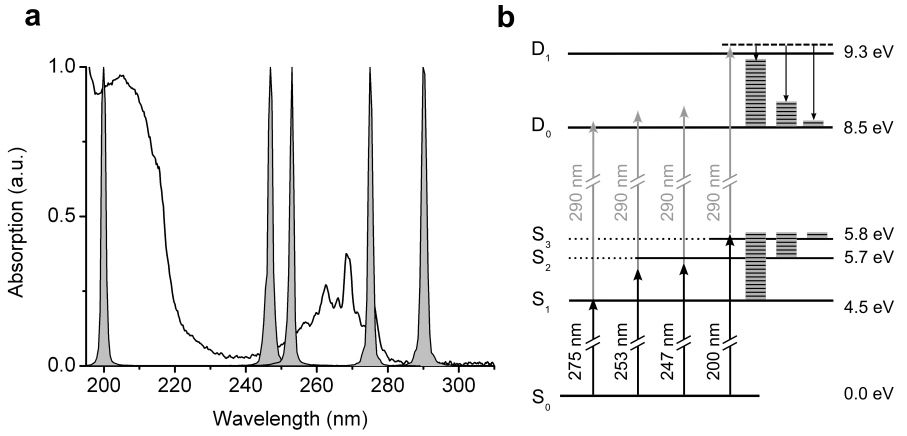

Figure 5.6: (a) Gas-phase UV absorption spectrum of phenol, with pump and probe pulse profiles superimposed. (b) Excitation scheme: phenol is excited using 275 nm (4.51 eV), 253 nm (4.90 eV), 247 nm (5.02 eV), and 200 nm (6.20 eV) pump pulses. The excited state population is projected onto the photoionisation continuum using a delayed 290 nm (4.28 eV) probe pulse. The vibrational energies (blocks of horizontal lines) and corresponding eKEs (downward vertical arrows) are illustrated for 200 nm excitation.

We excited phenol to the $S_1(\pi\pi^*)$ state using 275 nm (4.51 eV), to the $S_2(\pi\sigma^*)$ state using 253 nm (4.90 eV) and 247 nm (5.02 eV) and to the $S_3(\pi\pi^*)$ state using 200 nm (6.20 eV) femtosecond excitation pulses, as shown in Figure 5.6. The excited state population is projected onto the photoionisation continuum using a delayed 290 nm (4.28 eV) femtosecond laser pulse, selected to access as much of the ionisation continuum as possible, whilst avoiding significant S_1–S_0 absorption (see Figure 5.6(a)), thereby reducing background signal. Photoelectron images are then recorded for a series of pump-probe delays between -250–5000 fs.

Photoelectron angular distributions are also obtained *via* our analysis with the pBasex inversion algorithm, producing the anisotropy parameters described in Section 1.2.2. These parameters were found to be isotropic ($|\beta_2| < 0.5$) throughout the energy ranges studied in this chapter, and are therefore not discussed further.

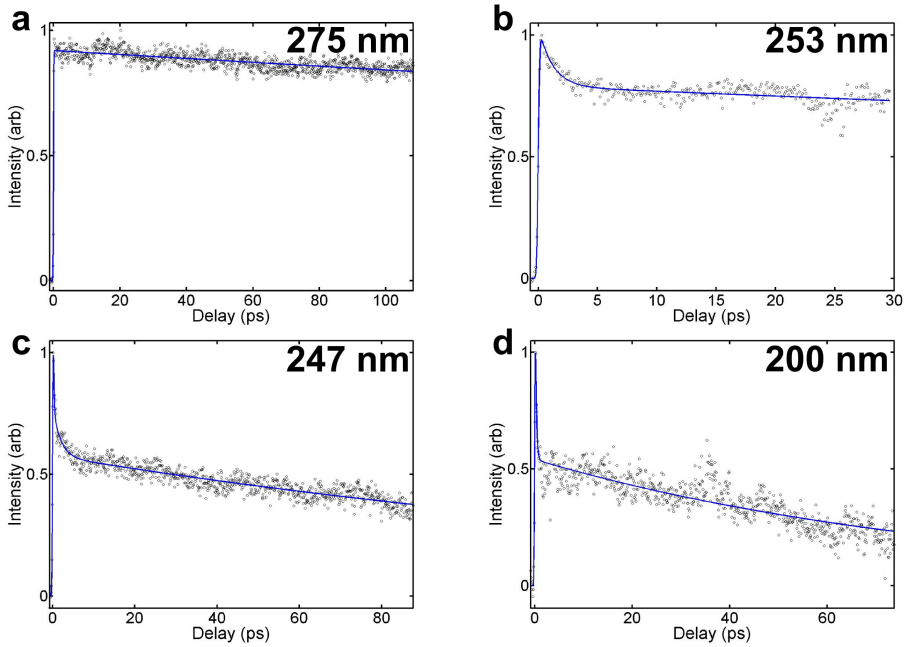

Figure 5.7: Total integrated photoelectron signal decay for phenol, excited at 275 nm (a), 252 nm (b), 247 nm (c) and 200 nm (d).

5.3 TRPEI results for phenol excited in the region 275–200 nm

5.3.1 Total integrated photoelectron signal

The evolution of the total integrated photoelectron signal, following excitation of phenol at 275, 253, 247 and 200 nm, is plotted with respect to the relative delay between pump and probe pulses in Figure 5.7. We fit this data to a sum of exponential decays, convoluted with an instrument function, as described by Equation 2.11. The fit is used to scale the integrated intensity of the photoelectron spectra recorded at each pump-probe delay, as described in Section 2.3, with the resultant surfaces shown in Figure 5.8.

Excitation of phenol at 275 nm occurs close to the S_1 origin and no ultrafast decay of the total photoelectron signal can be discerned. In this case, fitting a single decay

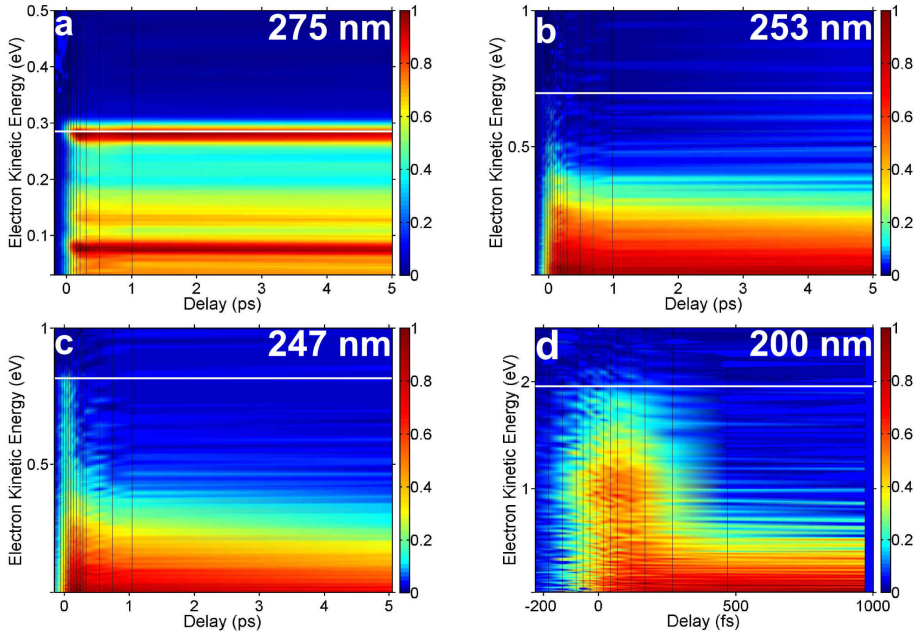

Figure 5.8: Surfaces produced by scaling the photoelectron images of pyrrole to the total photoelectron decays shown in Figure 5.7. Images are shown for 275 nm (a), 253 nm (b), 247 nm (c) and 200 nm (d) excitation wavelengths. Maximum accessible $(1+1')$ eKE are marked for each wavelength by solid white lines. Vertical black lines mark the delay times at which images were collected.

rate (blue line) to Equation 2.11 reproduced the data well, the lifetime fitted is $\tau_1 = 1100 \pm 100$ ps.

For all remaining excitation wavelengths, excitation is near or above the S_2/S_1 CI and we observe dynamics on more than one timescale. While the picosecond lifetime decays can be determined reliably from the total integrated photoelectron fits, the ultrafast timescales are extracted following the procedure in Section 5.3.2. Following 253 nm and 247 nm excitation, two decay lifetimes were necessary to reproduce the data, the longer of which was $\tau_1 = 382 \pm 85$ ps and $\tau_1 = 205 \pm 8$ ps, respectively.

In phenol excited at 200 nm, the $S_3(\pi\pi^*)$ state can be accessed, based upon the absorption spectrum this state is expected to account for much of the initial absorption. At this wavelength, three decay lifetimes were necessary to reproduce the data, the longest of which was $\tau_1 = 88 \pm 5$ ps.

These fits are used to scale the integrated intensity of the photoelectron spectra recorded at specific pump-probe delays (as described in Section 2.3), with the resultant surfaces are shown in Figure 5.8. The maximum accessible electron kinetic energy for a given excitation and probe wavelength is calculated using Equation 2.12. The D_0 of phenol (first ionisation potential) has been determined to be 8.508 eV [194]. Therefore, the maximum accessible electron kinetic energies for our selected pump wavelengths are 0.283 eV for 275 nm, 0.675 eV for 253 nm, 0.794 eV for 247 nm and 1.974 eV for 200 nm (all using 290 nm probe). These energies are marked by solid white lines on Figure 5.8. The second ionisation potential of phenol (D_1) lies at 9.32 eV [147] and is therefore not accessible at any wavelength, except at 200 nm excitation (where the maximum eKE would be 1.15 eV); however no evidence of ionisation to this state is observed in the photoelectron spectra.

5.3.2 Decay lifetimes

We extract the sub-picosecond lifetimes by integrating over limited energy regions of the photoelectron spectra for each time delay, and fitting an appropriate number of decay lifetimes to Equation 2.11. We usually fit the highest energy feature of the photoelectron spectrum, then move systematically towards the lowest energy feature. This is because the highest energy component is not usually as heavily overlapped with the other components, and is therefore a better candidate for extracting the cross-correlation and zero delay position (as well as the decay lifetime of the peak in question). However, in phenol the features are heavily overlapped and instead we select the most intense peak to be fitted first.

Following 275 nm excitation in phenol, we do not observe any ultrafast decays and therefore additional fitting was not required. The decay lifetime of $\tau_1 = 1100$ ps was extracted in the previous section and Figure 5.9(a) shows an excellent match to the spectrum integrated over the range 0.03–0.3 eV.

For phenol excited at 253 nm, a lifetime of $\tau_1 = 382$ ps was extracted from the total integrated photoelectron decay fit. This lifetime was fixed and included in

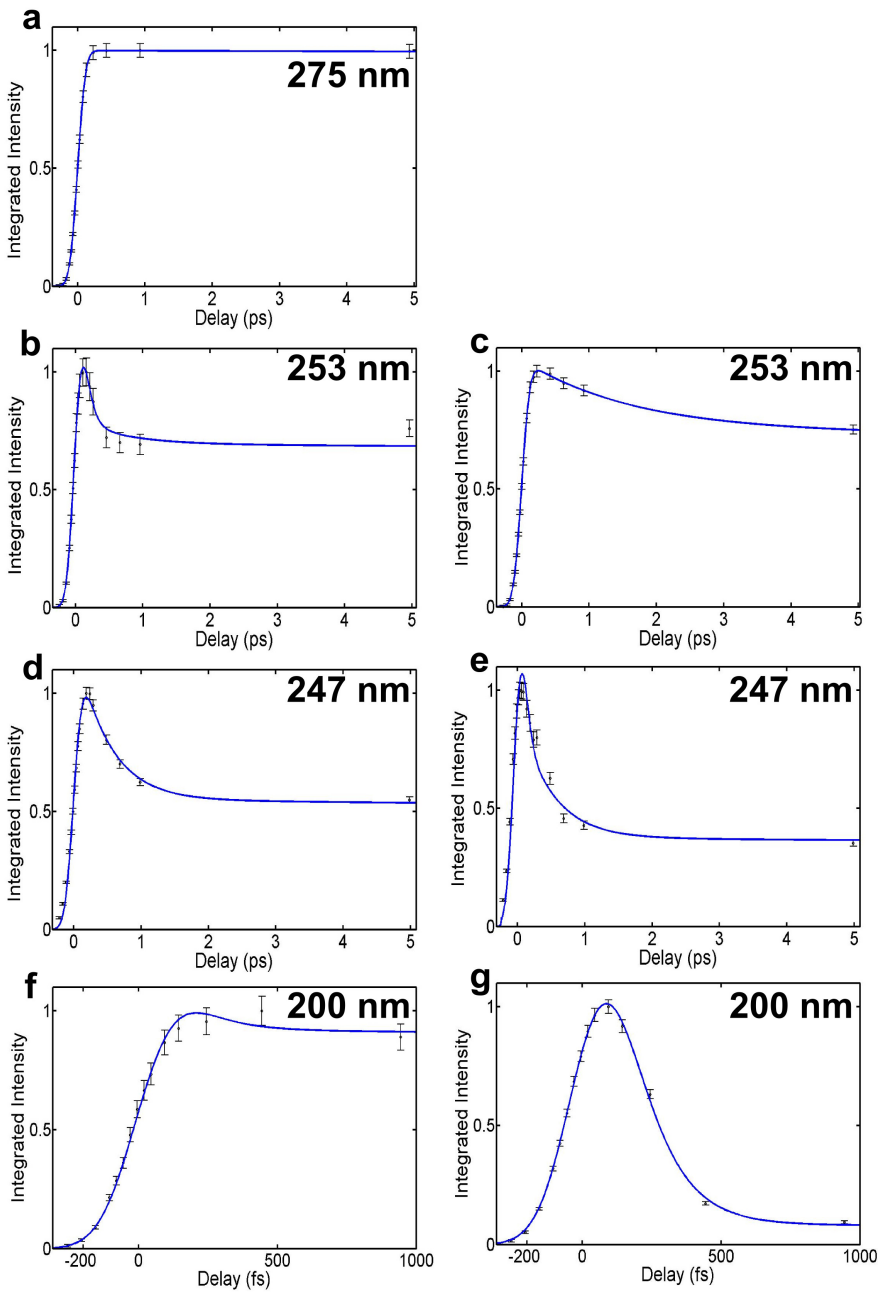

Figure 5.9: Fits to the photoelectron spectra integrated over discrete regions, used to obtain the lifetimes shown in Table 5.1. Fits are shown for integrations over the energy region 0.03–0.3 eV region for 275 nm (a), 253 nm (b) and 247 nm (d), over 0.2–0.45 eV region for 200 nm (f). A range of 0.35–0.8 eV was used for the integration of the 253 nm (c), 247 nm (e) data and 0.9–1.9 eV for the 200 nm data (g). Error bars are obtained from the (2σ) standard deviation in photoelectron intensity over the integrated region.

Table 5.1: Summary of phenol exponential decay lifetimes

Pump wavelength [nm]	τ_1 [ps]	τ_2 [fs]	τ_3 [fs]	τ_4 [fs]	Cross-correlation (FWHM) [fs]
275	1100 ± 100	-	-	-	207 ± 12
253	382 ± 85	692 ± 76	< 50	-	218 ± 10
247	205 ± 8	481 ± 119	< 50	-	239 ± 17
200	88 ± 5	-	-	124 ± 10	257 ± 10

all further fits at this wavelength. The cross-correlation and an additional lifetime were extracted by fitting over the range 0.03–0.3 eV (Figure 5.9(b)). The fitted cross-correlation FWHM was 218 ± 10 fs and a decay lifetime of $\tau_2 = 692 \pm 76$ fs was obtained. Fitting a third decay lifetime across the region 0.35–0.8 eV produces an additional (weak) lifetime of $\tau_3 < 50$ fs (Figure 5.9(c)).

The analysis of the 247 nm excitation followed the same procedure (and integration ranges) described in the previous paragraph and using the $\tau_1 = 205$ ps lifetime extracted from the total integrated decay. A cross-correlation FWHM of 218 ± 17 fs and decay lifetime of $\tau_2 = 481 \pm 119$ fs were extracted by integrating over the range 0.03–0.3 eV (Figure 5.9(d)). A further (weak) ultrafast lifetime of $\tau_3 < 50$ fs was observed by integrating over the range 0.35–0.8 eV (Figure 5.9(e)).

In phenol, 200 nm excitation is sufficient to access the $S_3(\pi\pi^*)$ state, leading to the intense peak observed in the region eKE > 1 eV of Figure 5.8(c). Using the $\tau_1 = 88$ ps obtained from the total integrated signal. Integrating over the region 0.9–1.9 eV, determined the instrument function FWHM to be 257 ± 10 fs and a further lifetime of $\tau_4 = 124 \pm 10$ fs (Figure 5.9(f)). Integrating over the eKE range 0.2–0.45 eV did not observe any further decay lifetime components (Figure 5.9(g)). The fact that these two decay components describe the data well suggests that the states associated with τ_2 and τ_3 components are not significant following 200 nm excitation.

The results are are summarised in Table 5.1.

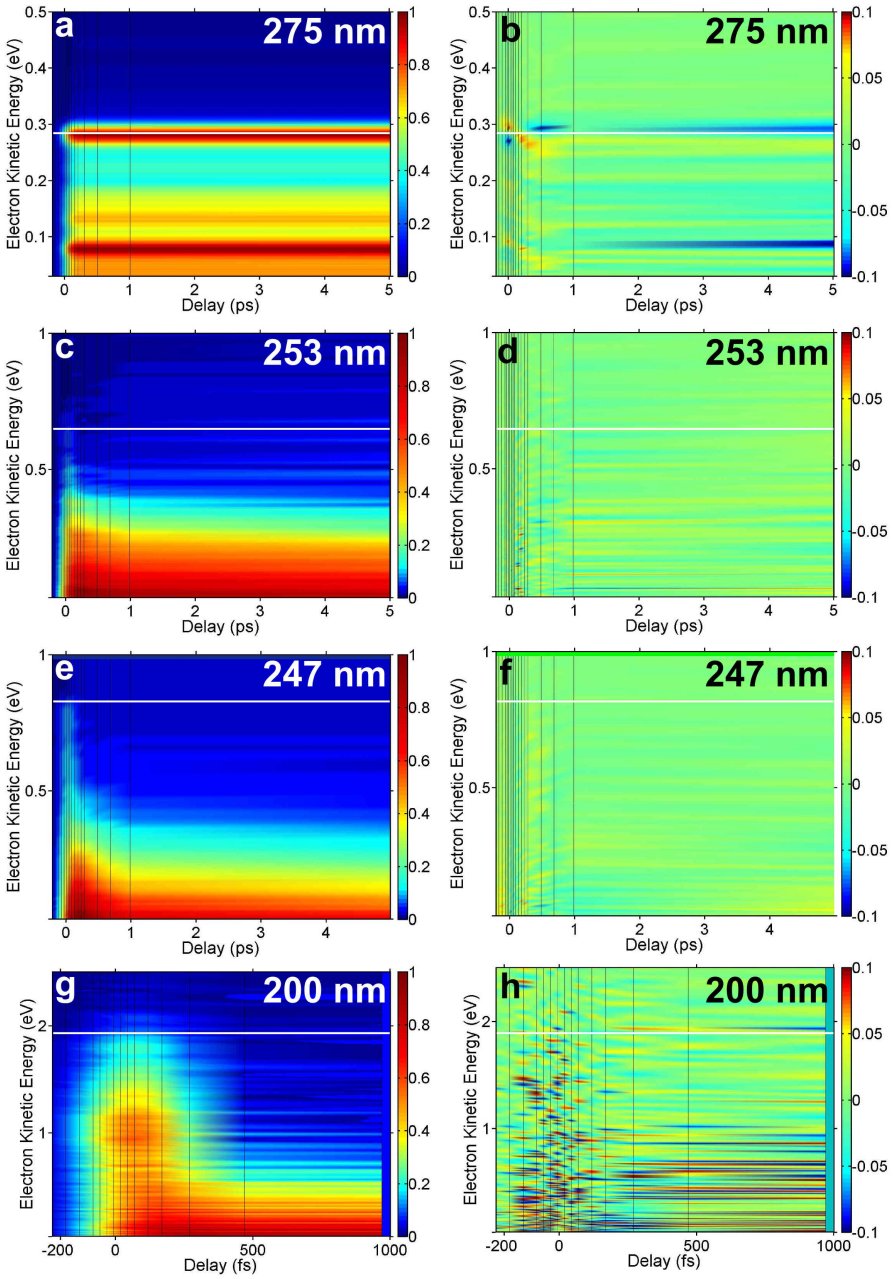

Figure 5.10: Fitted surfaces, using lifetimes detailed in Table 5.1. Surfaces are shown for 275 nm (a), 253 nm (c), 247 nm (e) and 200 nm (g) pump wavelengths. Residuals of the fit subtracted from the experimental data are shown for 275 nm (b), 253 nm (d), 247 nm (f) and 200 nm (h) pump wavelengths. Maximum accessible $(1 + 1')$ eKE are marked for each wavelength by solid white lines.

5.3.3 Global fitting

Our quasi-global fitting procedure (described in Section 2.3.2) uses the lifetimes obtained above, but examines their relative contribution across the eKE range. The

time-resolved photoelectron spectra can be reconstructed using the timescales, τ_i, determined in Section 5.3.2 and fitted coefficients, c_i(eKE).

The surface and residual generated by applying the quasi-global fitting procedure to our data for phenol following 275 nm excitation are shown in Figure 5.10(a) and (b), respectively. Examining the DAS in Figure 5.11(a) shows that only a single lifetime is observed and consequently the state associated with this lifetime must be populated directly. The DAS peak shapes show that this long-lived state displays several sharp vibrational peaks, separated by 0.202 eV, which are attribute to vibrational progressions on the D_0 state. Importantly, we do not observe evidence for a significant change in peak shape with respect to time, such as might be expected if IVR processes were present. These observations are consistent with excitation close to the origin of the $S_1(\pi\pi^*)$ state. Figure 5.11(b) shows that because the only decay lifetime observed at this wavelength is 1.1 ns, a negligible proportion of the photoelectron signal decays in the first 6 ps. A slight decay in the photoelectron signal does appear at short delays, however no corresponding change in the photoelectron spectrum is observed and we therefore believe this apparent peak is due to noise rather than a real decay in signal.

The surfaces obtained for our data following 253 nm excitation are shown in Figure 5.10(c) and (d) and show the presence of a broad peak at eKE < 0.6 eV, similar to that observed at 275 nm excitation although the vibrational structure can no longer be discerned. The DAS (Figure 5.11(c)) shows that three distinct decay lifetimes are discernible, but no significant negative coefficients are observed, suggesting that all three components are populated directly upon excitation. However, the τ_1 and τ_2 components are completely overlapped with respect to eKE, making it impossible to infer whether population transfer is occurring between the states associated with these components. At this wavelength, the signal associated with the τ_1 component is dominant, which given its long decay lifetime is likely to relate to the $S_1(\pi\pi^*)$ state. Figure 5.11(d) shows that approximately 60% of the total photoelectron signal decays out of our observation window within 3 ps due to the decay of τ_3 and τ_2 components, with the other population remaining in the state associated with the τ_1 component.

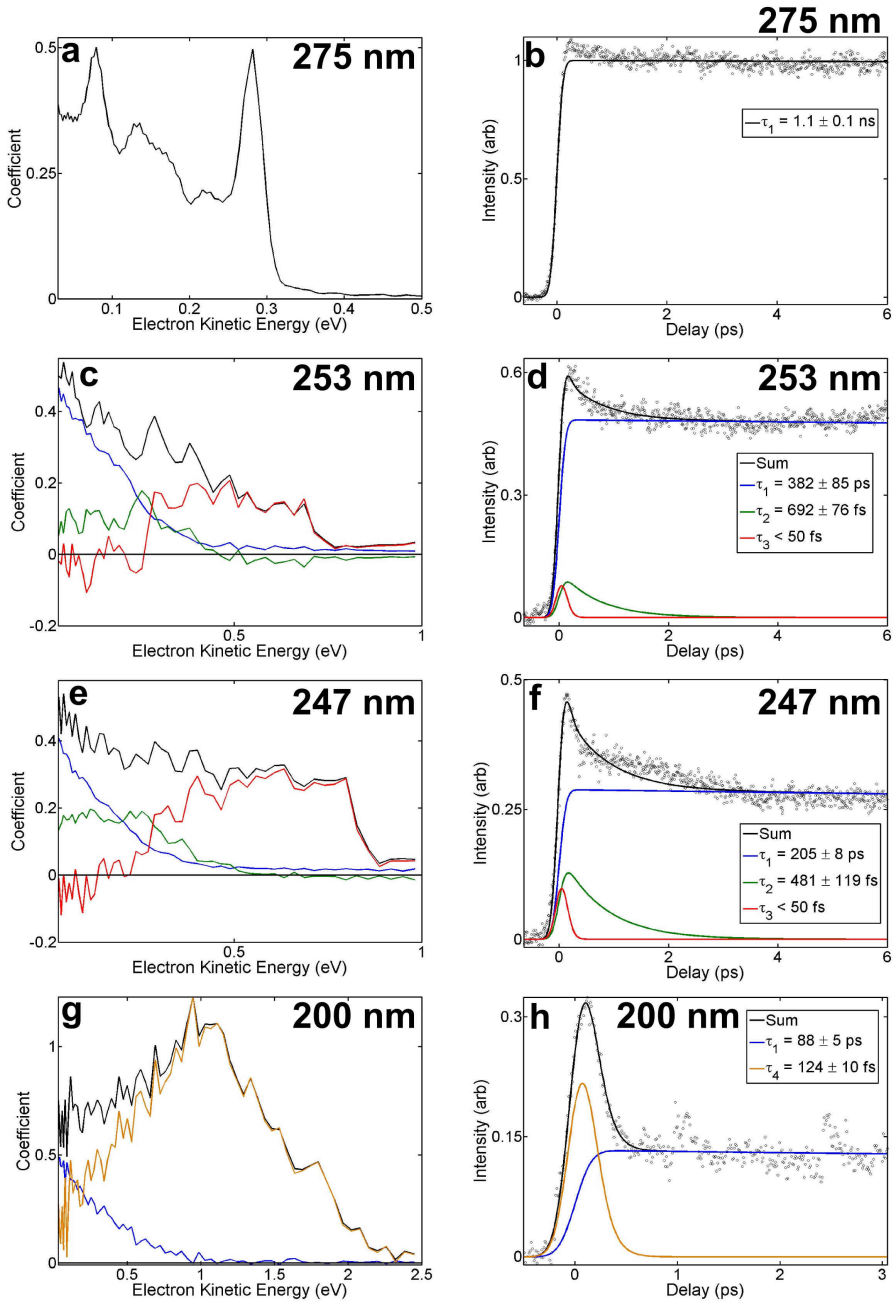

Figure 5.11: Decay associated spectra relating to the surfaces shown in Figure 5.10 are shown for 275 nm (a), 253 nm (c), 247 nm (e) and 200 nm (g) pump wavelengths. Refitting using the same lifetimes to the total integrated decay data presented in Figure 5.7 are also shown for 275 nm (b), 253 nm (d), 247 nm (f) and 200 nm (h) pump wavelengths, where these plots are normalised such that $\sum_i c_i = 1$, excluding states which feed other states that we observe. This has the consequence that the limit of the long lived state indicates the approximate proportion of the initially excited wavepacket remaining in the S_1 state after several picoseconds.

Similar to the data in the previous paragraph, the fitted surface and residual for the 247 nm excitation of phenol are presented in Figure 5.10(e) and (f), respectively. Furthermore, the nature and lifetimes of the peaks observed at 253 nm excitation are similar to those visible following exciting at 247 nm. The eKE ranges of the various decay components in the DAS (Figure 5.11(e)) and implications regarding evolution of the excited wavepacket are also analogous to the data collected at 253 nm excitation: no significant negative coefficients are observed, but we cannot exclude population transfer, due the overlap between components. The relative contributions of the τ_1 and τ_2 components seems analogous to that observed at 253 nm excitation, however the relative contribution of the τ_3 component appears stronger following 247 nm excitation. Figure 5.11(f) shows that approximately 75% of the total photoelectron signal decays out of our observation window within 3 ps, which is a slightly higher than observed following 253 nm excitation and would imply that the decay of the state associated with the τ_3 component does not transfer population into any other state we can observe.

The surfaces produced following 200 nm excitation are shown in Figure 5.10(g), and again a broad peak at eKE < 0.6 eV is visible, as observed at the other excitation wavelengths studied in this work. However, following 200 nm excitation an additional symmetric peak is observable across the eKE range, up to 2.0 eV. The DAS in Figure 5.11(g) show no evidence of the τ_2 or τ_3 components observed following 253 and 247 nm excitation and although a long lived τ_1 component is visible and has a similar spectral profile to those observed at longer wavelengths, the τ_4 component dominates the decay dynamics at this wavelength. No negative coefficients are observed for any eKE, but we cannot exclude the possibility of population transfer due the overlap between components. Figure 5.11(h) shows that approximately 85% of the total photoelectron signal decays out of our observation window within 2 ps, given that the state associated with the τ_1 component is long lived it is reasonable to believe that this is attributable to the decay of τ_4 component.

5.4 Discussion

5.4.1 $S_1(\pi\pi^*)$ decay

Following irradiation at 275 nm, population is excited close to the origin of the $S_1(\pi\pi^*)$ state in phenol. We observe population in several vibrational states due to the relatively broad spectral range of our excitation pulse (FWHM ∼1 nm, see Figure 5.6(a)), and we see that these vibrational states all remain populated over the entire observable temporal window (Figure 5.10(a)), decaying with a single lifetime of $\tau_1 = 1.1$ ns. Sur *et al.* [177] found that the dominant decay mechanism in the $S_1(\pi\pi^*)$ state of phenol is internal conversion to the ground state, rather than ISC to triplet states. They also found a fluorescence lifetime of 2 ns, which is in reasonable agreement with our observed decay lifetime of 1.1 ns.

Upon increasing the excitation energy, the vibrational resolution observed at 275 nm excitation disappears and the decay lifetime of this spectral component reduces to tens or hundreds of picoseconds. We find that this picosecond decay lifetime associated with the 0–0.3 eV spectral region decreases with increasing excitation energy, which is consistent with an internal conversion process because the density of states increases higher in the vibrational manifold, leading to more efficient coupling between the electronic states (Fermi's Golden Rule). We observe this picosecond spectral component at all wavelengths used in this study and believe it relates to population in the $S_1(\pi\pi^*)$ state. We also note that the intensity of this component is significantly diminished following 200 nm excitation, which would be expected of the $S_1(\pi\pi^*)$ state, because the absorption cross-section is expected to be very low in this region (see the absorption spectrum of phenol, Figure 5.1). We therefore conclude that the observed population in this S_1 state following 200 nm excitation must occur by coupling with higher lying states, as we do not observe a discernible rise time.

Our findings are also in good agreement with the work of Townsend *et al.* [170] who observe a 980 ps lifetime when exciting to the $S_1(\pi\pi^*)$ with 267 nm light. This

observation lies between the decay lifetimes we observe following 253 and 275 nm excitation and thus, is in keeping with the trend we observe.

Stavros *et al.* [176] observe a longer H atom rise time (> 1.2 ns), which remains constant for all excitation wavelengths in the range 275–253 nm. We do not observe an equivalent, wavelength-independent timescale, however the authors of this work acknowledge that the H atom loss mechanism is likely to be a minority decay pathway below the S_2/S_1 CI. Indeed, when these authors examine the decay of the phenol parent ion, lifetimes of 1.9 and 0.9 ns emerge at 275 and 258 nm excitation, respectively, broadly in keeping with the trend we observe. Our measurements are sensitive to the processes that give rise to these changes in the phenol$^+$ signal (in the vFC region), rather than those relating to the formation of H atoms.

At 275 nm excitation, we observe a single decay lifetime. However, at 253 and 247 nm excitation we find an additional, sub-picosecond, decay lifetime (τ_2). This agrees with the findings of Townsend *et al.*, who observe an analogous 720 fs decay attributed to IVR occurring on the $S_1(\pi\pi^*)$ surface. We agree with this assignment and find this interpretation to be consistent with our findings.

Finally, Stavros *et al.* [176] observe a weak H atom signal at all wavelengths in the range 275–253 nm, rising on a timescale of < 160 fs. This is associated with 'statistical' dissociation of phenol *via* the ground state surface. We do not observe a relaxation process which could return population to the ground state quickly enough to explain such a fast dissociation lifetime.

5.4.2 $S_2(\pi\sigma^*)$ decay

As described in the introduction to this chapter, Ashfold *et al.* [175] found that the CI linking the $S_1(\pi\pi^*)$ and the $S_2(\pi\sigma^*)$ states occurs at roughly 248 nm. In the current study, the excitation wavelengths 253 nm and 247 nm were selected to be slightly below and above this CI, respectively. We expected that the decay lifetime associated with the transfer of population onto the S_2 state would be slower at 253 nm excitation due to the necessary tunnelling motion, whereas at 247 nm excitation this transfer

ought to be barrierless and therefore significantly faster. Another reason for selecting 253 nm excitation was for comparison with the experiments of Stavros *et al.* [176] who examined H atom loss attributed to tunnelling into the S_2 state.

Interestingly, the ultrafast dynamics we observe at both 253 and 247 nm are extremely similar, with three decay lifetimes observed, the picosecond timescale τ_1, along with $\tau_2 \sim 600$ fs and $\tau_3 < 50$ fs. As described above, we attribute the τ_1 component to the dominant IC from $S_1(\pi\pi^*)$ to the ground state and the τ_2 component to IVR processes within the $S_1(\pi\pi^*)$ state. Despite the expectation that a new rapid decay pathway into the $S_2(\pi\sigma^*)$ state should open between 253 and 247 nm, such behaviour is not observed in our results. Instead, we observe a sub-50 fs lifetime with low intensity (at both wavelengths). Furthermore, the eKE range at which the τ_3 is observed cannot relate to population in the $S_1(\pi\pi^*)$ state (see Figure 5.11(c,e)). The contribution of this component is considerably weaker when exciting at 253 nm, compared to 247 nm excitation. This leads us to attribute the τ_3 component to population on the $S_2(\pi\sigma^*)$ state, either excited directly or populated by coupling to the S_1 state on a timescale much faster than our cross-correlation. Although direct excitation to the S_2 state is has not been previously reported in phenol, such a process is not unprecedented [152, 169]. The observation of direct excitation to this state at 253 nm is surprising, given that previous work has predicted the onset of the S_2/S_1 CI at 248 nm. However, we note that a sharp onset was not found, rather a gradual loss of observable $S_1(\pi\pi^*)$ vibrational modes. Given that the bandwidth of our excitation pulse is $\sim$1 nm (FWHM), we believe that the S_2/S_1 CI is likely to to be accessible at $\lambda \lesssim 252.5$ nm.

The contribution of the $\pi 3s$ component of the $S_2(\pi\sigma^*)$ state is expected to be weak in phenol (especially compared to aniline or pyrrole) and no bound vibrational states have been observed. Consequently, the sharp spectral peak (and the associated anisotropy) relating to this $\pi 3s$ component, as observed in aniline, would not necessarily be expected to be observed in phenol. Indeed, no such feature is observed in the current study.

5.4.3 $S_3(\pi\pi^*)$ decay

Following 200 nm excitation, we observe an ultrafast decay lifetime of 124 fs (τ_4) associated with a high eKE region (0.3–2.2 eV), in addition to the slow $S_1(\pi\pi^*)$ decay (τ_1 = 88 ps at 200 nm) discussed above. Figure 5.11(h) shows that 85% of the originally excited photoelectron signal decays within 1 ps, consequently this proportion must relate to decay of the τ_4 component. The eKE range of the τ_4 feature suggests that it is associated with rapid decay from the $S_3(\pi\pi^*)$ state. This is in keeping with the absorption spectrum, shown in Figure 5.6(a), where the S_3 state accounts for the majority of the strong absorption peak centered on 205 nm. The decay of the τ_4 component is not associated with any negative coefficients in the DAS (Figure 5.11(g)), suggesting that the population excited to this state leaves our observation window on the 124 fs timescale.

At 200 nm excitation, Stavros *et al.* [201] observed H atom emission with a rise time of 103 fs, which closely matches the decay lifetime we observe. It is therefore likely that this decay lifetime is associated with rapid relaxation through a S_3/S_2 CI, with subsequent dissociation occurring following propagation on the $S_2(\pi\sigma^*)$ surface. However, we note that because the population leaves our observation window, we cannot fully differentiate between dissociation, relaxation back to the ground state surface, or both. However, we note that the 124 fs decay observed in phenol is significantly longer than the equivalent excitation observed in aniline (see Section 4.3.3), where the 50 fs decay was attributed to rapid relaxation directly to the ground state *via* CIs coupled by out of plane, prefulvenic motions. The theoretical studies of the phenol excited states have typically focussed on the S_1 and S_2 states, so no analogous decay mechanism has been proposed for the $S_3(\pi\pi^*)$ state of phenol. We do not observe evidence for a similar, direct relaxation mechanism to the ground state occurring in phenol, but cannot exclude such a mechanism without support of further theoretical work.

Additionally, we note that no component associated with direct S_2 excitation is observed following 200 nm excitation. This is presumably because direct absorption to the S_2 state is naturally very low. Indeed, the excitations observed at longer

wavelengths are only possible due to coupling to the $S_1(\pi\pi^*)$ state, absorption to which is also greatly reduced at this wavelength.

5.5 Conclusion

Our time-resolved photoelectron imaging study has examined phenol, following excitation in the region 275–200 nm. Our experiments and analysis have provided detailed information about the relaxation mechanisms of this biologically important chromophore and our proposed scheme is summarised in Figure 5.12. Our observations are in excellent agreement with the findings of the existing TRPES study and many of the conclusions drawn following H atom photofragment translational spectroscopy studies by various groups.

Our results show that internal conversion to the ground state from the S_1 state appears to be the dominant relaxation mechanism, in keeping with previous experimental and theoretical studies. Furthermore, when exciting with greater excess vibrational energy in this state, we observe IVR processes, in addition to increasingly rapid IC to the ground state. We do not observe evidence for tunnelling onto the dissociative S_2 state, however we expect this mechanism to be a minority pathway and instead suggest that our technique is simply not sensitive enough to resolve this signature.

When exciting with higher energies, close to the S_1/S_2 CI, we find the first evidence for direct excitation to the $S_2(\pi\sigma^*)$. This signal decays on a sub-50 fs timescale, presumably leading to dissociation on the S_2 state surface. The low intensity of this signature, comprising less than 10% of the total photoelectron signal, leads us to believe that the majority of population continues to be excited to the S_1 state, which primarily decays to the ground state by internal conversion. Previous work [175, 198] has found that this S_1/S_2 CI is accessible at wavelengths $\lambda < 248$ nm. However, we find the transfer dynamics to the S_2 state effectively unchanged when exciting at 253 nm, suggesting that this conical intersection may be accessible at lower energies than previously anticipated.

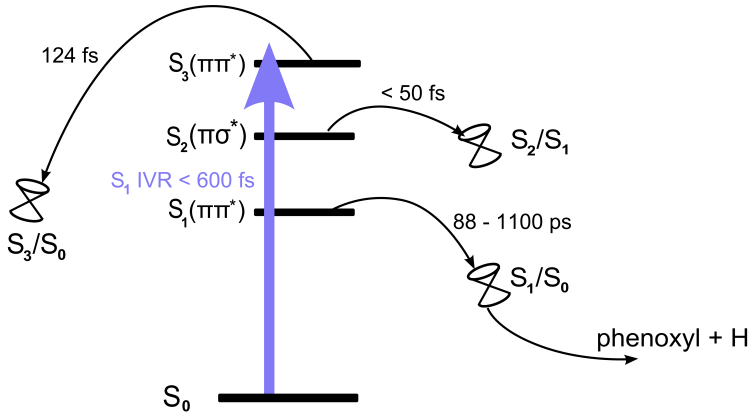

Figure 5.12: Schematic diagram of the proposed non-radiative decay pathways in phenol, along with the associated timescales.

Following excitation to the S_3 state, we observe rapid relaxation of this state. This population leaves our observation window in 124 fs, which closely matches the H atom formation lifetime observed in the literature [201]. The observation of It is likely that some of this relates to IC onto the S_2 surface followed by extremely rapid dissociation.

Chapter 6

Concluding remarks

The work of Sobolewski *et al.* [10] has stimulated a great deal of interest in the community regarding the mechanisms surrounding the non-radiative decay of prototypical molecules containing OH and NH groups. The description of a paradigm for the photostability of biomolecules, based upon detailed theoretical studies of the excited state potential energy surfaces, is a powerful and attractive concept. The studies which comprise this thesis provide additional insight into the action of these mixed Rydberg-valence character excited states and their ability to couple singlet states.

In pyrrole, it was found that electronic relaxation from the $S_1(\pi\sigma^*)$ state proceeds to completion on a sub-50 fs timescale for all wavelengths studied. When exciting to the $S_1(\pi\sigma^*)$ state, we find no evidence of trapping in the bound well in the vFC region, even when exciting close the state origin. Indeed, it is believed that virtually all of the $S_1(\pi\sigma^*)$ state population proceeds to H atom dissociation. However it is possible that trapping does occur in the region of the S_1/S_0 CI. Excitation to the $S_2(\pi\pi^*)$ state may allow a higher fraction to non-radiatively relax back to the ground state.

In aniline, it was found that excitation to the $S_3(\pi\pi^*)$ state results in ultrafast relaxation back to the ground state, without populating either of the lower lying singlet states. Subsequent theoretical modelling has found that the S_3 state is unbound in the prefulvene-like ring bending dimensions and the dissociative potential experienced can couple back to the ground state *via* a three-state conical intersection [160]. Direct excitation to the $S_2(\pi\sigma^*)$ state was found to result in two distinct non-radiative decay channels, one involving very rapid relaxation onto the $S_1(\pi\pi^*)$ state, with subsequent internal conversion back to the ground state. The other, weaker channel involving IVR on the $S_2(\pi\sigma^*)$ surface.

In phenol, excitations to the $S_1(\pi\pi^*)$ state were predominantly found to decay back to the ground state, by internal conversion, and no additional evidence was observed for the tunnelling mechanism which leads to the formation of phenoyl radicals by O-H dissociation [175]. Excitation above the onset of the $S_2(\pi\sigma^*)$ state does not predominantly couple onto the S_2 state surface, instead relaxing by IVR on the S_1

potential. However, excitation into $S_3(\pi\pi^*)$ state does induce ultrafast relaxation onto the S_2 state, with subsequent H atom loss.

These studies have shown that $\pi\sigma^*$ states are often involved in the ultrafast relaxation process, however a surprising variety is found in the mechanisms these states can facilitate, even in closely related molecules. Building a comprehensive understanding of the UV induced photodynamics occurring in complex biomolecules, requires continued study of each constituent chromophore present, as well as their interaction with one another and solvent induced effects [203].

The TRPEI technique used in this thesis is typically limited by the observation window enabled by the probe wavelength, if the photoexcited population moves to a region of the potential energy surface which can no longer be ionised by the probe wavelength, then no photoelectron signal is observed. Ideally, the observation window can be extended through the application of higher energy probe photons, allowing us to monitor the formation of dissociation products or the return of population to the electronic ground state. Such developments would greatly enhance our ability to monitor and identify relaxation mechanisms from excitation to completion, however development of the necessary experimental equipment is complex and the associated analysis is also difficult, primarily due to the large background produced when ionisation of the ground state is possible. Nevertheless, these studies have been shown to be possible [41, 204] and we suggest that pyrrole would make an interesting study system, as previous studies have identified multiple decay products following UV excitation, but the current study resolves only a single decay lifetime.

The pyrrole dimer was used as a model of microsolvation and used to examine the effect on relaxation dynamics. We found that some of the diffuse orbitals associated with the $\pi\sigma^*$, Rydberg states are stabilised by the proximity of the partner molecule, forming low energy charge-transfer states, which facilitate new relaxation mechanisms. These pathways suggest that, in some energy ranges, solvation can inhibit the formation of pyrrolyl radicals by N-H dissocation and consequently improve photostability in this common biological chromophore.

Bridging the gap between gas phase relaxation dynamics and those occurring in

the solution phase is of great interest for both experimental and theoretical studies, particularly when studying biologically related molecules. Gas phase studies allow for much greater resolution of individual states, without the spectral broadening typically present when molecules are solvated, however much of biological chemistry occurs in the solution phase. This contrast is particularly important when examining molecules with low lying $\pi 3s/\pi\sigma^*$ states, because the shape of this potential energy surface is highly sensitive to the relative stabilisations of $3s$ and σ^* components. Some impressive work has been carried out to this end [3, 144], but the relationship between behaviour in both phases remains relatively unexplored due to the high complexity. We have approached the problem in our study of pyrrole, using the dimer as a model of microsolvation to examine the opening of new decay pathways. However, further work is necessary to extend this understanding further towards complete aqueous solvation.

In recent years, the TRPEI technique has been extended to study the solution phase dynamics dynamics, by replacing the molecular gas beam with a liquid microjet [41, 205]. In such an arrangement, solution is forced through a nozzle inside the high vacuum chamber to produce a laminar jet of $\sim$30 μm diameter or less, which extends for several millimetres. The liquid jet in this laminar region can be probed in the usual fashion. Our group is currently working to construct a liquid-jet TRPEI detection chamber, which will provide a fantastic means of directly comparing excited state dynamics in the gas and solution phases, using the TRPEI technique in both cases.

References

[1]F. R. de Gruijl, "Skin cancer and solar UV radiation", Eur. J. Cancer **35**, 2003–2009 (1999).

[2]M. Ichihashi, M. Ueda, A. Budiyanto, T. Bito, M. Oka, M. Fukunaga, K. Tsuru, and T. Horikawa, "UV-induced skin damage", Toxicology **189**, 21–39 (2003).

[3]C. E. Crespo-Hernández, B. Cohen, P. M. Hare, and B. Kohler, "Ultrafast excited-state dynamics in nucleic acids", Chem. Rev. **104**, 1977–2020 (2004).

[4]C. Z. Bisgaard, H. Satzger, S. Ullrich, and A. Stolow, "Excited-state dynamics of isolated DNA bases: a case study of adenine", Chem. Phys. Chem. **10**, 101–110 (2009).

[5]A. Iqbal and V. G. Stavros, "Active participation of $^1\pi\sigma^*$ states in the photodissociation of tyrosine and its subunits", J. Phys. Chem. Lett. **1**, 2274–2278 (2010).

[6]H. Satzger, D. Townsend, M. Z. Zgierski, S. Patchkovskii, S. Ullrich, and A. Stolow, "Primary processes underlying the photostability of isolated DNA bases: adenine", P. Natl. Acad. Sci. USA **103**, 10196–10201 (2006).

[7]A. L. Sobolewski, W. Domcke, and C. Hättig, "Tautomeric selectivity of the excited-state lifetime of guanine/cytosine base pairs: the role of electron-driven proton-transfer processes", P. Natl. Acad. Sci. USA **102**, 17903–17906 (2005).

[8]C. T. Middleton, K. de La Harpe, C. Su, Y. K. Law, C. E. Crespo-Hernández, and B. Kohler, "DNA excited-state dynamics: from single bases to the double helix", Annu. Rev. Phys. Chem. **60**, 217–239 (2009).

[9]H. Reisler and A. I. Krylov, "Interacting Rydberg and valence states in radicals and molecules: experimental and theoretical studies", Int. Rev. Phys. Chem. **28**, 267–308 (2009).

[10]A. L. Sobolewski, W. Domcke, C. Dedonder-Lardeux, and C. Jouvet, "Excited-state hydrogen detachment and hydrogen transfer driven by repulsive $^1\pi\sigma^*$ states: a new paradigm for nonradiative decay in aromatic biomolecules", Phys. Chem. Chem. Phys. **4**, 1093–1100 (2002).

[11]M. N. R. Ashfold, G. A. King, D. Murdock, M. G. D. Nix, T. A. A. Oliver, and A. G. Sage, "$\pi\sigma^*$ excited states in molecular photochemistry.", Phys. Chem. Chem. Phys. **12**, 1218–1238 (2010).

[12]M. Staniforth and V. G. Stavros, "Recent advances in experimental techniques to probe fast excited-state dynamics in biological molecules in the gas phase: dynamics in nucleotides, amino acids and beyond", Proc. Roy. Soc. A **469**, 0458 (2013).

[13]M. Bixon and J. Jortner, "Intramolecular radiationless transitions", J. Chem. Phys. **48**, 715–726 (1968).

[14]J. Jortner, S. A. Rice, and R. M. Hochstrasser, "Radiationless transitions in photochemistry", in *Advances in photochemistry* (John Wiley & Sons, Inc., 2007), pp. 149–309.

[15]J. Franck and E. G. Dymond, "Elementary processes of photochemical reactions", Trans. Faraday Soc. **21**, 536–542 (1926).

[16]W. A. Noyes, "The correlation of spectroscopy and photochemistry", Rev. Mod. Phys. **5**, 280–287 (1933).

[17]M. Kasha, "Characterization of electronic transitions in complex molecules", Discuss. Faraday Soc. **9**, 14–19 (1950).

[18]M. Born and R. Oppenheimer, "Zur quantentheorie der molekeln", Ann. Phys. **389**, 457–484 (1927).

[19]P. Atkins and R. Friedman, *Molecular quantum mechanics*, 4th Edition (Oxford University Press, USA, 2005).

[20]F. Jensen, *Introduction to computational chemistry*, 2nd Edition (Wiley, 2006).

[21]G. A. Worth and L. S. Cederbaum, "Beyond Born-Oppenheimer: molecular dynamics through a conical intersection", Annu. Rev. Phys. Chem. **55**, 127–158 (2004).

[22]L. J. Butler, "Chemical reaction dynamics beyond the Born-Oppenheimer approximation", Annu. Rev. Phys. Chem. **49**, 125–171 (1998).

[23]S. Matsika and P. D. Krause, "Nonadiabatic events and conical intersections", Annu. Rev. Phys. Chem. **62**, 621–643 (2011).

[24]B. Dick, Y. Haas, and S. Zilberg, "Locating conical intersections relevant to photochemical reactions", Chem. Phys. **347**, 65–77 (2008).

[25]L. S. Cederbaum, H. Köppel, and W. Domcke, "Multimode vibronic coupling effects in molecules", Int. J. Quantum Chem. **20**, 251–267 (1981).

[26]W. Radloff, V. Stert, T. Freudenberg, I. V. Hertel, C. Jouvet, C. Dedonder-Lardeux, and D. Solgadi, "Internal conversion in highly excited benzene and benzene dimer: femtosecond time-resolved photoelectron spectroscopy", Chem. Phys. Lett. **281**, 20–26 (1997).

[27]P. Krause, S. Matsika, M. Kotur, and T. Weinacht, "The influence of excited state topology on wavepacket delocalization in the relaxation of photoexcited polyatomic molecules", J. Chem. Phys. **137**, 22A537 (2012).

[28]E. U. Condon, "A theory of intensity distribution in band systems", Phys. Rev. **28**, 1182–1201 (1926).

[29]E. U. Condon, "Nuclear motions associated with electron transitions in diatomic molecules", Phys. Rev. **32**, 858–872 (1928).

[30]A. S. Coolidge, H. M. James, and R. D. Present, "A study of the Franck-Condon principle", J. Chem. Phys. **4**, 193–211 (1936).

[31]A. Stolow and J. G. Underwood, "Time-resolved photoelectron spectroscopy of nonadiabatic dynamics in polyatomic molecules", in *Advances in chemical physics, volume 139*, edited by S. Rice (Wiley, Hoboken, NJ, 2008) Chap. 6, pp. 497–584.

[32]T. S. Rose, M. J. Rosker, and A. H. Zewail, "Femtosecond real-time observation of wave packet oscillations (resonance) in dissociation reactions", J. Chem. Phys. **88**, 6672–6673 (1988).

[33]A. H. Zewail, "Femtochemistry: Atomic-scale dynamics of the chemical bond", J. Phys. Chem. A **104**, 5660–5694 (2000).

[34]T. A. Carlson, "Photoelectron spectroscopy", Annu. Rev. Phys. Chem. **26**, 211–234 (1975).

[35]F. Reinert and S. Hüfner, "Photoemission spectroscopy: from early days to recent applications", New J. Phys. **7**, 97 (2005).

[36]I. V. Hertel and W. Radloff, "Ultrafast dynamics in isolated molecules and molecular clusters", Rep. Prog. Phys. **69**, 1897 (2006).

[37]J. Eland, *Photoelectron spectroscopy*, 2nd Edition (Butterworth & Co, 1984).

[38]T. Suzuki, "Femtosecond time-resolved photoelectron imaging", Annu. Rev. Phys. Chem. **57**, 555–592 (2006).

[39]A. Stolow, A. E. Bragg, and D. M. Neumark, "Femtosecond time-resolved photoelectron spectroscopy", Chem. Rev. **104**, 1719–1757 (2004).

[40]L. Wang, H. Kohguchi, and T. Suzuki, "Femtosecond time-resolved photoelectron imaging", Faraday Discuss. **113**, 37–46 (1999).

[41]T. Suzuki, "Time-resolved photoelectron spectroscopy of non-adiabatic electronic dynamics in gas and liquid phases", Int. Rev. Phys. Chem. **31**, 265–318 (2012).

[42]G. Wu, P. Hockett, and A. Stolow, "Time-resolved photoelectron spectroscopy: from wavepackets to observables", Phys. Chem. Chem. Phys. **13**, 18447–18467 (2011).

[43]A. D. G. Nunn, R. S. Minns, R. Spesyvtsev, M. J. Bearpark, M. A. Robb, and H. H. Fielding, "Ultrafast dynamics through conical intersections and intramolecular vibrational energy redistribution in styrene", Phys. Chem. Chem. Phys. **12**, 15751–15759 (2010).

[44]V. Blanchet, M. Z. Zgierski, T. Seideman, and A. Stolow, "Discerning vibronic molecular dynamics using time-resolved photoelectron spectroscopy", Nature **401**, 52–54 (1999).

[45]P. G. Burke, N. Chandra, and F. A. Gianturco, "Electron-molecule interactions. IV. scattering by polyatomic molecules", J. Phys. B: At. Mol. Phys. **5**, 2212 (1972).

[46]N. Chandra, "Photoelectron spectroscopic studies of polyatomic molecules. I. theory", J. Phys. B: At. Mol. Phys. **20**, 3405 (1987).

[47]C. N. Yang, "On the angular distribution in nuclear reactions and coincidence measurements", Phys. Rev. **74**, 764–772 (1948).

[48]K. L. Reid, "Photoelectron angular distributions", Annu. Rev. Phys. Chem. **54**, 397–424 (2003).

[49]J. Cooper and R. N. Zare, "Angular distribution of photoelectrons", J. Chem. Phys. **48**, 942–943 (1968).

[50]M. N. R. Ashfold, B. Cronin, A. L. Devine, R. N. Dixon, and M. G. D. Nix, "The role of $\pi\sigma^*$ excited states in the photodissociation of heteroaromatic molecules", Science **312**, 1637–1640 (2006).

[51]G. A. King, T. A. A. Oliver, and M. N. R. Ashfold, "Dynamical insights into $^1\pi\sigma^*$ state mediated photodissociation of aniline", J. Chem. Phys. **132**, 214307 (2010).

[52]R. Montero, Á. Peralta Conde, V. Ovejas, R. Martínez, F. Castaño, and A. Longarte, "Ultrafast dynamics of aniline in the 294-234 nm excitation range: the role of the $\pi\sigma^*$ state.", J. Chem. Phys. **135**, 54308 (2011).

[53]Y. Honda, M. Hada, M. Ehara, and H. Nakatsuji, "Excited and ionized states of aniline: symmetry adapted cluster configuration interaction theoretical study", J. Chem. Phys. **117**, 2045–2052 (2002).

[54]Z. Lan, W. Domcke, V. Vallet, A. L. Sobolewski, and S. Mahapatra, "Time-dependent quantum wave-packet description of the $^1\pi\sigma^*$ photochemistry of phenol", J. Chem. Phys. **122**, 224315 (2005).

[55]E. Gloaguen, J. Mestdagh, L. Poisson, F. Lepetit, J. Visticot, B. Soep, M. Coroiu, A. T. J. B. Eppink, and D. H. Parker, "Experimental evidence for ultrafast electronic relaxation in molecules, mediated by diffuse states", J. Am. Chem. Soc. **127**, 16529–16534 (2005).

[56]B. Chmura, M. F. Rode, A. L. Sobolewski, L. Lapinski, and M. J. Nowak, "A computational study on the mechanism of intramolecular oxo-hydroxy phototautomerism driven by repulsive $\pi\sigma^*$ state", J. Phys. Chem. A **112**, 13655–13661 (2008).

[57]G. Scoles, D. Bassi, U. Buck, and D. C. Laine, eds., *Atomic and molecular beam methods* (Oxford University Press, 1988).

[58]J. B. Anderson and J. B. Fenn, "Velocity distributions in molecular beams from nozzle sources", Phys. Fluids **8**, 780–787 (1965).

[59]U. Even, J. Jortner, D. Noy, N. Lavie, and C. Cossart-Magos, "Cooling of large molecules below 1 K and He clusters formation", J. Chem. Phys. **112**, 8068–8071 (2000).

[60]A. Amirav, U. Even, and J. Jortner, "Cooling of large and heavy molecules in seeded supersonic beams", Chem. Phys. **51**, 31–42 (1980).

[61]D. H. Levy, "The spectroscopy of very cold gases", Science **214**, 263–269 (1981).

[62]T. A. Miller, "Chemistry and chemical intermediates in supersonic free jet expansions", Science **223**, 545–553 (1984).

[63]*Even-Lavie valves*, `https://sites.google.com/site/evenlavievalve/home`.

[64]R. Campargue, "Progress in overexpanded supersonic jets and skimmed molecular beams in free-jet zones of silence", J. Phys. Chem. **88**, 4466–4474 (1984).

[65]U. Keller, "Recent developments in compact ultrafast lasers", Nature **424**, 831–838 (2003).

[66]K. Yanamouchi, M. Nisoli, and W. T. Hill III, eds., *Progress in ultrafast intense laser science VIII* (Springer, 2012).

[67]W. T. Silfvast, *Laser fundamentals* (Cambridge University Press, 2004).

[68]P. F. Moulton, "Spectroscopic and laser characteristics of Ti:Al_2O_3", J. Opt. Soc. Am. B **3**, 125–133 (1986).

[69]P. Albers, E. Stark, and G. Huber, "Continuous-wave laser operation and quantum efficiency of titanium-doped sapphire", J. Opt. Soc. Am. B **3**, 134–139 (1986).

[70]D. H. Sutter, G. Steinmeyer, L. Gallmann, N. Matuschek, F. Morier-Genoud, U. Keller, V. Scheuer, G. Angelow, and T. Tschudi, "Semiconductor saturable-absorber mirror assisted Kerr-lens mode-locked Ti:sapphire laser producing pulses in the two-cycle regime", Opt. Lett. **24**, 631–633 (1999).

[71]U. Morgner, F. X. Kärtner, S. H. Cho, Y. Chen, H. A. Haus, J. G. Fujimoto, E. P. Ippen, V. Scheuer, G. Angelow, and T. Tschudi, "Sub-two-cycle pulses from a Kerr-lens mode-locked Ti:sapphire laser", Opt. Lett. **24**, 411–413 (1999).

[72]D. C. Edelstein, E. S. Wachman, L. K. Cheng, W. R. Bosenberg, and C. L. Tang, "Femtosecond ultraviolet pulse generation in beta-BaB_2O_4", Appl. Phys. Lett. **52**, 2211–2213 (1988).

[73]M. K. Reed, M. K. Steiner-Shepard, M. S. Armas, and D. K. Negus, "Microjoule-energy ultrafast optical parametric amplifiers", J. Opt. Soc. Am. B **12**, 2229–2236 (1995).

[74]M. Nisoli, R. Danielius, A. Piskarskas, S. de Silvestri, V. Magni, G. Valiulis, A. Varanavicius, and O. Svelto, "Highly efficient parametric conversion of femtosecond Ti:sapphire laser pulses at 1 kHz", Opt. Lett. **19**, 1973–1975 (1994).

[75]T. Wilhelm, J. Piel, and E. Riedle, "Sub-20 fs pulses tunable across the visible from a blue-pumped single-pass noncollinear parametric converter", Opt. Lett. **22**, 1494–1496 (1997).

[76]A. Brodeur and S. L. Chin, "Ultrafast white-light continuum generation and self-focusing in transparent condensed media", J. Opt. Soc. Am. B **16**, 637–650 (1999).

[77]A. D. Bandrauk. and F. Légaré, "Enhanced ionization of molecules in intense laser fields", in *Progress in ultrafast intense laser science VIII* (Springer, 2012).

[78]S. L. Anderson, D. M. Rider, and R. N. Zare, "Multiphoton ionization photoelectron spectroscopy: a new method for determining vibrational structure of molecular ions", Chem. Phys. Lett. **93**, 11–15 (1982).

[79]P. Kruit and F. H. Read, "Magnetic field paralleliser for 2π electron-spectrometer and electron-image magnifier", J. Phys. E **16**, 313 (1983).

[80]A. T. J. B. Eppink and D. H. Parker, "Velocity map imaging of ions and electrons using electrostatic lenses: application in photoelectron and photofragment ion imaging of molecular oxygen", Rev. Sci. Instrum. **68**, 3477 (1997).

[81]D. Townsend, M. P. Minitti, and A. G. Suits, "Direct current slice imaging", Rev. Sci. Instrum. **74**, 2530 (2003).

[82]D. S. N. Parker, "Experimental investigation of the dynamics of S_1 benzene and the development of a new UV femtosecond pulse shaper", PhD thesis (University College London, 2009).

[83]A. T. J. B. Eppink, S. Wu, and B. J. Whitaker, eds., *Imaging in molecular dynamics: technology and applications* (Cambridge University Press, 2003).

[84]G. A. Garcia, L. Nahon, and I. Powis, "Two-dimensional charged particle image inversion using a polar basis function expansion", Rev. Sci. Instrum. **75**, 4989–4996 (2004).

[85]V. Dribinski, A. Ossadtchi, V. A. Mandelshtam, and H. Reisler, "Reconstruction of Abel-transformable images: the Gaussian basis-set expansion Abel transform method", Rev. Sci. Instrum. **73**, 2634–2642 (2002).

[86]A. S. Bracker, E. R. Wouters, A. G. Suits, and O. S. Vasyutinskii, "Imaging the alignment angular distribution: state symmetries, coherence effects, and nonadiabatic interactions in photodissociation", J. Chem. Phys. **110**, 6749 (1999).

[87]R. Spesyvtsev, "Experimental investigation of ultrafast internal conversion in aniline and 1,4-diazabicycl[2.2.2]octane (DABCO)", PhD thesis (University College London, 2013).

[88]G. M. Roberts, J. L. Nixon, J. Lecointre, E. Wrede, and J. R. R. Verlet, "Toward real-time charged-particle image reconstruction using polar onion-peeling", Rev. Sci. Instrum. **80**, 53104 (2009).

[89]J. E. Hansen and W. Persson, "Revised analysis of singly ionized xenon, Xe II", Phys. Scr. **36**, 602–643 (1987).

[90]A. Vredenborg, W. G. Roeterdink, and M. H. M. Janssen, "A photoelectron-photoion coincidence imaging apparatus for femtosecond time-resolved molecular dynamics with electron time-of-flight resolution of $\sigma = 18$ ps and energy resolution $\Delta E/E = 3.5\%$", Rev. Sci. Instrum. **79**, 63108–63109 (2008).

[91]V. Profant, V. Poterya, M. Fárník, P. Slavíček, and U. Buck, "Experimental and theoretical study of the pyrrole cluster photochemistry: closing the $\pi\sigma^*$ dissociation pathway by complexation", J. Chem. Phys. **127**, 064307 (2007).

[92]Various, "General discussion", Faraday Discuss. **163**, 513–543 (2013).

[93]A. M. Lee, J. D. Coe, S. Ullrich, M. L. Ho, S. J. Lee, B. M. Cheng, M. Z. Zgierski, I. C. Chen, T. J. Martinez, and A. Stolow, "Substituent effects on dynamics at conical intersections: α, β-enones", J. Phys. Chem. A **111**, 11948–11960 (2007).

[94]O. Schalk, A. E. Boguslavskiy, and A. Stolow, "Substituent effects on dynamics at conical intersections: cyclopentadienes", J. Phys. Chem. A **114**, 4058–4064 (2010).

[95]R. Livingstone, O. Schalk, A. E. Boguslavskiy, G. Wu, L. T. Bergendahl, A. Stolow, M. J. Paterson, and D. Townsend, "Following the excited state relaxation dynamics of indole and 5-hydroxyindole using time-resolved photoelectron spectroscopy", J. Chem. Phys. **135**, 194307 (2011).

[96]J. O. F. Thompson, R. A. Livingstone, and D. Townsend, "Following the relaxation dynamics of photoexcited aniline in the 273-266 nm region using time-resolved photoelectron imaging", J. Chem. Phys. **139**, 034316 (2013).

[97]B. Cronin, M. G. D. Nix, R. H. Qadiri, and M. N. R. Ashfold, "High resolution photofragment translational spectroscopy studies of the near ultraviolet photolysis of pyrrole", Phys. Chem. Chem. Phys. **6**, 5031–5041 (2004).

[98]L. W. Pickett, M. E. Corning, G. M. Wieder, D. A. Semenow, and J. M. Buckley, "The vacuum ultraviolet spectra of cyclic compounds. III. amines 1", J. Am. Chem. Soc. **75**, 1618–1622 (1953).

[99]G. Horvàth and Ĩ. Kiss, "The electronic spectra of five-membered heterocyclic compounds", Spectrochim. Acta A **23**, 921–924 (1967).

[100]P. A. Mullen and M. K. Orloff, "Ultraviolet absorption spectrum of pyrrole vapor including the observation of low-energy transitions in the far ultraviolet", J. Chem. Phys. **51**, 2276–2278 (1969).

[101]M. Bavia, F. Bertinelli, C. Taliani, and C. Zauli, "The electronic spectrum of pyrrole in the vapour and crystal", Mol. Phys. **31**, 479–489 (1976).

[102]W. M. Flicker, O. A. Mosher, and A. Kuppermann, "Triplet states of furan, thiophene, and pyrrole", Chem. Phys. Lett. **38**, 489–492 (1976).

[103]C. D. Cooper, A. D. Williamson, J. C. Miller, and R. N. Compton, "Resonantly enhanced multiphoton ionization of pyrrole, N-methyl pyrrole, and furan", J. Chem. Phys. **73**, 1527–1537 (1980).

[104]J. P. Dahl and A. E. Hansen, "Self consistent field molecular orbital calculation for pyrrole", English, Theor. Chim. Acta **1**, 199–205 (1963).

[105]P. Chiorboli, A. Rastelli, and F. Momicchioli, "Theoretical studies in the chemistry and physics of heterocycles", English, Theor. Chim. Acta **5**, 1–10 (1966).

[106]J. del Bene and H. H. Jaffe, "Use of the CNDO method in spectroscopy. II. Five-membered rings", J. Chem. Phys. **48**, 4050–4055 (1968).

[107]K. Tanaka, T. Nomura, T. Noro, H. Tatewaki, T. Takada, H. Kashiwagi, F. Sasaki, and K. Ohno, "Ab initio SCF CI calculations on the ground and $\pi - \pi^*$ excited states of the pyrrole molecule and its positive ion", J. Chem. Phys. **67**, 5738–5741 (1977).

[108]W. Butscher and K. Thunemann, "A non-empirical SCF and CI study of the electronic spectrum of pyrrole", Chem. Phys. Lett. **57**, 224–229 (1978).

[109]D. C. Rawlings and E. R. Davidson, "The Rayleigh-Schrödinger B_K method applied to the lower electronic states of pyrrole", Chem. Phys. Lett. **98**, 424–427 (1983).

[110]D. C. Rawlings, E. R. Davidson, and M. Gouterman, "Theoretical invstigations of the electronic states of porphyrins. I. basis set development and predicted spectrum of pyrrole", Int. J. Quantum Chem. **26**, 237–250 (1984).

[111]H. Nakatsuji, O. Kitao, and T. Yonezawa, "Cluster expansion of the wave function: valence and Rydberg excitations and ionizations of pyrrole, furan, and cyclopentadiene", J. Chem. Phys. **83**, 723–734 (1985).

[112]L. Serrano-Andres, M. Merchan, I. Nebot-Gil, B. O. Roos, and M. Fulscher, "Theoretical study of the electronic spectra of cyclopentadiene, pyrrole, and furan", J. Am. Chem. Soc. **115**, 6184–6197 (1993).

[113]H. Nakano, T. Tsuneda, T. Hashimoto, and K. Hirao, "Theoretical study of the excitation spectra of five-membered ring compounds: cyclopentadiene, furan, and pyrrole", J. Chem. Phys. **104**, 2312–2320 (1996).

[114]A. B. Trofimov, H. Köppel, and J. Schirmer, "Vibronic structure of the valence π-photoelectron bands in furan, pyrrole, and thiophene", J. Chem. Phys. **109**, 1025–1040 (1998).

[115]O. Christiansen, J. Gauss, J. F. Stanton, and P. Jørgensen, "The electronic spectrum of pyrrole", J. Chem. Phys. **111**, 525–537 (1999).

[116]R. Burcl, R. D. Amos, and N. C. Handy, "Study of excited states of furan and pyrrole by time-dependent density functional theory", Chem. Phys. Lett. **355**, 8–18 (2002).

[117]B. O. Roos, P. Malmqvist, V. Molina, L. Serrano-Andres, and M. Merchan, "Theoretical characterization of the lowest-energy absorption band of pyrrole", J. Chem. Phys. **116**, 7526–7536 (2002).

[118]M. Pastore, C. Angeli, and R. Cimiraglia, "The vertical electronic spectrum of pyrrole: a second and third order n-electron valence state perturbation theory study", Chem. Phys. Lett. **422**, 522–528 (2006).

[119]X. Li and J. Paldus, "A multireference coupled-cluster study of electronic excitations in furan and pyrrole", J. Phys. Chem. A **114**, 8591–8600 (2010).

[120]M. H. Palmer, I. C. Walker, and M. F. Guest, "The electronic states of pyrrole studied by optical (VUV) absorption, near-threshold electron energy-loss (EEL) spectroscopy and ab initio multi-reference configuration interaction calculations", Chem. Phys. **238**, 179–199 (1998).

[121]H. Lippert, H. Ritze, I. V. Hertel, and W. Radloff, "Femtosecond time-resolved hydrogen-atom elimination from photoexcited pyrrole molecules", Chem. Phys. Chem. **5**, 1423–1427 (2004).

[122]Z. Lan, A. Dupays, V. Vallet, S. Mahapatra, and W. Domcke, "Photoinduced multi-mode quantum dynamics of pyrrole at the $^1\pi\sigma^*$-S_0 conical intersections", J. Photochem. Photobiol. A **190**, 177–189 (2007).

[123]L. Klasinc, A. Sabljic, G. Kluge, J. Rieger, and M. Scholz, "Chemistry of excited states. Part 13. Assignment of lowest π-ionizations in photoelectron spectra of thiophen, furan, and pyrrole", J. Chem. Soc., Perkin Trans. 2, 539–543 (1982).

[124]P. J. Derrick, L. Åsbrink, O. Edqvist, B. Jonsson, and E. Lindholm, "Rydberg series in small molecules: XII. photoelectron spectroscopy and electronic structure of pyrrole", J. Mass Spectrom. Ion Phys. **6**, 191–202 (1971).

[125]U. Gelius, C. J. Allan, G. Johansson, H. Siegbahn, D. A. Allison, and K. Siegbahn, "The ESCA spectra of benzene and the iso-electronic series, thiophene, pyrrole and furan", Phys. Scr. **3**, 237 (1971).

[126]K. Takeshita and Y. Yamamoto, "A theoretical study on the ionization of pyrrole with analysis of vibrational structure of the photoelectron spectra", J. Chem. Phys. **101**, 2198–2204 (1994).

[127]G. M. Roberts, C. A. Williams, H. Yu, A. S. Chatterley, J. D. Young, S. Ullrich, and V. G. Stavros, "Probing ultrafast dynamics in photoexcited pyrrole: timescales for $^1\pi\sigma^*$ mediated H-atom elimination", Faraday Discuss. **163**, 95–116 (2013).

[128]V. Vallet, Z. Lan, S. Mahapatra, A. L. Sobolewski, and W. Domcke, "Photochemistry of pyrrole: Time-dependent quantum wave-packet description of the dynamics at the $^1\pi\sigma^*$-S_0 conical intersections", J. Chem. Phys. **123**, 144307 (2005).

[129]D. A. Blank, S. W. North, and Y. T. Lee, "The ultraviolet photodissociation dynamics of pyrrole", Chem. Phys. **187**, 35–47 (1994).

[130]J. Wei, A. Kuczmann, J. Riedel, F. Renth, and F. Temps, "Photofragment velocity map imaging of H atom elimination in the first excited state of pyrrole", Phys. Chem. Chem. Phys. **5**, 315–320 (2003).

[131]J. Wei, J. Riedel, A. Kuczmann, F. Renth, and F. Temps, "Photodissociation dynamics of pyrrole: evidence for mode specific dynamics from conical intersections", Faraday Discuss. **127**, 267–282 (2004).

[132]A. J. van den Brom, M. Kapelios, T. N. Kitsopoulos, N. H. Nahler, B. Cronin, and M. N. R. Ashfold, "Photodissociation and photoionization of pyrrole following the multiphoton excitation at 243 and 364.7 nm", Phys. Chem. Chem. Phys. **7**, 892–899 (2005).

[133]D. J. Hadden, K. L. Wells, G. M. Roberts, L. T. Bergendahl, M. J. Paterson, and V. G. Stavros, "Time resolved velocity map imaging of H-atom elimination from photoexcited imidazole and its methyl substituted derivatives", Phys. Chem. Chem. Phys. **13**, 10342–10349 (2011).

[134]R. Montero, Á. Peralta Conde, V. Ovejas, M. Fernández-Fernández, F. Castaño, J. R. Vazquez de Aldana, and A. Longarte, "Femtosecond evolution of the pyrrole molecule excited in the near part of its UV spectrum", J. Chem. Phys. **137**, 064317 (2012).

[135]R. Montero, V. Ovejas, M. Fernández-Fernández, Á. Peralta Conde, and A. Longarte, "Revisiting the relaxation dynamics of isolated pyrrole", J. Chem. Phys. **141**, 014303, 014303 (2014).

[136]M. Vazdar, M. Eckert-Maksić, M. Barbatti, and H. Lischka, "Excited-state nonadiabatic dynamics simulations of pyrrole", Mol. Phys. **107**, 845–854 (2009).

[137]B. Sellner, M. Barbatti, and H. Lischka, "Dynamics starting at a conical intersection: application to the photochemistry of pyrrole", J. Chem. Phys. **131**, 024312 (2009).

[138]M. Barbatti, J. Pittner, M. Pederzoli, U. Werner, R. Mitrić, V. Bonačić-Koutecký, and H. Lischka, "Non-adiabatic dynamics of pyrrole: dependence of deactivation mechanisms on the excitation energy", Chem. Phys. **375**, 26–34 (2010).

[139]S. Faraji, M. Vazdar, V. Sivaranjana Reddy, M. Eckert-Maksić, H. Lischka, and H. Köppel, "Ab initio quantum dynamical study of the multi-state nonadiabatic photodissociation of pyrrole", J. Chem. Phys. **135**, 154310 (2011).

[140]K. Saita, M. G. D. Nix, and D. V. Shalashilin, "Simulation of ultrafast photodynamics of pyrrole with a multiconfigurational Ehrenfest method", Phys. Chem. Chem. Phys. **15**, 16227–16235 (2013).

[141]R. M. Stratt and M. Maroncelli, "Nonreactive dynamics in solution: the emerging molecular view of solvation dynamics and vibrational relaxation", J. Phys. Chem. **100**, 12981–12996 (1996).

[142]P. N. Day, Z. Wang, and R. Pachter, "Calculation of the structure and absorption spectra of phthalocyanines in the gas-phase and in solution", J. Mol. Struc.-Theochem **455**, 33–50 (1998).

[143]T. A. A. Oliver, Y. Zhang, M. N. R. Ashfold, and S. E. Bradforth, "Linking photochemistry in the gas and solution phase: S-H bond fission in p-methylthiophenol following UV photoexcitation", Faraday Discuss. **150**, 439–458 (2011).

[144]Y. Zhang, T. A. A. Oliver, M. N. R. Ashfold, and S. E. Bradforth, "Contrasting the excited state reaction pathways of phenol and para-methylthiophenol in the gas and liquid phases", Faraday Discuss. **157**, 141–163 (2012).

[145]M. Kabelac, P. Hobza, and V. Spirko, "The structure and vibrational dynamics of the pyrrole dimer", Phys. Chem. Chem. Phys. **11**, 3885–3891 (2009).

[146]V. Profant, V. Poterya, M. Fárník, P. Slavíček, and U. Buck, "Fragmentation dynamics of size-selected pyrrole clusters prepared by electron impact ionization: forming a solvated dimer ion core", J. Phys. Chem. A **111**, 12477–12486 (2007).

[147]M. J. S. Dewar and S. D. Worley, "Photoelectron spectra of molecules. I. ionization potentials of some organic molecules and their interpretation", J. Chem. Phys. **50**, 654–667 (1969).

[148]M. Barbatti, M. Vazdar, A. J. A. Aquino, M. Eckert-Maksić, and H. Lischka, "The nonadiabatic deactivation paths of pyrrole", J. Chem. Phys. **125**, 164323 (2006).

[149]E. V. Gromov, C. Lévêque, F. Gatti, I. Burghardt, and H. Köppel, "Ab initio quantum dynamical study of photoinduced ring opening in furan", J. Chem. Phys. **135**, 164305 (2011).

[150]L. M. Frutos, A. Markmann, A. L. Sobolewski, and W. Domcke, "Photoinduced electron and proton transfer in the hydrogen-bonded pyridine-pyrrole system", J. Phys. Chem. B **111**, 6110–6112 (2007).

[151]C. Rensing, H. Mäder, and F. Temps, "Rotational spectrum, structure and internal dynamics of the pyrrole-ammonia complex", J. Mol. Spectrosc. **251**, 224–228 (2008).

[152]R. Spesyvtsev, O. M. Kirkby, and H. H. Fielding, "Ultrafast dynamics of aniline following 269-238 nm excitation and the role of the $S_2(\pi 3s/\pi\sigma^*)$ state", Faraday Discuss. **157**, 165–179 (2012).

[153]G. Worth and S. P. Neville, "Private communication", Oct, 2013.

[154]C. C. Cheng, C. Ma, C. T. Chan, K. Y. Ho, and W. Kwok, "The solvent effect and identification of a weakly emissive state in nonradiative dynamics of guanine nucleosides and nucleotides - a combined femtosecond broadband time-resolved fluorescence and transient absorption study", Photochem. Photobiol. Sci. **12**, 1351–1365 (2013).

[155]F. Wang, S. P. Neville, R. Wang, and G. A. Worth, "Quantum dynamics study of photoexcited aniline", J. Phys. Chem. A **117**, 7298–7307 (2013).

[156]G. M. Roberts, C. A. Williams, J. D. Young, S. Ullrich, M. J. Paterson, and V. G. Stavros, "Unraveling ultrafast dynamics in photoexcited aniline", J. Am. Chem. Soc. **134**, 12578–12589 (2012).

[157]R. S. Minns, D. S. N. Parker, T. J. Penfold, G. A. Worth, and H. H. Fielding, "Competing ultrafast intersystem crossing and internal conversion in the 'channel 3' region of benzene", Phys. Chem. Chem. Phys. **12**, 15607–15615 (2010).

[158]T. J. Penfold and G. A. Worth, "A model Hamiltonian to simulate the complex photochemistry of benzene II", J. Chem. Phys. **131**, 064303 (2009).

[159]T. J. Penfold, R. Spesyvtsev, O. M. Kirkby, R. S. Minns, D. S. N. Parker, H. H. Fielding, and G. A. Worth, "Quantum dynamics study of the competing ultrafast intersystem crossing and internal conversion in the 'channel 3' region of benzene", J. Chem. Phys. **137**, 204310 (2012).

[160]M. Sala, O. M. Kirkby, H. H. Fielding, and S. Guérin, "New insight into the potential energy landscape and relaxation pathways of photoexcited aniline from CASSCF and XMCQDPT2 electronic structure calculations", Phys. Chem. Chem. Phys. **16**, 3122–3133 (2014).

[161]X. Song, M. Yang, E. R. Davidson, and J. P. Reilly, "Zero-kinetic-energy photoelectron spectra of jet-cooled aniline", J. Chem. Phys. **99**, 3224 (1993).

[162]T. Ebata, C. Minejima, and N. Mikami, "A new electronic state of aniline observed in the transient IR absorption spectrum from S_1 in a supersonic jet", J. Phys. Chem. A **106**, 11070–11074 (2002).

[163]E. R. T. Kerstel, M. Beucci, G. Petraperzia, and E. Castellucci, "High-resolution absorption, excitation, and microwave-UV double-resonance spectroscopy on a molecular-beam: S_1 aniline", Chem. Phys. **199**, 263–273 (1995).

[164]K. Kimura, H. Tsubomura, and S. Nagakura, "The vacuum ultraviolet absorption spectra of aniline and some of its N-derivatives", Bull. Chem. Soc. Jpn. **37**, 1336–1346 (1964).

[165]R. Scheps, D. Florida, and S. A. Rice, "Influence of large amplitude vibrational motion on the rate of intersystem crossing: a study of single vibronic level fluorescence from aniline-h_7, aniline N, N-d_2, aniline-d_5, and aniline-d_7", J. Chem. Phys. **61**, 1730–1747 (1974).

[166]B. Kim, C. P. Schick, and P. M. Weber, "Time-delayed two-color photoelectron spectra of aniline, 2-aminopyridine, and 3-aminopyridine: snapshots of the nonadiabatic curve crossings", J. Chem. Phys. **103**, 6903 (1995).

[167]W. E. Sinclair and D. W. Pratt, "Structure and vibrational dynamics of aniline and aniline–Ar from high resolution electronic spectroscopy in the gas phase", J. Chem. Phys. **105**, 7942–7956 (1996).

[168]E. R. T. Kerstel, M. Becucci, G. Pietraperzia, D. Consalvo, and E. Castellucci, "Molecular beam spectroscopy of S_1 aniline: assignments for the 0_0^0, $6a_0^1$, I_0^2, and 1_0^1 rovibronic bands", J. Mol. Spectrosc. **177**, 74–78 (1996).

[169]R. Spesyvtsev, O. M. Kirkby, M. Vacher, and H. H. Fielding, "Shedding new light on the role of the Rydberg state in the photochemistry of aniline", Phys. Chem. Chem. Phys. **14**, 9942–9947 (2012).

[170]R. A. Livingstone, J. O. F. Thompson, M. Iljina, R. J. Donaldson, B. J. Sussman, M. J. Paterson, and D. Townsend, "Time-resolved photoelectron imaging of excited state relaxation dynamics in phenol, catechol, resorcinol, and hydroquinone", J. Chem. Phys. **137**, 184304 (2012).

[171]P. M. Wojciechowski, W. Zierkiewicz, D. Michalska, and P. Hobza, "Electronic structures, vibrational spectra, and revised assignment of aniline and its radical cation: theoretical study", J. Chem. Phys. **118**, 10900–10911 (2003).

[172]T. J. Penfold and G. A. Worth, "The effect of molecular distortions on spin-orbit coupling in simple hydrocarbons", Chem. Phys. **375**, 58–66 (2010).

[173]D. S. N. Parker, R. S. Minns, T. J. Penfold, G. A. Worth, and H. H. Fielding, "Ultrafast dynamics of the S_1 excited state of benzene", Chem. Phys. Lett. **469**, 43–47 (2009).

[174]G. Wu, A. E. Boguslavskiy, O. Schalk, M. S. Schuurman, and A. Stolow, "Ultrafast non-adiabatic dynamics of methyl substituted ethylenes: the $\pi 3s$ Rydberg state", J. Chem. Phys. **135**, 164309 (2011).

[175]R. N. Dixon, T. A. A. Oliver, and M. N. R. Ashfold, "Tunnelling under a conical intersection: application to the product vibrational state distributions in the UV photodissociation of phenols.", J. Chem. Phys. **134**, 194303 (2011).

[176]G. M. Roberts, A. S. Chatterley, J. D. Young, and V. G. Stavros, "Direct observation of hydrogen tunneling dynamics in photoexcited phenol", J. Phys. Chem. Lett. **3**, 348–352 (2012).

[177]A. Sur and P. M. Johnson, "Radiationless transitions in gas phase phenol and the effects of hydrogen bonding", J. Chem. Phys. **84**, 1206–1209 (1986).

[178]M. Krauss, J. O. Jensen, and H. F. Hameka, "Electronic structure of the excited states and phenol fluorescence", J. Phys. Chem. **98**, 9955–9959 (1994).

[179]B. A. Barry, M. K. el-Deeb, P. O. Sandusky, and G. T. Babcock, "Tyrosine radicals in photosystem II and related model compounds. characterization by isotopic labeling and EPR spectroscopy", J. Biol. Chem. **265**, 20139–20143 (1990).

[180]J. Lorentzon, P. Malmqvist, M. Fülscher, and B. O. Roos, "A CASPT2 study of the valence and lowest Rydberg electronic states of benzene and phenol", English, Theor. Chim. Acta **91**, 91–108 (1995).

[181]G. Berden, W. L. Meerts, M. Schmitt, and K. Kleinermanns, "High resolution UV spectroscopy of phenol and the hydrogen bonded phenol-water cluster", J. Chem. Phys. **104**, 972–982 (1996).

[182]S. G. Ramesh and W. Domcke, "A multi-sheeted three-dimensional potential-energy surface for the H-atom photodissociation of phenol", Faraday Discuss. **163**, 73–94 (2013).

[183]O. P. J. Vieuxmaire, Z. Lan, A. L. Sobolewski, and W. Domcke, "Ab initio characterization of the conical intersections involved in the photochemistry of phenol", J. Chem. Phys. **129**, 224307 (2008).

[184]H. An and K. K. Baeck, "Quantum wave packet propagation study of the photochemistry of phenol: isotope effects (Ph-OD) and the direct excitation to the $^1\pi\sigma^*$ state", J. Phys. Chem. A **115**, 13309–13315 (2011).

[185]H. D. Bist, J. C. D. Brand, and D. R. Williams, "The 2750-Å electronic band system of phenol: part I. the in-plane vibrational spectrum", J. Mol. Spectrosc. **21**, 76–98 (1966).

[186]S. J. Martinez III, J. C. Alfano, and D. H. Levy, "Rotationally resolved fluorescence excitation spectra of phenol and 4-ethylphenol in a supersonic jet", J. Mol. Spectrosc. **152**, 80–88 (1992).

[187]M. Takayanagi and I. Hanazaki, "Stimulated-emission-pumping laser-induced-fluorescence spectroscopy of phenol and anisole", Laser Chem. **14**, 103 (1994).

[188]C. Ratzer, J. Küpper, D. Spangenberg, and M. Schmitt, "The structure of phenol in the S_1-state determined by high resolution UV-spectroscopy", Chem. Phys. **283**, 153–169 (2002).

[189]D. Spangenberg, P. Imhof, and K. Kleinermanns, "The S_1 state geometry of phenol determined by simultaneous Franck-Condon and rotational constants fits", Phys. Chem. Chem. Phys. **5**, 2505–2514 (2003).

[190]R. Hermann, G. R. Mahalaxmi, T. Jochum, S. Naumov, and O. Brede, "Balance of the deactivation channels of the first excited singlet state of phenols: effect of alkyl substitution, sterical hindrance, and solvent polarity", J. Phys. Chem. A **106**, 2379–2389 (2002).

[191]R. J. Lipert, G. Bermudez, and S. D. Colson, "Pathways of S_1 decay in phenol, indoles, and water complexes of phenol and indole in a free jet expansion", J. Phys. Chem. **92**, 3801–3805 (1988).

[192]R. J. Lipert and S. D. Colson, "Deuterium isotope effects on S_1 radiationless decay in phenol and on intermolecular vibrations in the phenol-water complex", J. Phys. Chem. **93**, 135–139 (1989).

[193]K. Kimura and S. Nagakura, "Vacuum ultra-violet absorption spectra of various mono-substituted benzenes", Mol. Phys. **9**, 117–135 (1965).

[194]R. J. Lipert and S. D. Colson, "Accurate ionization potentials of phenol and phenol-(H_2O) from the electric field dependence of the pump-probe photoionization threshold", J. Phys. Chem. **92**, 3240–3241 (1990).

[195]G. A. Pino, C. Dedonder-Lardeux, G. Grégoire, C. Jouvet, S. Martrenchard, and D. Solgadi, "Intracluster hydrogen transfer followed by dissociation in the phenol–$(NH_3)_3$ excited state: $PhOH(S_1)$–$(NH_3)_3 \rightarrow PhO^{\bullet} + (NH_4)(NH_3)_2$", J. Chem. Phys. **111**, 10747–10749 (1999).

[196]G. Grégoire, C. Dedonder-Lardeux, C. Jouvet, S. Martrenchard, and D. Solgadi, "Has the excited state proton transfer ever been observed in phenol $(NH_3)_n$ molecular clusters?", J. Phys. Chem. A **105**, 5971–5976 (2001).

[197]C. Tseng, Y. T. Lee, and C. Ni, "H atom elimination from the $\pi\sigma^*$ state in the photodissociation of phenol", J. Chem. Phys. **121**, 2459–2461 (2004).

[198]M. G. D. Nix, A. L. Devine, B. Cronin, R. N. Dixon, and M. N. R. Ashfold, "High resolution photofragment translational spectroscopy studies of the near ultraviolet photolysis of phenol", J. Chem. Phys. **125**, 133318 (2006).

[199]J. G. Radziszewski, M. Gil, A. Gorski, J. Spanget-Larsen, J. Waluk, and B. J. Mróz, "Electronic states of the phenoxyl radical", J. Chem. Phys. **115**, 9733–9738 (2001).

[200]G. A. King, T. A. A. Oliver, M. G. D. Nix, and M. N. R. Ashfold, "High resolution photofragment translational spectroscopy studies of the ultraviolet photolysis of phenol-d_5", J. Phys. Chem. A **113**, 7984–7993 (2009).

[201]A. Iqbal, L. Pegg, and V. G. Stavros, "Direct versus indirect H atom elimination from photoexcited phenol molecules", J. Phys. Chem. A **112**, 9531–9534 (2008).

[202]A. Iqbal, M. S. Y. Cheung, M. G. D. Nix, and V. G. Stavros, "Exploring the time-scales of H-atom detachment from photoexcited phenol-h_6 and phenol-d_5: statistical *vs* nonstatistical decay", J. Phys. Chem. A **113**, 8157–8163 (2009).

[203]G. M. Roberts and V. G. Stavros, "The role of $\pi\sigma^*$ states in the photochemistry of heteroaromatic biomolecules and their subunits: insights from gas-phase femtosecond spectroscopy", Chem. Sci. **5**, 1698–1722 (2014).

[204]P. Ranitovic, C. W. Hogle, P. Rivière, A. Palacios, X. Tong, N. Toshima, A. González-Castrillo, L. Martin, F. Martín, M. M. Murnane, and H. Kapteyn, "Attosecond vacuum UV coherent control of molecular dynamics", P. Natl. Acad. Sci. USA **111**, 912–917 (2014).

[205]F. Buchner, H. Ritze, J. Lahl, and A. Lubcke, "Time-resolved photoelectron spectroscopy of adenine and adenosine in aqueous solution", Phys. Chem. Chem. Phys. **15**, 11402–11408 (2013).

[206]R. Brun and F. Rademakers, "ROOT an object oriented data analysis framework", Nucl. Instrum. Meth. A **389**, 81–86 (1997).

Appendix A

FSfit

This appendix section contains the description and user manual for the software, FSfit, which was designed and built to assist in the data analysis procedure for our TRPEI equipment. This data analysis requires handling large numbers of images (several hundred separate images are usually required for the analysis of each wavelength for each molecule). The program was designed and built to increase the ease with which our analysis procedure can be conducted, and also to ensure that such a complex procedure can be followed in a standardised and reproducible fashion. The program is based around a graphical user interface (GUI), which reduces the risk of accidental manipulation of the underlying code.

Our data analysis procedure has been described in Section 2.3, but the necessary steps are described herein with more practical details.

Following data acquisition we have a series of raw, time-integrated images, which are usually stored in a series of sequentially named folders. Our data acquisition software (Image32) collects images in 20 second cycles, between pump only signal, probe only signal and pump + probe signal. Therefore, each folder contains a series of images and it is necessary to sum each of the signals and then subtract each of the one-colour background images from the pump + probe signal. Please note that the Image32 program may attempt this process, but an error occurs wherein

pixels which should have negative values following subtraction are set to zero. This can lead to biasing of the data, therefore FSfit contains a tool for subtracting these images correctly.

FSfit does not contain a tool to invert the raw images, however it is recommended that the program 'Image Inversion' is used for this purpose (designed and built by Roman Spesyvtsev). [87]

Before analysis of the images, it is usual to calibrate the VMI imaging apparatus. Experimentally, we do this by by collecting a TRPEI of xenon, usually ionised by $2 + 1$ excitation at 249.5 nm, prior to each data run. A tool is provided in FSfit to easily derive a calibration value from an inverted image of the Xe spectrum.

A.1 User manual

FSfit was programmed in MATLAB and must be run from within the MATLAB environment. To install the program is simple, copy the folder containing the latest version onto the local computer. Open MATLAB and browse to the location where you copied FSfit. Right-click on the FSfit folder and select add folder and subfolders to PATH and save (this step is only necessary the first time). Then, to run simply type 'FSfit' in the main MATLAB window. N.B. Although it should be possible to compile an executable using the built-in MATLAB libraries, such that FSfit can be run on a computer without MATLAB installed, this process results in a inoperable program and is therefore not recommended.

The program was designed with a tabbed interface. This allows the user examine each part of the fitting procedure in appropriate detail. Please note that data is stored in the files FSfit_TEMPX.mat (where X is the number of the tab), in the installation directory, and these files pass information between the tabs sequentially *i.e.* Tab 2 can see the data loaded in Tab 1, but Tab 1 does not obtain data from Tab 2 (as this is not necessary). If the contents of Tab 1 (or the calibration value) is changed, it is necessary to re-load the data files and work through the

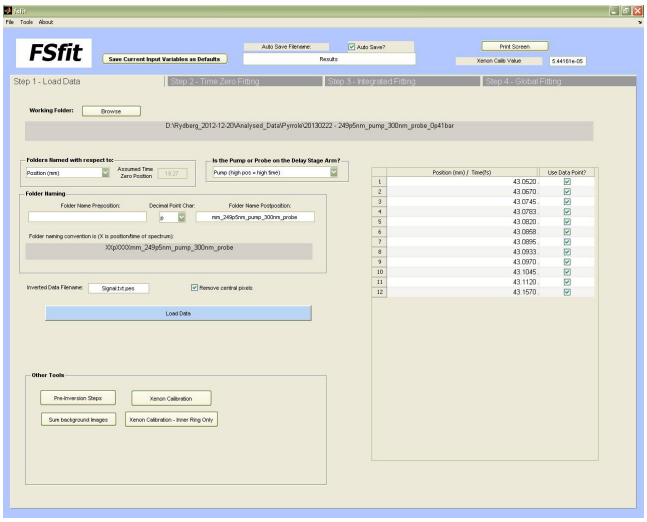

Figure A.1: FSfit, Tab 1: Designed to locate and cache the inverted photoelectron spectra comprising a single data set. Tools for background subtraction and calibration of the images are also provided.

tabs sequentially. This process allows the user to concentrate on the single relevant portion of the fitting process and then use the results of this for all further steps, without having to repeatedly refer to the data each time. As a note, Tab 4 does not require the data from Tab 3 (but does require the data from Tab 2).

Above the tabbed section of the screen are several general options. The 'Save Current Input Variables as Defaults' saves the data containing in each editable box in the program (and all drop-down menus), so that next time the program is opened these do not have to repopulated. The 'Auto-Save' feature of FSfit generates a file with all of the input and output variables of the last fit run in FSfit (saved in the working folder), the box at the top selects the name of this file. The 'Print Screen' button takes a screen grab and offers the option to choose the name it is saved under. This can be useful as a method of rapidly saving the input and output data used to obtain a specific fit. The final, critical box contains the calibration factor, used to convert the photoelectron spectra from velocity space to energy space.

Tab 1: Loading data

This tab (screen grab shown in Figure A.1) contains options required to locate and cache the inverted (and background subtracted) photoelectron images, which

comprise our experimental data. This is a requirement, before further analysis can occur.

The 'Working Folder' button allows the user to locate the parent (or working folder) in which the dataset of interest is contained. This folder should contain a series of sub-folders containing the individual spectra.

Prior to inverting the photoelectron spectra for each pump-probe delay, it is first necessary to subtract out the one-colour (pump + pump and probe + probe) contributions. The 'Pre-Inversion Steps' button in the bottom left corner is provided to rapidly conduct this subtraction for each temporal delay. The resultant file is named 'Signal.txt' and is placed in the relevant folder.

The folder names are chosen by the experimenter, but the usually contain information regarding the pump and probe wavelengths and absolute position of the linear translation stage, which introduces the temporal delay between the two. Alternatively, some previous experimenters have chosen to name the folders with respect to the assumed temporal position (relative to some approximate time zero position). This convention is discouraged, because the calculated position of time zero may move slightly during analysis and consequently the folder names become misleading. However, FSfit has sufficient options to accept folders named by either convention and the user must select which from the 'Folders Named with respect to' drop-down menu. If the folders are named by temporal delay (e.g. +200 fs) with respect to an assumed time zero position, this position must be indicated in the box provided.

The three input boxes allow the user to specify the naming convention they chose when saving the experimental data. Pump and probe wavelengths and other information should be common between a given dataset. In order for FSfit to be able to determine which folders contain relevant data, it will only search for data in folders which EXACTLY match the strings provided here.

Moving the linear translation stage used to introduce delays between the pump and probe pulses would be practically difficult, so it is more common to change the

emission wavelengths of the OPAs. The result is that sometimes the pump beam uses the mirrors on the translation stage and sometimes the probe beam does. Altering this also alters whether moving the translation stage in the 'positive' or 'negative' direction (as defined by the Physik Instruments software) induces an increase in the pump-probe delay or a decrease. If the data folders are named with respect to position, it is therefore necessary to specify whether the pump or probe beam traverses the translation stage - a drop down menu is provided for this purpose.

The 'Inverted Data Filename' box requires the user to state the name of the file containing the (must be common to all data-containing folders in the dataset). This file is assumed to have been generated by the 'Image Inversion' program and data is extracted accordingly.

The 'Remove Central Pixels' checkbox removes the central 12 pixels from the used data. Due to the nature of the pBasex inversion algorithm, these data point often contain significant noise. If suitable VMI voltages are selected they contain little relevant data, therefore it is recommended that this option remains selected.

The 'Load Data' button loads the data, ready for subsequent analysis in the later tabs. The data points located will be displayed in the table on the right hand side. If some data points do not appear when the data is loaded, please check that the folder names adhere to the naming convention specified.

An additional tool is provided to determine the calibration factor from an inverted image of Xenon ionised by $2 + 1$ non-resonant ionisation (usually using 249.5 nm). Following this procedure will auto-populate the calibration value box in the top right of the FSfit window. If another method is used to calibrate the detector, the user can manually enter the calibration factor into this box.

Tab 2: Time zero fit

This tab (screen grab shown in Figure A.2) allows the user to scale the individual spectra collected to the total integrated photoelectron signal, with respect to pump-probe delay.

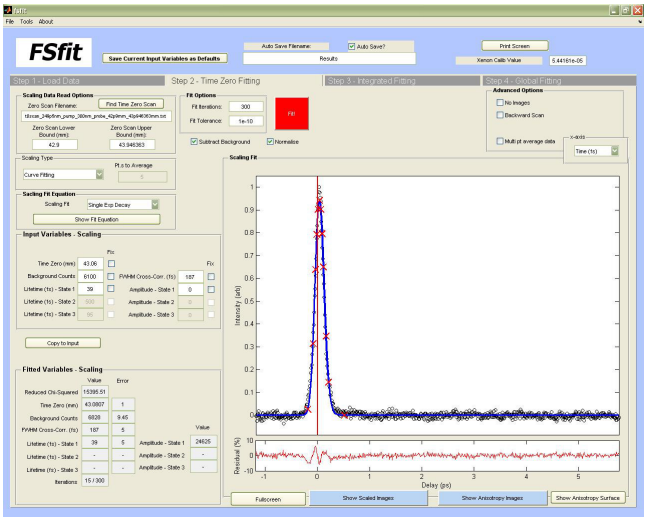

Figure A.2: FSfit, Tab 2: Fitting to the total integrated photoelectron signal, with respect to time, allows for scaling of individual spectra.

The top left options require the user to locate the file containing this data and to manually input the lower and upper positions of the delay stage, when the data was collected. It is assumed that the translation stage was moving at a constant velocity between these two points. If the

The 'Scaling Type' menu allows the user to choose between normalise to a running average or to a curve fitted to the data points. Using a running average is recommended only in the case where the curve fitting option fails to adequately describe the data.

Selecting the curve fitting option requires the user to select an appropriate fit function. A simple Gaussian can be chosen, or more complex linear combinations of exponential decays convoluted with a Gaussian instrument response function (see Equation 2.10).

The input variables box allows the user to specify the initial values for the variables in the curve function. Checking the 'Fix' box next to each input means that the selected value will not be optimised by the solver.

The 'Fit Options' box allows specifications of the various parameters used by the fitting algorithm. The red 'Fit' button will attempt to fit the specified curve function

to the data (the button turns green whilst calculating), this should generally take less than 20 seconds. The fitting optimisation procedure is based upon least-squares fitting using the Levenberg-Marquardt algorithm (for all of the fitting in FSfit). Uncertainties in the various parameters are derived from the Jacobian of this least-squares fit and are quoted to the 2σ level. The fitted values will be displayed in the boxes in the bottom left hand corner of the screen. Although the time zero and cross-correlation can be extracted from this fit, the values produced are usually slightly less reliable than those determined by fitting the highest eKE (or most separable) peak in the photoelectron spectrum in Tab 3.

Once a fit has been successfully completed, a plot will be generated showing the data points (open circles), the fitted function (blue line) and the positions of the photoelectron spectra which have been loaded (red crosses). A residual plot is also generated, showing the difference between the fit and the data points, so that a fit which poorly describes the data at particular delays can be readily identified. The residual should generally be $\sim$5%.

The user can choose whether to display the x-axis with respect to translation stage position, or time. If this options changed, the graph must be refreshed by clicking the 'Fit' button again.

Buttons are provided at the bottom of the screen, which will generate the fitted plot in a separate MATLAB window, this allows the user to manipulate the appearance of the plot and save it to various image formats for later use.

Tab 3: Energy integrated fitting

This tab (screen grab shown in Figure A.3) allows the user to integrate over a particular energy range of the photoelectron spectrum (for each pump-probe delay) and fit to the data obtained. If states can be readily identified by prior knowledge or by features in the spectrum. In cases where separable states exist, this approach allows for much more rapid and reliable fitting than a 'blind' global fit, which can often converge to local minima. The lifetimes obtained from this fit can, however be fed into a constrained, quasi-global fit, to ensure convergence.

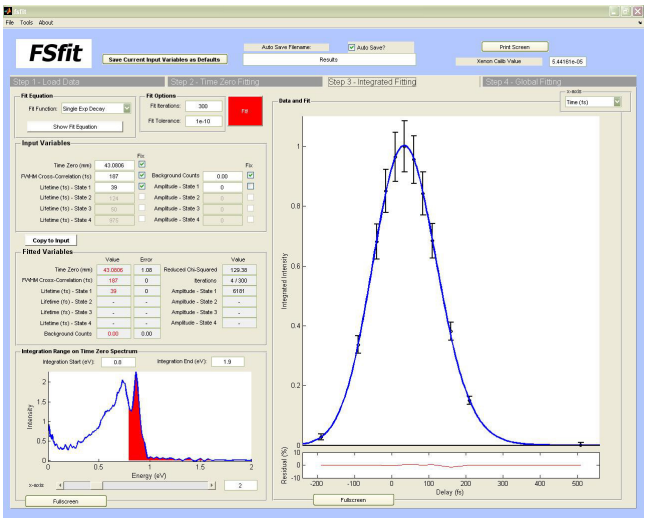

Figure A.3: FSfit, Tab 3: Fitting to energy integrated ranges of the photoelectron spectrum, when combined with prior knowledge, allows for relatively easy identification of the contributing states.

Selecting the curve fitting option requires the user to select an appropriate fit function, using linear combinations of exponential decays convoluted with a Gaussian instrument response function (see Equation 2.10).

The input variables box allows the user to specify the initial values for the variables in the curve function. Checking the 'Fix' box next to each input means that the selected value will not be optimised by the solver.

The 'Fit Options' box allows specifications of the various parameters used by the fitting algorithm. The red 'Fit' button will attempt to fit the specified curve function to the data (the button turns green whilst calculating), this should generally take less than 20 seconds. The fitting optimisation procedure is based upon least-squares fitting using the Levenberg-Marquardt algorithm (for all of the fitting in FSfit). Uncertainties in the various parameters are derived from the Jacobian of this least-squares fit and are quoted to the 2σ level. The fitted values will be displayed in the boxes in the left hand side of the screen.

The plot in the bottom left shows the photoelectron spectrum closest to the fitted time zero position (blue line) and the integration area (red area).

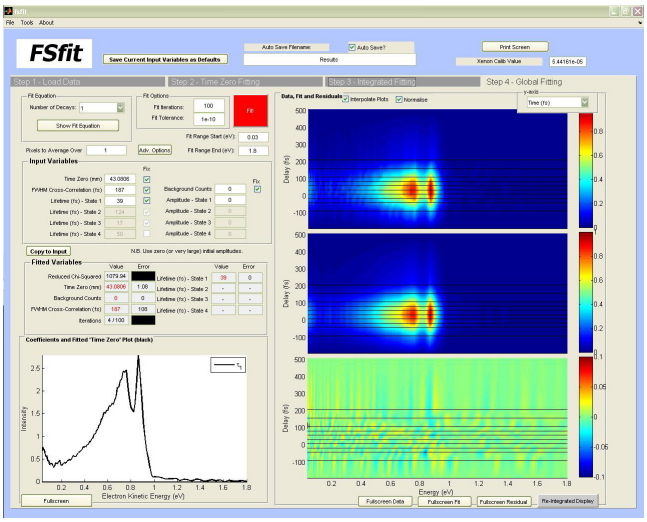

Figure A.4: FSfit, Tab 4: Global fitting is the most unbiased approach to obtaining decay lifetimes, but can be susceptible to finding local minima. Combination with the energy integrated fitting on Tab 3 can provide a powerful tool for disentangling decay lifetimes.

The large plot on the right shows the data points, with 2σ error bars (black) and the fit function (blue line). Below this is a residual plot, showing the difference between the fit and the data points, so that a fit which poorly describes the data at particular delays can be readily identified.

Buttons are provided at the bottom of the screen, which will generate the fitted plot in a separate MATLAB window, this allows the user to manipulate the appearance of the plot and save it to various image formats for later use.

Tab 4: Global fitting

This tab (screen grab shown in Figure A.4) allows the user to globally fit decay functions (of the form in Equation 2.10) to the photoelectron spectra. This can be done completely freely (no constraints), or by using values obtained by energy integrated fitting (and fixing them).

Selecting the curve fitting option requires the user to select an appropriate number of fit functions to use in the linear combinations of exponential decays convoluted with a Gaussian instrument response function (see Equation 2.10).

The user is also able to average the spectrum over any (odd) number of energy pixels prior to fitting. The user is also able select the eKE range, over which the fit is carried out, it is not recommended that this be used to truncate data containing portions of the spectrum (Tab 3 is better for this purpose). Instead this option is designed to remove the outer edge of the image, which contains no useful information, but will significantly contribute to the number of degrees of freedom available to the fitting algorithm and the subsequent calculation time.

The input variables box allows the user to specify the initial values for the variables in the curve function. Checking the 'Fix' box next to each input means that the selected value will not be optimised by the solver. The spectra which are to be fitted can be averaged over several pixels (an odd number), which is useful for initial examination of the data, as it drastically reduces the time taken to converge on a result. It is also possible to use the 'Adv. Options' dialog button to specify one pixel must lie in the center of an averaged bin. Use of this option is critical if the spectrum contains a very sharp feature, which might be obscured or lost if averaged over two separate bins.

The 'Fit Options' box allows specifications of the various parameters used by the fitting algorithm. The red 'Fit' button will attempt to fit the specified curve function to the data (the button turns green whilst calculating), this should generally take less than 5 minutes although significant variation will occur depending upon the initial values used and the number of degrees of freedom in the fit (eKE range and number of decaying states). The fitting optimisation procedure is based upon least-squares fitting using the Levenberg-Marquardt algorithm (for all of the fitting in FSfit). Uncertainties in the various parameters are derived from the Jacobian of this least-squares fit and are quoted to the 2σ level. The fitted values will be displayed in the boxes on the left hand side of the screen.

Following fitting, three plots will be displayed on the right hand side of the screen. The top graph shows the surface formed by the evolving photoelectron spectra, with respect to pump-probe delay. The middle plot depicts the fitted surface and the bottom plot shows the residual produced by subtracting the fitted surface (middle)

from the original data surface (top). The residual surface is included to illustrate any discrepancies between the fitted surfaces and the original data, for example if the time zero/zero delay position is poorly fitted, a large systematic error will be visible. An option above these three graphs allows the user to interpolate the surface between each data point, which produces a smoother surface.

A further plot is shown in the bottom left hand side of the screen, which depicts the decay associated spectrum (DAS). DAS plots have been shown to provide valuable information for interpreting energy flow between electronic states. [93–96]. Positive coefficients indicate a decay in photoelectron signal on the stated timescale and negative coefficients indicate a rise in photoelectron signal. The sum of all of the DAS coefficients is shown in black, the shape of which gives the shape of the initially excited states, without cross-correlational broadening (i.e. the 'true' $t = 0$ photoelectron spectrum).

Buttons are provided at the bottom of the screen, which will generate the fitted plot in a separate MATLAB window, this allows the user to manipulate the appearance of the plot and save it to various image formats for later use.

Appendix B

Aniline lifetime re-analysis

All of the data presented in Chapter 4 is newly collected, although in some instances there is a strong overlap with our previously published work. [87, 152, 169] The program FSfit was written in between these publications and uses a slightly adapted fitting and data analysis procedure. The fitting optimisation algorithm has also been changed, from the MIGARD procedure (Davidon–Fletcher–Powell variable-metric algorithm) implemented in ROOT [206] to the more commonly used Levenberg-Marquardt least squares fitting algorithm.

Due to this change in data analysis procedure, this appendix section re-examines one of the datasets in our previously published paper on aniline, using our new data analysis procedure. We present this comparison to show that the results presented in this Thesis and those in our previous work are equivalent. The lifetimes produced by the new fitting procedure are shown in the upper part of Table B.1, with the lower half recording the original results for ease of comparison (this table is also reproduced in the aniline chapter for ease of reading).

The picosecond lifetimes associated with the $S_1(\pi\pi^*)$ state have not changed and are simply re-quoted, because they are extracted from the total integrated count rate and our method of analysing this has not altered. Additionally, the lifetimes associated with the extremely fast $S_3(\pi\pi^*)$ have not changed significantly, which is

Table B.1: Summary of exponential decay lifetimes for aniline, comparison of re-evaluated data with our previous analysis

Lifetimes (This work)					
Pump wavelength [nm]	$S_3(\pi\pi^*)$ lifetime [fs]	$\pi 3s$ lifetime [fs]	$\pi\sigma^*$ lifetime [ps]	$S_1(\pi\pi^*)$ lifetime [ps]	Cross–correlation (FWHM) [fs]
269	-	181 ± 41	-	$>>$ 1 ns	150 ± 10
250	-	141 ± 16	1.0 ± 0.2	600 ± 35	180 ± 15
240	52 ± 10	91 ± 27	1.4 ± 0.3	185 ± 15	192 ± 10
238	50 ± 10	112 ± 33	1.3 ± 0.7	100 ± 10	203 ± 10
236	123 ± 10	185 ± 47	1.2 ± 0.3	81 ± 10	202 ± 12
Lifetimes (Refs. [169] and [152])					
269	-	230 ± 70	$0.9^{+0.9}_{-0.3}$	$>>$ 1 ns	150 ± 45
250	-	200 ± 45	$1.6^{+2.0}_{-0.8}$	600 ± 35	200 ± 40
240	65 ± 20	280 ± 170	$1.8^{+4.7}_{-1.5}$	185 ± 15	210 ± 20
238	70 ± 15	330 ± 150	$2.4^{+4.8}_{-1.1}$	100 ± 10	185 ± 15
236	116 ± 13	259 ± 133	$1.2^{+4.1}_{-0.8}$	81 ± 10	210 ± 20

not surprising as this lifetime is essentially limited by our cross-correlation width. It is notable that the lifetime associated with the $S_2(\pi 3s/\pi\sigma^*)$ state has reduced from 0.9–2.4 ps to 1.0–1.4 ps. Also, one of the lifetimes associated with this state (at 269 nm) is now deemed too weak to reliably extract a decay lifetime from and therefore this entry is blank in the table. The most notable difference produced by the re–analysis is the changes in the decay lifetimes associated with the $S_2(\pi 3s)$ state, these have reduced from 200–330 fs to 91–185 fs. The new results are more consistent with the results presented in this chapter, but also those in the literature.[52, 96, 156] It should also be noted that the 95% confidence interval (error) associated with the new fitting procedure are noticeably smaller than those previously assigned, presumably due to the change in optimisation algorithm.

In addition to modifying the data analysis methodology, several minor alterations have also been made to our experimental procedure since the previously published work. Firstly, the data presented in this work (*c.f.* Chapter 4) involves several additional data collection points in the region of zero delay position and at negative time delays (the probe–pump region). This allows for more reliable fitting of the zero delay position and the cross-correlation, which subsequently leads to more stable extraction of decay lifetimes.

We have also discovered that due to a software issue, the total integrated count scans previously collected on our experimental equipment had a minor systematic shift. The software used to collect our photoelectron images did not count time correctly and this timing was used, in combination with the scanning velocity of the linear translation stage, to calculate the delays between pump and probe pulses. The error introduced was very small, approximately 1 additional second was counted every 150 seconds. This issue exclusively affected the total integrated photoelectron signals, however our data analysis methodology uses this to normalise the area under individual photoelectron images, so a small error will have propagated into our subsequent data analysis. We have subsequently adapted our data collection methodology, such that the temporal counting issue is eliminated from all data presented in this thesis.

Additionally, our the photoelectron images in our previous publication on aniline were four-way symmetrised, due to damaged portions of the microchannel plate (MCP) photoelectron multiplier. This type of symmetrisation is common amongst the VMI community and there should be no effect upon the decay lifetimes observed. However, we have repaired this damage since the published results were collected, thus the change should be noted.

Finally, we have also slightly altered the experimental setup since the published results, introducing a gate valve into the VMI flight tube, in order to protect the MCPs when venting the vacuum chamber to replenish samples in the pulsed nozzle. The introduction of this gate valve slightly modified the length of the photoelectron flight path, increasing it by $\sim$15 mm. This alteration could affect the ratio of VMI voltages applied to the extractor and repellor plates, however the change did not seem to significantly affect the optimal VMI focussing voltages.

The data presented in Chapter 4 contains several excitation wavelengths which overlap with the previously published work. Comparison of the lifetimes presented in Table B.1 and those in Chapter 4 shows that no significant difference in results has been caused by any of the experimental alterations described above.